PHOTOPHYSICAL STUDIES OF EMERGING NANOCRYSTALS

By

MRINAL KANTI PANDA

CHEM11202104016

National Institute of Science Education and Research, Bhubaneshwar, Odisha - 752050

A thesis submitted to the

Board of Studies in Chemical Sciences

In partial fulfillment of requirements

for the Degree of

DOCTOR OF PHILOSOPHY

of

HOMI BHABHA NATIONAL INSTITUTE

February, 2026

Homi Bhabha National Institute[1]

Recommendations of the Viva Voce Committee

As members of the Viva Voce Committee, we certify that we have read the dissertation prepared by Mrinal Kanti Panda entitled "Photophysical Studies of Emerging Nanocrystals" and recommend that it may be accepted as fulfilling the thesis requirement for the award of Degree of Doctor of Philosophy.

S. No.	Doctoral Committee	Name	Signature	Date
1.	Chairman	Prof. Sudip Barman		02/09/2026
2.	Guide/ Convener	Prof. Subhadip Ghosh		2/09/26
3.	*Examiner	Prof. Saptarshi Mukherjee		02/09/2026
4.	Member - 1	Dr. Bidraha Bagh		02.09.2026
5.	Member - 2	Dr. Dipak Samanta		02.09.2026
6.	Member - 3	Dr. Nimai Mishra		2/9/26

* Attended Online

Final approval and acceptance of this thesis is contingent upon the candidate's submission of the final copies of the thesis to HBNI.
I/We hereby certify that I/we have read this thesis prepared under my/our direction and recommend that it may be accepted as fulfilling the thesis requirement.

Date: 02/09/2026
Place: NISER, Bhubaneswar

Signature
Guide: Prof. Subhadip Ghosh

---

[1] This page is to be included only for final submission after successful completion of viva voce.

STATEMENT BY AUTHOR

This dissertation has been submitted in partial fulfillment of requirements for an advanced degree at Homi Bhabha National Institute (HBNI) and is deposited in the Library to be made available to borrowers under rules of the HBNI.

Brief quotations from this dissertation are allowable without special permission, provided that accurate acknowledgement of source is made. Requests for permission for extended quotation from or reproduction of this manuscript in whole or in part may be granted by the Competent Authority of HBNI when in his or her judgment the proposed use of the material is in the interests of scholarship. In all other instances, however, permission must be obtained from the author.

Mrinal Kanti Panda

DECLARATION

I, hereby declare that the investigation presented in the thesis has been carried out by me. The work is original and has not been submitted earlier as a whole or in part for a degree / diploma at this or any other Institution / University.

Mrinal Kanti Panda

CERTIFICATION ON ACADEMIC INTEGRITY

Undertaking by the Student

I, Mr. Mrinal Kanti Panda, HBNI Enrolment No. CHEM11202104016 hereby undertake that the Thesis, titled "PHOTOPHYSICAL STUDIES OF EMERGING NANOCRYSTALS" Is prepared by me and is the original work undertaken by me.

I also hereby undertake that this document has been duly checked through a plagiarism detection tool and the document is found to be plagiarism free as per the guidelines of the Institute/UGC.

I am aware and undertake that if plagiarism is detected in my thesis at any stage in the future, suitable penalty will be imposed as applicable as per the guidelines of the Institute/UGC.

MK Panda

Mrinal Kanti Panda

Endorsed by the Thesis Supervisor:

I certify that the thesis written by the Researcher is plagiarism free as mentioned above by the student.

Sghosh 02/09/26

Prof. Subhadip Ghosh

Professor

School of Chemical Science

National Institute of Science Education and Research (NISER), Bhubaneswar

List of Publications arising from the thesis

Journals

[#]**1. Mrinal Kanti Panda**, Debopam Acharjee, Nilanjana Nandi, Somnath Koley and Subhadip Ghosh, Unveiling the Influence of Brightness Heterogeneity in Fluorescence Correlation Spectroscopy of Perovskite Nanocrystals, *Chem. Eur. J.* **2024,** 30**,** e202401938. **(Chapter 3)**

[#]**2. Mrinal Kanti Panda**, Debopam Acharjee, Asit Baran Mahato and Subhadip Ghosh, Facet Dependent Photoluminescence Blinking from Perovskite Nanocrystals, *Small,* **2024**, 30, 2311559. **(Chapter 4)**

[#]**3. Mrinal Kanti Panda**, Debopam Acharjee, Asit Baran Mahato and Subhadip Ghosh, Hot Carrier Trapping in Light-Soaked Mixed Phase $CsPbI_3$ Perovskite Nanocrystals, *Adv. Opt. Mater.*, **2025**, 13, 2402899. **(Chapter 5)**

[#]**4. Mrinal Kanti Panda**, Soumik De, Asit Baran Mahato and Subhadip Ghosh, Unveiling Facet-Controlled Energy Transfer from Individual Perovskite Nanocrystals to Dyes, *ACS Energy Lett.*, **2025,** 10, 4834-4841. **(Chapter 6)**

([#] Pertaining to the thesis)

Others:

5. Subarna Biswas[†], **Mrinal Kanti Panda**[†], Shovon Chatterjee, Jit Satra, Shilendra Kumar Sharma, Jyotisman Rath, Abhijit Dutta, Debopam Acharjee, Sudip Chakraborty, Subhadip Ghosh and Nimai Mishra, Synergistic Mitigation of Phase Segregation and Blinking Suppression Along with Enhanced Electrocatalytic Activity in $CsPbBrI_2$ Perovskite Nanocrystals via Ascorbic Acid Surface Treatment, *Adv. Funct. Mater.* **2025**, 35, 2505506. ([†]Contributed Equally)

6. Rahul Murali[†], **Mrinal Kanti Panda**[†], Rajendra Kumar Challa, Debopam Acharjee, Venugopal Rao Soma, Subhadip Ghosh, Sai Santosh Kumar Raavi, Bright and Stable

Single-Photon Emission in Zinc-Alloyed $CsPbBr_3$ Nanocrystals Through Controlled Auger Recombination, *Small*, **2025**, 22, e05011. ([†]Contributed Equally)

7. Debopam Acharjee, Ayendrila Das, **Mrinal Kanti Panda**, Manas Barai and Subhadip Ghosh, Facet engineering for decelerated carrier cooling in polyhedral perovskite nanocrystals, *Nano Lett.*, **2023**, 23, 1946-1953.

8. Ayendrila Das, Debopam Acharjee, **Mrinal Kanti Panda**, Asit Baran Mahato and Subhadip Ghosh, Dodecahedron $CsPbBr_3$ Perovskite Nanocrystals Enable Facile Harvesting of Hot Electrons and Holes, *J. Phys. Chem. Lett.*, **2023**, 14, 3953-3960.

9. Debopam Acharjee, **Mrinal Kanti Panda**, Asit Baran Mahato, Ayendrila Das and Subhadip Ghosh, Evidence of carrier diffusion between emission states in CdSe/ZnS core–shell quantum dots: a comprehensive investigation combining fluorescence lifetime correlation spectroscopy (FLCS) and single dot photoluminescence studies**,** *Nanoscale***,** **2024**, 16, 18444-18454.

10. Asit Baran Mahato, Debopam Acharjee, **Mrinal Kanti Panda**, Dipak Samanta and Subhadip Ghosh, Investigation of Carrier Dynamics in CdSe/ZnS Core–Shell Quantum Dots via Scanning Fluorescence Correlation Spectroscopy, *J. Phys. Chem. C*, **2024**, 128, 16588–16596.

11. Debopam Acharjee, Shreya Mishra, Asit Baran Mahato, **Mrinal Kanti Panda**, Dipak Samanta and Subhadip Ghosh, Hot carrier harvesting at the interface of $CsPbI_3$ nanocrystals, *Nanoscale*, **2025**, 17, 11615-11623.

12. Shreya Mishra, Debopam Acharjee, Soumik De, Asit Baran Mahato, **Mrinal Kanti Panda**, Dipak Samanta, Surajit Ghosh and Subhadip Ghosh, Benzoquinone-Induced Hot Carrier Extraction in Red-Emitting Perovskite Nanocrystals, *J. Phys. Chem. C*, **2025,** 129, 14458-14466.

13. Debopam Acharjee, Asit Baran Mahato, **Mrinal Kanti Panda** and Subhadip Ghosh,

Non-convergence of the blinking timescale of twelve-faceted perovskite nanocrystals observed through an advanced fluorescence correlation spectroscopy study, *Phys. Chem. Chem. Phys.*, **2025**, 27, 824-833.

14. Somnath Koley, Shraban Dey, Debopam Acharjee, Mrinal Kanti Panda, Jit Satra, Sachindra Nath Sarangi, Tapas Kuila and Karuna Kar Nanda, Reconfigurable Phototactic Micromotors from Fractal Self-Assembly of Dark Carbon Nanodot Sols: A Perfect Mimic of Colonial Green Algae, *Adv. Mater. Technol.* **2025**, 10, e00363.

15. **Mrinal Kanti Panda**, Ankita Ganguli, Supriya Panda, Asit Baran Mahato and Subhadip Ghosh,* Watching Blinking- and Photobleaching-Regulated Dexter Energy Transfer in Single Perovskite Nanocrystal-Dye Hybrids. (Submitted)

Conferences and Presentation

1. **Poster Presentation:** International Conference on Interdisciplinary Approaches in Chemical and Biological Sciences (IACBS-2025) IIT (ISM) Dhanbad, India (1^{st} -2^{nd} December, 2025).

(**ACS Omega Best Poster Award**)

2. **Poster Presentation:** Inter IISER-NISER Chemistry Meet-2025 IISER Pune, India (20^{th} -22^{th} March, 2025).

(**ACS Inorganic Chemistry Best Poster Award**)

3. **Poster Presentation:** National Conference on Fluorescence and Raman Spectroscopy (FCS-XVI) SINP, Kolkata, India (8^{th} -10^{th} December, 2025).

(**Top 17 Posters**)

4. **Oral Presentation:** Symposium on Interdisciplinary Sciences (SIS II-2025) NISER Bhubaneswar, India.

5. **Poster Presentation:** Society of Physical Chemistry Symposium (SoPhyC-2025) IIT Patna, India (11^{th}-12^{th} October, 2025).

6. **Poster Presentation:** 16th National Symposium on Radiation & Photochemistry (NSRP-2025), NISER Bhubaneswar, India (23^{th}-25^{th} January, 2025).

7. **Poster Presentation:** 4^{th} Materials Chemistry Symposium, NISER Bhubaneswar, India (28^{th}-29^{th} August, 2025)

8. **Poster Presentation:** International Conference on Metal Halide Perovskites (HyPe-2024) NISER Bhubaneswar, India (19^{th}-22^{nd} December, 2024).

9. **Poster Presentation:** Physical Chemistry Symposium -2024 (SoPhyC-2024), IIT Bombay, Powai, Mumbai 400076, Maharashtra, India (22^{th}-25^{th} October, 2024).

10. **Poster Presentation:** Ultrafast Science (UFS-2024) NISER, Bhubaneswar, India (28^{th} -30^{th} 2024).

11. **Poster Presentation:** International Conference on Functional Materials and Polymer Technology (ICFMPT-2024) Institute of Physics (IOP), Bhubaneswar, India (14th -16th March, 2024).

Mrinal Kanti Panda

Dedicated

to

Maa Baba

ACKNOWLEDGEMENTS

This thesis presents an overview of the research work I carried out during my five-year PhD tenure. The progress and accomplishments of my academic journey are deeply rooted in my enduring passion for science and unwavering dedication to research. However, this achievement would not have been possible without the generous support, guidance, and encouragement of numerous individuals and institutions. I express my profound and heartfelt gratitude to all those who, in diverse ways, have played a pivotal role in shaping my academic growth and contributing to the successful completion of my doctoral studies.

I would like to extend my heartfelt thanks to my thesis supervisor and mentor ***Prof. Subhadip Ghosh****. He has been more than just a supervisor; he has been a mentor whose guidance extended beyond academics into my personal growth. His dedication to research served as a constant source of inspiration, helping me remain resilient during the challenges of the PhD. His exceptional command over fundamental concepts, coupled with his deep insight into contemporary advances in science, played a pivotal role in shaping my research direction and enabling the publication of significant findings that would have been difficult to achieve otherwise. I sincerely admire his profound dedication to research, and I have endeavoured to incorporate this approach into my own academic and future research pursuits.*

Furthermore, I sincerely and profoundly acknowledge the ***Department of Atomic Energy (DAE)****, India, for their generous financial support, which greatly eased the challenges associated with my doctoral studies. I am deeply grateful to the* ***National Institute of Science Education and Research (NISER), Bhubaneswar****, India, for providing an excellent research environment and state-of-the-art infrastructure, and to the* ***Homi Bhabha National Institute (HBNI)****, India, for facilitating my academic registration. I also extend my heartfelt thanks to the esteemed members of my doctoral committee—Prof. Sudip Barman, Dr. Bidraha Bagh, Dr. Dipak Samanta, Dr. Nimai Mishra and Dr. Sai Santosh Kumar Raavi—whose invaluable insights, constructive feedback, and continued guidance have been instrumental in shaping both the direction and the overall quality of my research work.*

I extend my gratitude to the esteemed faculty members and dedicated staff of the School of Chemical Science (SCS) for the support and guidance throughout my academic journey. I also thank the whole team of Centre of Interdisciplinary Sciences (CIS) and all the working stuff members who has made my path easier is every possible way.

My sincere gratitude also goes out to my fellow researchers and labmates, including ***Dr. Krishna Mishra, Dr. Ayendrila Das, Dr. Debopam Acharjee, Mr. Asit Baran Mahato, Dr.***

Somnath Koley, Dr. Nilanjana Nandi, Ms. Shreya Mishra, Mr. Soumik De, Ms. Supriya Panda, Ms. Ankita Ganguly, Dr. Manas Barai, Mr. Subarna Biswas, Dr. Shovon Chatterjee Mr. Sayantan Maity, Mr. Rahul Murali, Mr. Sanat K. Mahankudo, Mr. Akash B. Sonwane, Mr. Prajna Pratima Malik, Mr. Umakant Malik. *The collaborative atmosphere and support from these colleagues have made my Ph.D. journey smoother and more enriching. I really respect Krishnadi for emotional support in my difficult times and keeping motivated towards research. I fondly remember the wonderful days spent learning confocal microscopy from Ayendriladi, along with our meaningful discussions on maintaining a healthy balance between career and life. I deeply admire her remarkable presence of mind and her ability to efficiently resolve the challenges encountered during various experimental measurements. Debopamda has been like a brother to me; we have struggled together, celebrated successes together, and shared countless moments along the way. My PhD journey would have been far more challenging without his constant support and comforting presence. I truly miss his companionship. Asit, my little brother, holds a very special place in my heart—perhaps I love him the most—and I wish him nothing but the greatest success in life. I have also been fortunate to experience love, care, and warmth from my dear juniors, and I feel truly blessed to have had their companionship right up to my last day in the lab.*

Beyond the realm of research, I was fortunate to cultivate an outstanding group of friends who made my doctoral journey truly memorable. Our BMRS group holds a very special place in my heart. ***Dr. Buddhadev Pal, Mr. Raghunath Singha, and Mr. Subhajit Kar*** *and I came together at NISER with great hope and enthusiasm to pursue research and explore the vast world of science. They have been an inseparable part of my PhD journey, providing constant support, encouragement, and companionship. I am also deeply grateful to* ***Dr. Subhadip Banerjee, Dr. Surajit Panda, Mr. Manatosh Dalapati, Mr. Biplab Manna, Dr. Pankaj Maity, and Mr. Pijush De*** *for their friendship, support, and invaluable moments that enriched my time at NISER.*

I would like to acknowledge my batch mates, ***Saiprakash Rout, Satyapriya Nath, Ankita Panda, Sagarika Rajput, Rosalin Bhanja*** *and others whose companionship has been an integral part of academic and personal growth.*

I express my deepest and most heartfelt gratitude to my first teacher, Uttam Kumar Panda, who ignited my curiosity for learning and laid the very foundation of my educational journey. I remain sincerely thankful to all my school teachers and college professors whose constant encouragement, guidance, and faith in me inspired my pursuit of academics and helped me stay committed to the right path. I am especially grateful to my college professor, ***Dr. Samir***

***Kumar Mandal**, and my M.Sc. supervisor, **Prof. Bidhu Bhusan Das**, for believing in my abilities and for their unwavering support, mentorship, and encouragement at every stage of my academic and professional growth.*

*Finally, I own everything that I have achieved, everything I have and everything that I will get to my family. Their constant support, love and encouragement acts as a fuel to my journey. I dedicated my PhD thesis to my mother **Mira** and father **Sukumar**. What I am today is because of them, their countless sacrifice to make me a better human being. My father used say "□□□□□ □□□ □□□ □□□□ □□□□□□□ □□□□□□□, □□□ □□□ □□□ □□ □□□□□□□ □□□□□□" and I follow those words in every aspect of my life. My mother always dreamed of seeing me achieve higher education, and I consider myself truly fortunate to be fulfilling her cherished dream. I want to acknowledge **Nilanjana**, my best friend and life guide. I really own every ounce of my PhD journey. Your unwavering support, hope, and encouragement have carried me forward through every challenge Your words have given me the strength—the Shakti—to overcome even the most daunting obstacles. In my darkest days, you have been the light that illuminated my path, and for that, I am eternally grateful. I am also deeply grateful to my sister, **Subhasree**, and my brother-in-law, **Dhananjay Mahanty**, for their unwavering belief in me and their constant support in every possible way. I share my deepest love with my beloved niece, **Sana**; countless times, her cheerful giggles and radiant smile have brightened my most stressful days. I sincerely thank **Bhagabati Bhowmik** and **Ananta Bhaumik** for loving me like a son, and **Anurag** for supporting me like a brother at every step of this journey. My love and gratitude for them are truly boundless. Lastly, I wish to honor the memory of my beloved great-grandfather and great-grandmother. Though they are no longer here to witness my achievements, I feel their blessings and love guiding me, and I am certain that from heaven, they are smiling upon their cherished grandchild.*

Mrinal Kanti Panda

CONTENTS

SYNOPSIS

CHAPTER 1: Introduction

Quantum-confined materials exhibit a remarkable optical phenomenon known as fluorescence, in which photoexcited charge carriers relax to lower energy states through radiative emission at longer wavelengths. Fluorescence underpins a broad spectrum of scientific, biomedical, and technological applications and is governed by materials known as fluorophores. Among emerging fluorophores, perovskite nanocrystals (PNCs) have attracted significant attention owing to their outstanding optoelectronic properties, including tunable emission, narrow spectral linewidths, high photoluminescence quantum yields, and notable defect tolerance. These attributes make PNCs highly promising for next-generation optoelectronic devices such as light-emitting diodes, lasers, and solar cells. [1-5]

Despite their relative defect tolerance, PNCs are not entirely free from imperfections. The presence of trap states often gives rise to photoluminescence intermittency (blinking), while their susceptibility to moisture, heat, and prolonged illumination can lead to rapid degradation. Stability challenges are further exacerbated when nanocrystals exhibit heterogeneous size or spatial distributions, often originating from limitations in synthetic protocols. Nevertheless, perovskite quantum dots remain compelling candidates as single-photon emitters, a key requirement for quantum communication technologies. [6,7]

In this thesis, these challenges are systematically addressed through a combination of ensemble-level and advanced single-particle spectroscopic techniques. The carrier dynamics of lead halide perovskite nanocrystals with varying size, shape, and morphology are investigated to uncover the underlying photophysical mechanisms that govern their performance and limitations. In addition, the functional efficiency of these nanocrystals is evaluated through detailed studies of energy and charge transfer processes. Recent advances in

morphology-controlled PNCs beyond the conventional cubic structure, particularly faceted architectures, have demonstrated superior photophysical behaviours. Motivated by these developments, this chapter focuses on the photophysical properties of recently developed 6-faceted cubic (c-PNCs), 12-faceted rhombic dodecahedra PNCs (d-PNCs), 26 faceted rhombicuboctahedron PNCs (r-PNCs) highlighting their potential for advanced device applications. [8-10] The chapter also provides an overview of the materials, key photophysical concepts, and single-particle spectroscopic methodologies employed to elucidate carrier dynamics in lead halide perovskite nanocrystals.

CHAPTER 2: Advanced Instrumentation and Methodology

This chapter presents the instrumentation and analytical strategies used to investigate light–matter interactions in semiconductor nanostructures, with particular emphasis on techniques capable of resolving dynamics at the single-particle level. A suite of time-resolved fluorescence methods is employed to probe excited-state behaviour, transport, and emission intermittency. Excited-state decay dynamics are examined using photon-timing approaches, while particle diffusion, heterogeneity in emissive states, and lifetime fluctuations are accessed through correlation-based analyses under tailored excitation schemes. Single-emitter photon statistics, including intermittency and non-classical light emission, are measured using coincidence detection in a confocal geometry, providing insight into charge trapping, carrier localization, and nanoscale energy transfer pathways. Ultrafast optical measurements are additionally used to capture sub-picosecond carrier relaxation and charge transfer events. Structural and morphological properties of the nanomaterials are independently assessed using electron microscopy and diffraction techniques, enabling correlation between optical response and material structure. The chapter concludes with an overview of the core data analysis principles applied throughout this work, while detailed computational workflows and representative case studies are introduced in later four chapters.

CHAPTER 3: Unveiling the Influence of Brightness Heterogeneity in Fluorescence Correlation Spectroscopy of Perovskite Nanocrystals

(Ref: M. K. Panda, D. Acharjee, N. Nandi, S. Koley, S. Ghosh,* *Chem. Eur. J.*, **2024**, *30*, e202401938)

Nanoparticles, including perovskite nanocrystals that exhibit single-photon emission, pose unique challenges for fluorescence correlation spectroscopy (FCS) because their emission dynamics differ fundamentally from those of conventional molecular fluorophores. In these systems, both the zero-lag correlation amplitude, $g^2(0)$, and the characteristic diffusion time extracted from FCS measurements display a pronounced dependence on excitation power. Such behavior cannot be satisfactorily explained by optical saturation, which typically governs power-dependent effects in dye molecules but fails to account for the response observed in nanoparticle-based emitters. Earlier interpretations have attributed the reduction in $g^2(0)$ at high excitation intensities to an apparent increase in particle number within the detection volume, arising from mechanisms such as photoactivation or optical trapping. However, advanced FCS experiments employing pulsed interleaved excitation (PIE) at two distinct power levels demonstrate that these mechanisms do not govern the observed trends.

By correlating ensemble FCS measurements with single-particle photoluminescence trajectories, we identify brightness variability among individual nanoparticles as the primary origin of the excitation-power dependence seen in conventional FCS. This intrinsic heterogeneity, manifested as stochastic blinking, leads to substantial deviations of the correlation curves from ideal behaviour, particularly at elevated pump intensities. While minor contributions from saturation cannot be completely excluded, they play only a secondary role. Notably, when pulsed interleaved excitation FCS (PIE-FCS) is employed, both $g^2(0)$ and the diffusion time become largely independent of excitation power, in stark contrast to their strong power sensitivity under continuous-wave excitation. This finding conclusively eliminates

photo-brightening and optical trapping as dominant factors influencing FCS measurements of nanoparticles at high excitation densities.

Further insight is obtained from single-particle intensity time traces, which reveal that nanoparticle blinking follows power-law statistics, with excitation-dependent ON and OFF transition rates. The coexistence of power-law intermittency and diffusive motion, coupled with overlapping timescales, precludes the use of standard analytical models for quantitative fitting of FCS data.

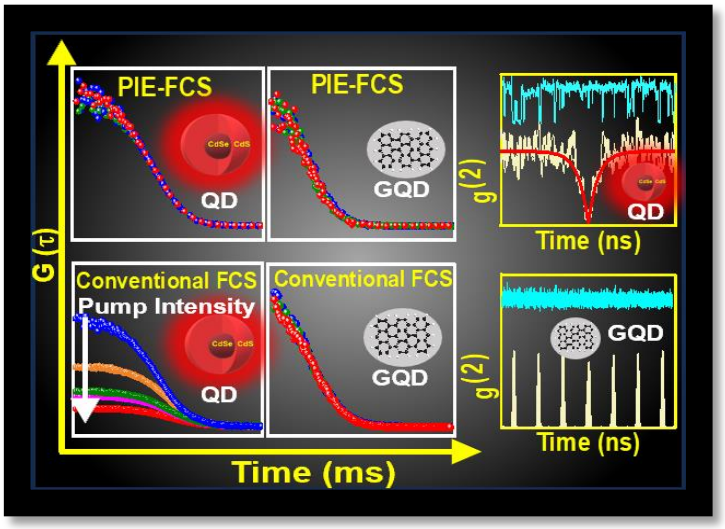

As a result, brightness heterogeneity can easily masquerade as other excitation-induced phenomena if not properly accounted for. Our analysis shows that increasing excitation power qualitatively alters the FCS response across all correlation times due to changes in the OFF-time statistics, underscoring the need for caution when applying high excitation powers in FCS studies of strongly blinking nanomaterials. Ultimately, rigorous theoretical and computational modelling will be required to establish a quantitative framework linking power-law blinking dynamics to their impact on FCS observables.

CHAPTER 4: Facet Dependent Photoluminescence Blinking from Perovskite Nanocrystals

(Ref: M. K. Panda, D. Acharjee, A. B. Mahato, S. Ghosh,* *Small* **2024**, *20,* 2311559)

Emission fluctuations in nanoparticles are commonly viewed as an obstacle for optical

imaging, yet these fluctuations can become a desirable feature for advanced display technologies if charge states are deliberately and reversibly controlled. Realizing such control depends on a clear understanding of how charges are generated, stored, and released at the nanoscale. Although electrochemical methods have been widely used to stabilize charged excitonic states and regulate emission dynamics in various nanomaterials, approaches that rely on intrinsic surface characteristics have received little attention in the context of perovskite nanocrystals (PNCs). Modifying surface structure therefore presents an attractive and chemically accessible pathway for influencing photoinduced charging behaviour.

Here, we show that engineering the crystallographic facet architecture of PNCs leads to pronounced differences in their emission intermittency. Analysis of time-resolved photoluminescence from individual nanocrystals reveals a clear rise in the fraction of dark states as the number of exposed facets increases from six to twenty-six. This behaviour suggests that nanocrystals with higher number of facets are more susceptible to light-driven charge accumulation. The increased sensitivity to photo charging can be traced to the polar nature of additional facets and the expanded surface interface, both of which enhance the likelihood of charge localization. Supporting evidence from fluorescence correlation spectroscopy (FCS) further indicates that facet-rich nanocrystals more readily associate with nearby molecular species, promoting charge-transfer interactions that favour photo charging.

Direct comparison between ensemble measurements in solution and single-particle experiments in the solid state uncovers a strong morphology-dependent contrast in blinking behaviour. In solution, where long-lived charging is largely suppressed, nanocrystals of different shapes exhibit similar emission dynamics. In the solid state, however, nanocrystals with a higher number of facets display significantly greater probabilities of entering charged states, leading to a substantial increase in dark-state occupancy. This behaviour originates from a combination of factors inherent to extra-faceted nanocrystals, including polar surface

terminations, enhanced interactions with environmental charge scavengers, and increased surface area. These influences are largely neutralized in solution, resulting in uniformly lower dark-state populations regardless of morphology.

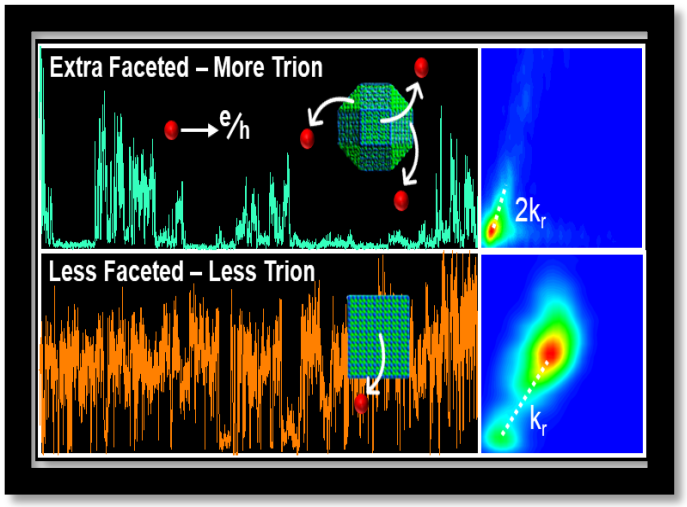

Further analysis of the underlying recombination pathways reveals that, when photo charging is negligible, emission intermittency in solution is governed primarily by non-blinking channel recombination mediated by shallow traps near the band edge, despite the intrinsically high defect tolerance and strong photoluminescence efficiency of the PNCs. In contrast, at the single-particle level, Auger recombination dominates the blinking process and exhibits a pronounced dependence on nanocrystal shape. This sensitivity of Auger-driven blinking to surface morphology provides a practical means to tune emission behavior through deliberate surface design. Altogether, these findings demonstrate that facet engineering offers a powerful strategy for controlling photoluminescence intermittency and positions extra-faceted perovskite nanocrystals as compelling candidates for future display technologies.

CHAPTER 5: Hot Carrier Trapping in Light-Soaked Mixed Phase $CsPbI_3$ Perovskite Nanocrystals

(Ref: M. K. Panda, D. Acharjee, A. B. Mahato, S. Ghosh,* *Adv. Optical Mater.* **2025**, *13*, 2402899.)

Red-emitting $CsPbI_3$ perovskite nanocrystals (r-PNCs) have attracted considerable attention

for optoelectronic applications because of their narrow bandgap, yet their performance is severely limited by pronounced photoluminescence (PL) blinking and photoinduced structural instability. Under ultraviolet illumination, the optically bright and structurally stable α-phase rapidly evolves into a poorly emissive mixture of δ- and γ-phases, whereas nanocrystals synthesized using advanced protocols can retain their α-phase and high PL intensity for extended periods in the dark. To elucidate the mechanisms underlying these contrasting behaviors, we systematically investigate PL intermittency and carrier recombination pathways in both α-phase and light-transformed mixed-phase r-PNCs. Single-particle measurements reveal that even nanocrystals initially stabilized in the α-phase experience rapid structural and electronic modifications during optical excitation, as reflected by a gradual reduction in ON-state emission intensity and corroborated by changes in X-ray diffraction patterns. Detailed blinking analyses using fluorescence lifetime–intensity distribution (FLID) mapping and fluorescence lifetime correlation spectroscopy (FLCS) demonstrate that freshly prepared α-phase r-PNCs are dominated by dynamically fluctuating shallow trap states located near the band edge. These traps act as multiple non-radiative recombination centers, giving rise to short-lived blinking events. In contrast, prolonged light exposure generates mixed-phase nanocrystals characterized by the emergence of long-lived trap states, which promote dispersive blinking behavior governed primarily by hot-carrier recombination. A combined single-particle and ensemble-level investigation, incorporating intensity–lifetime scaling, FLID analysis, and FLCS measurements, uncovers fundamentally distinct recombination landscapes in the two structural phases. In α-phase nanocrystals, blinking is largely controlled by shallow trap-assisted non-blinking channel (NBC) recombination, with only a minor contribution from hot-carrier pathways. Conversely, mixed-phase nanocrystals exhibit blinking dominated by deep trap-mediated hot-carrier recombination, accompanied by additional contributions from trion formation and NBC processes. FLCS measurements further confirm

the enhanced role of trap states in mixed-phase systems, with the appearance of a characteristic growth feature at short correlation times providing direct evidence for the dynamic nature of shallow traps in solution-dispersed nanocrystals.

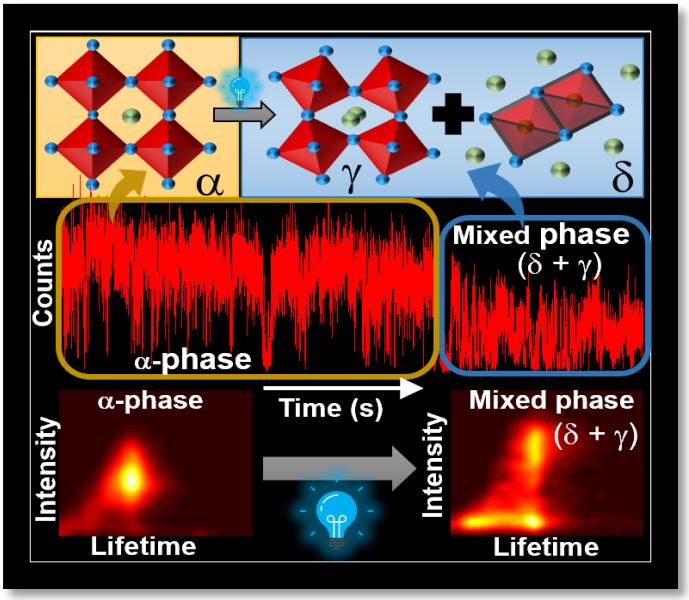

By clarifying how phase evolution and trap-state energetics govern carrier dynamics in red-emitting $CsPbI_3$ nanocrystals, this work delivers critical insights for improving their photophysical stability. These findings establish an essential foundation for the rational engineering of perovskite nanocrystals and advance their prospects for integration into high-performance optoelectronic and photovoltaic devices.

CHAPTER 6: Unveiling Facet-Controlled Energy Transfer from Individual Perovskite Nanocrystals to Dyes

(**Ref: M. K. Panda,** S. De, A. B. Mahato, S. Ghosh,* *ACS Energy Lett.* **2025**, *10*, 4834-4841)

Expanding the facet count of $CsPbBr_3$ perovskite nanocrystals from conventional cubic (6 facets) to more complex geometries with 12 and 26 facets-while keeping the overall surface area nearly constant leads to a pronounced improvement in energy transfer (ET) performance in nanocrystal–dye hybrid systems, as evidenced by ensemble-level solution studies. The dye employed in this work is 1,1′-dioctadecyl-3,3,3′,3′-tetramethylindocarbocyanine perchlorate (DiIC18). The observed enhancement arises from stronger dye–nanocrystal interactions in

facet-rich structures, a conclusion supported by fluorescence correlation spectroscopy (FCS) measurements and double-reciprocal analysis of steady-state emission data.

When examined at the single-particle level, the ET efficiency normalized per dye molecule remains nearly identical across nanocrystals with different facet numbers. To quantify this, per-dye ET efficiencies were extracted using laser-induced stepwise photobleaching of individual dye molecules at the single-particle scale. The ET process is found to proceed predominantly via a Dexter-type mechanism. In DiIC18, the long alkyl chain [–$(CH_2)_{17}$–CH_3], denoted as "R," extends outward from the chromophore, while the emissive core consists of two nitrogen-containing indoline units that are intrinsically polar and responsible for fluorescence. Analogous to oleylamine binding, these polar nitrogen centers are expected to interact directly with the nanocrystal surface, facilitating short-range Dexter energy transfer and bypassing the need for spectral overlap that is typically required for resonant ET processes.

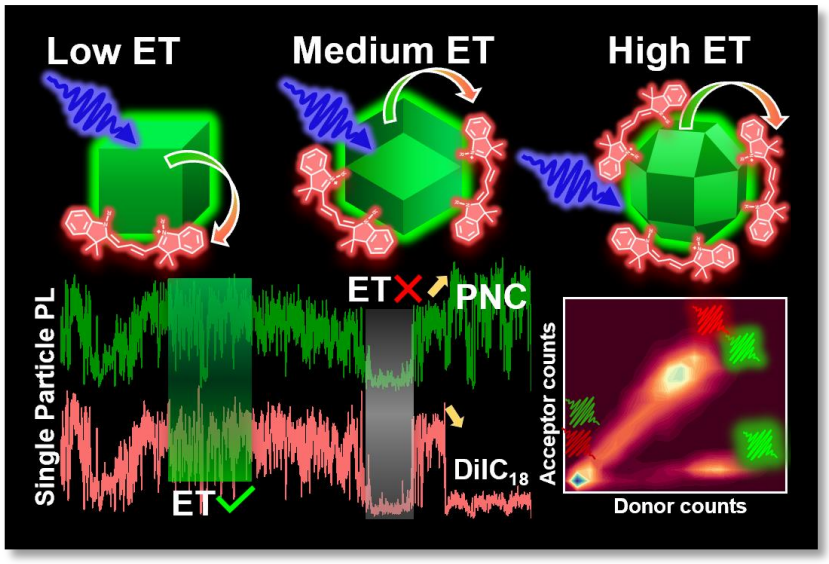

Additional carrier extraction experiments further demonstrate that nanocrystals with higher facet densities exhibit superior charge extraction capabilities compared to their cubic counterparts, attributable to their enhanced surface binding affinities. Taken together, these results establish facet engineering as a powerful and general approach for tuning interfacial interactions in perovskite nanocrystals. The exceptional performance of extra-faceted $CsPbBr_3$

nanocrystals underscores their strong potential for advanced applications in photovoltaics, photocatalysis, sensing, and light-harvesting technologies.

References

[1] J. T. DuBose, P. V. Kamat, *Chem. Rev.* **2022**, *122*, 12475–12494.

[2] L.Wu, F. He, H. Du, Y. Zhang, S. Ghimire, M. Stein, H. Huang, L. Polavarapu, Q. Zhang, J. Feldmann, T. Debnath, Y. Wang, *ACS Energy Letters*, **2025**, *10*, 2978-2985.

[3] B. Hötzer, I. L. Medintz, N. Hildebrandt, Small, 2012, 8, 2297-2326.

[4] J.G Mann, F.He, Q. A Akkerman, T.Debnath, J. Feldmann, *J. Phys. Chem. Lett.* **2024**, *15*, 2169–2176.

[5] S. K. Bera, S. Bera, M. Shrivastava, N. Pradhan, K. V. Adarsh, *Nano Lett.* **2022**, *22*, 8908–8916.

[6] Y-S Park, S. Guo, N. S. Makarov, V. I. Klimov, *ACS Nano* **2015**, *9*, 10386–10393.

[7] F. Hu, H. Zhang, C. Sun, C. Yin, B. Lv, C. Zhang, W. W. Yu, X. Wang, Y. Zhang, M. Xiao *ACS Nano*. **2015**, *9*, 12410–12416.

[8] N. Pradhan, *Acc. Chem. Res.* **2021**, *54*, 1200–1208.

[9] S. Bera, R. K. Behera, N. Pradhan, *J. Am. Chem. Soc.* **2020**, *142*, 20865–20874.

[10] T. Titus, E. K. Vishnu, A. Garai, S. K. Dutta, K. Sandeep, A. Shelke, T. Ajithkumar, A. Shaji, N. Pradhan, K. G. Thomas, *Nano Lett.* **2024**, *24*, 10434–10442.

Summary

This thesis is divided into six chapters. The first chapter is the introductory chapter and it discusses about the nanomaterials we have used and its photophysical properties. It also tells the approaches we have applied to study the photophysics of those nanomaterials. Second chapter is all about the instrumentation techniques we have applied and rigorous data analysis. The next four chapters are the working chapters. The third chapter explores fundamental understanding of photoinduced brightness heterogeneity present in every nanomaterial and how easily it has been misinterpreted by photo brightening or optical trapping. An advanced PIE-FCS technique has been used to verify this phenomenon. Fourth chapter introduces facet engineered lead halide perovskites and their single particle blinking which concludes more facet gives you more room for interaction with the surface sentimental molecules which ultimately creates more trap defects. Thus, the blinking mechanism changes from less facet to more facet concluding more facet gives more trion. In the next chapter i.e., the fifth chapter we have explored the changes in trap states and optical properties in various phases of red perovskite and found that upon illumination the phase changes from emissive to non-emissive/low emissive. While the immobilized states dictate towards dominance of hot carrier trapping and trion formation in photobleached state, mobilized state nullifies the trion formation and supports multicarrier recombination model to explain the blinking behavious in solution state. The last chapter i.e., sixth chapter explores the effectivity of energy transfer efficiency from faceted nanocrystals to organic dye. Higher facet shows higher energy transfer efficiency via dexter pathway. Though efficiency increases with facet in ensemble study, single particle study tells similar per-dye efficiency irrespective of facetes. Across the working chapters, rigorous single-particle spectroscopy has been used to uncover the intrinsic photophysics of these nanomaterials before their deployment in practical optoelectronic

devices. We hope that the insights from this thesis will inspire young researchers and contribute to the informed design of next-generation quantum communication and photovoltaic technologies.

LIST OF SCHEMES

radiative recombination, leads to lower PL intensity for the short-lifetime state (bottom figure). **Right panel (traps active):** The probability of radiative recombination alone decreases, lowering the PL intensity of the long-lifetime component (top figure). However, the higher likelihood of combined radiative and non-radiative recombination increases the PL intensity of the short-lifetime component (bottom figure). The MRC model thus predicts a PL anti-correlation between the two lifetime states, consistent with the growth feature observed in the CCF. The timescale of growth kinetics τ_R is persuasive to the appearance and disappearance rates of trap states.

LIST OF FIGURES

nm) with a pulse switching rate of 1/(100 ns) (B). While the intensity of PLr (I_{PLr}) was fixed at ~0.04 kW/cm^2, the power of SLr (I_{SLr}) was stepwise increased from ~0.04 kW/cm^2 to ~1.2 kW/cm^2 in 5 different sets of experiments.

12. **3.5.** Time gating scheme for PIE FCS. Our PIE scheme uses two excitation cycles: (i) 375 nm high-intensity SLr (for photo-brightening) and (ii) weakly intense 422 nm PLr (for FCS recordings). A 100 ns delay separates these two cycles. Utilizing time-tagged-time-resolved (TTTR) mode and subsequent time-gating enabled us to not only the extractions of PL-photons related to PLr excitation cycle in the presence of the SLr cycle but the unwanted PL-photons related to SLr excitations are also simultaneously discarded. PL-photons related to PLr excitations are correlated to construct FCS curves at different intensities of SLr. **132**

13. **3.6.** (A-F) Conventional (A-C) and PIE (D-F) FCS curves of c-PNCs (A, D), r-PNCs (B, E), and QDs (C, F), dispersed in toluene. The pump power in conventional FCS and SLr power in PIE FCS were varied stepwise from ~0.04 kW/cm^2 to ~1.2 kW/cm^2. Only the PL photons related to PLr excitations are correlated in PIE FCS (D-F). **134**

14. **3.7.** (A-B) Conventional FCS curves of r6g (A) and GQD (B) as a function of excitation intensity (I_P). For r6g, I_P was varied from ~0.08 times saturation intensity (I_s) to 0.3×I_s. **136**

I_P increases. Saturation intensities (I_s) were derived from fitting the plots by Equation 3.1.

18. **3.11.** Graphs depicting occupancy (N) and diffusion time (τ_D) as a function of pump intensity (I_P) plotted on the absolute scale along the bottom x-axis, and relative to saturation intensity (I_s) along the top x-axis, respectively, for (A) r6g (B) c-PNC and (C) QD. r6g data in Figure A illustrates that the saturation effect can change FCS parameters only when pump intensity reaches $>0.4\times I_s$. However, for c-PNC and QD, N, and τ_D apparently increase >6-to-9 folds (N) and >2 times(τ_D), respectively, as the excitation power changes within a range much lower than their respective I_ss; i.e., from ~ $0.0003\times I_s$ (0.04 kW/cm^2) to ~$0.010\times I_s$ (1.2 kW/cm^2). Therefore, saturation alone can't explain the significant power dependency of the FCS curves of our NPs. **140**

19. **3.12.** (A-C) The second-order cross-correlation functions [$g^{(2)}$] recorded on individual surface immobilized c-PNC (A), QD (B), and GQD (C), under low pump intensity [excitonic occupancy ~<0.008, λ_{ex} ~422 nm]. While $g^{(2)}$ of c-PNC and QD exhibits a dip at time zero, GQD excludes this feature, implying unlike the other two, GQD is not a single quantum emitter. (D) PL intensity trajectories recorded on a single QD at different intensities show a larger OFF state fraction at high pump intensity, accompanied by a higher ON/OFF switching rate. We attribute this behavior to brightness heterogeneity. (E) GQD's PL trajectory comprises only ON states with a uniform intensity distribution unaffected by **143**

excitation power, indicating minimal brightness heterogeneity. In all the cases, NPs were embedded in the PMMA matrix.

20. **3.13.** (A-C) Probability distribution of OFF-times for c-PNC (A), r-PNC (B), and QD (C) at differnt pump intensities along with the fitted lines, showing their OFF-times are not only power-law distributed but also extended across all time scales, that can influence the entire FCS curves of these NPs based on the excitation power. **145**

21. **3.14.** FLIDs of (A, D) c-PNC, (B, E) QD and (C, F) GQD at low (upper panel) and high (lower panel) pump-intensities, obtained from correlating single particle lifetime (τ_{PL}) and intensity (I_{PL}) histograms shown on the top (τ_{PL} histogram) and right side (I_{PL} histogram) of the FLID plots. The occurrence probability of a given state in the τ_{PL}-I_{PL} space is represented by false color, changing from red (most probable) to blue (least probable). While the single photon emitter NPs exhibit occurrence probabilities of ON (bright) and OFF (dim) states in I_{PL}-τ_{PL} space are pump-intensity dependent, multichromophoric GQD keeps ON state probability unity irrespective of the excitation power (C, F). This observation suggests that except for GQD, all other NPs exhibit a pronounced brightness heterogeneity at a high pump intensity, as indicated by the shape-changing of their probability states from near-circular or oval at low intensity (A-B), to distorted ones comprised of multiple sub-states with non-negligible probabilities at high intensity (D-E). **148**

22.	**4.1.**	(A–C) HRTEM images of PNCs with 6-facets (cube, c-PNC) (A), 12-facets (dodecahedron, d-PNC) (B), and 26 facets (rhombicuboctahedron, r-PNC) (C), (D) The powder XRD patterns of (A) c-PNCs, (B) d-PNCs, and (C) r-PNCs closely resemble with the reported ones. (G) PL lifetime curves of all three PNC samples dispersed in toluene. Lifetimes were recorded at their respective emission peak positions. Samples were excited by a ~405 nm diode laser (IRF ~ 90 ps). (H, I, K, L) XPS patterns of d-PNC (full range and survey scan), along with peak assignments. (J) PL (λ_{ex} ~400 nm) and absorption spectra of PNCs dispersed in toluene.	**160**
23.	**4.2.**	PL spectra of c-, d-, and r-PNCs dispersed in toluene when excited at 400 nm, normalized by their respective ODs at 400 nm at different dilutions (up to 5x) in the presence (A,C,E) and absence (B,D,F) of 3% PMMA. Insets show PLQYs as a function of the dilution factor. In the absence of PMMA, PLQY decreases for all three samples with dilution but remains nearly the same in the presence of PMMA**.** (G-I) Second-order cross-correlation functions [$g^2(t)$], recorded on three randomly selected PMMA embedded dots (particle numbers 1, 2, and 3 in the above confocal images) from each PNC sample. We observed nearly 30-40% photon-coincidence fraction, which is expected for our bigger-sized particles due to the slower Auger recombination rate reported earlier by Masuo and coworkers using similar-sized particles.[6] (J-L) Few representatives of the PL trajectory of c-	**162**

PNC without PMMA, show photodegradation within the first 60 s of exposure. The right sides of the main figures show corresponding intensity histograms with larger populations of OFF-states. (M) PL intensity decay curves were recorded from two c-PNCs, one embedded in PMMA and the other on the bare coverslip. Faster decay of the latter signifies photodegradation. This trend is consistent across repeated studies involving other particles. (N) An example of a typical PL trajectory of PNC embedded in PMMA is considered a stable particle if the average ON-state intensity remains stable for at least 3 minutes and the emission spectra collected during the first and the last 30 s remain identical in their peak PL positions and FWHMs. This behaviour cannot be obtained without PMMA. A 422 nm pulse laser (5 MHz repetition rate) with I_P ~2 W/cm^2 was used for the excitation. (O) TEM images of r-PNCs at single particle dilution. Insets show high-resolution images. Structural integrity is preserved even at single-particle dilution.

24. **4.3.** PL intensity trajectories (upper panel, 20 ms binning time) along with statistical distributions of intensities (middle panel) and PL dynamics of ON and OFF states (lower panel) recorded in single dot measurements on c-PNC (A, D, G), d-PNC (B, E, H), and r-PNC (C, F, I). PL lifetime profiles of ON and OFF states are constructed by the photons collected from the highest and lowest intensity regimes of the PL trajectories shown by pairs of horizontal slabs of similar colors with lifetime curves. A ~422 nm **165**

pulse laser (≈5 MHz repetition rate and ≈150 ps IRF) with excitation power (I_P) ~2 W cm^{-2} was used for the excitation.

25. **4.4.** PL intensity blinking (A) and lifetime blinking (B) recorded simultaneously on the same d-PNC dot show an excellent correlation. **167**

26. **4.5.** FLID maps were obtained by correlating intensity (along the vertical axis) and lifetime (along the horizontal axis) histograms of (A) c-PNC, (B) d-PNC, and (C) r-PNC. The probability of occurrence of a given state within FLID is depicted by a color change from red, indicating the highest probability, to blue, indicating the lowest probability. Linear correlation of intensity and lifetime in Figure A implying NBC recombination, whereas, linear and nonlinear correlations in Figure B are attributed to NBC and trion recombination. The red triangle in Figure C shows trion emission. (D-F) Pump-fluence dependent FLID maps of d-PNC. The occurrence probability of a given state within FLID is represented by a color change from red with the highest probability to blue with the lowest probability. Both NBC (linear trajectory) and Auger (nonlinear trajectory) blinking are present at low fluence, whereas Auger blinking predominates over NBC at high fluence. **171**

27. **4.6.** (A) Probability distribution of ON-times of d-PNC at different pump powers (I_P). Inset shows the photocharging probability ($1/\tau_C$) as a function I_P. (B) Probability distribution of ON-times of all three PNCs under low excitation power [<N> ~0.008], along **173**

in a cuvette was placed in front of the UV lamp (~350 nm) for phase transformation. (D) XRD spectra of freshly prepared r-PNCs (brown line), resembling the α-phase, and after UV irradiation for 14 hours (black line), matching the reported patterns of the δ and γ phases. Blue, green, and red lines correspond to the reference diffraction peaks for α, δ, and γ phases. [1,12,14,17,47] (E) Absorbance and emission spectra of α-phase and converted mixed-phase respectively after UV illumination. (G) PL Lifetime change during phase change. (H) Confocal scanning image of r-PNCs embedded in PMMA matrix in false color. The inset shows single-particle PL spectrum with 3 seconds accumulation time, not specific to ON or OFF state. (I) The second-order cross-correlation function [$g^2(\tau)$] from a confocal spot under ~3 MHz pulsed laser excitation shows sub-Poissonian statistics, confirming single-photon emission.

31. **5.2.** (A) Single-particle PL spectra recorded from the same freshly prepared nanocrystal after laser irradiation for different durations: ~0 seconds (red), ~350 seconds (green), and ~480 seconds (blue). Experimental conditions, including excitation wavelength (~375 nm) and power density (~4 W/cm^2), were consistent with those used in the PL blinking study. The 0-second spectrum corresponds to the α-phase nanocrystal, while the 480-second spectrum represents mixed-phase nanocrystal. (B-C) Statistical distributions of FWHMs (B) and PL peak positions (C) for α-phase (red) and mixed-phase (blue) nanocrystals. (D-F) Single- **195**

particle PL spectra recorded from three additional randomly selected nanocrystals. All experiments were performed at room temperature.

32. **5.3.** (A) PL intensity (upper panel) and lifetime (lower panel) trajectories of a single r-PNC recorded using a ~375 nm pulsed excitation laser at low power density (~2 W/cm^2). The vertical green dotted line indicates the phase change from α to mixed (δ + γ), with carrier dynamics analyzed separately for both phases. (B-C) Time-resolved PLs of OFF (green) and ON (red) states of the α-phase (b) and mixed-phase (c), derived from low- and high-intensity regions of PL intensity trajectory. (D-F) Fluorescence lifetime intensity distribution (FLID) maps in false color, correlating intensity-, and lifetime-histogram, derived from PL intensity- and lifetime-trajectory with different lengths: (D) full length (α-and mixed-phase), (E) up to 300 s (only α-phase), and (F) after 300 s (only mixed-phase). The change in occurrence probability of a state in FLID is indicated by intensity change with higher intensity implies a larger probability. **197**

33. **5.4.** (A, C) The same PL intensity trajectory (upper panel, A) and corresponding lifetime trajectory (lower panel, C) from Figure 5.2A were further analyzed here by zooming in on specific regions within the α phase (yellow slab) and mixed-phase (green slab). (B, D) The zoomed-in intensity (black line) and lifetime (blue line) trajectories for the α phase (upper panel, B) and the mixed phase (lower panel, D) are overlaid to highlight non-correlative **200**

behaviour due to HC recombination. Such behaviour, characterized by intensity drops with insignificant changes in PL lifetime, was frequently observed in both the phases, with a higher density of occurrences in the mixed phase compared to the α phase.

34. **5.5.** (A) PL intensity (upper panel) and lifetime (lower panel) trajectories of a single r-PNC recorded using a ~375 nm pulsed excitation laser at high power density (~20 W/cm^2). The vertical green dotted line indicates the phase change from α to mixed, with carrier dynamics analyzed separately for both phases. (B-C) Time-resolved PLs of OFF (green) and ON (red) states of the α-(B) and mixed-phase (C), derived from low- and high-intensity regions of PL intensity trajectory. (D-F) Fluorescence lifetime intensity distribution (FLID) maps in false color, correlating intensity- and lifetime-histogram derived from PL intensity- and lifetime-trajectory with different lengths: (D) full length (α-and mixed-phase), (E) up to 190 s (only α-phase), and (F) after 190 s (only mixed-phase). The change in occurrence probability of a state in FLID is indicated by intensity change with higher intensity implies a larger probability. All experiments were performed at room temperature. **203**

35. **5.6.** (A, B, E, F) Representatives of probability distribution functions of ON and OFF time durations (ρ_{ON} and ρ_{OFF}), derived from low power PL intensity trajectories of two randomly selected nanocrystals. (C, G) Statistical distributions of power-law **205**

coefficients m_{ON} and m_{OFF} whose average values represent the relative carrier trapping and detrapping rates in nanocrystals. [41,48] (D, H) Schematics of carrier trapping (black arrow) and de-trapping (white arrow) in both phases with potential wells. Figures in the upper panel represent the α-phase, whereas the lower panel figures are related to the mixed phase. ΔE_1 and ΔE_2 represent the activation barriers between neutral and charged potential wells.

36. **5.7.** (A) PL spectra of nanocrystals dispersed in toluene, shown before (α-phase) and after prolonged UV illumination (>14 hours, mixed-phase). (B) Schematic representation of anti-correlated PL patterns between two states with distinct PL lifetimes, evidenced by the initial rise in the interstate cross-correlation function (CCF, shown in panel c), consistent with experimental observations depicted in the insets of panels e and f. (C) Schematics of intrastate autocorrelation functions (ACFs) for long (red) and short (green) lifetime components, along with the interstate CCF (red-green) illustrating the cross-correlation of the two components. The initial growth in the CCF corresponds to the anti-correlated PL behavior shown in panel b. (D) Time-resolved PL of α-phase nanocrystals (grey), recorded alongside FLCS, decomposed into two single-exponential decay profiles representing the lifetimes of the interacting emission states. The inset shows similar data for mixed-phase nanocrystals. (E, F) ACFs for long (red) and short (green) lifetime states, along with **207**

D) Double-reciprocal plots fitted to Equation S4 yield apparent binding constants for NC–$DiIC_{18}$ complexes. The results indicate stronger binding of $DiIC_{18}$ with extra-faceted PNCs.

42. **6.4.** (A–C) Area-normalized PL spectra of c6-/d12-/r26-PNC–$DiIC_{18}$ systems in hexane showing iso-emissive points, confirming ET (λ_{ex}~ 375 nm). (D-F) TRPLs of $DiIC_{18}$ dye (red) and PNC (green) in PNC–$DiIC_{18}$ systems, recorded at their respective PL peaks at varying dye/PNC ratio (λ_{ex}~ 375 nm). (G) PNC PL quenching efficiency vs. dye/PNC ratio. All these observations suggest ET from PNC to the dye proceeds via the singlet state. (H, I) Gradual Cl alloying of c6-PNC reduces spectral overlap, yet ET efficiency remains comparable or higher than in undoped PNCs (I), suggesting a Dexter-type mechanism. **233**

43. **6.5.** (A) Confocal images showing co-localized green PL from d12-PNCs and red PL from $DiIC_{18}$ (λex~375 nm, I_P ~2 W/cm^2). (B) PL intensity trajectories with 50 ms bin time exciting donor only (λex~375 nm) reveal three temporal behaviors: (i) donor in dark state—no ET, no acceptor PL (left-grey slab); (ii) donor in bright state—ET induces acceptor PL (middle-grey slab); (iii) acceptor bleached—enhanced donor PL, no acceptor PL (right grey slab). (C) TRPL of donor channel shows lifetime quenching before dye bleaching, accompanied with rise component in TRPL of acceptor's channel, indicating ET. Acceptor channel TRPL without PNC shows no rise. (D) 2D donor-acceptor intensity correlation map highlighting three correlation regimes reflecting **235**

46. **6.8.** TRPLs of PNCs dispersed in hexane under varying NMA concentrations recorded in TCSPC (upper panel) and femtosecond upconversion (lower panel). Y-axis is in linear scale. Samples were excited at 405 nm and TRPLs were recorded at their respective PL maxima. **240**

LIST OF TABLES

CHAPTER 1

Introduction

1.1 Fluorescence

Fluorescence is a photophysical process in which a molecule or nanomaterial absorbs light and subsequently emits light at a longer wavelength. Upon absorption of a photon, an electron is promoted from the ground electronic state to an excited state results one hole at valance band and one electron at the conduction band which is called exciton. Due to coulombic attraction the electron recombines with the hole via radiative emission or non-radiative emission, we call it excitonic recombination. This emission typically occurs on nanosecond timescales and is characterized by a Stokes shift, where the emitted photon has lower energy than the absorbed photon.[1]

Fluorescence of a material is a powerful tool for probing molecular structure, dynamics, and interactions at both ensemble and single-particle levels. Owing to its high sensitivity and temporal resolution, fluorescence underpins many spectroscopic techniques used in chemical physics, materials science, and biological imaging.

1.2 Types of Fluorophores

Fluorophores are materials capable of exhibiting fluorescence and can be broadly classified based on their chemical nature and emission mechanism. [1]

1.2.1 Organic Fluorophores

Organic fluorophores are small molecules containing conjugated π-electron systems. [2,3]

Example: Rhodamine, Cyanine Dyes

Key features: High absorption cross sections, Fast fluorescence lifetimes (∼1–5 ns), Susceptible to photobleaching, widely used in biological imaging and labeling.[4]

1.2.2 Semiconductor Nanocrystals (Quantum Dots)

Quantum dots are inorganic semiconductor nanocrystals whose emission properties are governed by quantum confinement. [5,6,7,8]

Examples: CdSe, CdTe, Lead halide perovskite nanocrystals

Key features: Size- and composition-tunable emission, high photoluminescence quantum yield, enhanced photostability compared to organic dyes, exhibit single-particle phenomena such as blinking and single photon source.

1.2.3 Lanthanide-Based Fluorophores [9,10]

Lanthanide ions exhibit fluorescence arising from f–f electronic transitions.

Examples: Eu^{3+}, Tb^{3+}, Er^{3+}-doped nanoparticles

Key features: Long fluorescence lifetimes (microseconds–milliseconds), Sharp emission lines, Weak absorption, often requiring sensitization, Useful for time-gated and upconversion applications.

1.2.4 Fluorescent Proteins [11]

Fluorescent proteins are genetically encoded fluorophores derived from biological systems.

Examples: GFP, YFP

Key features: Biocompatibility, genetically targetable, moderate brightness and photostability.

1.2.5 Plasmon-Enhanced Fluorophores [12,13]

These fluorophores interact with metallic nanostructures to modify emission behaviour.

Examples: Dye–gold nanoparticle hybrids

Key features: Enhanced or quenched fluorescence depending on distance, modified radiative rates, useful for sensing and nano-optics studies.

1.3 Semiconductor Nanocrystals: An Overview

A semiconductor is a solid-state material characterized by an intermediate electrical conductivity arising from its electronic band structure, consisting of a filled valence band and an empty conduction band separated by a finite band gap (typically 0.1–3 eV).[14] Upon thermal or optical excitation, electrons are promoted across the band gap, generating mobile charge carriers (a) electrons in the conduction band and (b) holes in the valence band whose transport and recombination govern the electrical and optical properties of the material. In direct band gap semiconductors, radiative electron–hole recombination efficiently produces photoluminescence, whereas indirect band gap materials require phonon assistance and exhibit weak emission. The optical response is often dominated by excitons, bound electron–hole pairs, whose dynamics are strongly influenced by quantum confinement, defects, and surface states in nanostructured semiconductors.[15] These factors control key processes such as radiative and non-radiative recombination, Auger recombination, biexciton formation, and carrier trapping, making semiconductors particularly nanocrystals central to optoelectronic applications and single-particle spectroscopic investigations which is discussed later.

1.3.1 Quantum Confinement Effect

The quantum confinement effect is a phenomenon that occurs when the physical size of a semiconductor nanocrystal is reduced to a scale comparable to or smaller than the exciton Bohr radius—essentially the "natural" space an electron and its corresponding hole prefer to occupy. In general words, this is like squeezing a vibrating guitar string into a progressively smaller box; as the space shrinks, the vibration (energy) becomes higher and more intense. Thus, the spatial restriction forces the electronic wavefunctions to overlap, transforming the material's energy spectrum from a continuous "bulk" band into a set of discrete, quantized energy levels, much like those of a single atom.

As a direct result of this confinement, the energy band gap (E_g) increases as the particle size decreases, typically modelled by the Brus equation:[16]

$$E_{confinement} \approx \frac{h^2}{8R^2}\left(\frac{1}{m_e^*} + \frac{1}{m_h^*}\right) \qquad (1.1)$$

where R is the nanocrystal radius and m* represents the effective masses of the charge carriers. This relationship allows scientists to "tune" the optical properties of the material; by simply changing the size of the crystal, one can shift its light emission from red to blue (blue shift).

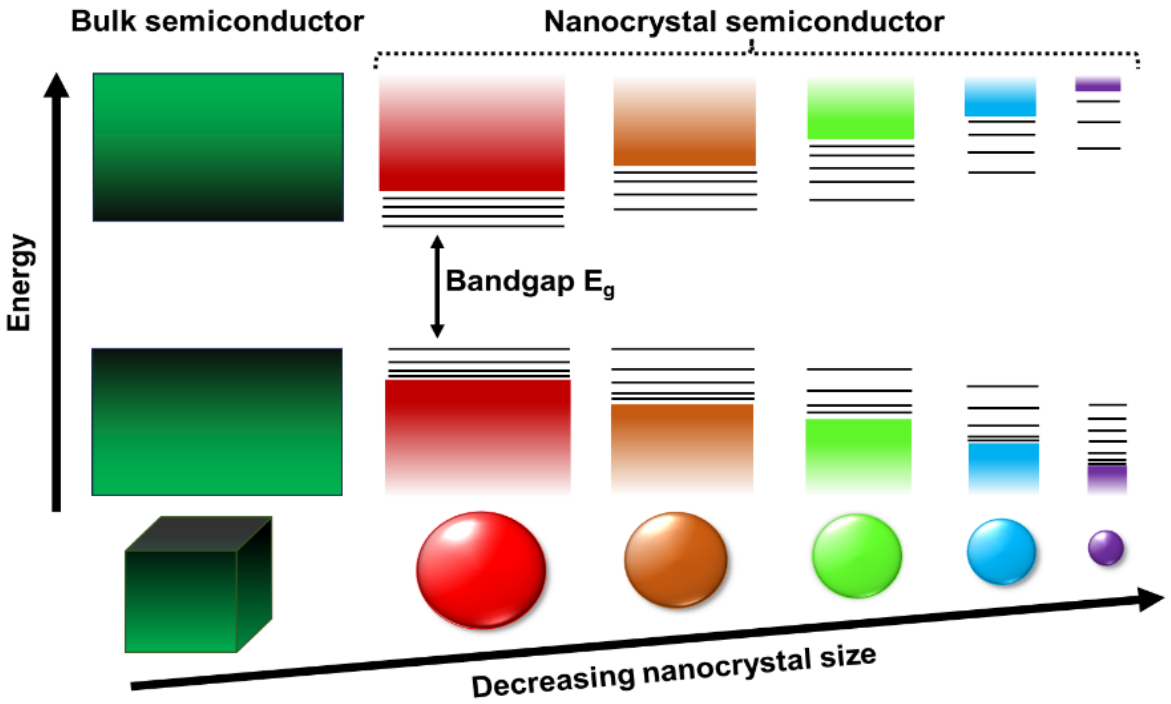

Scheme 1.1. Illustration of size-dependent bandgap. In nanocrystals, quantum confinement leads to an increase in the band gap with decreasing particle size, resulting in the formation of more discrete energy levels near the band edges.

This unique ability to control electronic behaviour through geometry rather than chemistry makes semiconductor nanocrystals (or quantum dots) invaluable for everything from vibrant television displays to high-precision medical imaging. [17,18]

1.4 Perovskite material and Perovskite nanocrystals

Owing to their facile synthetic routes and versatile optical properties, lead halide perovskites (LHPs) have attracted tremendous attention from the research community. (LHPs) are a class of semiconducting materials that have revolutionized the fields of photovoltaics and optoelectronics over the last decade. They are defined by their unique crystal structure and "soft" ionic nature, which allows them to be fabricated using simple, low-cost solution processing while maintaining performance comparable to high-end semiconductors like Gallium Arsenide (GaAs). [20-22]

The term "Perovskite" originally referred to the mineral Calcium Titanate ($CaTiO_3$), discovered in the Ural Mountains in 1839 and named after Russian mineralogist Count Lev Perovski. While oxide perovskites (like $BaTiO_3$) were known for decades for their ferroelectric properties, the first synthetic halide perovskites (based on Cesium and Lead) were synthesized by Horace L. Wells at Yale in 1892. For over a century, they remained a laboratory curiosity until Tsutomu Miyasaka first used them as light-sensitizers in liquid-electrolyte solar cells. Though initial efficiency was a modest 3.8%, this sparked global research "gold rush."

Lead halide perovskites follow the general chemical formula ABX_3. Where, A: large cation, typically organic like Methylammonium ($CH_3NH_3^+$, MA) or Formamidinium ($CH(NH_2)_2^+$, FA), or inorganic like Caesium (Cs^+). B-site: A divalent metal cation, most commonly Lead (Pb^{2+}).X-site: A halide anion (Cl^-, Br^-, or I^-). The structure consists of a 3D network of corner-sharing $[PbX_6]^{4-}$ octahedra, with the large A-site cations sitting in the "cages" formed between these octahedra.

The stability of the ABX_3 structure is governed primarily by geometry. The Goldschmidt Tolerance Factor is a dimensionless number that predicts whether a set of ions can actually form a stable perovskite lattice: [23,24]

$$t = \frac{r_A + r_X}{\sqrt{2}(r_B + r_X)} \quad (1.1)$$

Where r_A, r_B, and r_X are the ionic radii of the respective components.

Empirical guidelines suggest that favourable perovskite structures are achieved when the tolerance factor (t) lies between 0.81 and 1.0, while the octahedral factor must also satisfy the range $0.44 \leq \mu \leq 0.9$. [25]

$$\mu = \frac{r_B}{r_X}$$

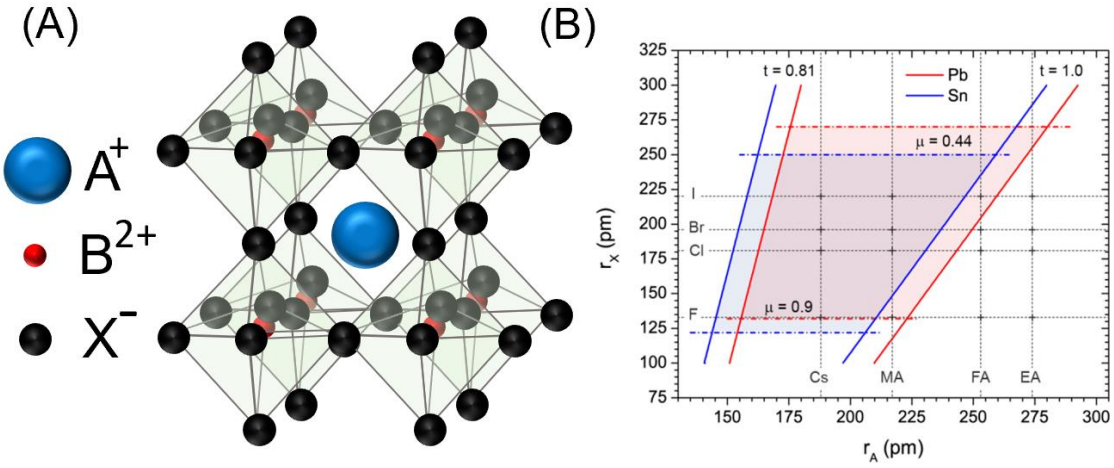

Figure 1.1. (A)Illustration of the crystal architecture of halide perovskites described by the ABX_3 composition. (B) Stability map showing the structural viability of three-dimensional tin-based (blue) and lead-based (red) halide perovskites as a function of the ionic radii of the halide ions and A-site cations. The limiting regions defined by the octahedral criterion and the tolerance factor are indicated by dashed and solid boundaries, respectively (taken from ref. 25).

In recent years, synthetically engineered metal halide perovskites have emerged as a prominent class of materials owing to their remarkable optical and electronic characteristics, positioning them as strong contenders for optoelectronic and photovoltaic technologies. Although metal halide perovskites were first documented as early as 1893,[26] initial investigations were largely

limited to their structural aspects and exploratory use in light-emitting components and transistor-based devices. A major breakthrough occurred in 2009 when Miyasaka and co-workers demonstrated their successful integration into solar cells, triggering widespread interest in the field. [27] Since then, intensive research efforts have focused on both enhancing material performance and broadening their applicability across diverse optoelectronic platforms.

Structurally, halide perovskites adopt the ABX_3 framework, where X represents a halide anion (Cl^-, Br^-, or I^-), B denotes a divalent metal cation such as Pb^{2+} or Sn^{2+}, and A corresponds to a monovalent cation, which may be inorganic (Cs^+, Rb^+) or organic (methylammonium, formamidinium). This compositional flexibility enables wide tunability of emission properties, particularly through halide substitution, and allows classification into fully inorganic or hybrid organic–inorganic systems depending on the A-site species. Rapid progress following the 2009 discovery led to dramatic improvements in solar-cell performance, with power conversion efficiencies surpassing 25% within a decade. [27-29]

Beyond photovoltaics, the combination of narrow emission linewidths, high color purity, and suppressed non-radiative recombination has made halide perovskites highly attractive for light-emitting diodes and laser applications. [30,31] However, bulk perovskite materials typically exhibit limited photoluminescence quantum yields, primarily due to weak exciton binding energies and the ease of defect formation associated with ionic migration. Thin films derived from solution processing further suffer from heterogeneous emissive behaviours, with pronounced photoluminescence quenching at grain boundaries arising from defect-rich regions. [32,33] These limitations motivated a shift toward perovskite nanocrystals, which not only significantly enhance emission efficiency but also enable access to the quantum confinement regime, allowing precise control over optical properties via size modulation. The first reports of $CsPbX_3$ nanocrystals in 2015 marked a pivotal advancement in this direction.[34]

Overall, the exceptional absorption strength, compositional and size-dependent color tunability, defect tolerance, and favourable charge-carrier dynamics of lead halide perovskites establish them as promising candidates for next-generation semiconductor technologies. [30, 35]

The first successful preparation of colloidal $CsPbX_3$ nanocrystals was demonstrated by Kovalenko and co-workers at the year 2015 using a hot-injection synthesis strategy, yielding materials with remarkably high photoluminescence quantum yields in the range of approximately 50–90%. [34] Following this breakthrough, extensive efforts have been devoted to both in situ synthetic optimization and post-synthetic treatments to further enhance their optoelectronic performance and expand their applicability across multiple research domains. One of the most attractive features of these nanocrystals is the ability to systematically tailor their band gaps through halide composition, enabling emission tuning across the entire visible spectrum (Figure 1.2).[34] Notably, halide exchange reactions can be readily achieved under ambient conditions, highlighting the exceptional compositional flexibility of this material system.

Metal halide perovskite nanocrystals are characterized by a pronounced ionic bonding character, which significantly lowers the energetic barrier for nucleation and growth, enabling their synthesis even under ambient or near-room-temperature conditions. Following the initial demonstrations of perovskite nanocrystals, a wide range of synthetic strategies have been developed to precisely regulate their dimensionality, morphology, and size. [27] Organic surface ligands play a critical role during nanocrystal formation by directing crystal growth and simultaneously passivating surface imperfections. Commonly employed ligands such as oleic acid and oleylamine effectively stabilize nanocrystals during synthesis; however, their weak and dynamic binding to the nanocrystal surface has prompted continued efforts to identify alternative ligand systems that provide stronger and more robust surface coordination. [36]

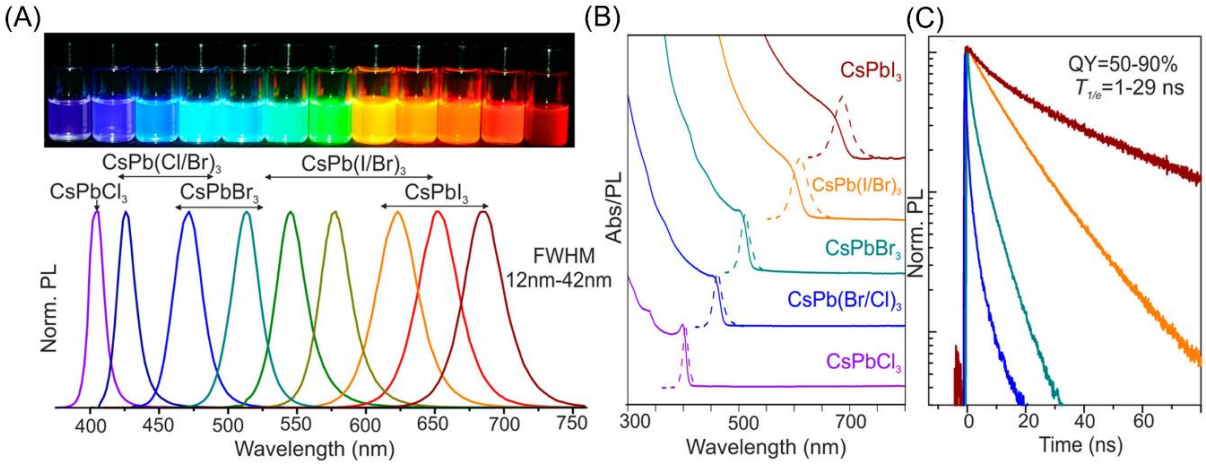

Figure 1.2. (A) Colloidal solution of perovskite NCs exhibiting composition dependent emission over the entire visible spectral region under UV lamp, and tunability of emission spectra with the variation of halide (lower panel) and (B) Typical optical absorption and emission spectra of perovskite NCs. (C) Excited state lifetime of different perovskites with varying halide composition. Each color lifetime curve corresponds the emission color of the NC. Adapted from ref. 34.

From an electronic-structure perspective, the valence band of lead halide perovskites originates primarily from the hybridization of Pb-6s orbitals with halide np orbitals, while the conduction band is dominated by Pb-6p states. Unlike conventional covalent semiconductors such as GaAs or CdSe, where the band gap arises from the separation between bonding and antibonding orbitals, perovskite materials exhibit band edges composed mainly of antibonding and nonbonding states. This unusual electronic configuration places many defect-related states energetically close to or within the band edges, resulting in shallow traps rather than deep recombination centers. Notably, the A-site cation does not directly participate in the formation of the electronic band structure, which contributes to the intrinsic defect tolerance and relatively high photoluminescence efficiencies observed in lead halide perovskites. [37-30]

Despite these favorable optoelectronic properties, the same ionic nature that facilitates facile synthesis also renders perovskite nanocrystals chemically vulnerable. Their solubility in polar solvents and susceptibility to degradation are exacerbated by exposure to moisture, oxygen, light, and elevated temperatures, making long-term structural and optical stability a major challenge.[40] Among hybrid compositions, formamidinium-based nanocrystals generally display greater stability than methylammonium-based counterparts, owing to their higher formation energies. To mitigate environmental degradation and improve durability for practical applications, encapsulation strategies using inert shells such as silica, alumina, barium sulfate, or polymer matrices have been widely explored.

Structural instability is particularly pronounced in red-emitting $CsPbI_3$ nanocrystals, where the large ionic radius of iodide induces octahedral tilting and drives a phase transition from an optically active to a non-emissive structure. Although substantial progress has been made toward stabilizing these materials, complete suppression of degradation pathways has yet to be achieved. Furthermore, while lead halide perovskite nanocrystals are often described as defect tolerant, they are not devoid of imperfections. Weakly bound surface ligands can leave undercoordinated sites exposed, which act as trap states for charge carriers. The low formation energy of point defects, particularly halide vacancies, further facilitates trap formation and can significantly reduce photoluminescence quantum yield.

Crystal lattice distortions arising from ionic size mismatch also contribute to defect generation. For instance, the large iodide ions in $CsPbI_3$ or the comparatively small chloride ions in $CsPbCl_3$ introduce intrinsic strain within the lattice, promoting the formation of defect sites that localize charge carriers. In addition, the mechanically soft and dynamically fluctuating nature of the perovskite lattice—often described as a “crystalline liquid”—allows strong coupling between photoexcited carriers and lattice vibrations. This electron–phonon interaction can give rise to polaron formation, wherein carriers become partially localized through lattice

distortion, potentially leading to self-trapping phenomena. A comprehensive understanding of how polaron formation influences carrier dynamics and optical performance remains an important and open area of investigation. [41-44]

Lead halide perovskites (LHPs) inherently host a variety of point defects, including halide and lead vacancies, A-site cation vacancies ($Cs^+/MA^+/FA^+$), interstitial halides or metals, and antisite defects such as halide–lead or halide–A-site substitutions. Among these, halide vacancies are the most frequently formed due to their low formation energies and play a dominant role in influencing charge-carrier dynamics (Figure 1.3A). Despite the presence of such defects, LHPs exhibit an unusual degree of defect tolerance, which originates from their distinctive molecular orbital–derived electronic structure. The valence band maximum (VBM) is primarily composed of antibonding interactions between Pb 6s and halide np orbitals, while the conduction band minimum (CBM) arises mainly from antibonding Pb-6p states. Because both band edges are antibonding in nature, most defect-induced electronic states do not introduce deep levels within the bandgap; instead, they either lie close to the band edges as shallow traps or become resonant with the valence or conduction bands. This is in stark contrast to conventional covalent semiconductors (ex, CdSe, ZnS etc.), where defects often generate deep mid-gap states that act as efficient nonradiative recombination centers. The molecular orbital picture (Figure 1.3B) therefore explains why structural imperfections in lead halide perovskites have a limited impact on radiative recombination efficiency, underpinning their high photoluminescence quantum yield despite a relatively high defect density.

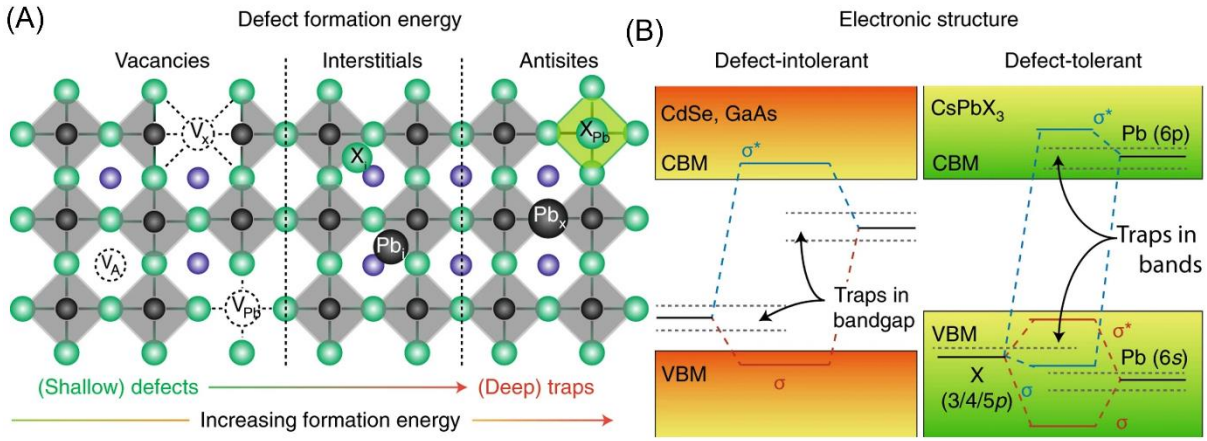

Figure 1.3. (A) Common atomic-scale imperfections in lead halide perovskites (LHPs), such as vacancies, interstitial species, and antisite substitutions, arranged according to their relative formation energies—ranging from the most easily formed to the least probable—and their corresponding energetic positions within the bandgap. (B) Conceptual comparison of the electronic band structures of defect-sensitive semiconductors and lead halide perovskites. In traditional semiconductors (e.g., cadmium chalcogenides), the energy gap arises from the separation between bonding and antibonding electronic states. As a result, structural imperfections and dangling bonds typically introduce localized electronic states deep within the bandgap, acting as efficient nonradiative recombination centres. In contrast, in lead halide perovskites the valence and conduction band edges are derived from antibonding states. Consequently, defect-induced states are energetically positioned close to the band edges or merge into the bulk bands, forming shallow traps that have a minimal impact on radiative recombination and the overall optical response. Adapted from ref.37

1.5 Photophysical Processes in Perovskite Nanocrystals

The interaction of light with matter lies at the heart of photophysical phenomena. Gaining insight into how a material responds to optical excitation is crucial for revealing and tailoring its intrinsic properties. In quantum dots, absorption of photons promotes charge carriers from

the valence band to the conduction band, generating electron–hole pairs. These photoexcited carriers subsequently relax through multiple pathways, which may involve light emission or energy loss via nonradiative channels such as lattice vibrations. A comprehensive understanding of these relaxation mechanisms is vital for improving the performance of quantum dots in technologies including solar cells, light-emitting diodes, and lasers. Moreover, controlling parameters such as particle size, geometry, and structural morphology enables deliberate tuning of these processes, thereby expanding the functional versatility of quantum dots across diverse optoelectronic applications. The key photophysical mechanisms relevant to quantum dots, discussed below, are typically explored using advanced experimental tools and methodologies, which are detailed in Chapter 2.

1.5.1 Absorption

Lead halide perovskite nanocrystals exhibit exceptionally strong and broadband optical absorption due to their direct bandgap and large oscillator strength. Optical absorption promotes electrons from the valence band (VB), primarily composed of antibonding Pb-6s and halide-np orbitals, to the conduction band (CB), dominated by Pb-6p antibonding orbitals. The absorption edge can be tuned by halide composition (Cl/Br/I), nanocrystal size (quantum confinement), and dimensionality. Unlike many conventional semiconductor nanocrystals, excitonic features in LHP NCs are often weak at room temperature due to relatively low exciton binding energies, though they become more pronounced under strong confinement or at low temperatures. [45]

1.5.2 Fluorescence (Radiative Recombination)

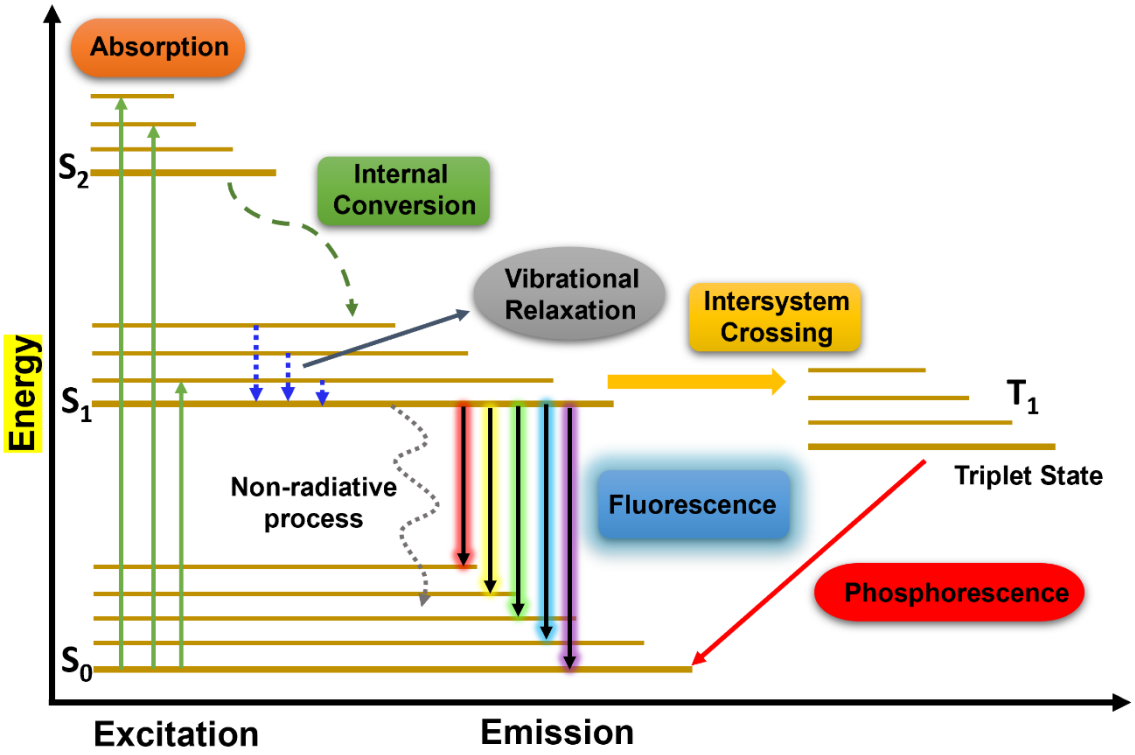

Scheme 1.2. Jablonski diagram: Illustrating after excitation many optical processes occur. The exited photon relaxes back by both non-radiative and radiative processes.

Following excitation and relaxation to the band edges, radiative recombination of electrons and holes results in photoluminescence (PL). LHP NCs typically display high PL quantum yields, narrow emission linewidths, and short radiative lifetimes due to their direct bandgap and defect-tolerant electronic structure. The antibonding nature of both VB and CB suppresses the formation of deep mid-gap defect states, allowing efficient band-edge emission even in the presence of structural imperfections. Emission wavelength can be precisely tuned through halide substitution and quantum confinement effects.

Following the Kasha's rule. fluorescence happens from the lowest vibrational level of the excited state S_1 and it is independent of excitation wavelength. [Demonstrated in Scheme 1.2.]. [46,47]

1.5.3 Auger Recombination and Biexciton Formation

Under high excitation fluence, multiple electron–hole pairs can be generated within a single nanocrystal, leading to biexciton or multiexciton states. These states predominantly decay via nonradiative Auger recombination, where the recombination energy of one exciton is transferred to another charge carrier. (Scheme 1.3) Auger recombination limits optical gain and lasing performance in LHP NCs, although their relatively large dielectric constant and defect tolerance can partially mitigate Auger losses compared to traditional QDs. [48-50]

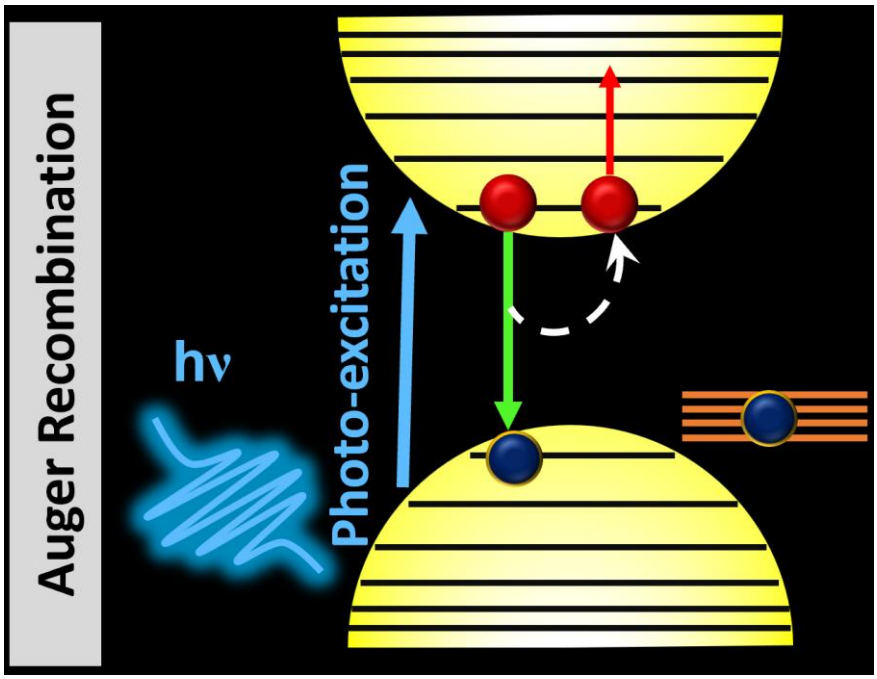

Scheme 1.3. Representation of auger assisted carrier recombination.

1.5.4 Defect-Mediated Intermittency (Trap-Mediated Recombination)

Despite being defect tolerant, LHP NCs are not entirely defect free. Surface defects, particularly halide vacancies, can act as transient charge traps. Trapping and detrapping of charge carriers lead to photoluminescence intermittency, commonly known as blinking. Unlike conventional semiconductor NCs where deep traps dominate, defects in LHP NCs generally

form shallow states near the band edges, resulting in reduced blinking severity and faster recovery to emissive states. [51-58]

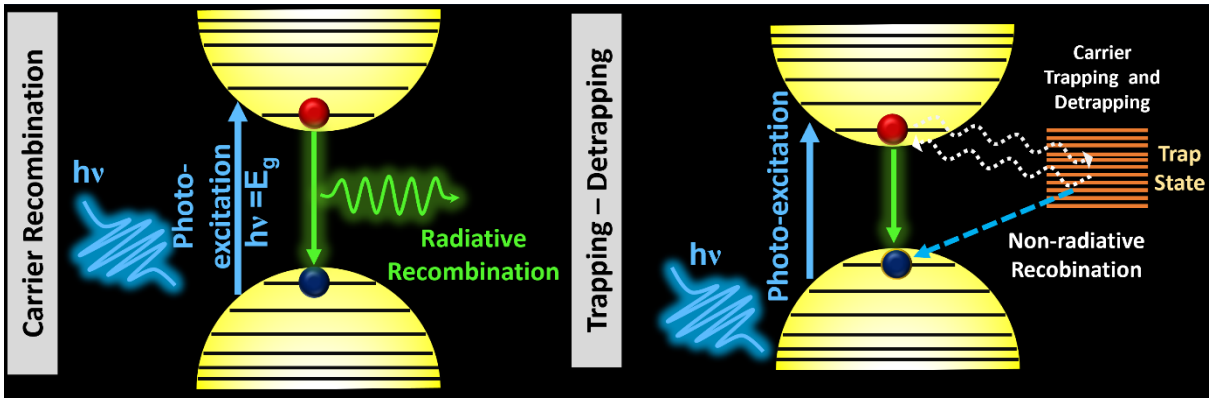

Scheme1.4. Mechanism of radiative recombination pathway and trap induced recombination via radiative and non-radiative channel.

1.5.5 Energy Transfer

Excitation energy in LHP NC assemblies can migrate between neighbouring nanocrystals or to adjacent molecular species via nonradiative energy transfer mechanisms such as Förster resonance energy transfer (FRET). Energy transfer efficiency depends on spectral overlap, interparticle distance, and dipole orientation. In densely packed films or mixed-halide systems, energy transfer influences emission dynamics, spectral diffusion, and overall device performance. [59-65]

1.5.5.1 Förster Resonance Energy Transfer (FRET) in Perovskite–Dye Systems

FRET is a long-range, dipole–dipole interaction–mediated energy transfer process that occurs without charge transfer and does not require direct orbital overlap. In perovskite–dye hybrids, the perovskite nanocrystal typically acts as the energy donor, while the organic dye serves as the acceptor. [65,64]

LHP NCs are exceptionally efficient FRET donors due to their large absorption cross-sections, high photoluminescence quantum yields, and strong transition dipole moments. Efficient FRET occurs when there is a substantial spectral overlap between the perovskite emission spectrum and the dye absorption spectrum, typically quantified by the overlap integral. The FRET efficiency decays with the sixth power of donor–acceptor separation ($\propto R^{-6}$), making it effective over distances of approximately 1–10 nm, which is comparable to the ligand length separating dyes from the perovskite surface.

In perovskite NC–dye assemblies, FRET manifests experimentally as:

- Quenching of perovskite PL intensity and lifetime
- Sensitized emission from the dye
- Power- and distance-dependent transfer efficiency

Importantly, the defect-tolerant band structure of LHP NCs minimizes competitive nonradiative losses, enabling high FRET efficiencies even in ensemble and single-particle measurements. Additionally, the tunable bandgap of perovskites (via halide composition or size) allows spectral matching with a wide range of organic dyes.

1.5.5.2 Dexter Energy Transfer in Perovskite–Dye Systems

Dexter energy transfer is a short-range exchange mechanism that involves simultaneous electron exchange between donor and acceptor. Unlike FRET, Dexter transfer requires direct wavefunction overlap and therefore occurs over very short distances, typically < 1 nm. As a result, Dexter transfer is highly sensitive to surface chemistry, ligand length, and interfacial electronic coupling. [59]

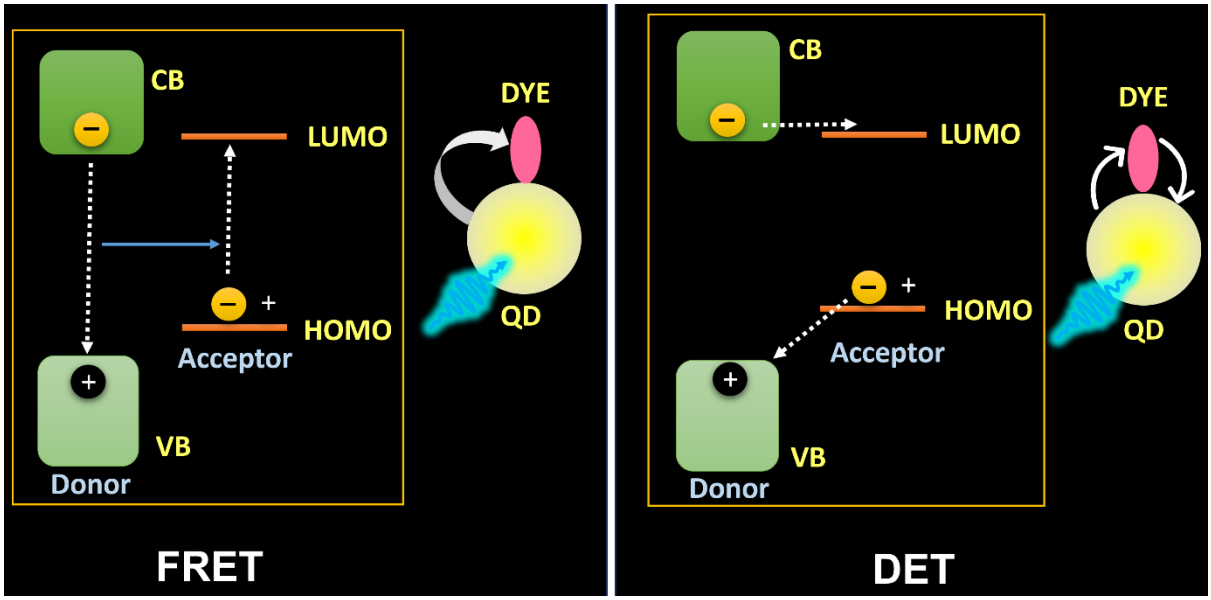

Scheme 1.5. Illustration of mechanistic pathways of energy transfer from perovskite nanocrystals (donor) to organic dye molecule (acceptor).

In perovskite NC–organic dye hybrids, dexter transfer becomes relevant when dyes are directly bound to the nanocrystal surface or when ultrashort ligands or ligand-free interfaces are employed. This mechanism is particularly important for triplet energy transfer, as Dexter exchange allows spin conservation and is therefore the dominant pathway for populating dye triplet states from photoexcited perovskites.

However, in conventional ligand-capped LHP NCs (e.g., oleic acid/oleylamine), dexter transfer is often suppressed due to the spatial separation imposed by long insulating ligands. Engineering stronger electronic coupling—through ligand shortening, conjugated ligands, or direct chemical anchoring, is therefore essential to activate Dexter-type interactions. Band gap also dictates the mechanistic pathway by which energy transfer happens. For, $CsPbI_3$ follows triplet energy transfer while $CsPbBr_3$ follows singlet energy transfer for particular reference due (e.g. Rose B) to its band gap change from $CsPbI_3$ to $CsPbBr_3$ and mixed $CsPb(BrI)_3$ will follow both single and triplet energy transfer.

1.5.6 Photo-Induced Charge Transfer in QDs

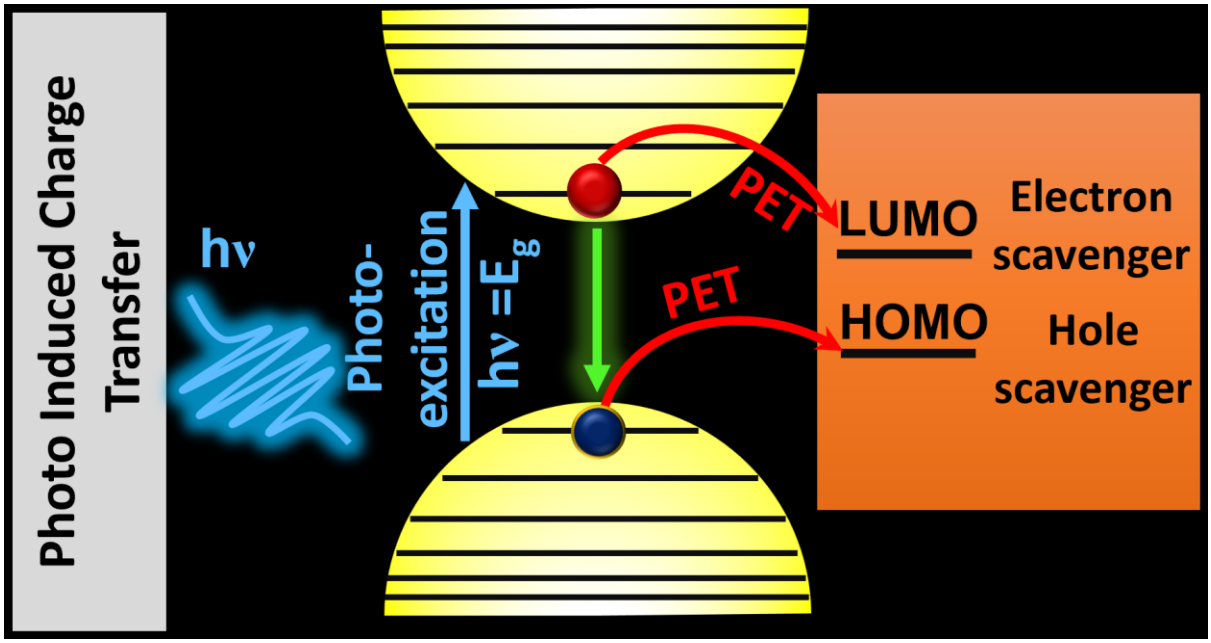

Scheme 1.6. Representation of how photo induced charge transfer happens from perovskite nanomaterials to a hole or electron scavenger.

Photo-induced charge transfer in lead halide perovskite nanocrystals occurs when photoexcitation generates electron–hole pairs and one type of carrier is selectively extracted by an external electron or hole scavenger. Electron transfer takes place when the conduction band minimum of the perovskite lies higher in energy than the LUMO or reduction potential of the acceptor, enabling downhill electron injection, while hole transfer occurs when the valence band maximum is energetically aligned above the HOMO or oxidation potential of a donor molecule. Such charge extraction competes with radiative recombination, leading to photoluminescence quenching and modified excited-state lifetimes. Owing to the defect-tolerant electronic structure of perovskites, shallow surface states and dynamic ligands can facilitate carrier transfer without introducing deep nonradiative losses. The efficiency of this process is governed by band-edge alignment, interfacial coupling, and the energetic driving

force, making photo-induced charge transfer a key mechanism in perovskite-based optoelectronic, photovoltaic, and photocatalytic applications. [66,67,68]

The bandgap of the perovskite defines the energetic window for charge transfer. Wide-bandgap perovskites (e.g., $CsPbCl_3$) provide higher CB energies favouring electron transfer, while narrower-bandgap perovskites (e.g., $CsPbI_3$) have shallower band edges that may favour hole transfer depending on the scavenger. [69]

The driving force (ΔG) for charge transfer is governed by:

- Band edge positions
- Scavenger redox levels
- Coulombic stabilization
- Interfacial dipoles and surface states

Excessive driving force, however, can enhance nonradiative losses via strong electronic coupling, while insufficient driving force limits transfer efficiency.

1.6 Single Particle Intensity Fluctuation or PL Blinking

Despite their outstanding photoluminescence efficiency and size-tunable optical properties, quantum dots often display stochastic emission fluctuations when examined at the single-particle level. This behavior, first revealed through single-nanocrystal spectroscopy in CdSe nanocrystals in the year 1996 by Nirmal et. al, is characterized by abrupt and unpredictable transitions between emissive and non-emissive states under steady illumination, a phenomenon commonly referred to as photoluminescence intermittency or blinking. [70] Such emission instability is a distinctive feature of colloidal quantum dots and is absent in conventional bulk or molecular light emitters. Early mechanistic interpretations linked blinking to charge accumulation within the nanocrystal, arising from multiexciton Auger ionization processes that

activate highly efficient nonradiative decay pathways. [71,72] At nanoscale dimensions, relaxed momentum conservation substantially increases the probability of Auger recombination, leading to effective quenching of emission. Because stable and uninterrupted photon output is critical for practical optoelectronic and photonic applications, blinking remains a significant limitation. Consequently, systematic investigations aimed at understanding and mitigating emission intermittency are essential for advancing quantum dot performance and enabling their reliable integration into functional devices.

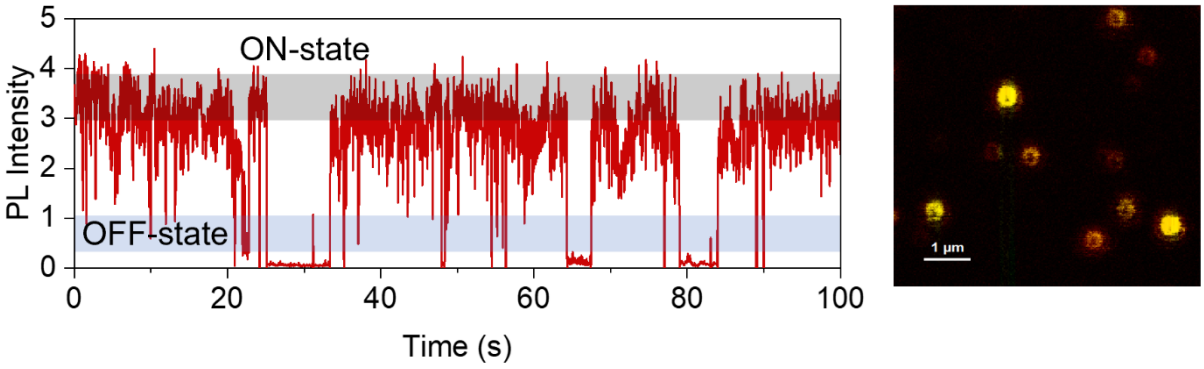

Figure 1.4. PL trajectory for a perovskite QD showing random intensity fluctuations. High intensity state (grey strip) is called ON state or, Bright state and low intensity region (light blue strip) is called OFF state or, Dark state and corresponding confocal image of well dispersed spin coated QDs in a glass coverslip under a laser.

Investigation of photoluminescence intermittency at the single–quantum-dot level requires sample preparation in which individual emitters are spatially well separated. When multiple quantum dots are located within the excitation volume, their collective emission masks the stochastic blinking behaviour of individual particles. [70,73-75] To achieve isolated emitters, single-particle samples are typically prepared through a controlled, multi-step procedure. First, the stock quantum dot dispersion is serially diluted to an ultralow concentration (~ pM), to minimize interparticle proximity. An aliquot of this diluted solution is then deposited onto a

clean substrate using techniques such as spin coating or drop casting to ensure sparse surface coverage with a polymer matrix coating to avoid environmental degradation. After deposition, the solvent is removed by allowing the substrate to dry either under ambient conditions or within a controlled atmosphere, yielding well-dispersed, individual quantum dots suitable for single-particle blinking measurements.

Several blinking mechanisms have been proposed to explain the different fluctuating events in a blinking trajectory. Among those main three recombination mechanisms are: (a) Auger mediated blinking (AC) due to charging/discharging of QDs, (b) Near band edge carrier recombination (NBC) which involves trapping/detrapping and (c) Hot carrier blinking (HC) due to hot carrier trapping and subsequent recombination. [76,77] All these mechanisms are discussed below for better understanding my thesis works.

1.6.1 Auger blinking

In the absence of excess charge, a quantum dot remains electrically neutral, and radiative recombination of a single exciton gives rise to a stable, emissive “ON” state in the photoluminescence time trace. Upon photoinduced charging, however, the presence of an additional electron or hole opens an efficient nonradiative decay channel through Auger recombination. In this process, the recombination energy of an exciton is transferred to a third charge carrier rather than being emitted as a photon, leading to strong suppression of photoluminescence and the emergence of a non-emissive “OFF” state. Emission intermittency governed by this mechanism is commonly referred to as Auger-type blinking (AC-blinking). Understanding Auger blinking requires careful consideration of the mechanisms responsible for both charge generation and charge removal. One charging route involves resonant tunnelling of a carrier from a photoexcited exciton, followed by trapping at surface states or within the surrounding matrix or substrate. [76,77,78] Alternatively, charging can occur through

non-resonant multiexciton processes, most notably biexciton-mediated Auger ionization, in which the nonradiative recombination of one exciton provides sufficient energy to expel a charge carrier from another exciton. Sustained blinking behavior relies on the existence of long-lived trap states that stabilize the charged (trion) configuration, allowing sufficient time for additional excitations to occur (Scheme 1.7.). Neutral emission is recovered once the trapped carrier returns to the nanocrystal via tunnelling or when the remaining counter charge is removed, thereby restoring radiative recombination and the bright state.

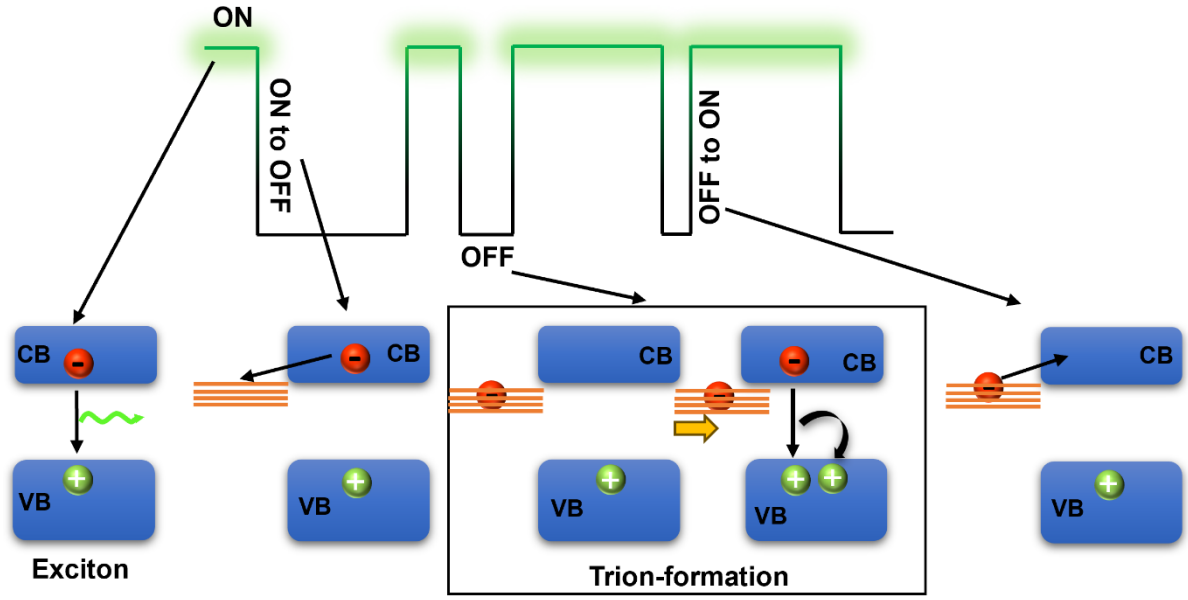

Scheme 1.7. PL blinking and the probable mechanism for ON/OFF events in a nanocrystal. This model is based on auger mediated non-radiative recombination called AC blinking.

1.6.2 Non-radiative Band Edge Carrier (NBC) blinking

In the band-edge carrier (BC) blinking model, one of the charge carriers generated upon photoexcitation either an electron or a hole—is temporarily captured by shallow, short-lived trap states. This trapped carrier subsequently undergoes rapid nonradiative recombination with its opposite charge remaining in the nanocrystal core. Because these traps have brief lifetimes, the quantum dot is promptly restored to its neutral ground state following each trapping event. Emission intermittency in this mechanism arises from the dynamic balance between a time-

dependent nonradiative trapping pathway and a comparatively stable radiative recombination channel. As illustrated schematically in Scheme 1.8., bright emission is observed when radiative decay dominates over carrier trapping, whereas emission is strongly suppressed when nonradiative trapping becomes the primary relaxation route. Situations in which the radiative and nonradiative rates are of similar magnitude give rise to intermediate intensity levels in the photoluminescence time trace.

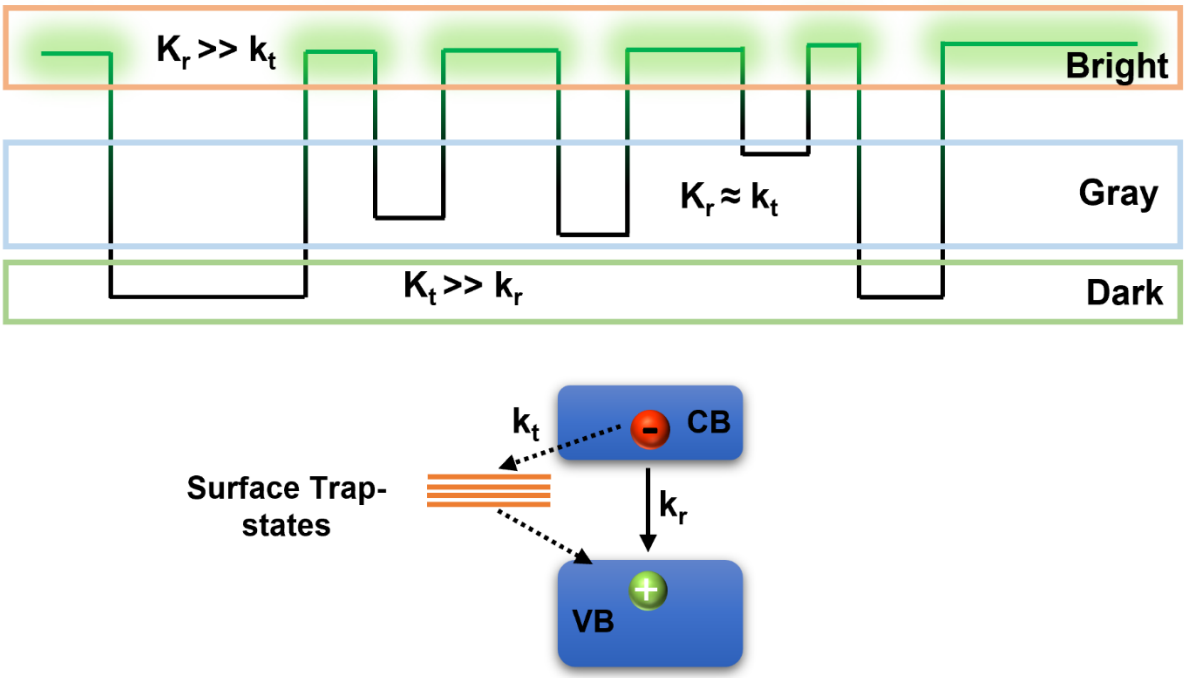

Scheme 1.8. Trapping-detrapping model: When radiative rate is way more than trapping rate of the charged carrier then ON state is observed (upper panel), when k_r and k_t is comparative, gray state fluctuations are observed and when trapping rate is more, OFF state or dark state emerges.

Frantsuzov and co-workers introduced a distinct explanation for temporal variations in nonradiative decay, referred to as the multiple recombination center (MRC) framework. [78-80] Within this picture, emission intermittency originates from gradual fluctuations in the population of effective trap sites rather than from a single dominant trapping event. Numerous

surface-associated quenching sites are assumed to be present, each capable of capturing band-edge charge carriers and promoting rapid nonradiative recombination. Importantly, these quenching centers can reversibly transition between configurations that are either efficient or inefficient in trapping carriers. When a larger fraction of centers is in the active state, the overall nonradiative recombination rate increases substantially, whereas predominately inactive centers result in much slower carrier trapping.

1.6.3 Hot Carrier (HC) Blinking

Beyond BC-type intermittency, another form of emission fluctuation has been reported that can also be interpreted within the multiple recombination centre (MRC) framework. This blinking mode, however, is fundamentally distinct from BC-blinking because the photoluminescence (PL) lifetime does not vary as the emission intensity switches between bright and dark levels. This phenomenon has been ascribed to hot-carrier-related processes and is therefore termed hot-carrier (HC) blinking.[77] In this mechanism, charge carriers generated at high excess energies are captured by short-lived trap states present above the conduction band during their relaxation toward the band edge. These trapped hot carriers then recombine non-radiatively with the remaining counter charges, resulting in a loss of PL signal. Because this trapping pathway competes with carrier cooling rather than with band-edge radiative recombination, the excited-state lifetime remains unchanged throughout HC-blinking events. Temporal fluctuations in emission intensity arise from changes in the efficiency of hot-carrier trapping, which can again be rationalized by dynamic activation and deactivation of multiple recombination centres as described by the MRC model. Notably, HC-blinking has been infrequently observed across most quantum dot systems, which has limited the number of experimental studies addressing this behaviour. [77,79]

1.6.4 Fluorescence Lifetime Intensity Distribution (FLID)

FLID is a 2D false colour plot of information of photons from the intensity and lifetime of single nanocrystal for a certain measurement time (Scheme 1.9.). FLID helps to find out the correlation between intensity and lifetime to resolve the mechanism of blinking involved for a single particle. [77,79,81]

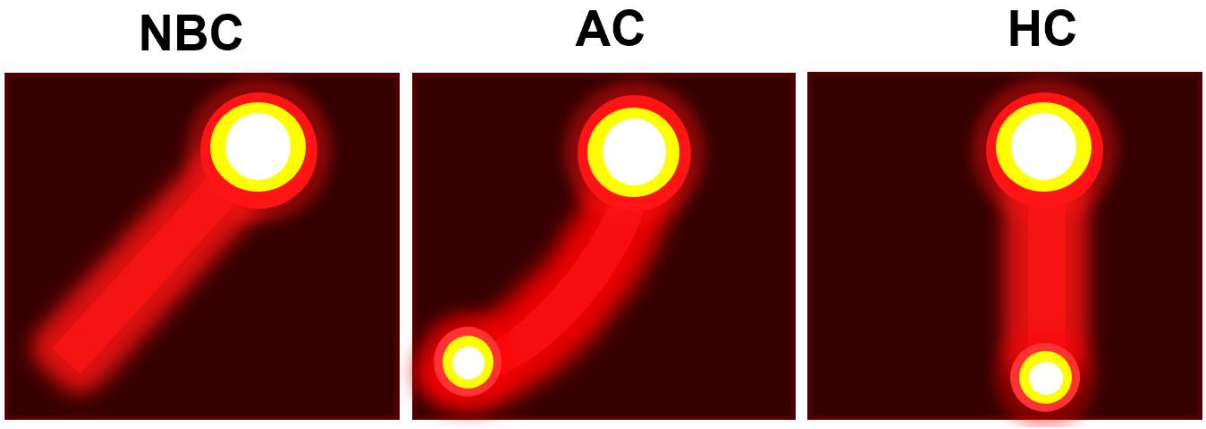

Scheme 1.9. FLID pattern of different of blinking in a nanocrystal.

Auger-blinking produces a curved fluorescence lifetime–intensity distribution (FLID) due to temporal mixing of neutral and charged states rather than true intermediate emissive levels. Identification of these states is achieved by comparing radiative rates extracted from the on- and off-states. In Auger-blinking, the charged state follows statistical scaling, exhibiting a radiative rate approximately twice that of the neutral state. This relationship is quantified by

$$\eta = \frac{I_{ON}\tau_{OFF}}{I_{OFF}\tau_{ON}},$$

where $\eta \approx 2$ confirms neutral–charged state assignment. The FLID map is then fitted by treating intermediate points as artifacts arising from state mixing. [76]

BC-blinking yields a linear fluorescence lifetime–intensity distribution (FLID), as the radiative recombination rate remains constant while intensity fluctuations arise solely from variations in

the non-radiative trapping rate. The PL intensity follows the quantum yield relation resulting in a direct linear correlation between PL intensity and lifetime.

$$I \propto \mathrm{QY} = \frac{k_r}{k_r + k_t(t)} = \frac{\tau}{\tau_r}$$

HC-blinking originates from the trapping of hot carriers during their relaxation process. Because this trapping occurs prior to band-edge recombination, the photoluminescence lifetime remains largely unaffected by intensity fluctuations, resulting in little to no correlation between PL lifetime and intensity in the FLID map. Owing to the scarcity of hot-carrier trap states—likely a consequence of their high formation energies—HC-blinking is infrequently observed and has been reported in only a limited number of studies. The distinct FLID signatures associated with different blinking pathways enable straightforward discrimination between blinking mechanisms. [76,77]

1.6.5 Power Law Kinetic Study of ON/OFF Events

In many nanomaterials, especially quantum dots and perovskite nanocrystals, photoluminescence (PL) blinking shows power-law on/off kinetics, meaning that the durations of bright (ON) and dark (OFF) states do not follow simple exponential decay. Instead, the probability distribution of ON or OFF times, $P(t)$, scales as a power law, $P(t) \propto t^{-\alpha}$, where α typically lies between ~1 and 2. This behavior indicates the absence of a single characteristic timescale and reflects a broad distribution of trapping and detrapping processes. Physically, power-law blinking arises from multiple charge-trapping pathways, a wide range of trap depths, or dynamic fluctuations of surface and environmental states, rather than a single well-defined trap. As a result, both short and extremely long ON or OFF events can occur, giving rise to intermittency over many orders of magnitude in time and highlighting the complex, heterogeneous nature of charge carrier dynamics in nanoscale emitters. [78]

As the rate of blinking is highly nonexponential, the probability of ON and OFF events follows power law kinetics. But, in ON events it has been observed that in the short time period ON events follow exponential behaviour but in longer time due to multiphoton emission it follows power law kinetics. The point where the ON events start deviating from exponential behaviours is called fall-off point or fall-off time ($\tau_{fall\text{-}off}$). Following these points scientist have given the fitting formula for both ON and OFF probability as follows: [75-77,80,82,83]

$$\rho_{OFF} \propto t^{-m_{OFF}}$$

$$\rho_{ON} \propto t^{-m_{ON}} \exp(-\frac{t}{\tau_{fall-off}})$$

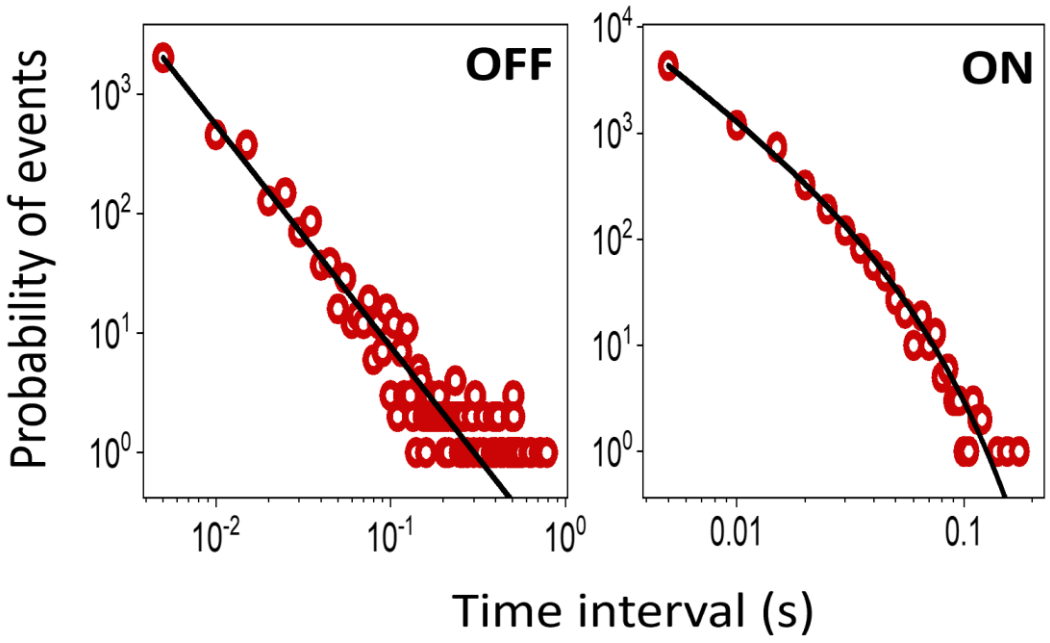

Figure 1.5. Probability of ON and OFF events for a particular QD and corresponding fitted lines from the above-mentioned equation.

As probability of ON events follows both power law and exponential nature it shows truncation behaviour whereas OFF events follow only power law behaviour thus no truncation nature.

1.7 Single Photon Emission from QDs

QDs can act as a single photon source which has a vast advantage in quantum technologies. A perfect single-photon source is expected to generate one and only one photon at a time, with negligible likelihood of emitting two or more photons simultaneously. [84,85] The degree of single-photon purity is quantified using the second-order intensity correlation function, $g^{(2)}(\tau)$, which describes the correlation between photon detection events separated by a time delay τ. This function is experimentally obtained using a Hanbury Brown–Twiss (HBT) interferometric setup. The hallmark of high-quality single-photon emission is a pronounced minimum at zero delay time, known as photon antibunching. In the ideal limit, this corresponds to $g^{(2)}(0) = 0$ (Figure 1.6.A). In practice, a light source is classified as a single-photon source when $g^{(2)}(0) < 0.5$. For demanding applications such as quantum key distribution and quantum imaging, much stricter requirements are imposed, with $g^{(2)}(0)$ typically well below 0.1 to ensure exceptional photon purity. [85, 86,87]

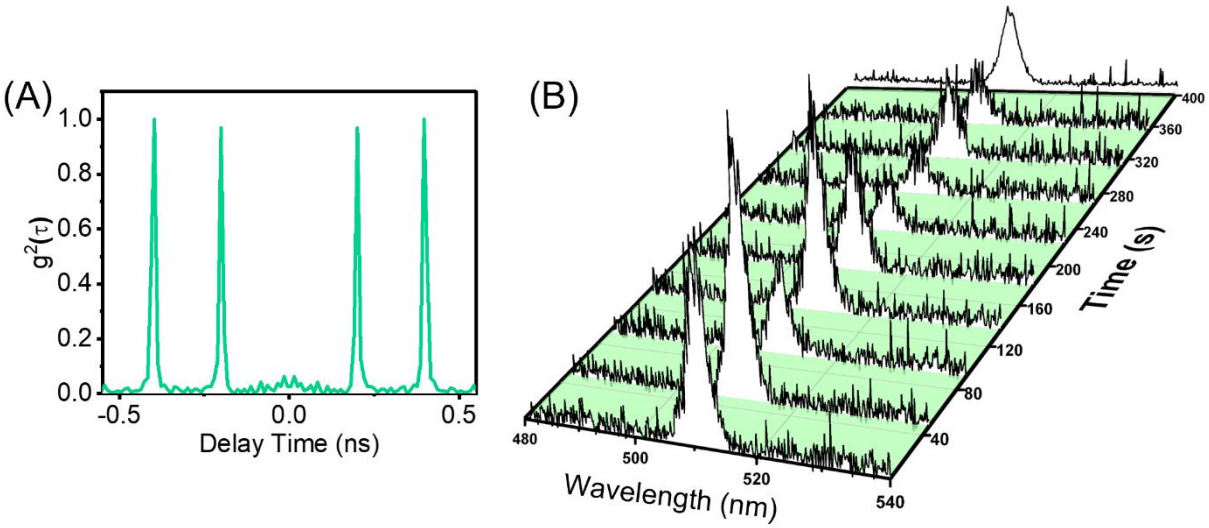

Figure 1.6. Single particle study to ensure the single photon emitting property of a nanoparticle. (A) Photon antibunching study which shows very low $g^2(0)$ amplitude showcasing its high single photon purity, (B) The Single photon emission of a nanoparticle recorded in a EMCCD camera in a spectrograph showing time dependent intensity fluctuations of a single QD.

Another vital measurement to ensure the single particle characteristic is single photon emission spectra in an EMCCD camera. Single-photon emission from an individual quantum dot can be directly visualized and analyzed using a highly sensitive EMCCD camera coupled to a fluorescence microscope or spectrograph. Under weak optical excitation, a single quantum dot behaves as a true quantum emitter, producing one photon per excitation cycle through single-exciton recombination. In EMCCD-based measurements, the emission from a single dot appears as a spatially localized diffraction-limited spot or as a sharp spectral feature when dispersed through a grating (Figure 1.6.B). The peak position of this emission corresponds to the band-edge recombination energy of the single exciton and is extremely sensitive to the dot's size, composition, local dielectric environment, and spectral diffusion.

The full width at half maximum (FWHM) of the single-dot emission peak provides critical information about homogeneous and inhomogeneous broadening mechanisms, including exciton–phonon coupling, charge-induced spectral wandering, and instrumental resolution. Narrow FWHM values indicate reduced dephasing and minimal environmental fluctuations, which are essential for high-purity single-photon generation. By tracking changes in peak position, linewidth, and intensity over time using EMCCD imaging or spectroscopy, one can correlate single-photon emission with blinking behaviour, local charge dynamics, and defect interactions. Thus, EMCCD-based detection of peak energy and FWHM is a powerful approach for characterizing the optical quality, stability, and quantum nature of single-photon emission from individual quantum dots.[87]

1.8 Motivation and Scope of my Thesis Work

Current advances in solar-energy conversion focus on transforming sunlight into electrical power or chemical fuels by constructing molecular and semiconductor systems inspired by natural light-harvesting processes. In biological photosynthesis, light absorption by pigment

molecules initiates a sequence of energy migration and charge-separation events within specialized reaction centers. To emulate these processes and to gain deeper mechanistic understanding, a variety of artificial architectures—ranging from biomolecular frameworks and porphyrin arrays to dendritic structures and organic–inorganic hybrids—have been extensively explored. Within these engineered platforms, semiconductor nanocrystals have emerged as highly effective light absorbers owing to their strong optical cross sections and adjustable electronic structure. Their absorption profiles and excited-state dynamics can be precisely tailored through control over composition, morphology, and dimensionality. In particular, narrow-bandgap semiconductors, including metal chalcogenides, layered two-dimensional materials, and halide perovskites, are especially attractive for capturing photons across the visible and near-infrared spectral regions. Upon photoexcitation, the generated charge carriers can be exploited either for electrical energy generation or to drive redox reactions relevant to solar fuel production. Beyond charge extraction, semiconductor nanomaterials can also act as efficient energy donors to molecular species anchored at their surfaces. In such systems, the fate of the excited state whether it undergoes energy transfer or electron transfer is governed by the relative alignment of the semiconductor band edges with the electronic energy levels or redox potentials of the accepting molecules. In this regard, a thorough understanding of the photophysical behaviour of perovskite materials is crucial for fully exploiting their properties and enabling efficient device development. Exploring novel nanocrystal morphologies that retain the same underlying crystal structure offers new opportunities to uncover structure–property relationships. In this work, various lead halide perovskite nanocrystals were synthesized to investigate different aspects of their optical behaviour at the nanoscale. This highlights the essential role of advanced spectroscopic methods in probing excited-state dynamics. The central objective of this thesis is to examine the photophysical processes occurring in various photoexcited perovskite nanocrystals using a

range of spectroscopic approaches, with particular emphasis on single-particle fluorescence techniques.

This thesis is organized into six chapters. The first two chapters focus on the background and experimental framework of the study. The introductory chapter presents essential fundamental concepts, an overview of the current progress in perovskite nanocrystals (PNCs), and a discussion of their key photophysical properties. The second chapter describes the experimental instrumentation, providing detailed insight into the techniques and equipment employed, their operating principles, and the data analysis procedures used to interpret the results and understand the underlying physical processes. The remaining four chapters are devoted to in-depth experimental investigations, data analysis, and the presentation of the key results and conclusions arising from that work.

The third chapter focuses on the application of an advanced fluorescence correlation spectroscopy approach, namely Pulsed Interleaved Excitation (PIE)-FCS, also referred to as Alternating Laser Excitation (ALEX)-FCS, to investigate the origin of the decrease in the zero-time correlation amplitude, $g^2(0)$, with increasing excitation intensity. Conventionally, this reduction in $g^2(0)$ is attributed to photoactivation processes, where permanently dark or weakly emissive nanoparticles are converted into bright emitters, effectively increasing the number of fluorescent particles within the excitation volume. Through the implementation of PIE-FCS, it is demonstrated that the primary factor responsible for the observed decrease in $g^2(0)$ is brightness heterogeneity among the nanoparticles rather than an actual increase in particle number. At higher excitation powers, initially dim or dark particles become emissive and contribute disproportionately to the detected photon flux. Although the number of nanoparticles within the excitation volume remains unchanged, the enhanced photon emission leads to an apparent reduction in $g^2(0)$. Without a proper understanding, such effects of brightness heterogeneity may be mistakenly interpreted as photobrightening or optical trapping, as these

phenomena can produce similar experimental signatures. To further substantiate this interpretation, single-particle blinking analyses were carried out on a broad range of nanocrystal systems to probe brightness heterogeneity at the individual particle level. The conclusions derived from these studies are consistently supported across multiple nanomaterials, including conventional cubic $CsPbBr_3$ nanocrystals, faceted $CsPbBr_3$ nanocrystals, CdSe/CdS core–shell quantum dots, and graphene quantum dots.

In the fourth chapter, the photophysical properties of faceted $CsPbBr_3$ nanocrystals and their distinct blinking behaviours are investigated. Single-particle spectroscopic techniques, including PL blinking analysis, FLID mapping, photon antibunching measurements, and power-law analysis of ON/OFF time distributions, are employed. It is observed that as the number of facets increases from 6 to 12 to 26, the contribution of trion states becomes more pronounced, leading to a reduction in the ON-state fraction and a substantial increase in OFF-state events. Through a careful examination of facet-dependent charge transfer to the surrounding environment, it is concluded that nanocrystals with a higher number of facets are more susceptible to interactions with surface environments such as moisture or scavenger molecules. These interactions promote the formation of additional surface defects, thereby enhancing non-radiative recombination pathways via Auger-assisted trion channels. Furthermore, the probability of photoionization is evaluated by analysing the ON-state population under both low and high excitation powers, revealing an increased tendency for photoionization in highly faceted perovskite nanocrystals.

The fifth chapter is devoted to a detailed investigation of phase transfer in red-emitting $CsPbI_3$ perovskites and the associated changes in their optical properties, examined through single-particle blinking studies and advanced Fluorescence Lifetime Correlation Spectroscopy (FLCS) techniques. FLCS was employed to distinguish whether detected photons originated from the same emission centre or from different centres. In this study, a comprehensive analysis

of carrier dynamics was conducted on both α-phase and mixed-phase $CsPbI_3$ nanocrystals using single-particle blinking, FLCS, and ensemble measurements. Single-particle blinking analyses, including FLID mapping and intensity–lifetime scaling, revealed distinct recombination mechanisms in the two phases. In α-phase nanocrystals, blinking was found to be predominantly governed by shallow trap-induced NBC recombination, with a minor contribution from HC recombination. In contrast, blinking in mixed-phase nanocrystals was primarily attributed to deep trap-induced HC recombination, alongside moderate contributions from trion and NBC recombination. Consistent insights were provided by FLCS investigations, indicating a higher involvement of trap states in mixed-phase nanocrystals compared to α-phase nanocrystals. A notable observation from FLCS was the growth feature in the initial correlation of the CCF, confirming the dynamic behaviour of shallow trap states driving nanoparticle blinking in fluid-phase dispersions. A thorough understanding of carrier dynamics in red-emitting $CsPbI_3$ perovskite nanocrystals is critical for the rational design of next-generation optoelectronic and photovoltaic devices, as these nanocrystals are considered ideal candidates for such applications.

The final chapter investigates the energy transfer and charge transfer efficiencies of faceted $CsPbBr_3$ nanocrystals to organic dyes and surrounding molecules, respectively. Both ensemble and single-particle spectroscopy were employed to quantify the dexter energy transfer efficiency from these faceted nanoparticles to the dyes. Ensemble measurements indicated that the energy transfer efficiency increases with the number of facets, following a Dexter-type energy transfer pathway. However, single-particle studies, which accounted for the step-bleaching behaviour of the acceptor dye, revealed that the energy transfer efficiency remains largely similar regardless of the nanoparticle faceting. This observation is likely due to stronger binding of dye molecules to higher-faceted nanoparticles in solution, as confirmed by FCS measurements and double-reciprocal plots. The practical relevance of these extra-faceted

nanocrystals was further demonstrated through carrier extraction studies, in which facet-rich nanoparticles significantly outperformed their cubic counterparts. These results underscore the critical role of facet engineering in modulating interfacial interactions and establish extra-faceted $CsPbBr_3$ nanocrystals as highly promising candidates for advanced photovoltaic, photocatalytic, and light-harvesting applications.

The overarching aim of this thesis is to provide a comprehensive understanding of carrier dynamics in perovskite nanocrystals and to elucidate how variations in their morphology influence the intrinsic photophysics of these nanoparticles. Advanced single-particle spectroscopic techniques have been employed to reveal these fundamental processes, offering insights into strategies for enhancing photovoltaic performance and optimizing the efficiency of next-generation devices based on perovskite nanocrystals.

1.9 References

[1] S. G. Stenspil, J. Chen, M. B. Liisberg, A. H. Flood, B. W. Laursen *Chem. Sci.* **2024**, *15*, 5531-5538.

[2] B. Hötzer, I. L. Medintz, N. Hildebrandt, *Small* **2012**, *8*, 2297-2326.

[3] L. Yuan, W. Lin, K. Zheng, L. He, W. Huang, *Chem. Soc. Rev.* **2013**, *42*, 622-661.

[4] D. Svechkarev, A. M. Mohs, *Curr. Med. Chem.* **2019**, *26*, 4042-4064.

[5] B. K. Rajbongshi, S. Rafiq, S. Bhowmik, P. Sen, *J. Mol. Struct.* **2023**, *1275*, 134538.

[6] P. Ramasamy, N. Kim, Y.-S. Kang, O. Ramirez, J.-S. Lee, *Chem. Mater.* **2017**, *29*, 6893-6899.

[7] S. Kubendhiran, Z. Bao, K. Dave, R.-S. Liu, *ACS Appl. Nano Mater.* **2019**, *2*, 1773-1790.

[8] A. Patra, C. G. Chandaluri, T. P. Radhakrishnan, *Nanoscale* **2012**, *4*, 343-359.

[9] R. C. Ashoori, *Nature* **1996**, *379*, 413-419.

[10] S. Afzal, U. Maitra, *Helvetica Chimica Acta* **2022**, *105*, e202100194.

[11] Jean-Claude G. Bünzli, *Chem. Rev.* **2010**, *110*, 2729–2755.

[12] M. Chalfie, *Photochem. Photobiol.* **1995**, *62*, 651.

[13] D. Lee, J. Song, G. Song, Yoonsoo Pang, *Nanoscale Adv.* **2022**, *4*, 2794-2805.

[14] S. A. Lee, S. Link, *Acc. Chem. Res.* **2021**, *54*, 1950–1960.

[15] J. Zito, I. Infante, *Acc. Chem. Res.* **2021**, *54*, 1555–1564.

[16] Z. Jiang, A. Ren, Y. Yan, J. Yao, Y. S. Zhao, *Adv. Mater.* **2022**, *34*, 2106095.

[17] S. V. Gaponenko, *Cambridge University Press.* **2010**, ISBN-10: 0521763754.

[18] K. P. Sathe, N. S. Garud, V. B. Bangar, N. R. Gadakh, *J. Adv. Sci. Res.* **2022**, *13*, 23-27.

[19] A. Hoshino, S. Hanada, K. Yamamoto, *Arch. Toxicol.*, **2011**, *85*, 707-720.

[20] Q. Zhang, Y. Yin, *ACS Cent. Sci.* **2018**, *4*, 668-679.

[21] D. Chen, X. Chen, *J. Mater. Chem. C.* **2019**, *7*, 1413-1446.

[22] Q. A. Akkerman, G. Rainò, M. V. Kovalenko, L. Manna, *Nat. Mater.* **2018**, *17*, 394-405.

[23] A. Dey, J. Ye, A. De, E. Debroye, S. K. Ha, E. Bladt, A. S. Kshirsagar, Z. Wang, J. Yin, Y. Wang, L. N. Quan, F. Yan, M. Gao, X. Li, J. Shamsi, T. Debnath, M. Cao, M. A. Scheel, S. Kumar, J. A. Steele, M. Gerhard, L. Chouhan, K. Xu, X. Wu, Y. Li, Y. Zhang, A. Dutta, C. Han, I. Vincon, A. L. Rogach, et al., *ACS Nano* **2021**, *15,* 10775-10981.

[24] M. A. Pen˜a, J. L. G. Fierro, *Chem. Rev.* **2001**, *101*, 1981-2017.

[25] V. M. Goldschmidt, *Naturwissenschaften* **1926**, *14*, 477-485.

[26] J. S. Manser, J. A. Christians, P. V. Kamat, *Chem. Rev.* **2016**, *116*, 12956-13008.

[27] H. L. Wells, *Z. Anorg. Allg. Chem.* **1893**, *3*, 195-210.

[28] J. Shamsi, A. S. Urban, M. Imran, L. D. Trizio, L. Manna, *Chem. Rev.* **2019**, *119*, 3296−3348.

[29] A. K. Jena, A. Kulkarni, T. Miyasaka, *Chem. Rev.*, **2019**, *119*, 3036−3103.

[30] NREL Best Efficiency Chart: https://www.nrel.gov/pv/assets/pdfs/best-research_cell-efficiencies.20200104.pdf.

[31] Q. V. Le, H. W. Jang, S. Y. Kim, *Small Methods* **2018**, *2*, 1700419.

[32] S. D. Stranks, H. J. Snaith, *Nat. Nanotechnol.,* **2015**, *10*, 391−402.

[33] W. J. Yin, T. T. Shi, Y. F. Yan, *Appl. Phys. Lett.* **2014**, *104*, 63903.

[34] D. W. deQuilettes, S. M. Vorpahl, S. D. Stranks, H. Nagaoka, Eperon, G. E.; M. E. Ziffer, H. J. Snaith, D. S. Ginger, *Science* **2015**, *348*, 683−686.

[35] L. Protesescu, S. Yakunin, M. I. Bodnarchuk, F. Krieg, R. Caputo, C. H. Hendon, R. X. Yang, A. Walsh, M. V. Kovalenko, *Nano Lett.* **2015**, *15*, 3692−3696.

[36] A. Swarnkar, R. Chulliyil, V. K. Ravi, M. Irfanullah, A. Chowdhury, A. Nag, *Angew. Chem. Int. Ed.* **2015**, *54*, 15424-15428.

[37] S. Seth, T. Ahmed, A. De, A. Samanta, *ACS Energy Lett.* **2019**, *4*, 1610−1618.

[38] Q. A. Akkerman, G. Rainò, M. V. Kovalenko, L. Manna, Genesis, *Nature Mater.* **2018**, *17*, 394-405.

[39] H. Huang, M. I. Bodnarchuk, S. V. Kershaw, M. V. Kovalenko, A. L. Rogach, *ACS Energy Lett.* **2017**, *2*, 2071–2083.

[40] M. V. Kovalenko, L. Protesescu, M. I. Bodnarchuk, *Science* **2017**, *358*, 745-750.

[41] S. K. Mahankudo, A. Das, K. Mishra, M. Barai, P. Mal, S. Ghosh, *ACS Appl. Nano Mater.* **2022**, *5*, 4360-4366.

[42] A. Swarnkar, A. R. Marshall, E. M. Sanehira, B. D. Chernomordik, D. T. Moore, J. A. Christians, T. Chakrabarti, J. M. Luther, *Science* **2016**, *354*, 92–95.

[43] N. Mondal, A. De, A. Samanta, *ACS Energy Lett.* **2019**, *4*, 32 39.

[44] D. Ghosh, E. Welch, A. J. Neukirch, A. Zakhidov, S. Tretiak, *J. Phys. Chem. Lett.* **2020**, *11*, 3271-3286.

[45] K. Miyata, D. Meggiolaro, M. T. Trinh, P. P. Joshi, E. Mosconi, S. C. Jones, F. D. Angelis, X.-Y. Zhu, *Science* **2017**, *3*, 1701217.

[46] J. Puthenpurayil, O. H.-C. Cheng, T. Qiao, D. Rossi, D. H. Son, *J. Chem. Phys.* **2019**, *151*, 154706.

[47] C. De Los Santos, C.-W. Chang, M.-A. Mycek, R. A. Cardullo, *Mol. Reprod. Dev.*, **2015**, *82*, 587–604.

[48] J. R. Lakowicz, Principles of Fluorescence Spectroscopy, *Springer*, **2013**.

[49] C. Bi, Z. Yao, J. Hu, X. Wang, M. Zhang, S. Tian, A. Liu, Y. Lu, N. H. de Leeuw, M. Sui, J. Tian, *ACS Energy Lett.* **2023**, *8*, 731-739.

[50] W. K. Bae, L. A. Padilha, Y.-S. Park, H. McDaniel, I. Robel, J. M. Pietryga, V. I. Klimov, *ACS Nano*, **2013**, *7*, 3411-3419.

[51] S. Das, G. Rana, F. Ali, A. Datta, *Nanoscale*, **2023**, *15*, 4469-4476.

[52] M. J. Trimpl, A. D. Wright, K. Schutt, L. R. V. Buizza, Z. Wang, M. B.Johnston, H. J. Snaith, P. Müller-Buschbaum, L. M. Herz, *Adv. Funct.Mater.* **2020**, *30*, 2004312.

[53] T. Leijtens, G. E. Eperon, A. J. Barker, G. Grancini, W. Zhang, J. M. Ball, A. R. S. Kandada, H. J. Snaith, A. Petrozza, *Energy Environ. Sci.*, **2016**, *9*, 3472-3481.

[54] A. W. Cohn, A. M. Schimpf, C. E. Gunthardt, D. R. Gamelin, *Nano Lett.* **2013**, *13*, 1810–1815.

[55] D. Acharjee, A.B. Mahato, A. Das, S. Ghosh, *J. Phys. Chem. C*, **2023**, *127*, 19643-19650.

[56] K. Mishra, D. Acharjee, A. Das, S. Ghosh, *J. Phys. Chem. B*, **2021,** *125*, 11017-11025.

[57] Jin Z. Zhang, *J. Phys. Chem. B*, **2000**, *104*, 7239-7253.

[58] N. Mondal, A. Samanta, *J. Phys. Chem. C*, **2016**, *120*, 650-658.

[59] T. Ahmed, S. Paul, A. Samanta**,** *J. Phys. Chem. C*, **2022**, *126*, 9109-9116.

[60] M. Kurashvili, J. Llusar, L. S. Stickel, T. Würthner, D. Ederle, I. Infante, J. Feldmann, Q. A. Akkerman, *Angew. Chem.*, **2025**, *137*, e202420658.

[61] F. J. Hofmann, M. I. Bodnarchuk, D. N. Dirin, J. Vogelsang, M. V. Kovalenko, J. M. Lupton**,** *Nano Lett.* **2019**, *19*, 8896–8902.

[62] L. G. Feld, S. C. Boehme, V. Morad, Y. Sahin, C. J. Kaul, D. N. Dirin, G. Rainò**,** M. V. Kovalenko, *ACS Nano*, **2024**, *18*, 9997–10007.

[63] Michèle G. Greiner, Andreas Singldinger**,** Nina A. Henke, Carola Lampe, Ulrich Leo, Moritz Gramlich, Alexander S. Urban, *Nano Lett.*, **2022**, *22*, 6709–6715.

[64] J. T. DuBose, P. V. Kamat, *J. Am. Chem. Soc.*, **2023**, *145*, 4601–4612.

[65] J. T. DuBose, P. V. Kamat**,** *J. Am. Chem. Soc.*, **2021**, 143, 19214–19223.

[66] A. Cortés-Villena, A. Cadranel, K. Azizi, T. Torres, D. M. Guldi, J. Pérez-Prieto, R. E. Galian, *Adv. Sci.*, **2025**, *12*, 2414831.

[67] A. Das, D. Acharjee, M. K. Panda, A. B. Mahato and S. Ghosh, *J. Phys. Chem. Lett.*, **2023**, *14*, 3953-3960.

[68] S. Biswas, S. Akhil, N. Kumar, M. Palabathuni, R. Singh, V. G. V. Dutt, N. Mishra, *J. Phys. Chem. Lett.*, **2023**, *14*, 1910–1917.

[69] S. Y. Kim, Y.-J. Cho, A.-R. Lee, H.-j. Son, W.-S. Han, D. W. Cho and S. O. Kang, *Phys, Chem. Chem. Phys.* **2017**, *19*, 426–435.

[70] J. T. DuBose, P. V. Kamat, *Chem. Rev.* **2022**, *122*, 12475–12494.

[71] M. Nirmal, B. O. Dabbousi, M. G. Bawendi, J. J. Macklin, J. K. Trautman, T. D. Harris, L. E. Brus, *Nature* **1996**, *383*, 802–804.

[72] R. M. Kraus, P. G. Lagoudakis, J. Müller, A. L. Rogach, J. M. Lupton, J. Feldmann, D. V. Talapin, H. Weller, *J. Phys. Chem. B.* **2005**, *109*, 18214–18217.

[73] D. Harankahage, J. Cassidy, J. Beavon, J. Huang, N. Brown, D. B. Berkinsky, A. Marder, B. Kayira, M. Montemurri, P. Anzenbacher, R. D. Schaller, L.Sun, M. G.

Bawendi, A. V. Malko, B. T. Diroll, M. Zamkov, *J. Am. Chem. Soc.* **2023**, *145*, 13326–13334.

[74] M. K. Panda, D. Acharjee, A. B. Mahato, S. Ghosh, *Small* **2024**, *20*, 2311559.

[75] C. Galland, Y. Ghosh, A. Steinbruck, M. Sykora, J. A. Hollingsworth, V. I. Klimov, H. Htoon, *Nature*, **2011**, *479*, 203–207.

[76] H. Zang, Hongbo Li, N.S. Makarov, K. A. Velizhanin, K. Wu, Y-S Park, V. I. Klimov, *Nano Lett.* **2017**, *17*,1787–1795.

[77] G. Yuan, D.E. Gomez,´ N. Kirkwood, K. Boldt, P. Mulvaney, *ACS Nano* **2018**, *12*, 3397–3405.

[78] P. A. Frantsuzov, S. Volkan-Kacso, B Janko, *Phys. Rev. Lett.* **2009**, *103*, 207402.

[79] A. A. Cordones, S. R. Leone, *Chem. Soc. Rev.* **2013**, *42*, 3209—3221.

[80] Y-S Park, S. Guo, N. S. Makarov, V. I. Klimov, *ACS Nano* **2015**, *9*, 10386–10393.

[81] M. K. Panda, D. Acharjee, A. B. Mahato, S. Ghosh, *Adv. Optical Mater.* **2025**, *13*, 2402899.

[82] T. Ahmed, S. Seth, A. Samanta, *ACS Nano* **2019**, *13*, 13537−13544.

[83] M. K. Panda, D. Acharjee, N. Nandi, S. Koley, S. Ghosh, *Chem. Eur. J.* **2024**, *30*, e202401938.

[84] T. Kim, S. Il Jung, S. Ham, H. Chung, D. Kim, *Small* **2019**, *15*, 1900355.

[85] B. Lounis, M. Orrit *Rep. Prog. Phys.* **2005**, *68*, 1129.

[86] C. Zhu, M. Marczak, L. Feld, S. C. Boehme, C. Bernasconi, A. Moskalenko, Ihor Cherniukh, D. Dirin, M. I. Bodnarchuk, M. V. Kovalenko, G. Raino, *Nano Lett.* **2022**, *22*, 3751–3760.

[87] F. Hu, H. Zhang, C. Sun, C. Yin, B. Lv, C. Zhang, W. W. Yu, X. Wang,Y. Zhang, M. Xiao *ACS Nano*. **2015**, *9*, 12410–12416.

[88] S.Pierini, M.D'Amato, M. Goyal, Q. Glorieux, E. Giacobino, E.Lhuillier, C. Couteau, A. Bramati, *ACS Photonics.* **2020**, *7*, 2265-2272.

CHAPTER 2

Instrumentation and Adopted Methodologies

2.1 Abstract

This chapter systematically describes the experimental tools and theoretical approaches used to accomplish the objectives of this research. It offers an in-depth explanation of the measurement platforms, analytical methods, mathematical formalisms, and physical models applied to ensure the accuracy and robustness of the results. The discussion is structured to clarify how experimental data were acquired, processed, and interpreted to support the conclusions drawn in this work.

Each section starts with a description of the criteria guiding the choice of specific instruments, aligned with the aims of the study and the type of information required. This is followed by an explanation of the operating principles of the instruments, the justification for their suitability in obtaining reliable data, and the procedures adopted for quantitative analysis.

As this thesis primarily focuses on the photophysical properties of lead halide perovskite nanocrystals, techniques probing excited-state dynamics are extensively employed. These include optical absorption spectroscopy, steady-state and time-resolved photoluminescence measurements, fluorescence correlation spectroscopy (FCS), fluorescence lifetime correlation spectroscopy (FLCS), Single particle fluorescence Spectroscopy, Photon antibunching, Single photon emission and fluorescence upconversion spectroscopy. In addition to these, structural and compositional characterization of the samples was carried out using high-resolution transmission electron microscopy (HRTEM), X-ray diffraction (XRD), X-ray photoelectron spectroscopy (XPS), and energy-dispersive X-ray analysis (EDAX).

2.2 Single Particle Spectroscopy

Single-Particle Spectroscopy (SPS) is a powerful optical technique that probes the photophysical properties of individual nanoscale emitters such as quantum dots, perovskite nanocrystals, molecules, or defects, one particle at a time. Unlike ensemble measurements,

which average over many particles and mask intrinsic variations, SPS reveals heterogeneity in emission intensity, lifetime, spectral position, and dynamics that arise from differences in size, shape, surface chemistry, and local environment. By isolating single emitters, SPS provides direct access to fundamental processes such as exciton recombination, blinking, spectral diffusion, photon antibunching, energy transfer, and charge trapping, offering a microscopic understanding of light–matter interactions at the nanoscale.

The importance of SPS lies in its ability to uncover mechanisms that govern device performance but remain hidden in ensemble studies. Phenomena such as intermittency (blinking), multiexciton recombination, Auger processes, and single-photon emission can only be unambiguously identified at the single-particle level. Consequently, SPS has become essential for the rational design of high-performance optoelectronic devices, including single-photon sources, light-emitting diodes, lasers, photovoltaic systems, and quantum technologies.

Experimentally, SPS is most commonly implemented using a confocal fluorescence microscopy (CFM) setup, which provides high spatial resolution and efficient background rejection. In this configuration, a tightly focused diode laser excites a diffraction-limited volume containing a single emitter, and the emitted fluorescence is collected through a same objective with high numerical aperture and spatially filtered using a pinhole. The detected photons are then directed to highly sensitive single-photon detectors such as avalanche photodiodes (APDs) or micro photon device (MPDs) detectors. APDs offer high quantum efficiency, low dark counts, and excellent timing resolution, making them ideal for time-correlated single-photon counting (TCSPC) and photon antibunching measurements. MPDs, with their fast temporal response, are particularly useful for ultrafast timing applications. Together, the confocal setup and single-photon detectors form the backbone of SPS, enabling precise measurements of intensity, lifetime, and photon statistics from individual nano-emitters.[1]

2.2.1 Time-resolved confocal fluorescence microscope

The spatial resolving capability of an optical microscope is fundamentally limited by diffraction and can be expressed by the relation,

$$d=\lambda/2NA \qquad (2.1)$$

where λ represents the excitation wavelength and NA denotes the numerical aperture of the objective lens. The numerical aperture is defined as $NA = n \sin\theta$, with n being the refractive index of the immersion medium and θ the maximum half-angle of light collection by the objective. In conventional wide-field microscopy, the entire sample volume is illuminated simultaneously, which leads to significant background contributions from out-of-focus regions and degrades image contrast.

Confocal fluorescence microscopy (CFM) overcomes this limitation by employing point-wise excitation and spatial filtering. In this approach, a pinhole positioned at a plane conjugate to the focal point selectively transmits fluorescence originating only from the focal volume, effectively rejecting out-of-focus emission. As a result, the effective detection volume is confined to a small, three-dimensional ellipsoidal region defined by the objective lens and the pinhole aperture. A schematic illustration of the confocal microscope configuration and its detection volume is shown in Scheme 2.1.

All single-particle measurements in this work were carried out using a time-resolved confocal microscope (MicroTime 200, PicoQuant), built around an inverted optical microscope platform (Olympus IX71). Sample excitation was achieved using pulsed diode lasers operating at 375 nm and 425 nm, with repetition rates tunable between 3 and 40 MHz. The laser output was delivered to the main optical unit through a polarization-maintaining single-mode optical fiber. Within the optical unit, the excitation beam was directed into the microscope via a dichroic

mirror and tightly focused onto the sample deposited on a coverslip using a high-numerical-aperture water or oil immersion objective (60×, NA = 1.2 & 100×, NA = 1.4).

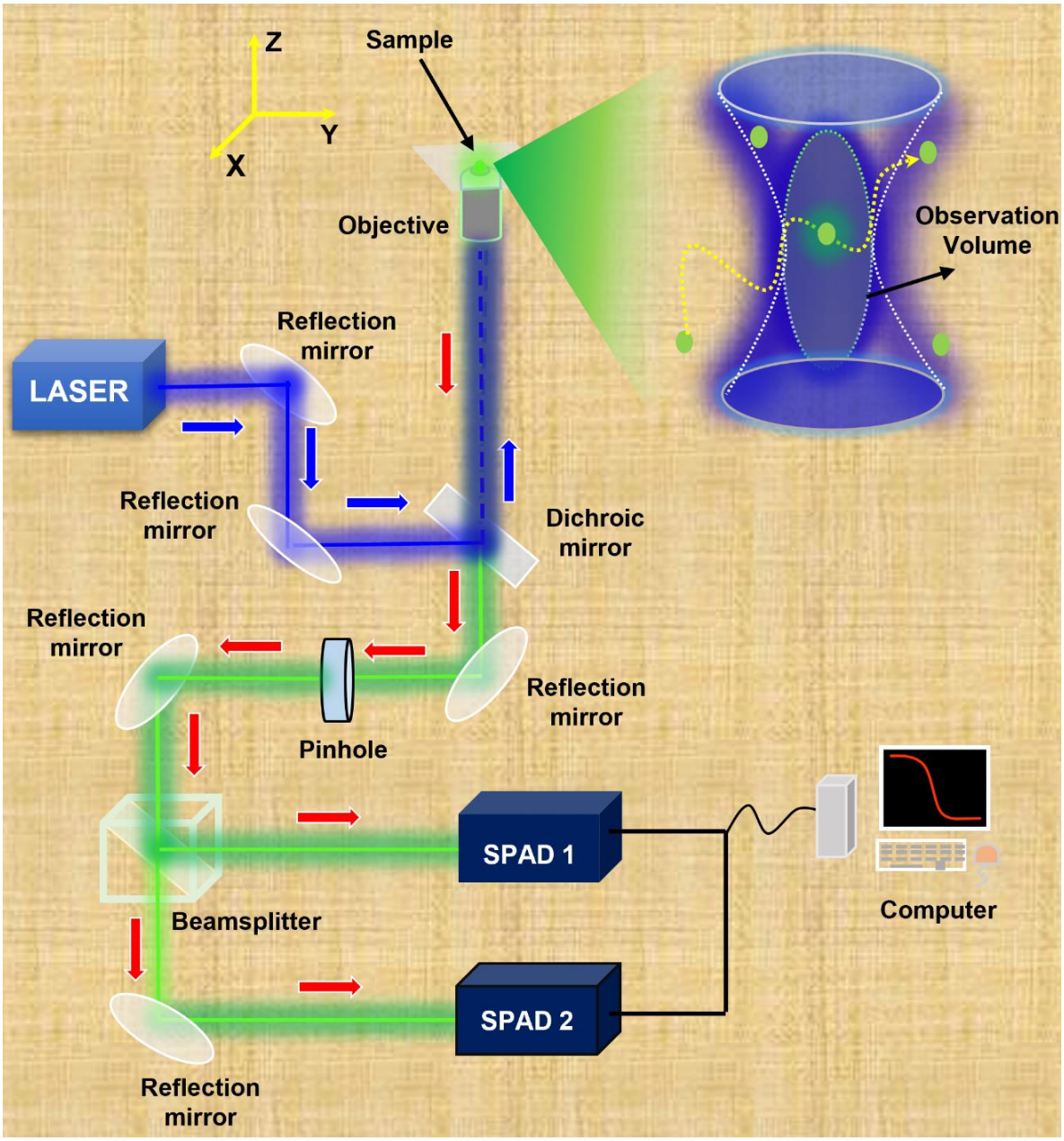

Scheme 2.1. Schematic diagram of time-resolved confocal fluorescence microscope setup.

The excitation power incident on the sample was continuously monitored using a photodiode. A portion of the back-reflected light was routed to a charge-coupled device (CCD) camera

through a beam splitter, enabling precise adjustment of the focal position and verification of the illumination profile.

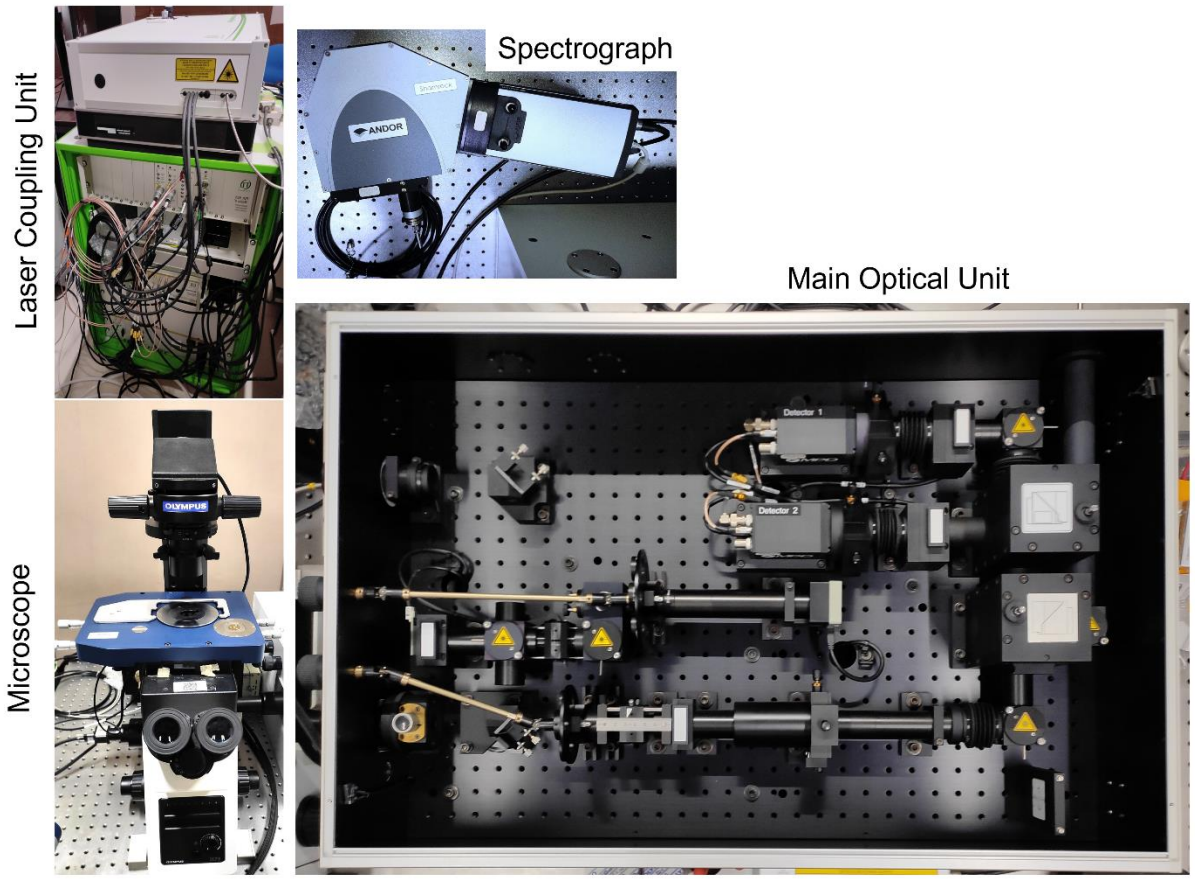

Figure 2.1. Our confocal fluorescence microscope setup (PicoQuant) with spectrograph (ANDOR).

Fluorescence emitted from the sample was collected by the same objective and spectrally separated from the excitation light using appropriate dichroic mirrors and long-pass filters (425 nm and 490 nm for 375 nm and 470 nm laser excitation, respectively). To ensure detection from the confined focal region, the emission was passed through a 50 µm pinhole before being re-collimated and directed toward single-photon avalanche photodiode (SPAD) detectors.

Photon detection was performed using either a single SPAD or a pair of SPADs, with a 50:50 beam splitter employed for dual-channel measurements. Raster scanning over areas up to 80 μm × 80 μm was implemented for imaging and localization. All fluorescence signals were recorded using a time-correlated single-photon counting (TCSPC) module (MultiHarp 150) operated in time-tagged time-resolved (TTTR) mode. In this acquisition scheme, both the delay between excitation and photon arrival (via the start–stop method) and the absolute arrival time of each detected photon relative to the start of the experiment are stored simultaneously. [1,2]

This confocal TCSPC platform was extensively utilized to investigate fluorescence characteristics and photoexcited carrier recombination dynamics in individual perovskite nanocrystals. Measurements included fluorescence correlation spectroscopy (FCS) on freely diffusing nanocrystals in solution, as well as photoluminescence intermittency (blinking) analyses of nanocrystals immobilized on substrates.

2.2.2 Fluorescence Correlation Spectroscopy

Fluorescence correlation spectroscopy (FCS) is a powerful and sensitive technique for probing molecular-scale dynamics and has found widespread use across physics, chemistry, and biology. By analyzing temporal fluctuations in fluorescence intensity arising from molecules traversing a tightly confined observation volume, FCS enables quantitative determination of key parameters such as molecular concentration, diffusion coefficients, and intermolecular interactions in both in vitro and in vivo environments. [1,3,4]

In a typical FCS experiment, fluorescence emission is collected from an extremely small detection volume on the order of ~10^{-15} L, most commonly defined using a confocal microscope. As fluorescent species randomly diffuse into and out of this volume, the detected fluorescence signal exhibits time-dependent fluctuations, δF(t), around an average intensity

⟨F⟩. These fluctuations are statistically analyzed using the normalized temporal autocorrelation function, G(τ), defined as

$$G(\tau) = \frac{\langle F(t+\tau)F(t)\rangle}{\langle F\rangle^2} = 1 + \frac{\langle \delta F(t+\tau)\delta F(t)\rangle}{\langle F\rangle^2} \qquad (2.2)$$

where δF(t) = F(t) − ⟨F⟩ and τ is the correlation delay time.

The dominant contribution to the autocorrelation signal originates from the stochastic diffusion of fluorescent molecules through the confocal volume. Analysis of the decay behavior of G(τ) yields the characteristic diffusion time, from which the hydrodynamic size of the diffusing species can be inferred. Beyond diffusion dynamics, FCS is also highly sensitive to photophysical and photochemical processes of excited fluorophores, such as triplet-state formation, blinking, and photoactivation. Furthermore, FCS can be employed to extract quantitative information on molecular interactions, including binding affinities, reaction kinetics, and changes in local microviscosity.

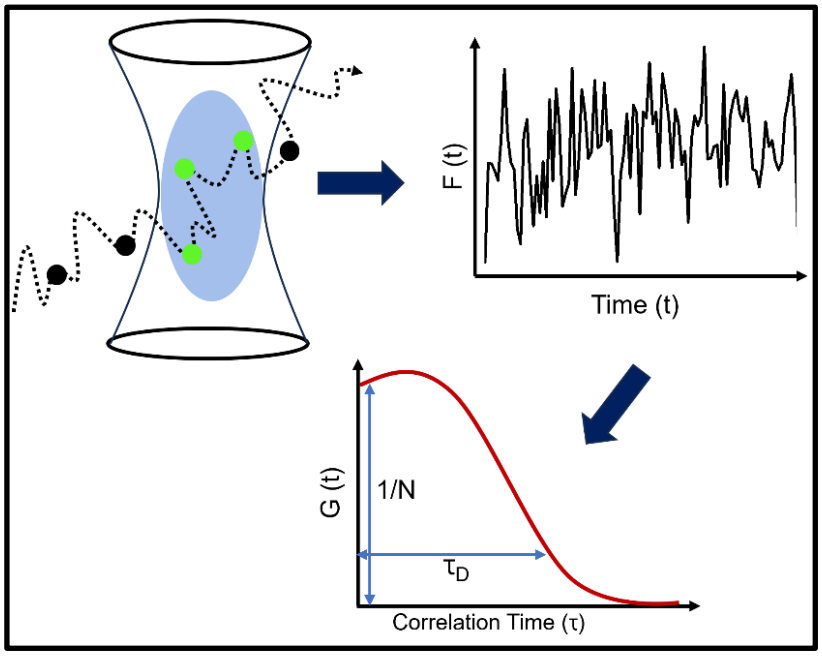

Scheme 2.2. The basic concept of fluorescence correlation spectroscopy is represented pictorially.

The exceptional sensitivity of modern photon detectors allows fluorescence intensity fluctuations from individual molecules to be accurately recorded. While the path followed by a molecule as it diffuses through the laser focus is inherently stochastic, statistical analysis of signals collected from a large number of such single-molecule events enables reliable extraction of parameters such as the average diffusion time and molecular size through temporal correlation methods. Although a laser beam propagating through a sample chamber nominally illuminates an extended region, precise optical focusing combined with appropriate spatial filtering in an FCS setup ensures that only photons originating from the immediate vicinity of the focal point are detected. As a result, the effective observation volume is confined to a minute region around the beam waist. This detection volume, schematically illustrated in Scheme 2.2, is commonly approximated by an ellipsoidal geometry. [5-8]

2.2.2.1 Working Principle

Fluorescence correlation spectroscopy (FCS) is typically implemented in a confocal microscope configuration, where the confocal geometry enables the definition of an extremely small detection volume on the order of ~0.3 femtoliters. Such spatial confinement significantly enhances the signal-to-noise ratio (SNR) of FCS measurements. The restricted observation volume is created by tightly focusing the excitation laser onto the sample and selectively collecting fluorescence only from this focal region. This is achieved using a high–numerical-aperture (high-NA) objective lens for strong optical confinement, in combination with a spatial pinhole placed in the detection path to reject out-of-focus emission. The numerical aperture of the objective determines the focusing capability and is defined as $NA = n \sin \theta$, where n is the refractive index of the immersion medium (e.g., $n_{air} \approx 1.00$, $n_{water} = 1.33$, $n_{oil} \approx 1.55$) and θ represents the maximum half-angle of collected light rays. In practice, however, light cannot be focused to an infinitesimal point, as it behaves as an electromagnetic wave and is therefore limited by diffraction. Consequently, the focal spot is broadened to a minimum lateral

dimension of approximately λ/2, which defines the theoretical lower limit of the transverse size of the observation volume. Further confinement of the detection region is accomplished by placing a pinhole at the conjugate image plane. Fluorescence emitted from the focal region is directed through a dichroic mirror and subsequently focused onto the pinhole before reaching a single-photon detector. Emission originating outside the focal plane is largely rejected by the pinhole, effectively reducing the axial extent of the observation volume. This spatial filtering improves the SNR and reduces the acquisition time required to obtain reliable autocorrelation curves. Although FCS can be performed using continuous-wave (CW) excitation, pulsed laser excitation combined with time-correlated single-photon counting (TCSPC) detection is often preferred. This approach provides superior background suppression and ensures that only photons emitted by fluorophores excited within the focal volume contribute to the detected signal.

Due to the stochastic translational motion of molecules within a confocal microscope, fluctuations in the detected fluorescence intensity, $F(t)$, arise as individual emitters randomly enter and exit the defined observation volume. These temporal intensity variations carry information about molecular dynamics and are quantitatively analyzed through autocorrelation. The normalized autocorrelation function is defined as

$$G(\tau) = \frac{\langle F(t+\tau)F(t)\rangle}{\langle F\rangle^2} \qquad (2.3)$$

where the angular brackets $\langle\cdot\rangle$denote time averaging and τ represents the correlation lag time. Physically, $G(\tau)$describes how closely the fluorescence signal resembles itself as a function of increasing delay time, thereby capturing the temporal self-similarity of the signal.

Assuming the detection volume can be approximated by a three-dimensional Gaussian intensity distribution, the experimentally obtained autocorrelation curve can be fitted using a standard 3D diffusion model, as expressed in Eq. (2.4).

$$G(\tau) = \frac{1}{N}\left(1 + \frac{\tau}{\tau_D}\right)^{-1}\left(1 + \frac{\tau r_0^2}{\tau_D z_0^2}\right)^{-\frac{1}{2}} \qquad (2.4)$$

In this model, τ_D corresponds to the mean residence time of a molecule within the observation volume due to diffusion, while Ndenotes the average number of fluorescent molecules present in the detection volume. The parameters r_0 and z_0 define the radial and axial dimensions of the confocal volume, respectively, corresponding to the distances at which the excitation intensity falls to $1/e^2$ of its maximum value. An important feature of the autocorrelation function is its amplitude at zero lag time, $G(0)$, which is inversely proportional to the number of fluorescent species in the observation volume, i.e., $G(0) \propto 1/N$. Consequently, changes in molecular concentration directly influence the height of the correlation curve. The temporal width of the correlation function, characterized by τ_D, reflects the average diffusion time of molecules through the focal volume.

Quantitative values of N and τ_D are extracted by fitting the experimental autocorrelation data using the diffusion model described in Eq. (2.4). Once the lateral dimension of the confocal volume, r_0, has been independently calibrated, the diffusion coefficient D can be calculated using

$$D = \frac{r_0^2}{4\tau_D} \qquad (2.5)$$

From the diffusion coefficient, the hydrodynamic radius R_H of the diffusing species can be estimated via the Stokes–Einstein relation:

$$R_H = \frac{k_B T}{6\pi\eta D} \qquad (2.6)$$

where k_B is the Boltzmann constant, T is the absolute temperature, and η is the viscosity of the solvent, which is a known parameter for a given medium at a specified temperature.

The correlation model presented in Eq. (2.4) represents a fundamental framework for analyzing diffusion-driven fluorescence fluctuations. While this model forms the basis of the present analysis, it is not exhaustive. As discussed in later chapters, modifications and extensions of this formalism are introduced to account for additional photophysical processes and experimental complexities. Thus, the equations introduced here should be regarded as a foundational starting point, which is further refined as the study progresses and deeper insights into the system are obtained.

2.2.3 Fluorescence Lifetime Correlation Spectroscopy (FLCS)

Fluorescence Lifetime Correlation Spectroscopy (FLCS) emerges from combining time-correlated single-photon counting (TCSPC) with fluorescence correlation spectroscopy (FCS). This approach exploits picosecond-resolved lifetime information together with microsecond-scale intensity fluctuations, enabling correlation analysis to be separated according to different fluorescent species. FLCS is particularly powerful when multiple emitters cannot be distinguished spectrally but exhibit different fluorescence decay characteristics. In such cases, independent correlation curves can be extracted for each species based on their distinct lifetime signatures, which originate from different emissive centers within the sample. [9-11]

The fundamental premise of FLCS is that photons emitted from different species generate distinguishable TCSPC decay profiles, most commonly reflected in different fluorescence lifetimes. By applying statistically derived weighting (filter) functions to individual photons, intensity contributions associated with specific lifetimes can be isolated at the single-photon level. This lifetime-based filtering allows photons with similar decay characteristics to be grouped together, enabling species-resolved correlation analysis. An additional advantage of FLCS is its ability to suppress unwanted effects such as spectral cross-talk, background

fluorescence, and detector afterpulsing, which can otherwise distort conventional FCS measurements.

In practical FLCS analysis, the procedure begins with constructing the total fluorescence decay histogram, denoted as I_j, acquired using a confocal microscope coupled with TCSPC detection. Each histogram channel j records the arrival times of detected photons on the nanosecond (t) timescale. The complete decay profile consists of a large ensemble of photons distributed across these channels. This overall decay is then mathematically decomposed into a sum of individual exponential components. If the system exhibits n distinct emissive species or decay channels (indexed as $z = 1$ to n), the total decay histogram can be expressed as a weighted superposition of n single-exponential decay functions, $p_j^{(z)}$, each representing the characteristic lifetime of one emission center. The weighting factors $A^{(z)}$ correspond to the relative contribution of each emissive center, determined by the fraction of photons originating from that center compared to the total detected photons.

$$I_j = \sum_{z=1}^{n} A^{(z)}\, p_j^{(z)} \qquad (2.7)$$

In contrast to classical FCS, which explores only the intensity correlation at a macroscopic time scale (τ-scale), FLCS utilizes both intensity correlation (at τ scale) and lifetime correlation (at t-scale) to garner more information about the system under study. This can be formulated by the following equation, which represents the autocorrelation function (ACF) for the z'th lifetime component (or z'th emission center).

$$G^{(Z)}(\tau) = \frac{<\sum_j f_j^{(Z)} I_j(t) \sum_j f_j^{(Z)} I_j(t+\tau)>}{<\sum_j f_j^{(Z)} I_j(t)><\sum_j f_j^{(Z)} I_j(t)>} \qquad (2.8)$$

Angular brackets in both the numerator and denominator signify an averaging that spans the entire FCS scale (from τ=0 to ∞). The function fj (z) represents the filtering function of the z component, which is computed from the single exponential decay of the z component [pj (z)],

along with the total intensity decay of NCs in the t-scale (Ij), as detailed in the existing literature. In a manner similar to eq 2.8, one can create a CCF between two lifetime components (or emission centers) by employing two distinct z values.

$$G^{(Z)}(\tau) = \frac{<\Sigma_j f_j^{(Z)} I_j(t) \Sigma_j f_j^{(z')} I_j(t+\tau) >}{<\Sigma_j f_j^{(Z)} I_j(t)> <\Sigma_j f_j^{(Z')} I_j(t)>} \qquad (2.9)$$

Lifetime fitting thereby FLCS filter generation and, subsequently, the ACF and CCF plots were performed using SymPhoTime 64 software provided by PicoQuant.[11]

2.2.4 Photoluminescence Intensity Time-trace

Time-dependent photoluminescence (PL) intensity trajectories are recorded on a real-time scale by exciting an immobilized individual fluorophore using a pulsed laser source. These intensity traces allow direct examination of the emission behaviours of a single emitter. A common feature observed for most single fluorophores is stochastic switching of the PL signal between different intensity levels over time, a phenomenon known as fluorescence intermittency or blinking. Periods of strong emission are referred to as ON states, whereas intervals where the signal drops to values comparable to the background are defined as OFF states, as illustrated schematically in Scheme 2.3.

To distinguish between ON and OFF states, an intensity threshold is introduced. In order to improve the signal-to-noise ratio and ensure reliable state discrimination, photon arrival times are temporally binned; generally bin widths of 10–20 ms were employed. For mechanistic insight into blinking behavior, the emission trajectory is further divided into multiple intensity regimes. Lifetime analysis of these individual states provides valuable information regarding the dominant recombination pathways of the photoexcited species. In cases where multiple intermediate intensity levels are present, assigning a single threshold becomes challenging.

Under such conditions, fluorescence lifetime–intensity distribution (FLID) analysis offers a more robust framework for identifying the physical processes underlying blinking dynamics.

All single-particle measurements were carried out using a confocal fluorescence microscope (CFM, Scheme 2.3) operated in the time-tagged time-resolved (TTTR) acquisition mode. The emitted fluorescence was detected using a single-photon avalanche diode (SPAD). To achieve spatial isolation of individual emitters, extremely dilute solutions (picomolar concentration) were prepared and deposited onto glass coverslips by incorporating a non-interacting polymer matrix such as polymethyl methacrylate (PMMA). Sample preparation for single-particle experiments was performed inside a nitrogen-filled glovebox to prevent environmental degradation during spin coating. During measurements, low excitation powers were maintained to suppress multiexciton generation. All data analysis was conducted using SymPhoTime 64 software, with detailed analytical procedures described in the relevant chapters of this thesis.

Photon antibunching experiments on single particles were performed using a Hanbury Brown and Twiss (HBT) configuration, employing a 50:50 beam splitter and appropriate optical band-pass filters placed before the detectors to minimize detector afterglow and background contributions. Additional optical filters, including long-pass and band-pass elements, were selected according to experimental requirements. Furthermore, single-quantum-dot emission was recorded using an ANDOR EMCCD camera to evaluate the spatial emission profile, enabling determination of the emission peak position and full width at half maximum (FWHM) of individual quantum dots.

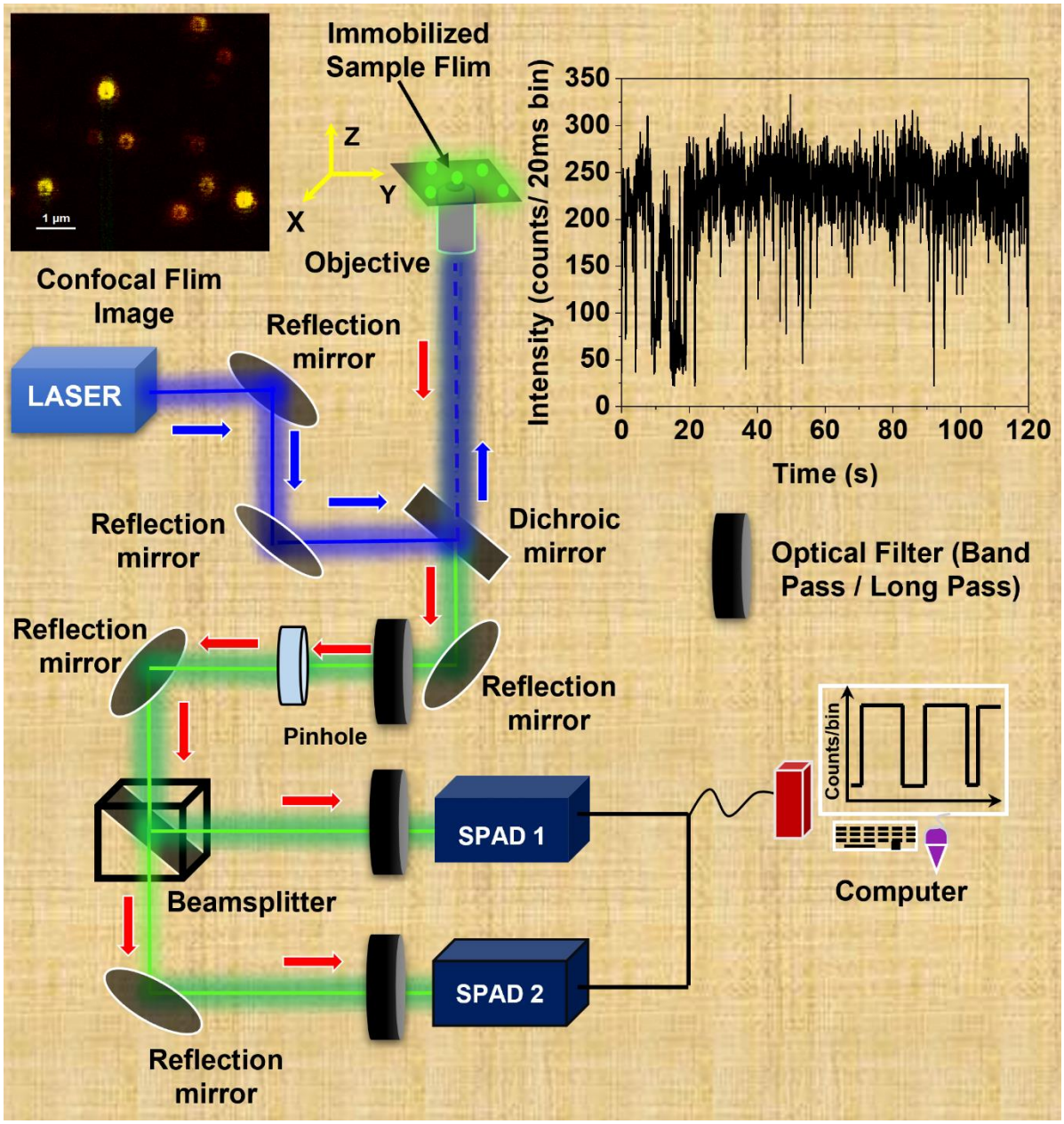

Scheme 2.3 Schematic representation of time resolved confocal fluorescence microscope for measuring immobilized state of nanoparticles.

Figure 2.1 Spectrograph Instrument which is connected to our confocal fluorescence microscope.

2.3. Fluorescence Up conversion Technique

Ultrafast fluorescence dynamics of the nanocrystals were investigated using a femtosecond fluorescence upconversion spectrometer (IB Photonics Ltd.). Femtosecond pulses were generated by a mode-locked Ti:sapphire laser (Spectra-Physics) operating at an 80 MHz repetition rate, delivering pulses with a full width at half maximum (FWHM) of ~260 fs and an average output power of 2.5 W at a central wavelength of 800 nm. A portion of the fundamental beam was frequency-doubled using a β-barium borate (BBO) crystal to produce the second harmonic (~20 mW at 400 nm), which served as the excitation source. The remaining 800 nm fundamental beam was routed through a computer-controlled optical delay stage to introduce a variable temporal delay with respect to the fluorescence signal, enabling time-resolved detection. Scattered near-infrared light was suppressed using a short-pass filter,

while a neutral density filter was employed to attenuate the excitation power and minimize photobleaching effects. The 400 nm excitation beam was tightly focused onto the sample contained in a 2 mm pathlength cuvette, which was continuously stirred to ensure homogeneous excitation and to reduce photodegradation. Fluorescence emission was separated from the excitation beam using a 430 nm long-pass filter, collected by off-axis parabolic mirrors, and spatially and temporally overlapped with the delayed gate pulse in a nonlinear crystal to generate sum-frequency signals. The upconverted fluorescence was subsequently dispersed using a grating monochromator and detected by a photomultiplier tube (PMT) connected to a photon-counting system. Fluorescence decay profiles were obtained by scanning the delay stage to vary the temporal overlap between the fluorescence and gate pulses. All measurements were carried out at a controlled temperature of approximately 20 °C. [1,12,13]

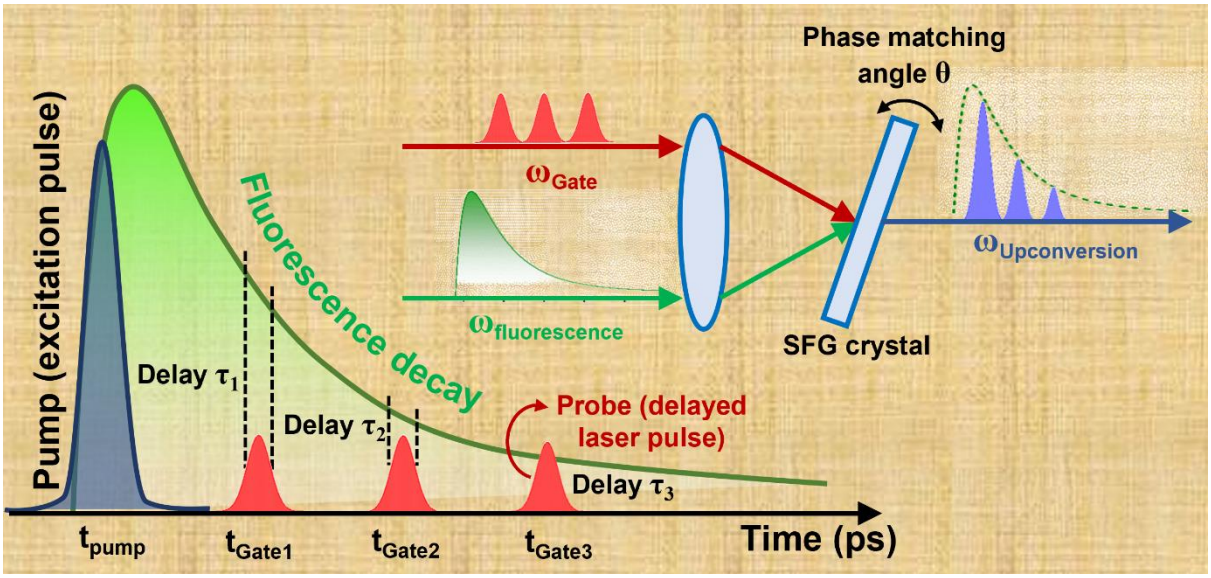

Scheme 2.4. A schematic representation depicting the working principle of the femtosecond upconversion setup.

2.5 Time Correlated Single Photon Counting (TCSPC)

Time-Correlated Single-Photon Counting (TCSPC) is a highly sensitive time-resolved technique used to measure fluorescence lifetimes with picosecond-level accuracy. In this

method, the sample is excited using ultrashort laser pulses, and the emission times of individual fluorescence photons are recorded relative to each excitation event. Accumulating these photon arrival times over many excitation cycles generates a time-resolved histogram that reflects the fluorescence decay behaviours of the system. During TCSPC measurements, brief excitation pulses promote fluorophores to excited electronic states, followed by photon emission as the molecules return to the ground state. To ensure accurate lifetime reconstruction and avoid pile-up artifacts, the detection probability is kept extremely low, such that on average far less than one photon is detected per excitation cycle—commonly around one detected photon for every hundred excitation pulses. This operating regime preserves the integrity of the measured decay profile.[1]

A TCSPC system consists of several key electronic units, including a constant fraction discriminator (CFD), time-to-amplitude converter (TAC), programmable gain amplifier (PGA), analog-to-digital converter (ADC), window discriminator (WD), and digital memory (MEM). Upon laser excitation, a timing signal is generated that initiates the TAC, which acts as a high-precision timer capable of resolving events on the picosecond scale. Following excitation, fluorophores relax from their excited states by emitting photons at random time delays. When an emitted photon reaches the photomultiplier tube (PMT), it is converted into an electrical pulse that terminates the TAC timing cycle. The TAC thus measures the time interval between excitation and photon detection for each event.

Each measured time interval is subsequently digitized by the ADC and assigned to a corresponding channel in memory, where repeated measurements accumulate to form a histogram of photon arrival times. This process is repeated over many excitation cycles to reconstruct the fluorescence decay profile. To enhance data collection efficiency, modern TCSPC systems commonly operate in reverse mode, in which photon detection initiates the

timing cycle and the subsequent laser pulse stops it. This configuration is particularly effective for high-repetition-rate lasers, as it reduces idle timing cycles and improves overall efficiency.

A fundamental limitation of TCSPC is that only the first detected photon per excitation cycle is recorded. Due to system dead time—ranging from microseconds in earlier systems to approximately 100 ns in modern electronics—additional photons arriving within the same cycle are ignored. Consequently, accurate lifetime measurements require operation at low photon count rates to ensure faithful reconstruction of the fluorescence decay.

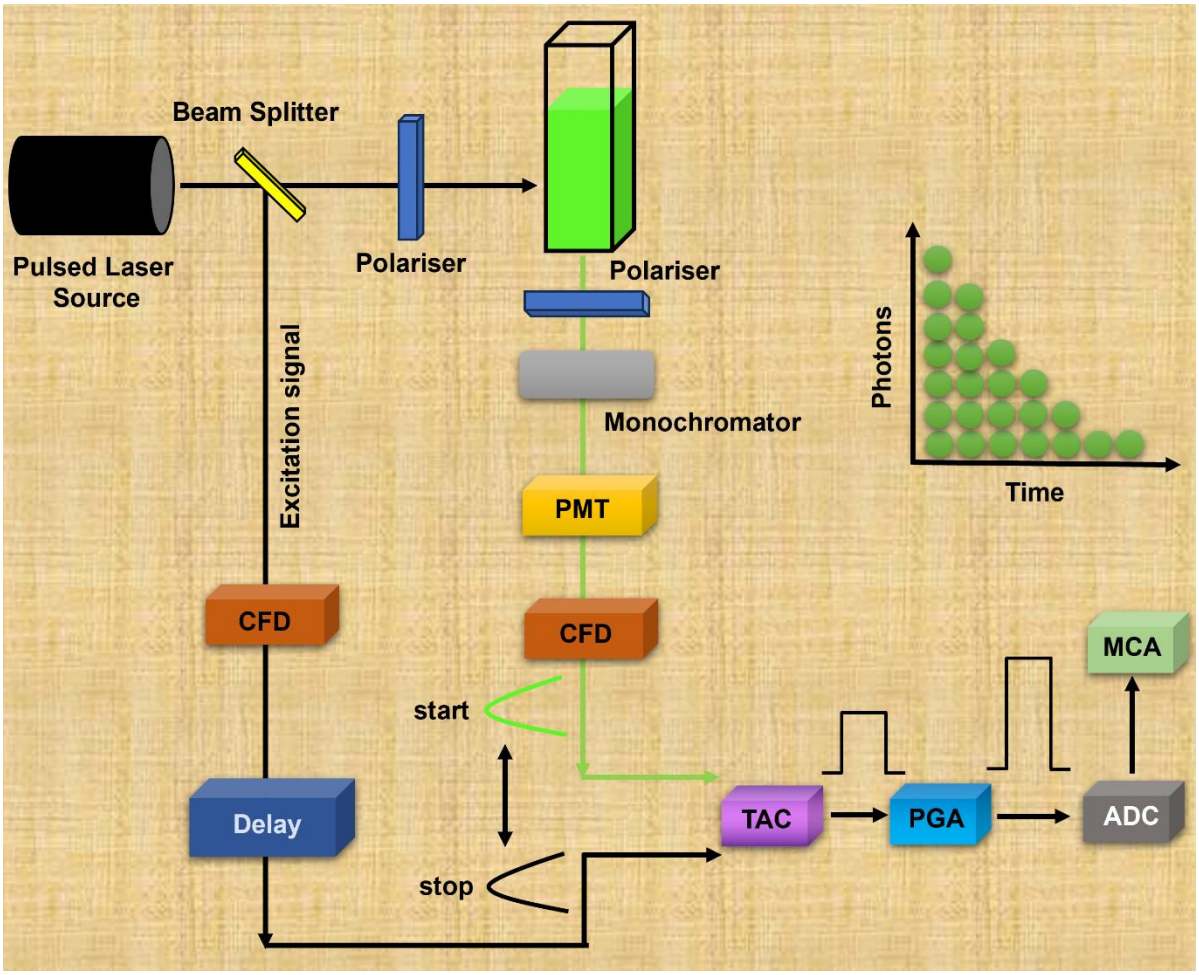

Scheme 2.5. The main components of the TCSPC setup and working principle.

In a TCSPC histogram, the horizontal axis represents the time delay between excitation and emission, while the vertical axis corresponds to the number of detected photons within each

time bin. In the conventional forward TCSPC configuration, the excitation pulse from the light source is applied to the START input, and the randomly arriving detector signal is connected to the STOP input. Because the laser repetition rate is typically much higher than the photon detection rate, most timing cycles initiated by the START signal do not receive a corresponding STOP pulse. Consequently, the TAC frequently reaches its maximum timing range and resets, leading to inefficient use of the electronics. This limitation becomes particularly severe at repetition rates exceeding 1 MHz.

To overcome this inefficiency, reverse TCSPC mode is employed for high-frequency excitation sources. In this configuration, photon detection events trigger the START signal, while the periodic laser pulses are connected to the STOP input. This arrangement ensures that timing cycles are initiated only when a photon is detected, thereby minimizing empty cycles, reducing dead time, and improving counting efficiency. Although the time axis of the histogram is internally inverted, the resulting decay profile remains equivalent to that obtained in forward mode. Reverse TCSPC is especially suitable for laser repetition rates between 1 MHz and 100 MHz and enables dead times as low as ~10 ns, resulting in enhanced accuracy and overall performance in fluorescence lifetime measurements.

2.6 Photoluminescence Quantum Yield Measurement

The photoluminescence quantum yields (PLQYs) of the perovskite nanocrystals were determined using a relative method by comparing the sample emission with that of reference dyes having known PLQYs. The reference standards were chosen such that they could be excited at the same wavelength as the samples and possessed emission spectra overlapping closely with that of the nanocrystals. The PLQYs were calculated using the following relation:

$$QY_S = QY_R \times \left(\frac{I_S}{I_R}\right) \times \left(\frac{OD_R}{OD_S}\right) \times \left(\frac{n_S^2}{n_R^2}\right) \qquad (2.10)$$

Here, *OD* denotes the optical density at the excitation wavelength, *I* represent the integrated area under the photoluminescence spectrum measured under identical experimental conditions, and *n* is the refractive index of the solvent. The subscripts *S* and *R* correspond to the sample and reference, respectively.

As reference standards, coumarin-153 in ethanol (QY = 0.546), and rhodamine-6G in aqueous medium (QY = 0.95) were employed.

2.7 Materials Characterization with Other Experimental Techniques

All steady state absorption and emission spectra were recorded using UV-vis spectrophotometer (JESCO V-730) and spectrofluorimeter (FS5 Spectrofluorometer by Edinburg instruments with a xenon lamp (XBO150 OFR) as the excitation source), respectively. To measure the size and shape of NCs transmission electron microscope (TEM) were used (JEOL JEM-2100 electron microscope) operated at an accelerating voltage of 200 kV. For XRD measurements, we used a Bruker D8 Advanced diffractometer (CuKα radiation, λ = 1.5418 Å). EDAX and elemental mapping were done using Carl Zeiss FESEM instrument.

2.8 References

[1] J. R. Lakowicz, P. o. F. S., 3rd edn., Springer, New York, **2006**.

[2] https://www.tcspc.com/doku.php/applications#single_molecule_detection_smd

[3] D. Magde, E. Elson, W. W. Webb, *Phys. Rev. Lett.*, **1972**, *29*, 705.

[4] K. Bacia, E. Haustein, Schwille, P., *Cold Spring Harb Protoc*. **2014**, *7*, 709-725.

[5] L. Yu, Y. Lei, Y. Ma, M. Liu, J. Zheng, D. Dan, P. Gao, *Front. Phys.,* **2021**, *9*, 644450.

[6]] P. Schwille, E. Haustein, A tutorial for the Biophysics Textbook Online (BTOL). Biophysical Society, Rockville, MD, **2002**.

[7] N. L. Thompson, in Topics in Fluorescence Spectroscopy: Techniques, ed. J. R. Lakowicz, Springer US, Boston, MA, **1999**, DOI: 10.1007/0-306-47057-8_6, 337-378.

[8] K. Oleg, B. Grégoire, *Rep. Prog. Phys.*, **2002**, *65*, 251.

[9] P. Kapusta, M. Wahl, A. Benda, M. Hof, J. Enderlein, *J. Fluoresc.*, **2007**, *17*, 43-48.

[10] P. Kapusta, R. Macháň, A. Benda, M. Hof, *Int. J. Mol. Sci.*, **2012**, *13*, 12890-12910.

[11] A. Ghosh, N. Karedla, J. C. Thiele, I. Gregor, *J. Enderlein, Methods*, **2018**, *140*, 32-39.

[12] M. A. Kahlow, W. o. Jarzęba, T. P. DuBruil, P. F. Barbara, *Rev. Sci. Instrum.*, **1988**, *59*, 1098-1109.

[13] J. Xu, J. R. Knutson, in Methods in Enzymology, Academic Press, **2008**, vol. *450*, pp. 159-183.

CHAPTER 3

Unveiling the Influence of Brightness Heterogeneity in Fluorescence Correlation Spectroscopy of Perovskite Nanocrystals

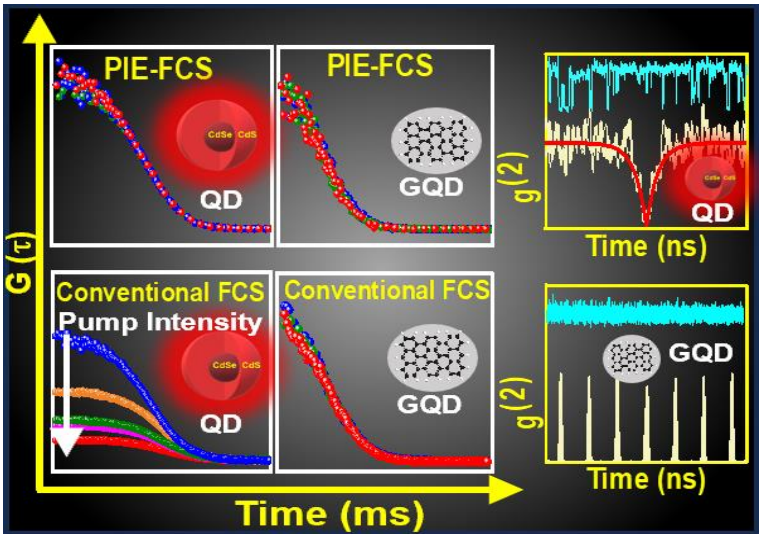

3.1 Abstract

Nanoparticles (NPs), including perovskite nanocrystals (PNCs) with single photon purity, present challenges in fluorescence correlation spectroscopy (FCS) studies due to their distinct photoluminescence (PL) behaviours. In particular, the zero-time correlation amplitude [$g^2(0)$] and the associated diffusion timescale (τ_D) of their FCS curves show substantial dependency on pump intensity (I_P). Optical saturation inadequately explains the origin of this FCS phenomenon in NPs, thus setting them apart from conventional dye molecules, which do not manifest such behaviour. This observation is apparently attributed to either photo-brightening or optical trapping, both lead to increased NP occupancy (N) in the excitation volume, consequently reducing the $g^2(0)$ amplitude [since $g^2(0)$ α 1/N] at high I_P. However, an advanced FCS study utilizing alternating laser excitation at two different intensities dismisses such possibilities. Further investigation into single-particle blinking behaviours as a function of I_P reveals that the intensity dependence of $g^2(0)$ primarily arises from the brightness heterogeneity prevalent in almost all types of NPs. This report delves into the complexities of the photophysical properties of NPs and their adverse impacts on FCS studies.

3.2 Introduction

The growing demand for optical materials in numerous real applications such as bioimaging, lasers, and light harvesting has prompted the synthesis of NPs endowed with features like high emissivity, compact size, non-toxicity, enhanced photostability, and, most importantly, the devoid of blinking even in single-quantum emission mode.[1-6] Initially, metal chalcogenide quantum dots (QDs) were favored for these applications due to the ease of their syntheses and meeting all essential criteria, except for the toxicity stemming from metal ions like Cs^+, Cd^{2+},

and Pb^{2+}.[7-8] Later, non-toxic graphene quantum dot (GQD) was introduced as a substitute, particularly in bio-related applications, to address the concerns related to cytotoxicity.[9-12] $CsPbX_3$ PNCs (where X=Cl, Br, or I and their mixtures) have recently gained attention for their exceptional optoelectronic properties, gradually replacing QDs from various devices and related applications.[1-3,13-20] While there is a visible improvement in device efficiency with the integration of perovskite materials into photovoltaic applications, their utilization in optoelectronics and imaging demands more stringent criteria in their optical properties. This particularly underscores the importance of synthesizing NPs with high photoluminescence quantum yield (PLQY), enhanced photostability, and devoid of blinking— qualities that are not readily available in PNCs. However, the current literature has extensively outlined the diverse synthetic methods and post-synthetic treatments that succeeded not only in improving the photostability of PNCs but also in achieving a near-unity PLQY.[2,17,21] Recently, there has been a growing interest in photo-brightening, a process that rapidly improves the optical properties of PNCs by converting dark PNCs into emissive ones under intense illumination.[22-25] The associated mechanism of photo-brightening involves the healing of defects by the swift migration of halide ions and oxygen to the defect sites, leading to long-lasting improvements in PLQY and PL lifetime (τ_{fl}), as evidenced by their sustained levels even after the terminating illumination.[22] On the contrary, the light-induced ON/OFF switching of individual NPs or brightness heterogeneity refers to an excited state phenomenon that continues as long as the illumination is ON without affecting the inherent optical properties of the NPs.[26-28] Unfortunately, both phenomena display identical responses to the FCS probe, posing a challenge in distinguishing the occurrence of the correct one through conventional FCS study. In response to varying illumination levels, brightness heterogeneity causes reversible changes in the blinking behaviors of NPs. Moreover, unlike photo-brightening, brightness heterogeneity cannot permanently improve the intrinsic optical properties of NPs.[26]

Studies of photo-brightening on surface-immobilized NPs face challenges such as the gradual loss of PL due to photodegradation, low throughput data acquisition, and the inevitable impact of surface immobilization.[3] Conversely, FCS, conducted in the liquid phase, continuously replaces NPs through diffusion.[29-32] This efficiently overcomes the above mentioned challenges and firmly establishes FCS as the preferred technique for photo-brightening study.[29,33-34] Given that FCS measurement relies on a small ensemble of NPs, it can provide evidence for sample heterogeneity and the distribution of characteristic timescales.[26-27] The origin of any heterogeneous optical property, including NP subpopulations with distinct brightness (sample heterogeneity), blinking (dynamic heterogeneity), non-exponential PL lifetime (static and dynamic heterogeneity), and brightness heterogeneity, cannot be examined without screening with a single-molecule fluorescence technique.

By employing the pulsed interleaved excitation (PIE) scheme in the FCS study and subsequent PL blinking analysis recorded on surface-immobilized NP, we realized that, at high I_p, brightness heterogeneity is ubiquitous in almost all types of single photon emitter NPs. This phenomenon perplexed researchers by deviating their FCS curves from ideality at high I_p. A careful analysis of the FCS curves of NPs, considering the effects of brightness heterogeneity in the analytical fitting function, is essential for accurately interpreting FCS parameters related to diffusion and trap state dynamics. Nevertheless, formulating a numerical FCS fitting model that can effectively capture the blinking kinetics of NPs is challenging, primarily due to the power-law behavior of the kinetics.[35-36] The average ON and OFF state durations in power-law blinking are significantly modified by the I_p and experimental integration time, resulting in alterations to the FCS curve across all timescales.[26] Because of all these factors, NP characterization by FCS is extremely difficult. The overlapping timescales of NP diffusion and

blinking along with influences from optical trapping further complicate the interpretation of FCS curves.[37-41] Saturation is also known to modify FCS curves by changing the τ_{fl} or blinking property itself at high I_P.[38]

3.3 Synthetic procedures of different nanoparticles

3.3.1 Synthesis of perovskite nanoparticles (PNCs)

3.3.1.1 Cs-oleate Preparation

In a 50 ml two-neck round-bottom (RB) flask, ~21.7 mg caesium carbonate (0.061 mmol) was dried under vacuum for 30 mins. Subsequently, ~110 µl OA and ~1 ml ODE were added and vacuum dried for 45 mins. Then the solution was transferred to the N_2 atmosphere under constant stirring at ~120 ^{0}C until a clear solution of Cs-oleate formed.[17] The Cs-oleate solution was heated to >100 ^{0}C, prior to using it in the next step.

3.3.1.2 Synthesis of Multi-faceted PNCs

In a 25 ml three-neck RB flask, ~44 mg PbO (~0.2 mmol) and ~86 mg DBDMH (~0.3 mmol) were added to ~5 ml pre-dried ODE solvent and kept under vacuum for 45 mins for drying. Subsequently, the resultant mixture was transferred to the N_2 environment with vigorous stirring at ~130 ^{0}C. After a few minutes, ~1 ml OA and ~1 ml OLm were injected into the mixture under heating. The temperature was then raised to ~200 ^{0}C. After the dissolution of all the materials, the pre-heated ~0.8 ml Cs-oleate was swiftly injected into the reaction mixture at ~200 ^{0}C. The reaction mixture was immediately transferred to an ice bath to quench the reaction. 2-3 ml methyl acetate was added to the crude and centrifuged at 7000 rpm for 5 mins. The obtained residue was dissolved in hexane and kept in the refrigerator for 40 mins.[17] This solution was again centrifuged for 10 mins at 12000 rpm. The supernatant was collected in a glass vial for characterization and spectroscopic measurements. PLQY of cube PNCs (c-PNCs)

was measured to be ~82%-90%. For 12-(d-PNC) and 26-faceted(r-PNC) nanocrystals synthesis, phenacyl bromide (~120mg, 0.6 mmol) was taken as a halide precursor.[44] Other steps are similar as previously discussed for cubic nanocrystal synthesis. Here, the temperature of the reaction mixture was increased to 220 ^{0}C under N_2 atmosphere followed by 0.5mL Cs-oleate solution injection. After 15 mins, red solution turned yellowish and then the reaction mixture was annealed for 20 mins and 45 mins for 12-faceted and 26-faceted NCs formation respectively. The green crude solution was then ice quenched and purified further for analysis. For purification, the crude was centrifuged at 8000 rpm for 10 mins and the precipitate was further centrifuged after dispersing in hexane: MeOAc (4:1) mixture for 5 mins at 6000 rpm. The obtained precipitate was dissolved again in hexane solvent. The bright green fluorescent nanocrystal solution was then kept at -20 ^{0}C freezing condition for future optical studies. The PLQY was found to be ~75-80% for both the particles.[44]

3.3.2 Synthesis of GQDs

Small, narrow bandwidth (<30 nm) GQDs were synthesized following the reported literature with slight modification.[9] In brief, ~500 mg PG was dissolved into ~12 ml of ethanol via ultrasonic treatment for 30 mins. Then, the clear solution was transferred into a Teflon-lined autoclave (25 ml) and placed in a hydrothermal oven, heated for ~5 hours at ~170° C. After the reaction, the autoclave reactor naturally cooled to room temperature. The crude product was then purified by silica (60-120 mesh) column chromatography, where a dichloromethane-methanol mixture was used as eluent. During column separation, the volume ratio of dichloromethane to methanol was altered dynamically from 10:1 to 5:1. The solid product of GQDs was obtained after evaporating the solvent in a rotary evaporator. This powder GQD sample was further dissolved in ethanol/water for characterization and spectroscopic measurements.[9] PLQY of GQDs was measured to be ~30%.

3.3.3 Synthesis of CdSe/CdS core-shell QDs

CdSe Core Preparation: The CdSe core was grown following the reported literature.[42] In brief, in a 50 ml flask, ~120 mg of CdO, ~560 mg of ODPA, and ~6 mg of TOPO was taken and subsequently degassed for 30 mins at ~120 ^{0}C. Then the reaction mixture was kept under an Ar environment at 350 ^{0}C. A solution of Se (~150 mg) in TOP (~1 ml) was injected along with ~1 ml TOP into the mixture obtained in the previous step when changing the solution colour from brown to colourless. After 30 s, the flask was cooled down to room temperature. Next, the resultant reaction mixture containing CdSe QDs was centrifuged for a few mins, washed, and finally stored in hexane to use in the next step.

Synthesis of CdSe/CdS Core-shell QDs: In a 50 ml flask, ~3 ml ODE, ~3 ml OLm, and ~100 nM CdSe core solution were added. The mixture was degassed at ~120 ^{0}C for ~1 hr to remove dissolved oxygen and hexane. Again, the mixture was heated to ~310 ^{0}C under an Ar environment. Meanwhile, at ~240 ^{0}C, ~6 ml Cd-oleate and octanethiol were added dropwise. Finally, the synthesized CdSe/CdS QDs were centrifuged and dispersed in toluene for further optical studies. PLQY of CdSe/CdS QDs was measured to be ~75%.

3.4 Sample Characterisation

After synthesizing three different types of PNPs- (i) $CsPbBr_3$ PNCs with different sizes (~8 and ~17 nm) and morphologies, (ii) spherical CdSe/CdS core-shell quantum dots (QDs), and (iii) GQDs following the reported literature.[9,15,42-44] Through surface engineering, we were able to produce PNCs with varying numbers of facets, including 6-faceted cube PNCs (c-PNCs, ~8 nm), 12-faceted dodecahedron PNCs (d-PNCs, ~17 nm), and 26-faceted rhombicuboctahedron PNCs (r-PNCs, ~17 nm).[15] High-resolution transmission electron microscopy (HRTEM) investigations unveil average particle sizes [~8 nm (c-PNCs), ~17 nm

(d- and r-PNCs), ~10 nm (CdSe/CdS QDs), and ~3 nm (GQDs)], along with narrow size distributions of our NPs (Figure 3.1A-E). Optical studies reveal their distinct PL spectra, featuring narrow spectral widths, emitting in the green (c-, d-, and r-PNCs), red (CdSe/CdS QDs), and cyan (GQDs) regions (Figure 3.2). We further characterized our samples by AFM, EDX, XRD, IR, and DLS, demonstrating excellent correlations with reported ones (Figure 3.1 F, Figure 3.2, Figure 3.3). [9-11,42-46]

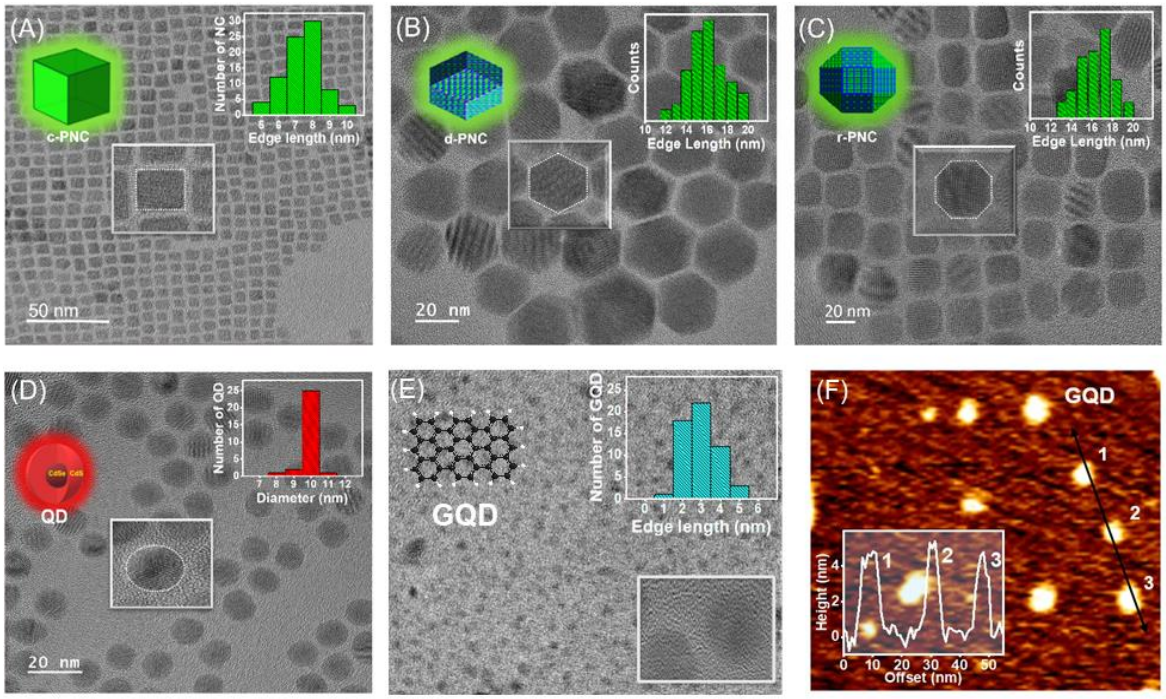

Figure 3.1. TEM images and particle distribution in (A) cubic PNC (B) Dodecahedron PNC, (C) Rhombicuboctahedron PNC, (D) CdSe/CdS QD (E) GQDs and (F) AFM image and hight profile of three GQDs 1, 2 & 3.

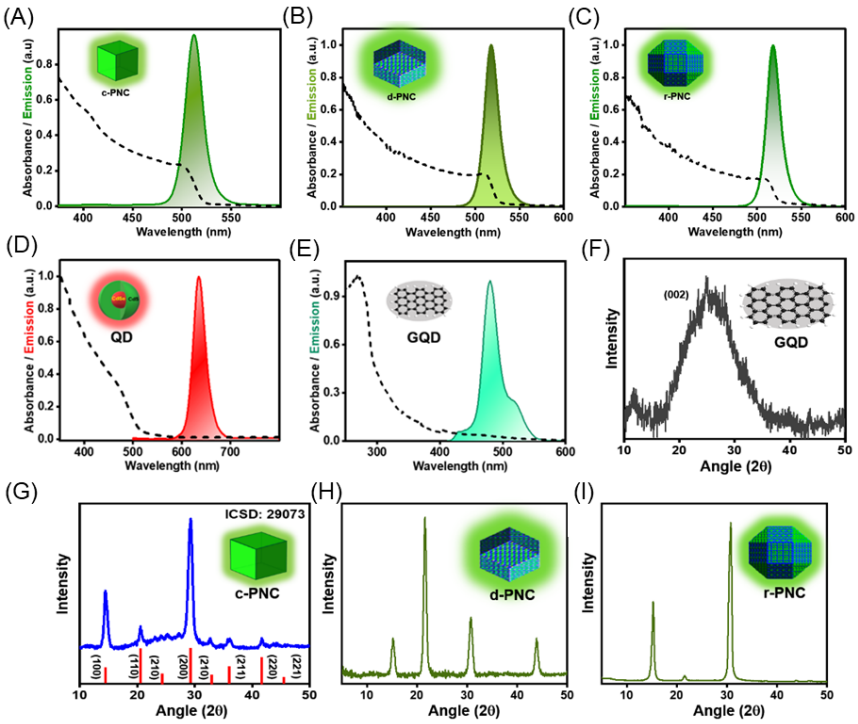

Figure 3.2. Absorption (dotted line) and PL (solid line) spectra of (A) c-PNCs, (B) d-PNCs, (C) r-PNCs, (D) CdSe/CdS QDs in toluene and (E) GQDs dispersed in ethanol under ambient conditions. Powder XRD pattern of (F) GQDs, (G) c-PNCs, (H) d-PNCs, and (I) r-PNCs.

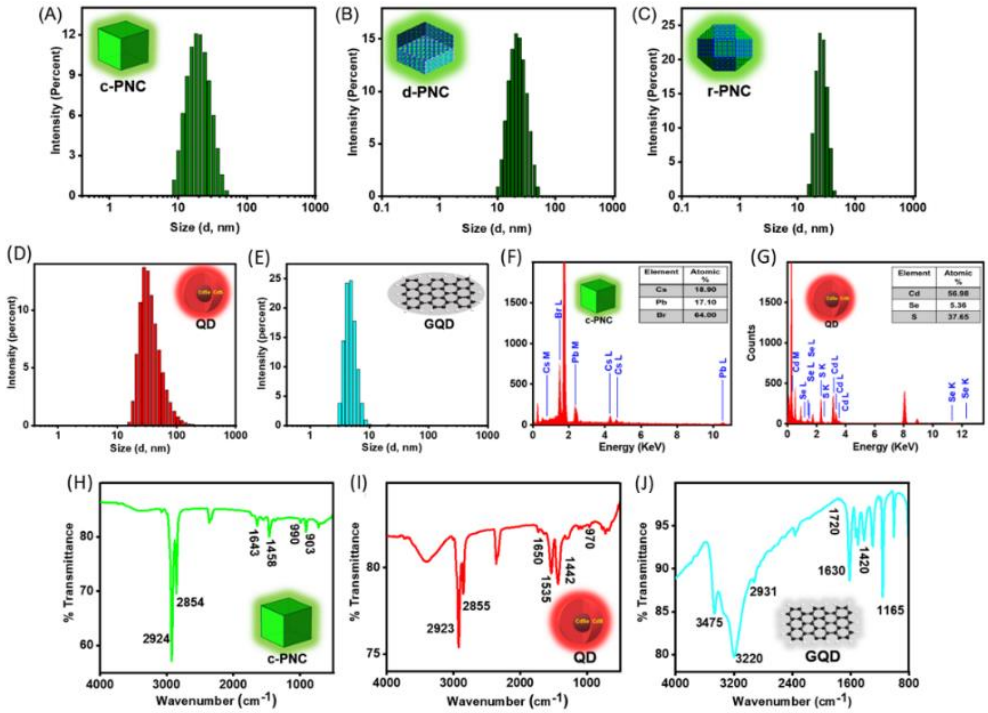

Figure 3.3. DLS studies of PNCs. The studies show the narrow size distributions of (A) c-PNCs, (B) d-PNCs, and (C) r-PNCs, (D) CdSe/CdS QDs dispersed in toluene and (E) GQDs dispersed in ethanol. EDAX spectrum of (F) c-PNCs and (G) QDs. Insets show the atomic percentage of constituent elements. Surface group characterizations of (H) c-PNCs, (I) QDs, and (J) GQDs by Fourier transform infrared (FTIR) spectroscopy studies show the presence of COOH, N-H, and O-H groups in the NP surface. Vibrations of C=C, C=N, and C-N= are also detected for GQDs.

3.5 Pulsed Interleaved Excitation (PIE)-FCS/ Alternating Laser Excitation (ALEX)-FCS

PIE-FCS, or ALEX-FCS, represents an advanced extension of the traditional FCS technique. PIE FCS is particularly notable for its enhanced capabilities in studying dynamic molecular interactions, especially in the realm of biophysics.

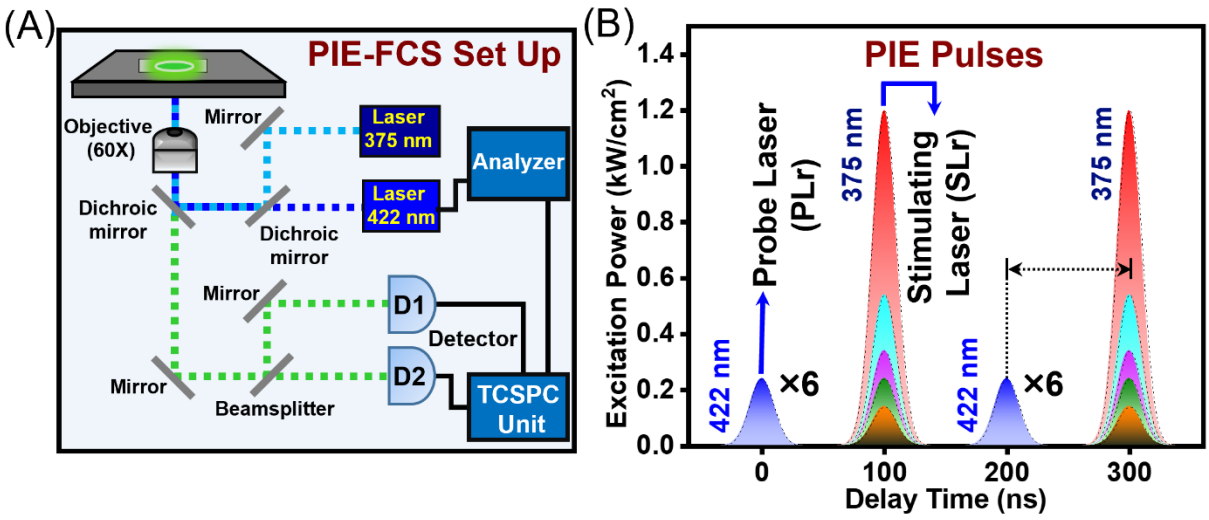

Figure 3.4. (A) Scemetaics of PIE FCS experimental set-up. PIE pulses consist of low-power PLr (~422 nm) and high-power SLr (~375 nm) with a pulse switching rate of 1/(100 ns) (B). While the intensity of PLr (I_{PLr}) was fixed at ~0.04 kW/cm^2, the power of SLr (I_{SLr}) was stepwise increased from ~0.04 kW/cm^2 to ~1.2 kW/cm^2 in 5 different sets of experiments.

This technique involves the use of alternating laser excitation of two different fluorophores, often labelled on interacting molecules. By employing two lasers with different wavelengths (Figure 3.4 A), PIE-FCS allows researchers to discern the different fluorescent signals emitted by each fluorophore, enabling the study of interactions such as molecular binding, dissociation, and conformational changes. PIE FCS is particularly valuable in elucidating complex biological processes, including protein-protein interactions, ligand-receptor binding, and other dynamic molecular events. The alternating excitation scheme enhances the specificity and accuracy of measurements, providing a more detailed understanding of molecular behaviour in biological systems.

Applying PIE-based excitation during FCS measurements, together with PL blinking studies on surface-bound nanoparticles, revealed that single-photon-emitting NPs frequently display strong brightness variations when subjected to high excitation powers. Such variability disrupts the expected form of FCS correlation curves, which has led to significant confusion in interpreting data acquired under these conditions. To obtain reliable parameters describing diffusion or trap-related processes, it becomes necessary to use fitting approaches that incorporate these fluctuations in emission.

Constructing an appropriate numerical model, however, is far from straightforward. The blinking dynamics of many NPs follow power-law statistics, and both the excitation power and the chosen temporal resolution of the experiment reshape the apparent ON and OFF intervals. Consequently, the entire FCS curve is altered. These factors make it exceptionally challenging to characterize nanoparticles through FCS alone. Additional complications arise because the motion of the particle and its blinking behaviour can occur on similar timescales, and optical forces may further influence the signal. At high excitation powers, saturation effects can also

reshape the correlation function by modifying either the fluorescence lifetime or the blinking characteristics of the emitter.

3.6 Results and Discussion

3.6.1 Roles of photo-brightening and optical trapping in the power dependent FCS studies of NPs

Classical FCS provides insights into the mechanisms causing PL fluctuations by analyzing autocorrelation curves.[39,47-52] These mechanisms include the diffusion of fluorophores, conformational changes of proteins, binding of ligands with macromolecules, changes in the photophysical properties of the fluorophores, and many others.[39,51] In our initial investigation using conventional FCS, we observed that all our NPs (except GQD) show a reduction in the $g^2(0)$ amplitude at high pump intensity, associated with a prolonged τ_D (Figure 3.6A-C). This observation aligns with similar findings reported earlier by other research groups.[26,29-31,33-34] One may reasonably attribute this observation to photo-brightening or optical trapping since $g^2(0) \alpha 1/N$, and both processes lead to accumulating NPs in the excitation volume.[29-32] Three known photoinduced processes that can explain the power dependency of $g^2(0)$ include (i) photo-brightening, (ii) optical trapping, and (iii) apparent broadening of the excitation profile via signal saturation.[26] Photo-brightening entails a sustained increase in the PLQY and τ_{fl} of NPs or the conversion of dark particles into emissive ones permanently.[26] This is achieved through one or more of the following light-induced processes: (i) Defect healing of NPs facilitated by the migration of halide ions and oxygen, (ii) reorganization of the crystal framework, (iii) photo-corrosion leading to surface smooth NPs, (iv) stabilization of surface ligands through photoinduced rearrangements, and (v) surface passivation by photo adsorbed molecules.[23,33,53-54] On the other hand, optical trapping caused by high radiation pressure decelerates the apparent diffusion timescale (τ_D), thereby altering the local concentration and

residence period of NPs traversing the excitation volume.[26,41] Saturation effects can be observed due to changes in τ_{fl} or the blinking property itself at high pump intensity. To comprehend the true impact of photo-brightening and optical trapping in regulating the $g^2(0)$ of our NPs under high intensity, we conducted an FCS study using an advanced pulsed interleaved excitation (PIE) scheme (Figure 3.4 A, B). Since the effect of photo-brightening and optical trapping retains "memory" in diffusion, PIE FCS can easily confirm their occurrences.

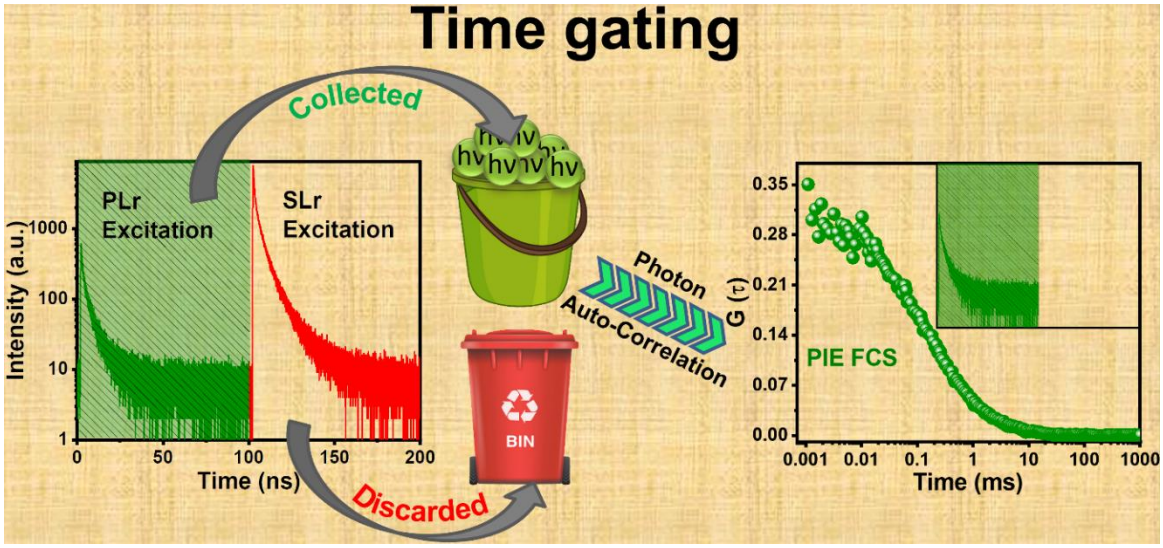

Figure 3.5. Time gating scheme for PIE FCS. Our PIE scheme uses two excitation cycles: (i) 375 nm high-intensity SLr (for photo-brightening) and (ii) weakly intense 422 nm PLr (for FCS recordings). A 100 ns delay separates these two cycles. Utilizing time-tagged-time-resolved (TTTR) mode and subsequent time-gating enabled us to not only the extractions of PL-photons related to PLr excitation cycle in the presence of the SLr cycle but the unwanted PL-photons related to SLr excitations are also simultaneously discarded. PL-photons related to PLr excitations are correlated to construct FCS curves at different intensities of SLr.

We employed two alternating excitations in the PIE scheme separated by ~100 ns delay time (Figure 3.4 B). The 100 ns laser alternation period (τ_{alt}) is about >10^4 times faster (and 2-14 times longer) than the diffusion time τ_D (and PL lifetime τ_{fl}) of our NPs traversing the excitation volume. The first laser (λ_{em}~ 422 nm, IRF~ 130 ps) operates at a fixed low intensity (I_{PLr} ~0.04 kW/cm²), and is designated as probe laser (PLr), used for FCS recording. On the other hand, the second laser, which emits at ~375 nm (IRF ~140 ps), serves as the high-intensity stimulus laser (SLr), illuminating the sample to initiate photo-brightening and optical trapping (if present at all).[26] The power of SLr (I_{SLr}) was stepwise increased from ~0.04 kW/cm^2 to ~1.2 kW/cm^2 in 5 different sets of experiments (Figure 3.4 B). Both lasers pass through the same objective (60x), generating uniquely overlapped (yet temporally separated) identical excitation profiles within the NP solution placed on a coverslip above the objective.[40] More details of the PIE FCS and its working principle can be found elsewhere.[26,40] PL photons produced during low-power PLr excitations are selectively correlated through time-gating in the PIE fitting scheme to extract them precisely (Figure 3.6 D-F, Figure 3.5). Conversely, PL photons related to SLr excitation are discarded, or if correlated, they would merely replicate the conventional power-dependent FCS curves illustrated in Figure 3.6A-C. Subsequently, PIE FCS curves recorded under fixed PLr intensity but varied SLr power (I_{SLr} ~0.04-1.2 kW/cm^2) are plotted in Figure 3.6 D-F, showing that unlike conventional FCS curves (Figure 3.6 A-C), they are independent of SLr power. The rapid pulse switching in PIE FCS would allow PLr to detect an enhanced NP population (if any) resulting from photo-brightening and/or optical trapping caused by SLr excitation. This can be observed through a reduced $g^2(0)$ amplitude in PIE FCS, given that the τ_D is significantly slower than the laser alternation period (τ_{alt}). Reducing τ_{alt} further would lead to excitation pile-up, particularly when τ_{alt} becomes shorter than τ_{fl} of NPs.

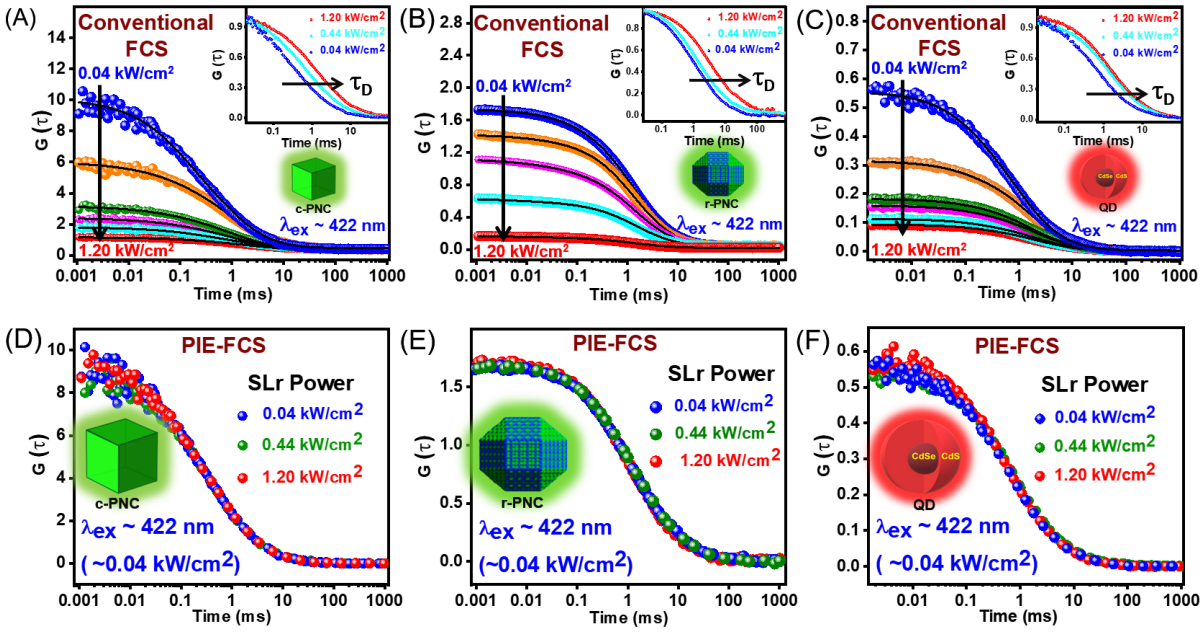

Figure 3.6. (A-F) Conventional (A-C) and PIE (D-F) FCS curves of c-PNCs (A, D), r-PNCs (B, E), and QDs (C, F), dispersed in toluene. The pump power in conventional FCS and SLr power in PIE FCS were varied stepwise from ~0.04 kW/cm^2 to ~1.2 kW/cm^2. Only the PL photons related to PLr excitations are correlated in PIE FCS (D-F).

While the conventional FCS curves of our NPs exhibit notable power dependency, autocorrelation curves derived from PIE FCS are unaffected by SLr power (Figure 3.6D-F). As mentioned previously, given that the laser switching time in PIE FCS is more than 10^4 times faster than the dwelling time of NPs in the excitation volume, optical trapping or photo-brightening, if caused by SLr, should be realized through an enhanced N [or a reduced $g^2(0)$] and a slower τ_D in PIE FCS recorded under PLr excitation at a high SLr intensity. The absence of such observations in the PIE FCS study unequivocally verifies that there is no actual alteration in the local concentration of NPs and their diffusion timescales, at least at excitation power up to 1.2 kW/cm² (Figure 3.6). Thus, PIE FCS rules out the involvement of photo brightening and optical trapping in the observed power-dependent FCS phenomena, at least within a timescale comparable to τ_D and pump intensity up to ~1.2 kW/cm^2. Furthermore,

identical PL-lifetime profiles of NPs and the zero-time amplitudes when recorded for the same integration time under PLr excitation (with constant I_p ~0.04 kW/cm²) in the presence of SLr at various intensities (0.04-1.2 kW/cm²), definitively establish that there is no alteration in actual NP occupancy within the excitation volume (Figure 3.6). It is noteworthy that all our NP samples (PNCs and QDs) demonstrate high PLQYs (>75%) before illumination, providing limited scope for additional enhancement of their PLQYs through photo-brightening. It is somewhat unusual for photo-brightening to explain a significant drop in $g^2(0)$ or manifolds increase in NP occupancy in excitation volume at a high pump intensity, as illustrated in conventional FCS studies (Figure 3.6 A-C). Acknowledging the benefits of high pump intensity and prolonged illumination time for photo brightening and the latter is difficult to attain in FCS due to the short illumination time dictated by the millisecond diffusion timescale of NPs, we undertook a series of experiments to examine the actual occurrence of photo brightening in our samples upon illuminating for an extended period. In our first experiment, we recorded PL intensity trajectories of QD embedded in the PMMA matrix for a long time (~300 seconds) at different excitation powers, showing no sign of increasing the average ON state intensity over time, contrasting with the typical behavior associated with photo-brightening. In the second experiment, we performed power-dependent conventional FCS studies on c-PNCs dispersed in (i) toluene (η ~0.56 cP) and (ii) octadecene (η ~5.04 cP) (Figure 3.8). Octadecene, being ~9 times more viscous than toluene, enables much slower diffusion of c-PNCs across the excitation volume that eventually results in longer irradiation time in the FCS study in octadecene. This is further confirmed by the much longer FCS-derived diffusion timescale of c-PNCs in octadecene (~5 ms) than that (~1 ms) in toluene.

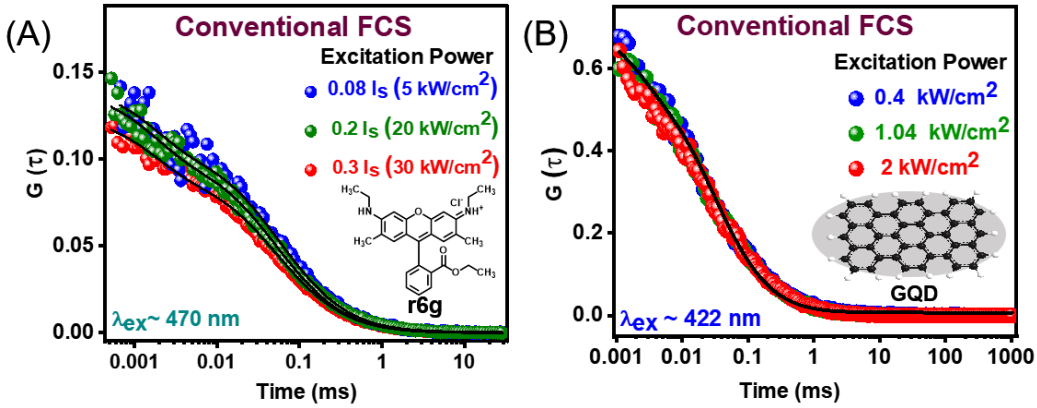

Figure 3.7. (A-B) Conventional FCS curves of r6g (A) and GQD (B) as a function of excitation intensity (I_P). For r6g, I_P was varied from ~0.08 times saturation intensity (I_s) to 0.3×I_s.

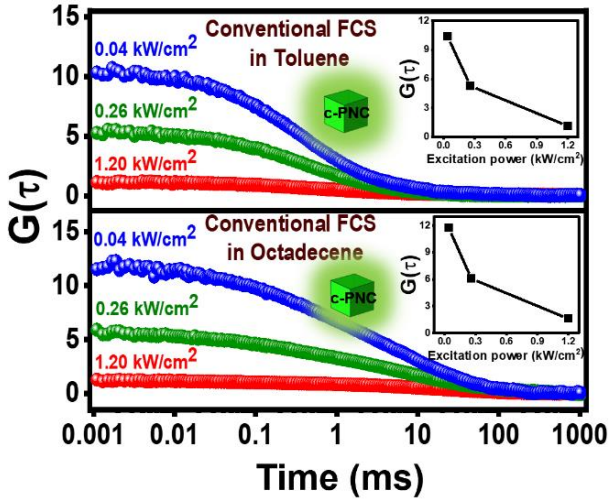

Figure 3.8. Conventional FCS curves of c-PNCs dispersed in toluene (top) and octadecene (bottom) at different excitation powers (0.04 kW/cm^2-1.2 kW/cm^2). Identical experimental conditions and similar sample concentrations were maintained in both experiments. Due to the higher viscosity of octadecene, the residential time of NPs in the excitation volume would be much longer in octadecene as compared to toluene. Even after that, the change in $g^2(0)$ with power remained similar in both the solvents for similar changes in excitation power. If photo brightening had caused reduced $g^2(0)$ at elevated power, we would have observed more reduction of $g^2(0)$ in octadecane. No such observation rules out the involvement of photo brightening in the observed FCS phenomenon.

We took the diffusion timescales from the lowest excitation power data for comparison since realistic FCS parameters are obtained only at low excitation power. Interestingly, no further reduction in $g^2(0)$ can be observed in octadecene when compared to toluene, despite longer irradiation time in octadecene (Figure 3.8). Figure 3.8 shows a side-by-side comparison between the FCS curves recorded in two solvents across the excitation powers under identical experimental conditions and sample concentration. $g^2(0)$ reduces by a similar extent in both the solvents upon increasing the excitation power from ~0.04 kW/cm^2 to 1.2 kW/cm^2.

If photo brightening were present, we would have observed a larger reduction of $g^2(0)$ amplitude in octadecene compared to that in toluene in the intermediate to high excitation power regime (insets of Figure 3.8). In the third experiment, we illuminated a colloidal solution of c-PNCs with UV light (~365 nm, ~0.4 mW/cm²) to confirm or disprove further the occurrence of photo-brightening. However, instead of observing an increase, we noted a gradual decrease in PLQY over time, again contrasting with the expectation of photo-brightening (Figure 3.9).

Furthermore, the possibility of photobleaching altering the conventional FCS curves at high intensity is eliminated by the fact that if an NP undergoes photodegradation within its diffusion time (τ_D), the apparent τ_D would be faster without changing its contribution to the autocorrelation amplitude. However, an opposing trend was observed, with longer τ_D at higher pump intensity (insets of Figure 3.6 A-C).

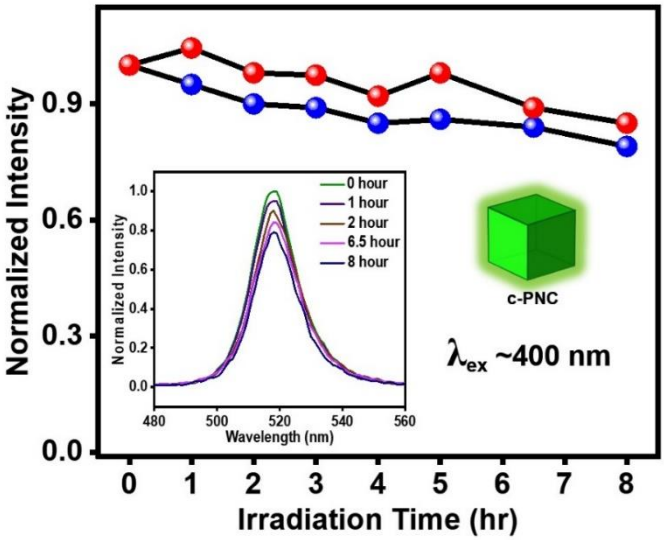

Figure 3.9. Steady-state PL intensity of c-PNCs (dispersed in toluene) as a function of time under UV irradiation (~365 nm, ~0.4 mW/cm^2). The plots show the relative PL intensity [I(t)/I(0)] of c-PNCs as a function of irradiation time. Experiments were performed in a quartz cuvette and repeated two times, showing identical deteriorations of PLQYs of PNCs even in the presence of weakly intense UV light. The inset shows typical PL spectra of PNCs at different irradiation times. This observation is clearly in contrast with the photo-brightening phenomenon.

3.6.2 Impact of Signal Saturation on the Power-Dependent FCS Studies of NPs

Signal saturation can significantly modify FCS curves of NPs at high intensity, which may result from a change in τ_{fl} or be inherent to the blinking phenomenon itself.[26] Unfortunately, PIE FCS can neither confirm nor dismiss the influences of saturation in power-dependent FCS behaviors of our NPs. In contrast to photo-brightening or optical trapping, excitation saturation by I_{SLr} does not leave any lasting impact on NP diffusion and occupancy after pulse switching.[26] Our PIE FCS can only detect photoinduced changes to NP if their effects persist for a duration longer than the pulse switching time, which is approximately 100 ns here.

However, the saturation of the signal induced by I_{SLr}, vanishes immediately upon pulse switching. Weakly intense PLr pulses consistently create identical excitation volumes without a saturation effect, regardless of SLr intensity. This characteristic renders PIE FCS curves under PLr excitations immune to excitation saturation by SLr.[26] The argument above implies that the absence of power dependency in PIE FCS cannot serve as conclusive evidence of the non-involvement of signal saturation. To assess the role of saturation in the observed power-dependent FCS phenomena, we first determined and then compared the saturation intensities (I_s) of our NPs (c-PNC and QD) whose FCS curves exhibited pronounced power dependency, and an organic dye molecule, rhodamine 6g (r6g) which demonstrated power independent FCS curves. The I_s was determined by fitting a saturation curve, which is a plot of PL count rate (S) as a function of pump intensity (I_P), to the following equation (Figure 3.10).

$$S=S_0\times I_P/(I_P+I_s) \qquad (3.1)$$

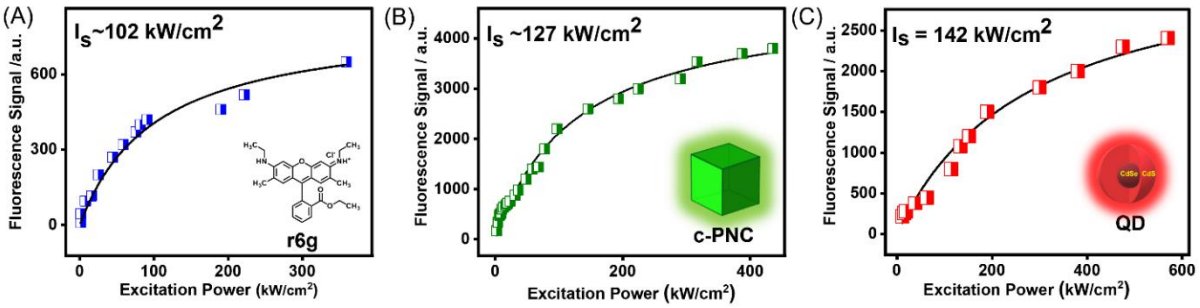

Figure 3.10. The fluorescence count rate as a function of pump intensity (I_P) for (A) r6g (B) c-PNC, and (C) QD, showing signal saturation as I_P increases. Saturation intensities (I_s) were derived from fitting the plots by Equation 3.1.

The best-fitted curves resulted in comparable I_s values from r6g (~102 kW/cm^2) and NPs (~127-142 kW/cm^2), although the expectation of much lower I_s values from the NPs due to

their longer τ_{fl} and larger absorption cross-sections (σ) are predicted by the following equation.[26]

$$I_s = (\sigma\tau_{fl})^{-1}/(1 + {}^{k_{ISC}}/_{k_{ph}}) \qquad (3.2)$$

The above equation is generally used for organic dyes to predict their I_s values based on their σ, τ_{fl}, intersystem crossing rate (k_{ISC}), and phosphorescence rate (k_{ph}).

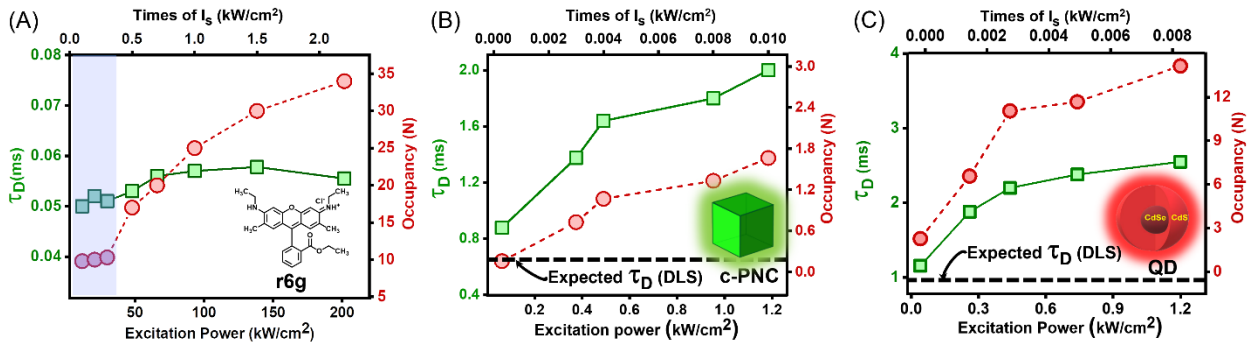

Figure 3.11. Graphs depicting occupancy (N) and diffusion time (τ_D) as a function of pump intensity (I_P) plotted on the absolute scale along the bottom x-axis, and relative to saturation intensity (I_s) along the top x-axis, respectively, for (A) r6g (B) c-PNC and (C) QD. r6g data in Figure A illustrates that the saturation effect can change FCS parameters only when pump intensity reaches >0.4×I_s. However, for c-PNC and QD, N, and τ_D apparently increase >6-to-9 folds (N) and >2 times(τ_D), respectively, as the excitation power changes within a range much lower than their respective I_ss; i.e., from ~ 0.0003×I_s (0.04 kW/cm^2) to ~0.010×I_s (1.2 kW/cm^2). Therefore, saturation alone can't explain the significant power dependency of the FCS curves of our NPs.

Since an analogous equation for NPs is not available because of their unknown dependence of blinking parameters on pump intensity, we directly derived I_ss of our NPs from the fittings to

the plots of PL count rate (S) as a function of pump intensity (I_P) by Equation 1 (Figure 3.10). Getting similar I_s values from r6g and NPs is not surprising to us because the predicted I_s from equation 2 is based on the assumption of exponential triplet kinetics, which is, although correct for dye molecules, not applicable to our NPs. Also, the τ_{fl} of NP experiences a significant quenching at high pump intensity due to Auger processes. These factors immediately provide an explanation for the relatively higher values of I_s of our NPs.

Next, we plotted N and τ_D as a function of pump intensity (and relative to I_s) derived from conventional FCS studies on r6g and compared them with the analogous plots for c-PNC and QD (Figure 3.11). The intention was to understand the effect of saturation on the power-dependent FCS phenomena of our NPs depicted in Figures 3.6A-C. Figure 3.11A illustrates the N and τ_D of r6g as a function of I_P in absolute scale (along the bottom x-axis) and relative to I_s (along the top x-axis). The graphs show that N begins to rise when the I_P surpasses ~0.4 times the saturation level I_s, indicating the onset of the saturation effect at a threshold of $0.4\times I_s$. Nevertheless, τ_D did not exhibit a notable change with I_P, and we attribute this observation to the photobleaching of r6g at high intensity. As mentioned earlier, if a dye undergoes photobleaching within its diffusion time, the resultant τ_D is shortened, while the dye's contribution to the correlation amplitude determining the occupancy remains constant. Hence, the actual deceleration of τ_D due to saturation cannot be observed if the dye undergoes photobleaching. Figures 3.11B and 3.11C depict the analogous plots from c-PNC and QD. In contrast to r6g, the power-dependent study in these cases was conducted in a regime much lower than their respective saturation intensities [I_s ~127 kW/cm^2 (c-PNC) and 142 kW/cm^2(QD)]. We made slight variations in the pump power, ranging from ~0.0003 to ~0.010 times their saturation intensities, leading to changes of more than 6-9 folds in N and 2 folds in τ_D, as illustrated in Figure 3.11B-C. The study on r6g has conclusively demonstrated that

discernible changes in FCS parameters due to saturation occur when the intensity level reaches at least half of its saturation intensity (Figure 3.11A). In fact, a simulation by Hess and coworkers also demonstrated an insignificant change in N in the power regime extended up to 0.3 times of I_s.[30] Thus, significant change in the FCS amplitude of c-PNC or, in general, any of our NP samples (except GQD) depicted in Figures 3.6A-C resulting from a power shift within a regime few orders of magnitude lower than their respective saturation intensities, cannot be attributed solely to the saturation effect. If we exclude the effects of photo-brightening and optical trapping, while also considering a minor contribution from saturation, the primary factor remaining to elucidate the power dependency of FCS curves of our NPs is brightness heterogeneity. Subsequent paragraphs elucidated brightness heterogeneity, which refers to the light-induced ON/OFF blinking of individual NPs.[26]

3.6.3 Manifestation of Brightness Heterogeneity in FCS Curves of NPs

With increasing laser intensity in an FCS study involving an organic dye with a high intersystem crossing rate, a distinct shoulder emerges at μs-correlation time regime. Given that transitions to triplet states follow well-characterized exponential kinetics at μs timescale, their impact is restricted to the initial time regime of the FCS curve. [39,51] Furthermore, irrespective of the pump power, the absence of distribution in characteristic triplet timescale implies that the PL blinking of a dye lacks brightness heterogeneity. In contrast, NP blinking follows power-law statistics, which is pump-intensity dependent and devoid of a distinctive timescale, indicating significant brightness heterogeneity.[55-58] The consequence of power-law blinking involves the occurrences of OFF-periods in NP blinking at various time scales with non-

negligible probabilities, consequently affecting FCS measurements across all temporal ranges.[26]

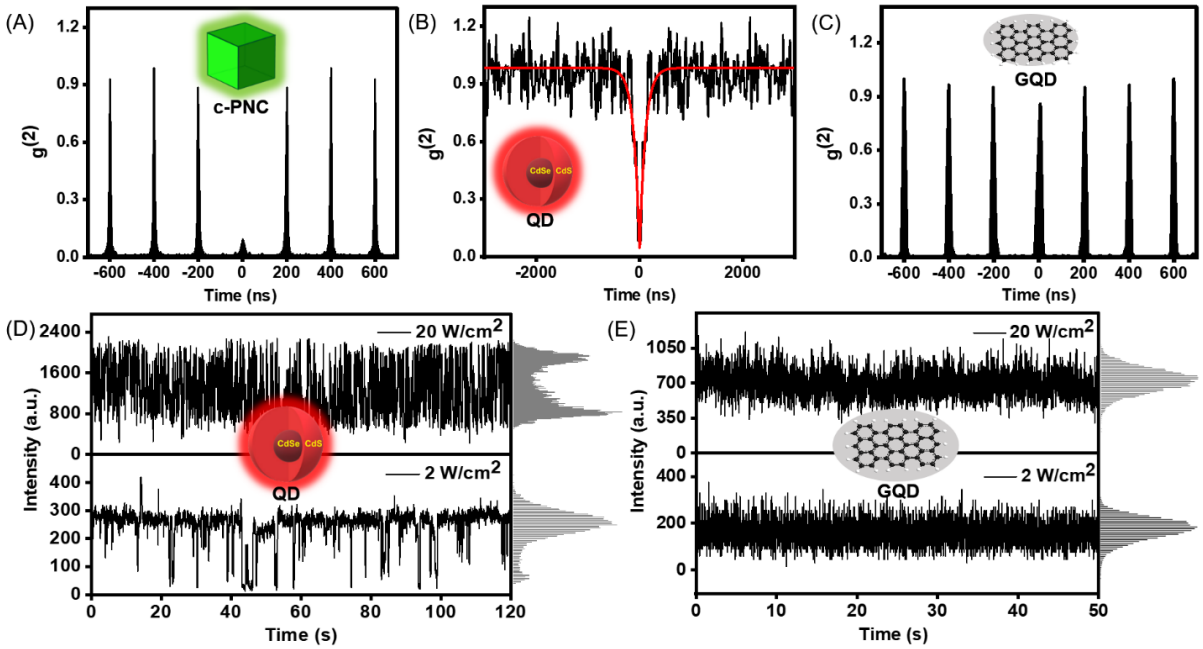

Figure 3.12. (A-C) The second-order cross-correlation functions [$g^{(2)}$] recorded on individual surface immobilized c-PNC (A), QD (B), and GQD (C), under low pump intensity [excitonic occupancy ~<0.008, λ_{ex} ~422 nm]. While $g^{(2)}$ of c-PNC and QD exhibits a dip at time zero, GQD excludes this feature, implying unlike the other two, GQD is not a single quantum emitter. (D) PL intensity trajectories recorded on a single QD at different intensities show a larger OFF state fraction at high pump intensity, accompanied by a higher ON/OFF switching rate. We attribute this behavior to brightness heterogeneity. (E) GQD's PL trajectory comprises only ON states with a uniform intensity distribution unaffected by excitation power, indicating minimal brightness heterogeneity. In all the cases, NPs were embedded in the PMMA matrix.

Brightness heterogeneity emerges when the PL from individual NPs involves blinking with an average ON/OFF time depending on the experimental observation time, allowing blinking to manifest across all timescales.[26] Furthermore, brightness heterogeneity renders ON/OFF time

distribution pump intensity dependent. [3,55] All these characteristics inevitably affect the entire FCS curves of NPs based on the pump intensity. To establish the brightness heterogeneity in the PL properties of our NPs that resulted in power-dependent FCS, we first studied the antibunching, which showed a dip at time zero (Figure 3.12 A-B). The antibunching effect is commonly observed in individual systems exhibiting PL blinking or intermittency, which is a prerequisite for demonstrating blinking and, thereby, brightness heterogeneity. [59-61] Subsequently, we investigated the PL intensity time trajectories recorded on individual surface immobilized NPs under varying pump intensities. The results revealed a higher OFF state fraction (Figure 3.12D) and longer OFF durations at elevated pump intensity.

Subsequently, we derived and plotted the occurrence probabilities of OFF times for our NPs in log-log representations at both low and high powers. The linear plots show significant modifications in occurrence probabilities of OFF-times at high power, pointing toward brightness heterogeneity (Figure 3.13).[3,35,55] The OFF-time probability function [$\rho(\tau_{off})$] was derived from analyzing the intensity states below a threshold level placed halfway between the average OFF and ON-intensity levels of a sufficiently long PL intensity trajectory.[55] While the bin size (5 ms) limits the shortest OFF-time, the longest OFF-time, however, can be comparable to the acquisition time (a few seconds or more). The probability distributions of OFF time periods [$\rho(_{\tau off})$], when represented in a log-log scale, exhibit a linear trend, fitting well to a power-law equation of the form $\rho(\tau_{off}) \propto \tau_{off}^{(-m)}$.[3,6] Power-law exponent (m), representing the relative rate of charge detrapping in NP, exhibits higher magnitude at lower excitation power (Figure 3.13).[6] Analysis of $\rho(\tau_{off})$ reveals two crucial observations that have direct implications with FCS: (i) The statistics of OFF times showcasing a wide distribution spanning six orders of magnitude in time are strongly influenced by excitation power. This implies that the FCS curve of NPs is subject to modification across all timescales depending

on the intensity. (ii) A relatively high rate of carrier de-traping (m) at low excitation power keeps the ON state predominant, leading to a lesser brightness heterogeneity. Further support for this assertion is provided by the fact that the diffusion times (τ_D) of NPs obtained from FCS closely match the ones calculated from the hydrodynamic radii (DLS derived) of NPs, only at low excitation power (Figure 3.11B-C).

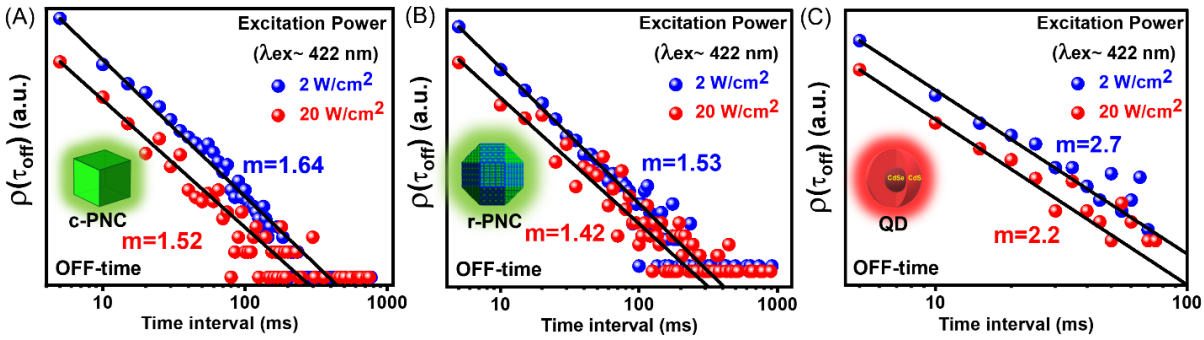

Figure 3.13. (A-C) Probability distribution of OFF-times for c-PNC (A), r-PNC (B), and QD (C) at differnt pump intensities along with the fitted lines, showing their OFF-times are not only power-law distributed but also extended across all time scales, that can influence the entire FCS curves of these NPs based on the excitation power.

To furnish additional evidence showing brightness heterogeneity as the underlying cause of power-dependent FCS curves of NPs, we performed FCS analysis on non-blinking GQDs, revealing FCS behaviors that are independent of excitation power. This observation provides direct proof of the correlation between the power-law blinking of NPs and their power-dependent FCS behaviors. Antibunching study on individual GQDs displays a high zero-time amplitude of second-order correlation [$g^2(0)$], suggesting multichromophoric emission, which agrees well with previous reports (Figure 3.12 C).[62] The absence of antibunching is generally observed in individual systems without possessing PL blinking, which is not an exception here, as depicted in Figure 3.12E; the PL intensity trajectory of GQD lacks OFF states even at a high

excitation power. These observations suggest minimal or no brightness heterogeneity in PL properties of GQD, rendering their FCS curves power-independent.

Importantly, even with the pronounced blinking and antibunching behaviors, r6g's FCS curves remain unaffected by excitation power (Figure 3.7).[63] These characteristic holds, at least within the power range similar to the one used for our NPs. In contrast to power-law blinking, the triplet kinetics of r6g are characterized by a well-defined timescale in the μs regime. This temporal characteristic impacts only the initial time correlation of the FCS curves. In fact, the lack of modifications in the initial correlation suggests that even the highest excitation power is insufficient to populate the triplet state of r6g (Figure 3.7). In light of the above observations, we conclude that well-characterized triplet blinking of organic dye molecules cannot result in brightness heterogeneity in their PL properties.

3.6.4 Deciphering Brightness Heterogeneity from Studying Fluorescence Lifetime Intensity Distribution (FLID) Map

To gain deeper insights into the brightness heterogeneity in the PL properties of our NPs, we examined FLID plots at various pump intensities.[3-4,57,64] These plots were derived from time-tagged-time-resolved (TTTR) measurements on individual surface-immobilized NPs (Figures 3.12D-E).[3-4,457,64] Our analyses show single photon emitter NPs (PNC and QD) demonstrate a direct correlation between PL lifetime (τ_{PL}) and intensity (I_{PL}) irrespective of the pump intensity with a bimodal characteristic of their FLIDs where the occupancy probability of the individual states in τ_{PL}-I_{PL} space is shown by a false color changing from blue (least-probable) to red (most-probable) (Figure 3.14). Since the drop in I_{PL} is accompanied by proportionate shortening of the τ_{PL}, we assign this blinking to type-A, a fingerprint of photoinduced charging/discharging of NPs.[3] Weakly intense OFF-states are referred to as trion states in the framework of type-A blinking. Trion is a charged exciton whose relaxation occurs either by an efficient

nonradioactive Auger process, by transferring recombination energy to a third carrier, or via radiative recombination with a rate twice faster than the radiative recombination rate of a neutral exciton.[3-4] While the OFF-states are weakly intense, short-lived trion states [τ_{x*} ~1.3 ns/2.0 ns/1.5 ns (c-PNCs/d-PNCs/r-PNCs) and ~2.3 ns (CdSe/CdS QD)], ON-states are bright and long-lived neutral excitonic states [τ_x ~9 ns/17 ns/18.5 ns (c-PNCs/d-PNCs/r-PNCs) and ~45 ns (CdSe/CdS QD)]. Since, in all the cases, excitation intensity was substantially low (~2 W/cm^2), the biexciton Auger recombination causing the OFF-state is unlikely. However, high pump intensity renders more trion states (and possibly biexcitons), indicated by increasing occurrence probability of short lifetime state in FLID at the cost of decreasing ON state probability (Figure 3.14 D-E). Also, the OFF-state fraction increases with pump intensity, pointing toward a photoinduced mechanism controlling the blinking of single photon emitter NPs (PNC and QD). As discussed earlier, a qualitatively similar observation was obtained in power-dependent PL intensity trajectory studies and subsequent analyses of OFF-time probabilities. All these observations suggest that the power-dependent ON/OFF blinking of individual NPs is the key to their unusual behaviors in conventional FCS studies. This assertion was further verified through the examination of FLID of non-blinking GQD. Unlike the bimodal distribution in FLIDs of PNC and QD, FLIDs of GQD involve a single probability state in I_{PL}-τ_{PL} space, irrespective of the pump intensity (Figures 3.14C and 3.14F). This is because our GQD emits a stream of photons, rendering its PL intensity trajectory devoid of OFF states (Figure 3.12E). The overall count rate increases at a higher pump intensity without introducing OFF-states (Figure 3.12E). Thus, the PL property remains largely intact with excitation intensity, leading to its FCS curve power independent (Figure 3.7). Unlike other NPs,

the FLID of GQD displays no change in the probability of ON-state and its distribution pattern with pump intensity, implying devoid of brightness heterogeneity.

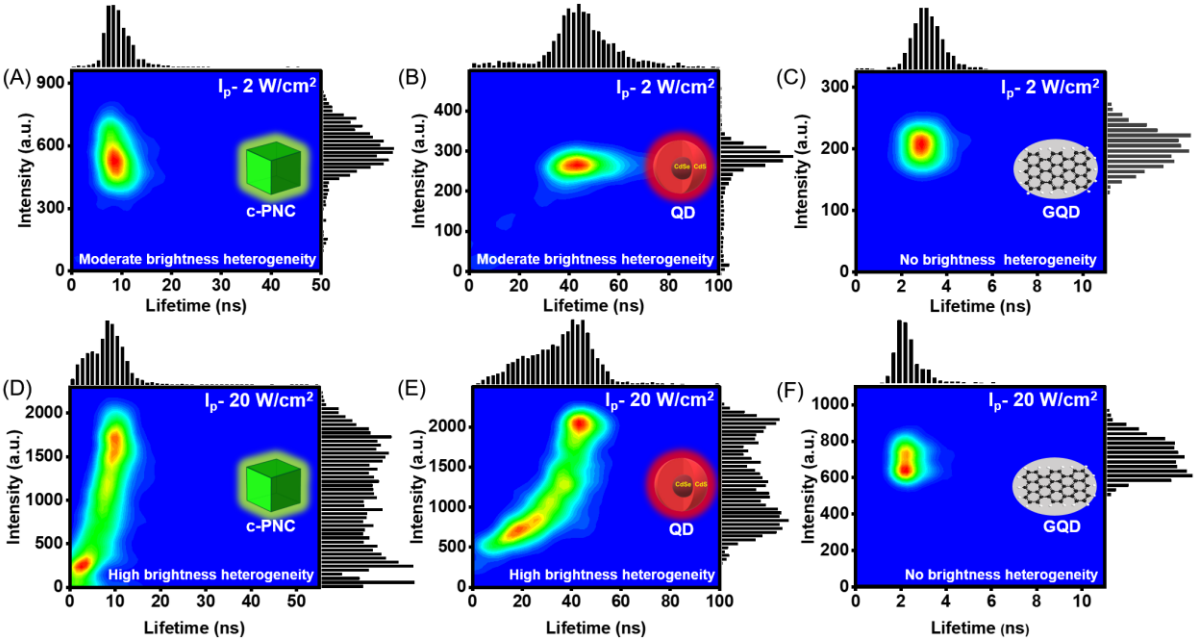

Figure 3.14. FLIDs of (A, D) c-PNC, (B, E) QD and (C, F) GQD at low (upper panel) and high (lower panel) pump-intensities, obtained from correlating single particle lifetime (τ_{PL}) and intensity (I_{PL}) histograms shown on the top (τ_{PL} histogram) and right side (I_{PL} histogram) of the FLID plots. The occurrence probability of a given state in the τ_{PL}-I_{PL} space is represented by false color, changing from red (most probable) to blue (least probable). While the single photon emitter NPs exhibit occurrence probabilities of ON (bright) and OFF (dim) states in I_{PL}-τ_{PL} space are pump-intensity dependent, multichromophoric GQD keeps ON state probability unity irrespective of the excitation power (C, F). This observation suggests that except for GQD, all other NPs exhibit a pronounced brightness heterogeneity at a high pump intensity, as indicated by the shape-changing of their probability states from near-circular or oval at low intensity (A-B), to distorted ones comprised of multiple sub-states with non-negligible probabilities at high intensity (D-E).

The PL intensity trajectories of single photon emitter NPs under low pump intensity display longer ON periods with less blinking (Figure 3.12D). Assuming minimal blinking or brightness heterogeneity of NPs at an extremely low pump intensity, we examined low-power autocorrelation curves to derive the most accurate τ_{DS}. These were then compared to the predicted values based on their hydrodynamic radii obtained from DLS studies, revealing an excellent correlation (dashed lines in Figure 3.11B-C). However, FCS-derived τ_{DS} defer significantly from the DLS-predicted ones as the pump intensity increases because of the enhanced brightness heterogeneity (Figure 3.11B-C). This observation suggests that characterizations of NPs by FCS are possible only at an exceptionally low pump intensity. However, samples like GQDs, which lack blinking, pose no interference to the FCS probe during characterization and allow their easy characterizations by this technique.

3.7 Conclusion

To summarise, the brightness heterogeneity or blinking of single photon emitter NPs causes a significant deviation of their FCS curves from ideality especially at an elevated pump intensity that can't be explained by optical saturation alone. Indeed one can't rule out a little contribution of saturation to the observed power dependent FCS behaviours of NPs. The most intriguing finding of our study is the power-independent behavior of the $g^2(0)$ amplitude and τ_D of single quantum emitter NPs in PIE FCS. However, these same parameters exhibit high sensitivity to variations in pump intensity in conventional FCS. This observation rules out the involvement of photo-brightening and optical trapping in modulating conventional FCS curves of NPs at high intensity. Further investigation of the PL-intensity trajectories of individual NPs reveals their blinking follows power-law statistics, with ON/OFF switching rates being pump-intensity dependent. Unfortunately, no numerical fitting function is available, which includes diffusion, power-law blinking, and their overlapping timescales.

Brightness heterogeneity often misleads researchers by causing deviations of FCS curves from ideality. Without a comprehensive understanding, brightness heterogeneity might be misinterpreted as photo brightening or optical trapping, as they can lead to similar observations. While characterizing NPs by FCS or, in general, any nanomaterial with intense blinking characteristics, one must refrain from using high excitation power to avoid enhanced blinking that can potentially alter the FCS parameters to unrealistic ones. Our analysis of OFF-times statistics indicates an alteration of the FCS curve of NPs across all timescales with increasing excitation power in a qualitative sense. However, further exploration through computational studies is essential to establish a direct correlation between the power-law blinking of NPs and its implications in FCS studies.

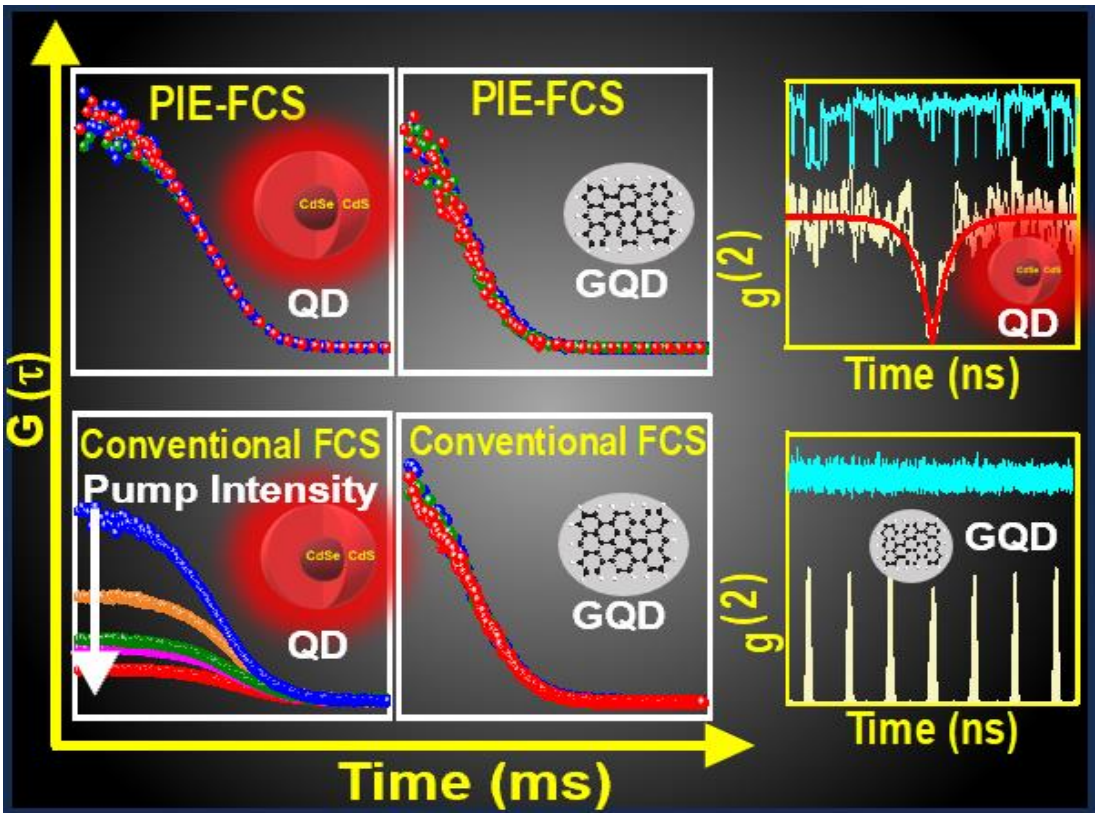

3.8 References

[1] J. S. Manser, J. A. Christians, P. V. Kamat, *Chem. Rev.* **2016**, *116*, 12956−13008.

[2] A. Dey, J. Ye, A. De, E. Debroye, S. K. Ha, E. Bladt, A. S. Kshirsagar, Z. Wang, J. Yin, Y. Wang, L. N. Quan, F. Yan, M. Gao, X. Li, J. Shamsi, T. Debnath, M. Cao, M. A. Scheel, S. Kumar, J. A. Steele, M. Gerhard, L. Chouhan, K. Xu, X.-g. Wu, Y. Li, Y. Zhang, A. Dutta,C. Han, I. Vincon, A. L. Rogach, et al., *ACS Nano* **2021**, *15*, 10775.

[3] Y. -S. Park, S. Guo, N. S. Makarov, V. I. Klimov, *ACS Nano* **2015**, *9*, 10386−10393.

[4] G. Yuan, D. E. Gómez, N. Kirkwood, K. Boldt, P. Mulvaney, *ACS Nano* **2018**, *12*, 3397−3405.

[5] S. K. Bera, S. Bera, M. Shrivastava, N. Pradhan, K. V. Adarsh, *Nano Lett.* **2022**, *22*, 8908−8916.

[6] T. Kim, S. Jung, S. Ham, H. Chung, D. Kim, *Small* **2019**, *15*, 1900355.

[7] Z. Piao, D. Yang, Z. Cui, H. He, S. Mei, H. Lu, Z. Fu, L. Wang, W. Zhang, R. Guo, *Adv. Funct. Mater*. **2022**, *32*, No. 2207662.

[8] K. M. Tsoi, Q. Dai, B. A. Alman, W. C. W. Chan, *Acc. Chem. Res.* **2013**, *46*, 662−671.

[9] F. Yuan, T. Yuan, L. Sui, Z. Wang, Z. Xi, Y. Li, X. Li, L. Fan, Z. Tan, A. Chen, et al., *Nat. Commun.* **2018**, *9*, 2249.

[10] K. Mishra, D. Acharjee, A. Das, S. Ghosh, *J. Phys. Chem. Lett.* **2022**, *13*, 606−613.

[11] K. Mishra, M. Barai, S. Ghosh, *J. Phys. Chem. C* **2022**, *126*, 16905−16918.

[12] K. Mishra, S. Koley, S. Ghosh, *J. Phys. Chem. Lett.* **2019**, *10*, 335−345.

[13] K. J. Babu, G. Kaur, A. Shukla, R. Saha, A. Kaur, M. Sachdeva, D. K. Yadav, H. N. Ghosh, *ACS Photonics* **2022**, *9*, 969−978.

[14] A. Das, D. Acharjee, M. K. Panda, A. B. Mahato, S. Ghosh, *J. Phys. Chem. Lett*. **2023**, *14*, 3953-3960.

[15] D. Acharjee, A. Das, M. K. Panda, M. Barai, S. Ghosh, *Nano Lett.* **2023**, *23*, 1946-1953.

[16] A. Manna, T.K. Dinda, S. Ghosh, P. Mal, *Chem. Mater.* **2023**, *35*, 628–637.

[17] S. K. Mahankudo, A. Das, K. Mishra, M. Barai, P. Mal, S. Ghosh, *ACS Appl. Nano Mater.* **2022**, *5*, 4360−4366.

[18] K. Mishra, D. Acharjee, A. Das, S. Ghosh, *J. Phys. Chem. B* **2021**, *125*, 11017−11025.

[19] A. Garai, E. K. Vishnu, S. Banerjee, A. A. K. Nair, S. Bera, K. G. Thomas, N. Pradhan, *J. Am. Chem. Soc.* **2023**, *145*, 13989–13999.

[20] A. Nag, *Nano Lett.* **2021,** *21*, 8529−8531.

[21] S. Das, M. Hossain, A. Samanta, *ACS Appl. Nano Mater.* **2023**, *6*, 4812−4820.

[22] D. W. deQuilettes, W. Zhang, V. M. Burlakov, D. J. Graham, T. Leijtens, A. Osherov, V. Bulović, H. J. Snaith, D. S. Ginger, S. D. Stranks, *Nat.Commun.* **2016**, *7*, No. 11683.

[23] L. Huang, Z. Ge, X. Zhang, Y. Zhu, *J. Mater. Chem. A* **2021**, *9*, 4379−4414.

[24] H. Choi, J. C.-R. Ke, S. Skalsky, C. A. Castle, K. Li, K. L. Moore, W. R. Flavell, P. Parkinson, *J. Mater. Chem. C* **2020**, *8*, 7509−7518.

[25] T. Tachikawa, I. Karimata, Y. Kobori, *J. Phys. Chem. Lett.* **2015**, *6*, 3195−3201.

[26] S. Doose, J. M. Tsay, F. Pinaud, S. Weiss, *Anal. Chem.* **2005**, *77*, 2235−2242.

[27] H. Sahoo, P. Schwille, *ChemPhysChem* **2011**, *12*, 532–541.

[28] A. Das, K. Mishra, S. Ghosh, *J. Phys. Chem. Lett.* **2021**, *12*, 5413−5422.

[29] C. Dong, H. Qian, N. Fang, J. Ren, *J. Phys. Chem. C* **2007**, *111*, 7918−7923.

[30] J. A. Rochira, M. V. Gudheti, T. J. Gould, R. R. Laughlin, J. L. Nadeau, S. T. Hess, *J. Phys. Chem. C* **2007**, *111*, 1695−1708.

[31] R. F. Heuff, J. L. Swift, D. T. Cramb, *Phys.Chem.Chem.Phys.* **2007**, *9,* 1870−1880.

[32] R. F. Heuff, M. Marrocco, D. T. Cramb, *J. Phys. Chem. C* **2007,** *111*, 18942–18949.

[33] C. Dong, H. Qian, N. Fang, J. Ren, *J. Phys. Chem. B* **2006**, *110*, 11069–11075.

[34] S. Das, G. Rana, F. Ali, A. Datta, *Nanoscale* **2023**, *15*, 4469−4476.

[35] J. J. Peterson, D. J. Nesbitt, *Nano Lett.* **2009**, *9*, 338−345.

[36] P. Bharadwaj, L. Novotny, *Nano Lett.* **2011**, *11*, 2137−2141.

[37] W. Y. Chiang, T. Okuhata, A. Usman, N. Tamai, H. Masuhara, *J. Phys. Chem. B* **2014**, *118*, 14010−14016.

[38] A. Loman, T. Dertinger, F. Koberling, J. Enderlein, *Chem. Phys. Lett*. **2008**, *459*, 18–21.

[39] P. Schwille, E. Haustein, **2002**; pp 10−25.

[40] A. N. Kapanidis, T. A. Laurence, N. K. Lee, E. Margeat, X. Kong, S. Weiss, *Acc. Chem. Res.* **2005**, *38*, 523−533.

[41] S. Ito, T. Sugiyama, N. Toitani, G. Katayama, H. Miyasaka, *J. Phys. Chem. B* **2007**, *111*, 2365−2371.

[42] J. Cui, S. Koley, Y. E. Panfil, A. Levi, Y. Ossia, N. Waiskopf, S. Remennik, M. Oded, U. Banin, *J. Am. Chem. Soc.* **2021**, *143*, 19816−19823.

[43] D. Acharjee, A. B. Mahato, A. Das, S. Ghosh, *J. Phys. Chem. C*. **2023**, *127*, 19643–19650.

[44] S. Bera, R. K. Behera, N. Pradhan, *J. Am. Chem. Soc.* **2020**, *142*, 20865−20874.

[45] N. V. S. Praneeth, S. Akhil, A. Mukherjee, S. Seth, S. Khatua, N. Mishra, *Adv. Opt. Matr.* **2024**, 2303222.

[46] S. Paul, A. Samanta, *ACS Energy Lett.* **2020**, *5*, 64−69.

[47] K. Mishra, A. Das, S. Ghosh, *J. Phys. Chem. C* **2020**, *124*, 24115−24125.

[48] S. Ghosh, U. Mandal, A. Adhikari, K. Bhattacharyya, *Chem. Asian J.* **2009**, *4*, 948−954.

[49] S. Ghosh, A. Adhikari, S. S. Mojumdar, K. Bhattacharyya, *J. Phys. Chem. B* **2010**, *114*, 5736−5741.

[50] N. Pal, S. D. Verma, M. K. Singh, S. Sen, *Anal. Chem.* **2011**, *83*, 7736−7744.

[51] T. Wohland, S. Maiti, R. Macháň, **2020**; pp 247−250.

[52] B. Sahoo, J. Balaji, S. Nag, S. K. Kaushalya, S. Maiti, *J. Chem. Phys.* **2008**, *129*, No. 075103.

[53] C. Carrillo-Carrión, S. Cárdenas, B. M. Simonet, M. Valcárcel, *Chem. Commun.* **2009**, 5214−5226.

[54] E. Moyen, A. Kanwat, S. Cho, H. Jun, R. Aad, J. Jang, *Nanoscale* **2018**, *10*, 8591−8599.

[55] A. A. Cordones, S. R. Leone, *Chem. Soc. Rev.* **2013**, *42*, 3209−3221.

[56] Y. S. Park, J. Lim, N. S. Makarov, V. I. Klimov, *Nano Lett.* **2017**, *17*, 5607−5613.

[57] E. M. Thomas, N. Pradhan, K. G. Thomas, *ACS Energy Lett.* **2022**, *7,* 2856−2863.

[58] Rashi, V. Kaur, A. Devi, D. Bain, T. Sen, A. Patra, *J. Phys. Chem. Lett.* **2023**, *14*, 10166-10172.

[59] I. Y. Eremchev, A. O. Tarasevich, J. Li, A. V. Naumov, I. G. Scheblykin, *Adv. Optical Mater.* **2021**, *9*, 2001596.

[60] H. Igarashi, M. Yamauchi, S. Masuo, *J. Phys. Chem. Lett.* **2023**, *14*, 2441−2447.

[61] M. Yoshioka, M. Yamauchi, N. Tamai, S. Masuo, *Nano Lett.* **2023**, *23*, 11548−11554.

[62] Q. Xu, Q. Zhou, Z. Hua, Q. Xue, C. Zhang, X. Wang, D. Pan, M. Xiao, *ACS Nano* **2013**, *7*, 10654−10661.

[63] W. P. Ambrose, P. M. Goodwin, J. Enderlein, D. J. Semin, J. C. Martin, R. A. Keller, *Chem. Phys. Lett.* **1997**, *269*, 365-370.

[64] M. K. Panda, D. Acharjee, A. B. Mahato, S. Ghosh, *Small* **2024**, 2311559.

CHAPTER 4

Facet Dependent Photoluminescence Blinking from Perovskite Nanocrystals

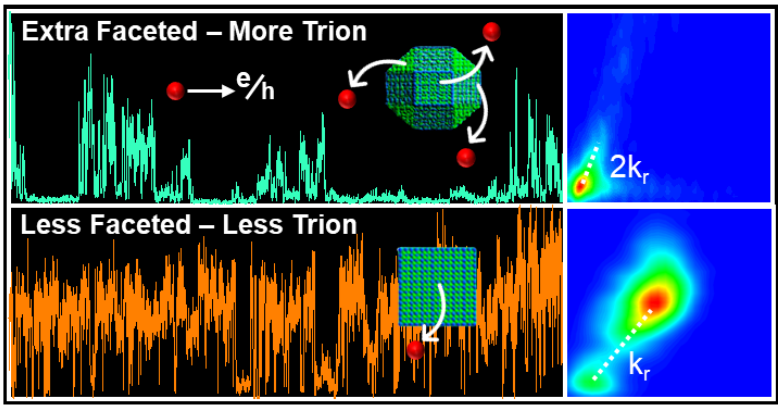

4.1 Abstract

Photoluminescence (PL) blinking of nanoparticles, while detrimental to their imaging applications, may benefit next-generation displays if the blinking is precisely controlled by reversible electron/hole injections from an external source. Considerable efforts are made to create well-characterized charged excitons within nanoparticles through electrochemical charging, which has led to enhanced control over PL-blinking in numerous instances. Manipulating the photocharging/discharging rates in nanoparticles by surface engineering can represent a straightforward method for regulating their blinking behaviors, an area largely unexplored for perovskite nanocrystals (PNCs). This work shows facet engineering leading to different morphologies of PNCs characterized by distinct blinking patterns. For instance, examining the PL intensity trajectories of single PNCs, representing the instantaneous photon count rate over time, reveals that the OFF-state population significantly increases as the number of facets increases from six to twenty-six. This study suggests that extra-faceted PNCs, owing to their polar facets and expanded surface area, render them more susceptible to photocharging, which results in larger OFF-state populations. Furthermore, the fluorescence correlation spectroscopy (FCS) study unveils that the augmented propensity for photocharging in extra-faceted PNCs can also originate from their greater tendency to form complexes with neighbouring molecules.

4.2 Introduction

Auger recombination in nanoparticles causes the transfer of the electron-hole binding energy non-radiatively to a third carrier, leading to intra-band excitation of the carrier that eventually relaxes by dissipating excess energy to heat.[1-6] Auger recombination in small nanoparticles, including PNCs, is exceptionally fast, attributed to the proximity of interacting charge carriers

and the contribution of momentum conservation relaxation to the dynamics. As a result, the overall recombination timescale significantly reduces to a few hundred picoseconds (ps) or even less.[3, 7, 8] The presence of a charged exciton in nanoparticles with a high Auger recombination rate leads to a weakly emissive state that presents detrimental effects on LED and imaging applications. For example, previous studies have shown that the emission of a quantum dot light-emitting diode (QD-LED) is significantly diminished by the charging of the emitting layer, leading to enhanced nonradiative Auger losses, that eventually limit the external quantum efficiency of a LED.[9-12] Nevertheless, deliberately engineered charged excitons (or trions) can hold significant promise for potential benefits in next-generation display applications whose operation may necessitate an imbalance between hole and electron injection rates. This would enable selective trion-induced darkening of specific pixels on a display while maintaining emissivity in others.[13-15]

To efficiently utilize charged excitons in a display application, harvesting well-characterized trion states and exercising meticulous control over their dynamics would be necessary.[15] Recent studies have unveiled several strategies, such as electrochemical charge injection, photochemical doping, and modifications in core/shell geometry, which can aid in the formation of well-characterized trion states in nanoparticles.[16-21] However, implementing these strategies in real-world applications remains challenging due to the inherent complexity of these processes. Numerous other studies have explored relatively simpler approaches, such as changing particle morphology, heterostructure, nanoparticle volume, etc., to regulate the Auger processes, including trion recombination, in both perovskite and non-perovskite quantum dots. However, many of these studies have uncovered rather intricate patterns of dependency of Auger dynamics on these parameters.[17, 18, 22-33] Several of them have proposed various recombination pathways in nanoparticles that can be further correlated in elucidating

their blinking behaviors. Therefore, these fundamental insights can serve as a foundation for integrating these nanoparticles into diverse optoelectronic applications.

The literature survey suggests that although surface engineering is believed to be one of the most straightforward strategies that can render greater control over nanoparticle blinking, there have been less number of studies on conventional quantum dots (QDs) and no reports on PNCs in this topic. Nevertheless, the relationship between blinking and particle size is well demonstrated for cube PNCs.[1, 34] A notable example lies in a study conducted by Kim and colleagues, where they examined the PL blinking of $CH_3NH_3PbBr_3$ PNCs of different sizes.[1] Statistical analyses of their single dot PL intensity trajectories showed a progressive rise in ON-time fraction as particle size increased, correlating with the observed higher photoluminescence quantum yields (PLQYs) of bigger particles.[1] A recent report by Pradhan and colleagues claimed the first instance of surface-engineered $CsPbBr_3$ PNCs, resulting in two unusual morphologies other than cubes.[35] Their surface-engineered PNCs exhibit uniform sizes but differ in their number of facets. Starting with six-faceted cube PNCs (c-PNCs), to twelve-faceted dodecahedron PNCs (d-PNCs), and finally to twenty-six-faceted rhombicuboctahedron PNCs (r-PNCs).[35] Numerous subsequent investigations have affirmed the enhanced potentials of PNCs with unusual morphologies, which have documented improvements in various parameters relevant to their optoelectronic and photovoltaic applications.[36-40] For instance, in seminal works, Ghosh et al., for the first time, and our group subsequently reported decelerated hot carrier cooling in extra faceted PNCs caused by an efficient polaron formation.[37, 38]

To the best of our knowledge, the present study constitutes the first report on facet-dependent PL blinking from $CsPbBr_3$ PNCs. Our work renders greater control on PL blinking of PNCs by altering particle morphology. Intriguingly, we observed an augmented propensity for forming

trions in extra-faceted PNCs. Our findings suggest that surface engineering is the most straightforward method for controlling the Auger processes in PNCs. The findings of our work would open a new avenue for the potential utilization of PNCs in next-generation optoelectronic devices.

4.3 Synthesis of Facet Engineered $CsPbBr_3$ Nanocrystals

Syntheses of 6 faceted cubic (cPNC), 12 faceted rhombic dodecahedron (dPNC), and 26 faceted rhombicuboctaheron (rPNC) followed the reported procedures. [36,38] High-temperature sample drying under an inert environment was considered in almost every step. In brief, first, we prepared cesium-oleate by heating the required amounts of Cs2CO3, oleic acid (OA), and octadecene (ODE) at ~130^{0}C for ~60 minutes under N2 environment. Obtained cesium-oleate was preheated to >100 0C, before using it in the following steps. Next, required amounts of PbO, phenacyl bromide, oleic acid (OA), oleylamine (OAm), and ODE were mixed together and heated to a temperature of ~130^{0}C under an inert atmosphere. A red-colored reaction mixture was obtained, and then the temperature was increased further to >200^{0}C. After prolonged heating (~1 hr), ~0.5 ml Cs-oleate (prepared in the first step) was quickly added to the reaction mixture. Then, the reaction was quenched in an ice bath after 20 minutes of annealing. The obtained d-PNC sample was purified through repeated centrifugations in a solvent mixture following a procedure described in the literature. [36,38] r-PNCs and c-PNCs were synthesized following an identical procedure discussed above for d-PNCs, except for the annealing time; here, it is ~45 minutes (for r-PNCs) and ~1 minute (for c-PNCs), respectively. The rest of the steps are similar to the synthesis of d-PNCs, apart from a few slight modifications reported elsewhere. [36,38]

4.4 Sample Characterisation

The synthesized $CsPbBr_3$ PNCs with 6- (cube, c-PNC), 12- (dodecahedron, d-PNC), and 26- (rhombicuboctahedron, r-PNC) facets shows almost similar PLQY of ~80%.[35-40] Figure 4.1(A-C) illustrates high-resolution transmission electron microscopy (HRTEM) images of our PNCs exhibiting various morphologies. The inset in each figure displays size distribution, showing comparable average edge lengths (≈16 ± 1 nm) across the morphologies, with 15–20% size dispersions.

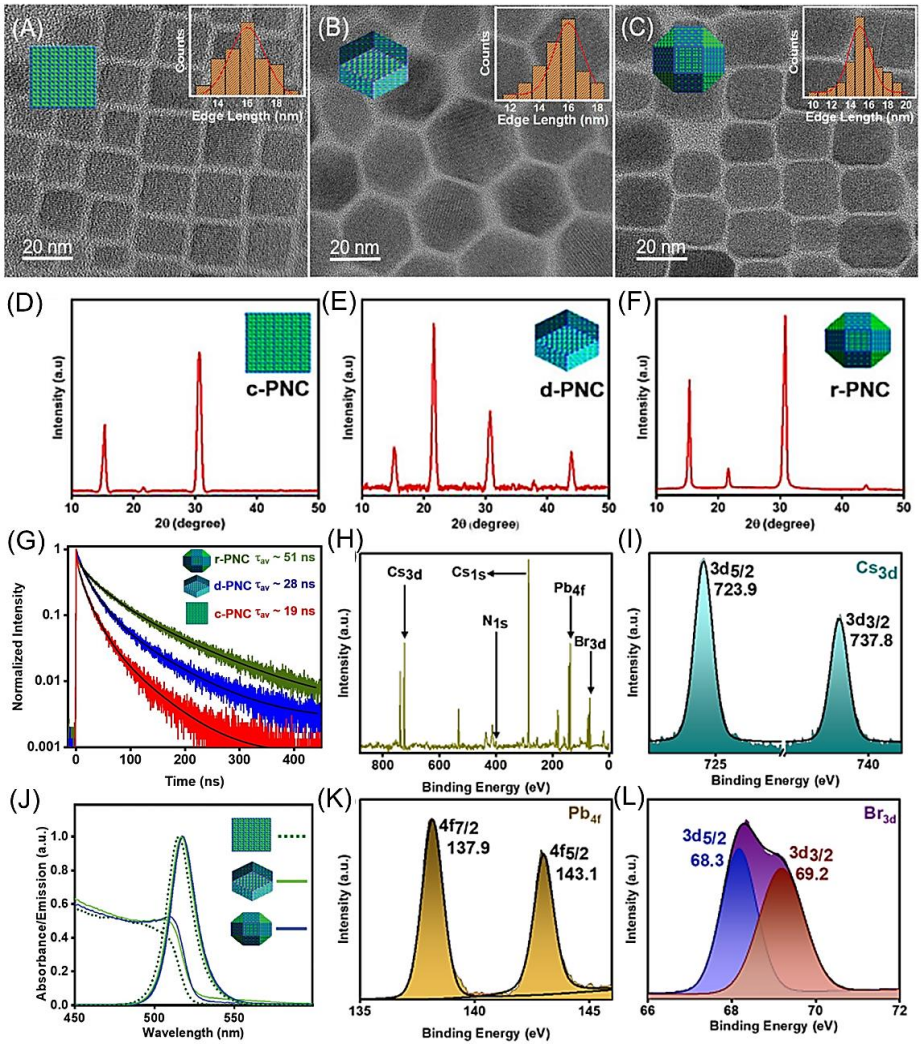

Figure 4.1. (A–C) HRTEM images of PNCs with 6-facets (cube, c-PNC) (A), 12-facets (dodecahedron, d-PNC) (B), and 26 facets (rhombicuboctahedron, r-PNC) (C), (D) The powder XRD patterns of (A) c-PNCs, (B) d-PNCs, and (C) r-PNCs closely resemble with the reported ones. (G) PL lifetime curves of all three PNC samples dispersed in toluene. Lifetimes were

recorded at their respective emission peak positions. Samples were excited by a ~405 nm diode laser (IRF ~ 90 ps). (H, I, K, L) XPS patterns of d-PNC (full range and survey scan), along with peak assignments. (J) PL (λ_{ex} ~400 nm) and absorption spectra of PNCs dispersed in toluene.

Larger and smaller particles were identified and eliminated through spectroscopic screening, involving critical analyses of their spectral signatures and lifetime profiles derived from single-dot studies. Spectral signature includes their PL peak positions and full width at half maxima (FWHMs) of their single dot emission spectra. Additional characterizations of our PNC samples were performed by XRD (Figure 4.1D-F), excited state lifetime plots (Figure 4.1G) XPS (Figure 4.1H,I,K,L), and steady-state optical studies (Figure 4.1J); all results nicely correlate with previous reports. XPS analysis confirms the binding energy signatures (Figure 4.1H,I,K,L) corresponding to Cs, Pb, Br, C, and N in the dodecahedral $CsPbBr_3$ nanocrystals. The elemental ratio of Cs:Pb:Br (~0.59:0.74:3.1) agrees well with the expected $CsPbBr_3$ stoichiometry. The observed binding energies for Cs $3d_{3/2}$ and Cs $3d_{5/2}$ appear at 738.15 eV and 724.11 eV, respectively. Similarly, Pb $4f_{7/2}$ and Pb $4f_{5/2}$ peaks are located at 138.1 eV and 143.1 eV. The spin–orbit doublet of Br 3d shows peaks at 68.02 eV ($3d_{5/2}$) and 69.26 eV ($3d_{3/2}$), consistent with earlier literature. A peak near 399 eV (N1s) indicates the presence of tertiary nitrogen, supporting the formation of tertiary ammonium ions via nucleophilic substitution between oleylamine and phenacyl bromide. This tertiary ammonium species likely serves as a ligand, promoting the dodecahedral morphology. The same reason is valid for synthesis of more faceted rhombicuboctahedron morphology while the primary ammonium ion gives normal cubic morphological structure.

4.5 Results and Discussion

4.5.1 PL Blinking and Antibunching Study of Different Faceted Nanocrystals

Considering the high dilution of PNC samples as a prerequisite for the blinking study, we conducted a thorough assessment of the surface quality and photochemical stability as a function of dilution across the morphologies through the following experiments: i) PLQY measurement which indicates a moderate decline with dilution in a pure solvent but can be mitigated by employing a solution containing ≈3% PMMA [poly(methyl methacrylate)] (Figure 4.2A-F). So, we performed single dot measurements in PMMA matrix.

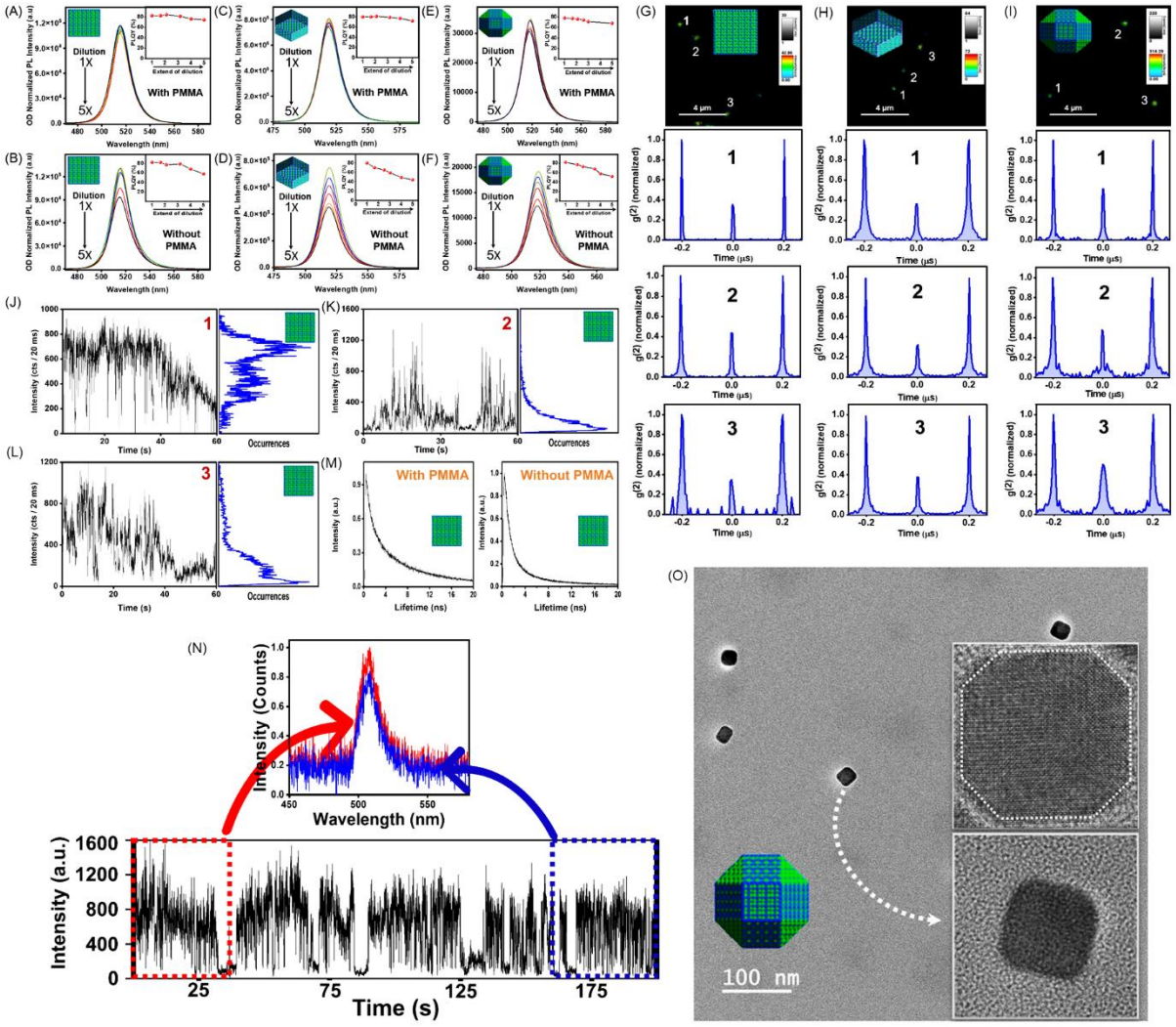

Figure 4.2. PL spectra of c-, d-, and r-PNCs dispersed in toluene when excited at 400 nm, normalized by their respective ODs at 400 nm at different dilutions (up to 5x) in the presence

(A,C,E) and absence (B,D,F) of 3% PMMA. Insets show PLQYs as a function of the dilution factor. In the absence of PMMA, PLQY decreases for all three samples with dilution but remains nearly the same in the presence of PMMA**.** (G-I) Second-order cross-correlation functions [$g^2(t)$], recorded on three randomly selected PMMA embedded dots (particle numbers 1, 2, and 3 in the above confocal images) from each PNC sample. We observed nearly 30-40% photon-coincidence fraction, which is expected for our bigger-sized particles due to the slower Auger recombination rate reported earlier by Masuo and coworkers using similar-sized particles.[6] (J-L) Few representatives of the PL trajectory of c-PNC without PMMA, show photodegradation within the first 60 s of exposure. The right sides of the main figures show corresponding intensity histograms with larger populations of OFF-states. (M) PL intensity decay curves were recorded from two c-PNCs, one embedded in PMMA and the other on the bare coverslip. Faster decay of the latter signifies photodegradation. This trend is consistent across repeated studies involving other particles. (N) An example of a typical PL trajectory of PNC embedded in PMMA is considered a stable particle if the average ON-state intensity remains stable for at least 3 minutes and the emission spectra collected during the first and the last 30 s remain identical in their peak PL positions and FWHMs. This behaviour cannot be obtained without PMMA. A 422 nm pulse laser (5 MHz repetition rate) with I_P ~2 W/cm^2 was used for the excitation. (O) TEM images of r-PNCs at single particle dilution. Insets show high-resolution images. Structural integrity is preserved even at single-particle dilution.

(ii) Statistical analysis of photons emitted from a PNC dot embedded in PMMA reveals antibunching behaviour, with an average photon-coincidence of ≈30–40% at time zero (Figure 4.2G, H, I). iii) PL-intensity traces of PNCs embedded in PMMA matrix show stable ON-state intensities with time. However, the same decreases significantly during the first 60 s of

exposure in the absence of PMMA, driven by photochemical degradation. This effect is more prominent in extra-faceted PNCs (Figure 4.2 J-M & N). iv) TEM measurement which shows retention of facet structure in extra-faceted PNCs even at single dot dilution (Figure 4.2 O). This observation rules out any involvement of nanocrystal clusters in our blinking study. All these studies collectively indicate that our extra-faceted PNCs maintain their structural and optical integrities at single dot dilutions only when embedded in a PMMA matrix.

Earlier studies on PNCs have reported arbitrary PL fluctuations between bright (ON) and weakly emissive (OFF) states, referred to as PL-blinking or intermittency, stemming from nonradiative band-edge carrier (NBC) and trion recombination.[2,45-49] Using time-tagged, time-correlated single photon counting (TCSPC) measurements of PL blinking on PNCs ($CsPbI_3$/ $CsPbBr_3$), Klimov and colleagues confirmed that the bright state emerges from charge-neutral excitonic recombination, while the OFF state stems from the charged exciton or trion recombination.[2] On the contrary, Xiao and colleagues observed that the origin of the OFF-state in $CsPbBr_3$ PNC lies in NBC recombination.[48] Samanta and coworkers observed both types of recombination in a $CsPbBr_3$ PNC.[49] If a photo-carrier is trapped in a deep trap state for an extended period, PNC becomes charged. The subsequent absorption of the second photon by charged PNC produces a trion.[2, 49] Recombination of trion may involve both i) a nonradioactive Auger process by transferring recombination energy to an uncompensated charge carrier and ii) a radiative process with a rate constant twice high (i.e., $2k_r$) compared to that (k_r) of the neutral exciton. The trion state recombination (radiative and nonradiative) causing PL-blinking is called Auger blinking and is also regarded as Type-A blinking. [4, 49-53] Auger blinking is prevalent in nanoparticles with deep trap states and is also observed at pump intensity. NBC recombination-induced blinking, triggered by the activation and deactivation of multiple recombination centers (MRCs) near the band edge, involves variable nonradiative

rates against a fixed radiative rate. [48, 51] A linear correlation between PL lifetime and intensity is expected for NBC blinking, which is also known as Type-C blinking. [1, 51, 53]

For the single dot PL-blinking study, a highly diluted solution of PNC in 3% poly(methyl methacrylate) (PMMA) was spin-coated on a coverslip. The low areal density (≈0.09 μm^2) of PNCs on the coverslip ensured their easy isolations by confocal. Throughout our experiment, we maintained a minimal average excitonic occupancy (<N> ~0.008), calculated from the relationship <N> = (photon fluence per pulse) × (absorption cross-section).[26] The typical single-dot PL spectra from most of the particles are characterized by similar FWHMs ($\Delta\lambda_{1/2}$) of ≈18 ± 2 nm (c-/d-/r-PNC) and PL peak positions at ≈505±3 (c-PNCs) and 508 ± 3 nm (d/r-PNC), respectively (Figure 4.1J). Any deviation, whether in the PL peak position or the FWHM, is attributed to change in particle size and/or morphology, resulting in the exclusion of that particle from further analysis.

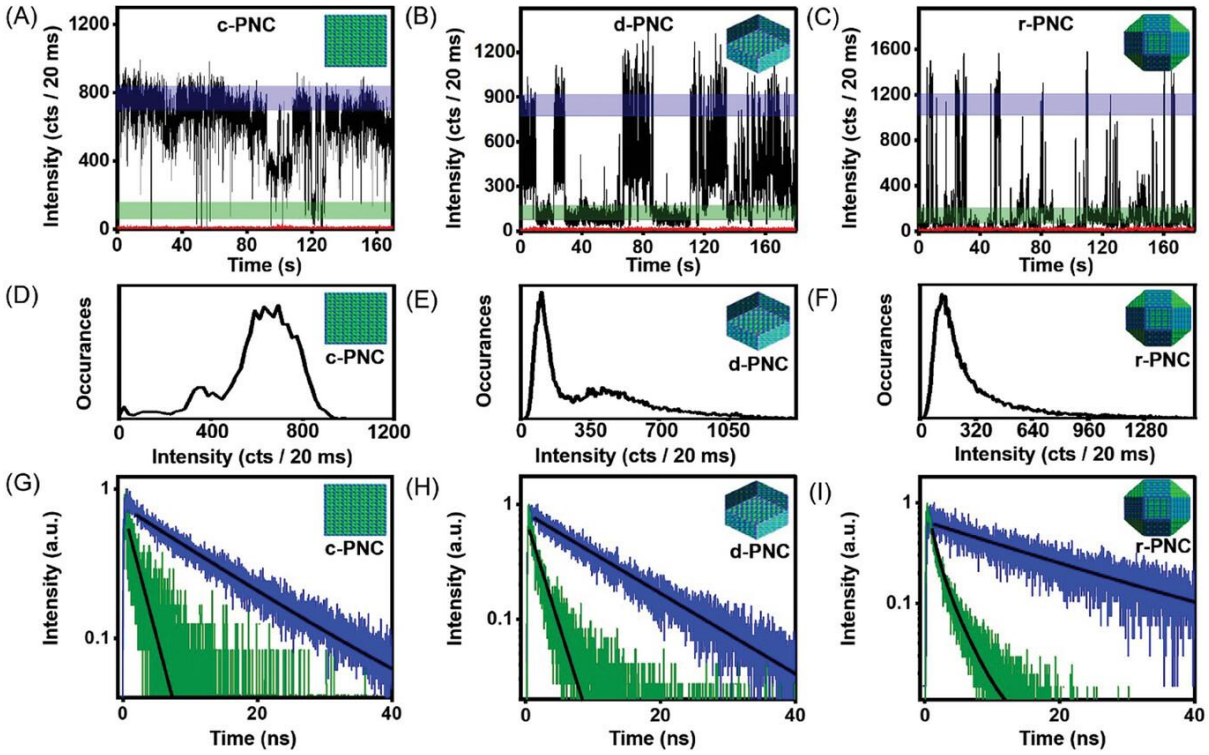

Figure 4.3. PL intensity trajectories (upper panel, 20 ms binning time) along with statistical distributions of intensities (middle panel) and PL dynamics of ON and OFF states (lower panel)

recorded in single dot measurements on c-PNC (A, D, G), d-PNC (B, E, H), and r-PNC (C, F, I). PL lifetime profiles of ON and OFF states are constructed by the photons collected from the highest and lowest intensity regimes of the PL trajectories shown by pairs of horizontal slabs of similar colors with lifetime curves. A ~422 nm pulse laser (≈5 MHz repetition rate and ≈150 ps IRF) with excitation power (I_P) ~2 W cm^{-2} was used for the excitation.

Figure 4.3(A–C) depicts representatives of PL trajectories of PNCs, each chosen from a different batch (c-, d-, and r-PNCs). These trajectories exhibit the highest similarity with others within the same batch and are selected for further analyses. To mitigate potential biases arising from randomly selected individual PNCs or exceptional outliers, single-dot measurements were repeated across 100 dots for each batch of PNCs. The statistical distributions of intensities, illustrated in Figure 4.2D–F, unveil a bimodal distribution for c- and d-PNC, whereas r-PNC exhibits a single modal distribution characterized by OFF states only. Thus, the ratio of ON-to-OFF state populations diminishes as the number of facets increases in PNC (Figure 4.3D–F).

The origin of the OFF-states here is attributed to either NBC or trion or both types of recombination, a conclusion supported by not only the direct correlation between PL intensity (I_{PL}) and lifetime (τ_{PL}) in single dot blinking study (Figure 4.4), but also from the analysis of fluorescence lifetime intensity distribution (FLID) maps. [1-4, 27, 49]

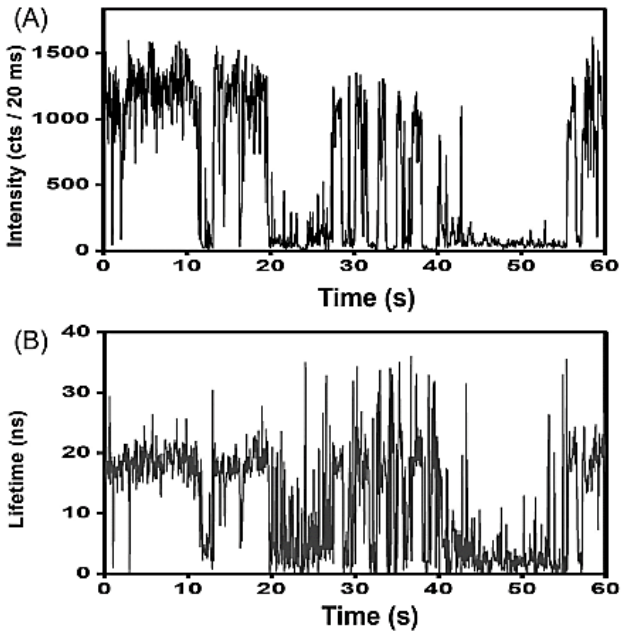

Figure 4.4. PL intensity blinking (A) and lifetime blinking (B) recorded simultaneously on the same d-PNC dot show an excellent correlation.

The Table 4.1 collected the PL lifetimes of ON and OFF states of all three PNCs (Figure 4.3G–I). The PL dynamics of the ON state, which represent radiative recombination, demonstrate single exponential behaviour across morphologies. Conversely, the OFF-state dynamics, representing NBC and/or trion recombination, exhibit single exponential behaviour for c- and d-PNC; however, the same demonstrates a biexponential behaviour for r-PNC. (Table 4.1 and Figure 4.3G,F). Further analysis implies that the origin of the biexponential lifetime of the OFF state in the latter stems from the involvement of both NBC and trion recombination, aligning with earlier reports showing type-A and type-C blinking from the same nanoparticle.[49] The radiative lifetime ratios of ON-to-OFF states ($\tau_{r,ON}/\tau_{r,OFF}$) were computed across the morphologies using the following equation (equation 4.1), incorporating their ON and OFF state lifetimes (τ_{ON} and τ_{OFF}) from Table 4.1, and intensities (I_{ON} and I_{OFF}) from Figure 4.3A–C.[1]

$$\eta = \frac{k_{r,OFF}}{k_{r,ON}} = \frac{\tau_{ON}}{\tau_{OFF}} \frac{I_{OFF}}{I_{ON}} \qquad (4.1)$$

η essentially represents the ratio of the radiative rate constants of OFF ($k_{r,OFF}$) and ON ($k_{r,ON}$) states. The values of this parameter were determined to be ≈0.97 and ≈1.2 for c-PNC and d-PNC, respectively, both of which are close to unity, implying NBC blinking. However, the relatively higher value of η for d-PNCs may be attributed to the participation of trion states, albeit with a minor contribution, in the overall blinking process. This is because the value of η would shift from 1 to 2 as the blinking nature changes from NBC to Auger (trion). In contrast to the other PNCs, the PL decay of the OFF state of r-PNCs exhibits biexponential behaviour, despite the absence of an additional intermediate intensity state in the FLID map for the second-lifetime component (Figure 4.5C and Table 4.1). Assuming that the two lifetime components of the OFF state are related to different types of recombination, and both yield OFF states with similar PL intensities, one can separately calculate η for each of the two lifetime components. This would help one to decide the fundamental origins of these two components. The faster lifetime component (≈0.9 ns), which contributes more to the PL dynamics, results in η ~ 2.5, while the slower component (≈2.8 ns) leads to η ~ 0.81. Based on these values, one can attribute the faster component to Auger blinking and the slower component to NBC blinking. The deviations of η from its ideal values in both cases are attributed to the uncertainties associated with the derived intensities since both lifetime components have similar intensities, making it difficult to get their exact values. From the above study, we can conclude that NBC blinking is present across all morphologies at an extremely low pump fluence (<N> ~0.008). However, NBC recombination is not the sole mechanism of blinking in extra-faceted PNCs, where trion-induced Auger blinking also plays a role and contributes more as the number of facets increases.

Calculation of η from Equation 4.1

For c-PNC:

$$\frac{14}{1.8} \times \frac{102-8(\text{background})}{758-8(\text{background})} = 0.97$$

For d-PNC:

$$\frac{17.5}{2} \times \frac{118-8(\text{background})}{828-8(\text{background})} = 1.2$$

For r-PNC:

Using short lifetime component

$$\frac{20}{2.8} \times \frac{132-8(\text{background})}{1108-8(\text{background})} = 0.81$$

Using long lifetime component

$$\frac{20}{0.9} \times \frac{132-8(\text{background})}{1108-8(\text{background})} = 2.50$$

Table 4.1. Lifetime components (τ_i) along with their contributions (α_i) at different intensity levels of PL trajectories of c-, d-, and r-PNCs (Figure 4.3 A-C).

Sample	Region	τ_1 (α_1), ns	τ_2 (α_2), ns
c-PNC	ON	14	-
	OFF	1.8	-
d-PNC	ON	17.5	-
	OFF	2	-
r-PNC	ON	20	-
	OFF	2.8 (0.25)	0.9 (0.75)

4.5.2 Fluorescence Lifetime Intensity Distribution (FLID) of Different PNCs

Manifestations of Auger and NBC blinking in FLID map are different (Figure 4.5 (A-C) & (D-F)).[1, 51] The FLID trajectory of Auger blinking exhibits a curved feature, whereas the trajectory of NBC blinking in FLID follows a linear relationship.[1, 15] This is demonstrated by the excitation power-dependent FLID study of d-PNC, illustrating the coexistence of linear and nonlinear correlations between I_{PL} and τ_{PL} at low pump fluence (<N> ~ 0.008). However, at high fluence (<N> ~ 0.032), only the nonlinear correlation is observed (Figure 4.5D-F). This is attributed to the higher probability of photocharging at an elevated pump power, making Auger blinking more intense.[48] Next, we analyzed the trajectories of the FLID maps of all three particles to confirm further the higher probabilities of photocharging in extra-faceted PNCs (Figure 4.5). FLID trajectory of c-PNC follows a linear diagonal relationship, implying NBC blinking (Figure 4.5A). On the other hand, the FLID of d-PNC shows the coexistence of linear and nonlinear trajectories, suggesting NBC and trion recombination (Figure 4.5B).

Unfortunately, similar trajectories cannot be obtained for r-PNC due to the scarcity of states with higher emissivity; however, trion emission is distinguishable in FLID and denoted by a red triangle. This observation suggests that the blinking of the highest faceted r-PNC is mostly controlled by photocharging and discharging of the r-PNC. A similar manifestation of trion emission in FLID was earlier observed by Mulvaney and coworkers.[4] Our FLID analysis also indicates a higher probability of photocharging in extra-faceted PNCs, consistent with what was observed in the lifetime analysis of ON and OFF states, discussed before.

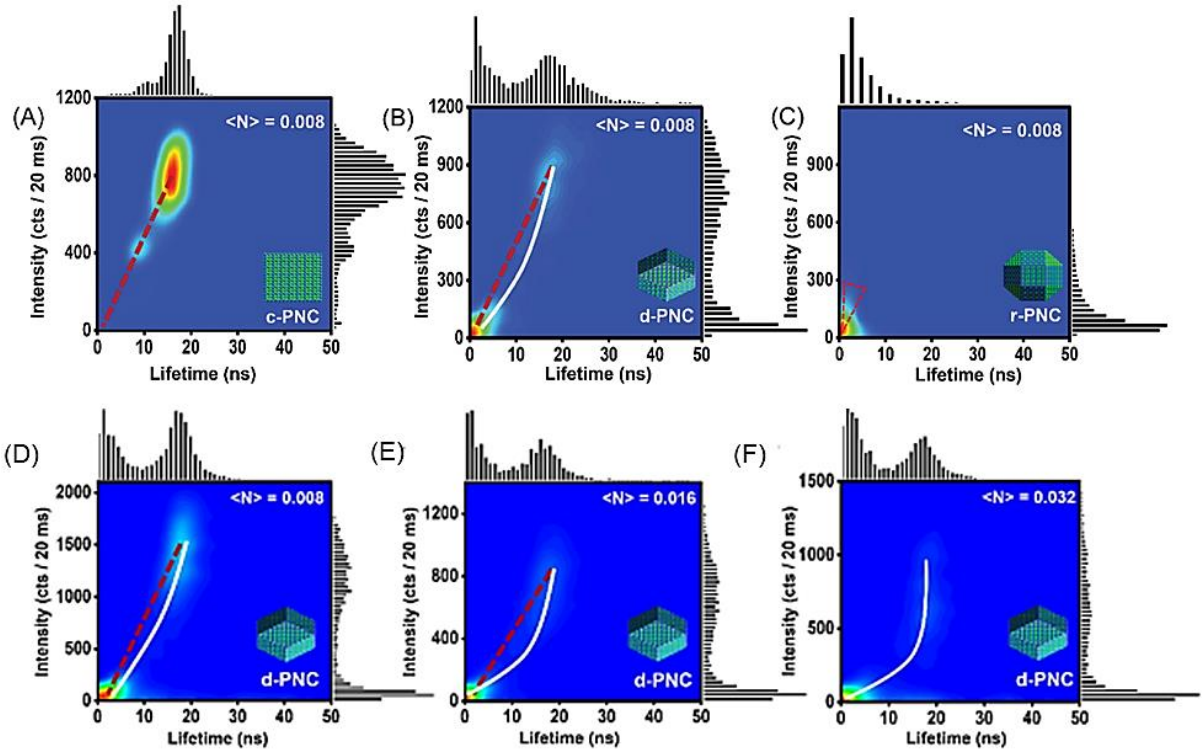

Figure 4.5. FLID maps were obtained by correlating intensity (along the vertical axis) and lifetime (along the horizontal axis) histograms of (A) c-PNC, (B) d-PNC, and (C) r-PNC. The probability of occurrence of a given state within FLID is depicted by a color change from red, indicating the highest probability, to blue, indicating the lowest probability. Linear correlation of intensity and lifetime in Figure A implying NBC recombination, whereas, linear and nonlinear correlations in Figure B are attributed to NBC and trion recombination. The red triangle in Figure C shows trion emission. (D-F) Pump-fluence dependent FLID maps of d-PNC. The occurrence probability of a given state within FLID is represented by a color change from red with the highest probability to blue with the lowest probability. Both NBC (linear trajectory) and Auger (nonlinear trajectory) blinking are present at low fluence, whereas Auger blinking predominates over NBC at high fluence.

Larger trion probability in extra-faceted PNCs is attributed to a number of factors: i) their larger surface area, which facilitates enhanced accessibility of surface trap states by charge carriers

across a reduced energetic barrier.[1] ii) In the single-dot blinking study, any external molecule in contact with PNC facets can participate in carrier trapping, which can easily occur in extra-faceted PNCs. An FCS investigation of the binding of PNC with a small organic molecule, discussed later, reveals higher binding constants for extra-faceted PNCs because of their larger surface area and unique orientations of facets. This suggests an increased risk of photocharging for extra-faceted PNCs in the solid-state blinking study. The geometrical calculation reveals that despite their similar edge lengths (a), the surface area (S) significantly increases from cube ($S = 6a^2$) to rhombic dodecahedron ($8a^2[\sqrt{2}]$) to rhombicuboctahedron ($S = 2a^2[9+\sqrt{3}]$).[36] It is noteworthy that previous studies with cube-shaped PNCs suggest that as the PNC surface area increases, the OFF fraction gradually decreases.[1, 34] This contradicts our observation, suggesting that particle morphology plays a bigger role than the surface area in determining the blinking behaviors of PNCs (Figure 4.5). Previously we have reported decelerated cooling of hot carriers in a twelve faceted d-PNC. This phenomenon was attributed to polaron-mediated cooling, where the polar nature of these new facets appeared to have a significant role in polaron formation.[37] Therefore, in our case, these new surface exposed polar facets might have facilitated the formation of charged exciton (that is also polar) in extra-faceted PNCs, leading to an enhanced OFF state fraction.

4.5.3 Power Law Kinetics of Faceted Nanocrystals

To validate further the involvement of trion recombination in the blinking of our extra faceted PNCs, we studied excitation power dependent ON-time statistics of one of our sample d-PNC, which shows intense photocharging at high pump intensity. We accomplished this by examining the pump-power dependent exponential cutoff time (τ_C) in the probability distribution plot of ON-time durations (t_{ON}), derived from the PL intensity trajectories recorded

at different powers. We observed that τ_C, which represents the truncation behaviour of the plot, becomes faster with increasing pump intensity. This pattern is indicative of the photocharging of PNC. (Figure 4.6A).[2, 5, 45, 52-55] ON-time probability (ρ_{ON}) in the log-log plot experiences a quick falloff at a longer delay, nicely fit to $t^{\beta}\exp(-t/\tau_C)$ with τ_C and β being ≈120 ms (≈10 ms) and −0.76 (−0.47) at a pump power of ≈2 W cm^{-2} (≈10 W cm^{-2}) (Figure 4.6A).[2] If the photo-charging limits ON durations, τ_C must depend on pump intensity. We indeed observed this behavior in our experiment with d-PNC, as depicted in Figure 4.6A. Further analysis of our power-dependent study reveals that the photoionization probability ($1/\tau_C$) exhibits a superlinear dependency on pump intensity (i.e., $1/\tau_C \propto I_p^{1.38}$), which is usually attributed to the nonlinear Auger process (Figure 4.6A).[2]

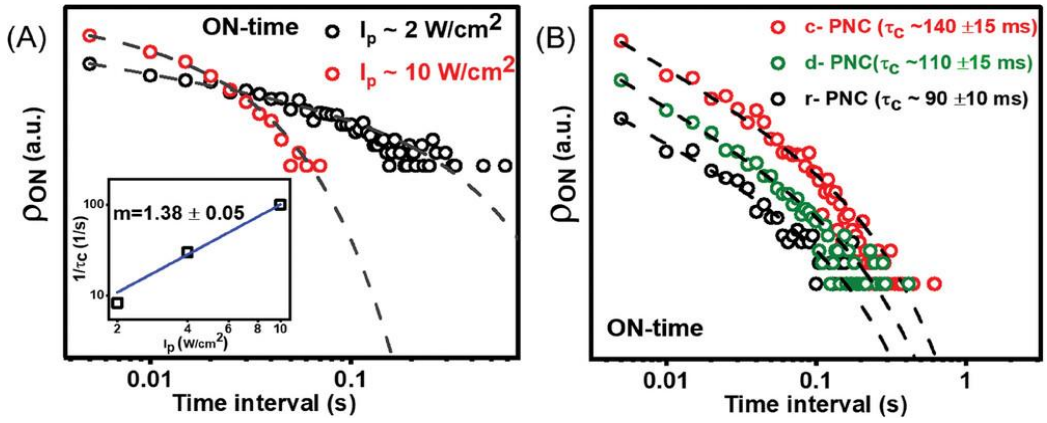

Figure 4.6. (A) Probability distribution of ON-times of d-PNC at different pump powers (I_P). Inset shows the photocharging probability ($1/\boldsymbol{\tau}_C$) as a function I_P. (B) Probability distribution of ON-times of all three PNCs under low excitation power [<N> ~0.008], along with a fit to $t^{\beta}\exp(-t/\tau_C)$ (dashed lines) yielding different τ_Cs based on the number of facets.

Next, we examined the probability distribution of ON-times (ρ_{ON}) for all three PNC samples at a constant pump intensity [<N>~ 0.008]. Our analysis demonstrates that the photoionization probability ($1/\tau_C$) increases with the number of facets in the PNCs (Figure 4.6B). This observation aligns well with our earlier analyses of FLIDs and PL trajectories. Statistical

analyses of ON-time probabilities with different durations were performed in SymPhoTime 64 software from PicoQuant.[5, 45, 52]

4.5.4 Understanding Solution Phase Blinking Behaviours via FCS study

We also conducted FCS measurements to understand the roles of the expanded surface area and distinctive orientations of the additional facets of extra-faceted PNCs in their solution phase blinking behaviours.[56-61] Although the FCS curve is based on measurements on a small ensemble of PNCs (at concentrations of about nM), it can offer insights into distributions of characteristic time constants and sample heterogeneities. The FCS analysis was conducted on PNCs, dispersing in an inert solvent, where the possibility of charge transfer to the external solvent is unlikely. Additionally, photocharging necessitates illuminating PNC for an extended duration, which is unfeasible in a solution phase study, as the PNCs are rapidly replaced (<1 ms) from the confocal volume through diffusion.[26] Another parameter that helps prevent the photocharging of PNCs in the FCS study is the use of a 60× objective, which results in a relatively less tightly focused laser beam than that of the 100× objective used in the single-dot study. All these considerations eliminate the possibility of trion states being formed in the solution phase study. The only remaining is type C blinking induced by NBC recombination, which ultimately resulted in identical FCS curves across the morphologies (Figure 4.7). PL blinking in the FCS study can arise from two separate phenomena: i) NBC-type recombination, which persists in the initial segment of the FCS curve, and ii) particle diffusion, which defines the later time evolution of the autocorrelation curve.[56, 62] Table 4.2 collected the FCS parameters of all three samples related to particle diffusion and intrinsic NBC blinking, showing identical values irrespective of their different number of facets. Furthermore, relatively less OFF-state fractions (T ~0.24–0.26) across the morphologies suggest PNCs mostly remain in the ON-state in the solution phase study. This observation indicates that all

three samples demonstrate identical blinking behaviors in the absence of trion states. This can be further rationalized by their similar PLQYs (≈78–82%), as determined from liquid-phase studies.

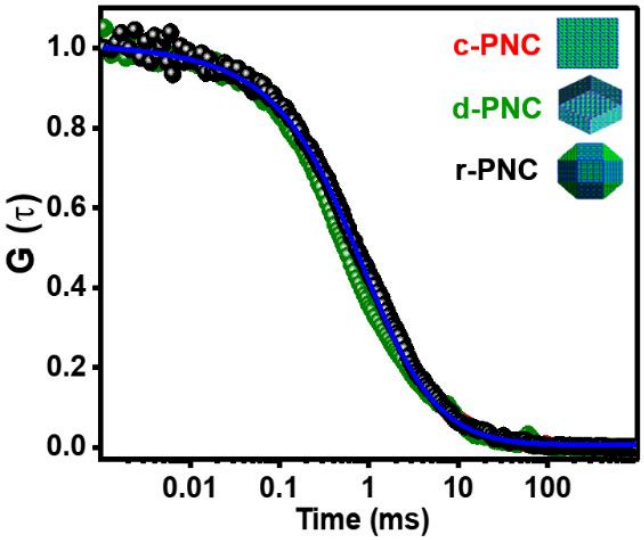

Figure 4.7. FCS curves of all three PNCs (symbols) dispersed in toluene. A ~422 nm pulse laser with a repetition rate of 5 MHz, and IP ~5 W/cm2 was used for the excitation.

Table 4.2. Best-fitted FCS Parameters for c-, d-, and r-PNCs Dispersed in Toluene

Sample	τ_T (μs)	T	β	τ_D (ms)
c-PNC	260	0.25	0.65	1
d-PNC	250	0.26	0.65	1.01
r-PNC	255	0.24	0.65	1

4.5.5 Solution-Phase Photoinduced Charge Transfer (PCT)

Next, we investigated solution-phase photoinduced charge transfer (PCT) from our PNCs with lowest and highest number of facets to an external molecule N-Methylaniline (NMA), anticipating a faster timescale for the highest-faceted PNC.[63-70] This expectation stemmed from the observed higher photocharging probabilities of extra-faceted PNCs in single-dot study. However, solvent diffusion often complicates the understanding of solution-phase bimolecular PCT, wherein the observed charge transfer timescales are predominantly diffusion-controlled.[66, 70, 71] Not an exception to our case, the Stern-Volmer plots reveal that observed PCT rates across the morphologies are diffusion-controlled ($k_{PCT} \sim 5 \times 10^9\ M^{-1}s^{-1}$), which restricted us from realizing the photocharging affinities of our PNC samples comparing their intrinsic PCT timescales. Nevertheless, Stern-Volmer analysis (Figure 4.8G) indicates that PCT rates are significantly high regardless of particle morphology. Being unsuccessful in deriving intrinsic timescales of PCT, we performed an FCS study of binding of the same two PNCs with NMA as an alternative. If greater binding affinities are observed for extra-faceted PNCs, they could potentially be correlated with their heightened propensity for photocharging in a single dot study.[72-74] PNC exhibiting stronger binding affinity with an electron or hole scavenger molecule in its adjacent environment would expedite the photocharging process, leading to a pronounced Auger blinking.[74]

Likewise, carrier trapping/de-trapping and PNCs diffusing across the excitation volume, causing PL-blinking in the FCS study of PNCs, binding/unbinding of a quencher molecule (NMA) with PNC can also cause similar blinking with a timescale that can essentially differ from the timescales of the other two processes [i.e., trapping/de-trapping (τ_T) and diffusion

(τ_D)]. FCS curves of PNCs in the presence of NMA fit nicely to the following equation, which includes one additional term to equation 4.2 (Figure 4.8).[38, 61]

$$G(\tau) = \frac{1}{<N>}\left(1 + A_R \exp\left[-\left(\frac{\tau}{\tau_R}\right)\right]\right)\left(1 + \left(\frac{T}{1-T}\right)\exp\left[-\left(\frac{\tau}{\tau_T}\right)^{\beta}\right]\right)\left(1 + \frac{\tau}{\tau_D}\right)^{-1}\left(1 + \frac{\tau}{\kappa^2\tau_D}\right)^{-1/2} \quad \ldots (4.2)$$

where τ_R is the characteristic timescale of the complexation reaction between PNC and NMA, and A_R is the reaction amplitude. Here, our primary focus would be on the binding reaction parameters (such as A_R, and τ_R), which can offer valuable insights into the binding affinities of PNCs (c-PNC and r-PNC) with quenchers. The equilibrium constant (K) of the PNC-NMA complex was derived from the relationship $A_R = K[NMA]$, assuming that the PLQY of the PNC-NMA complex is ≈0, and the binding reaction adheres to pseudo-first-order kinetics.[38, 61, 72]

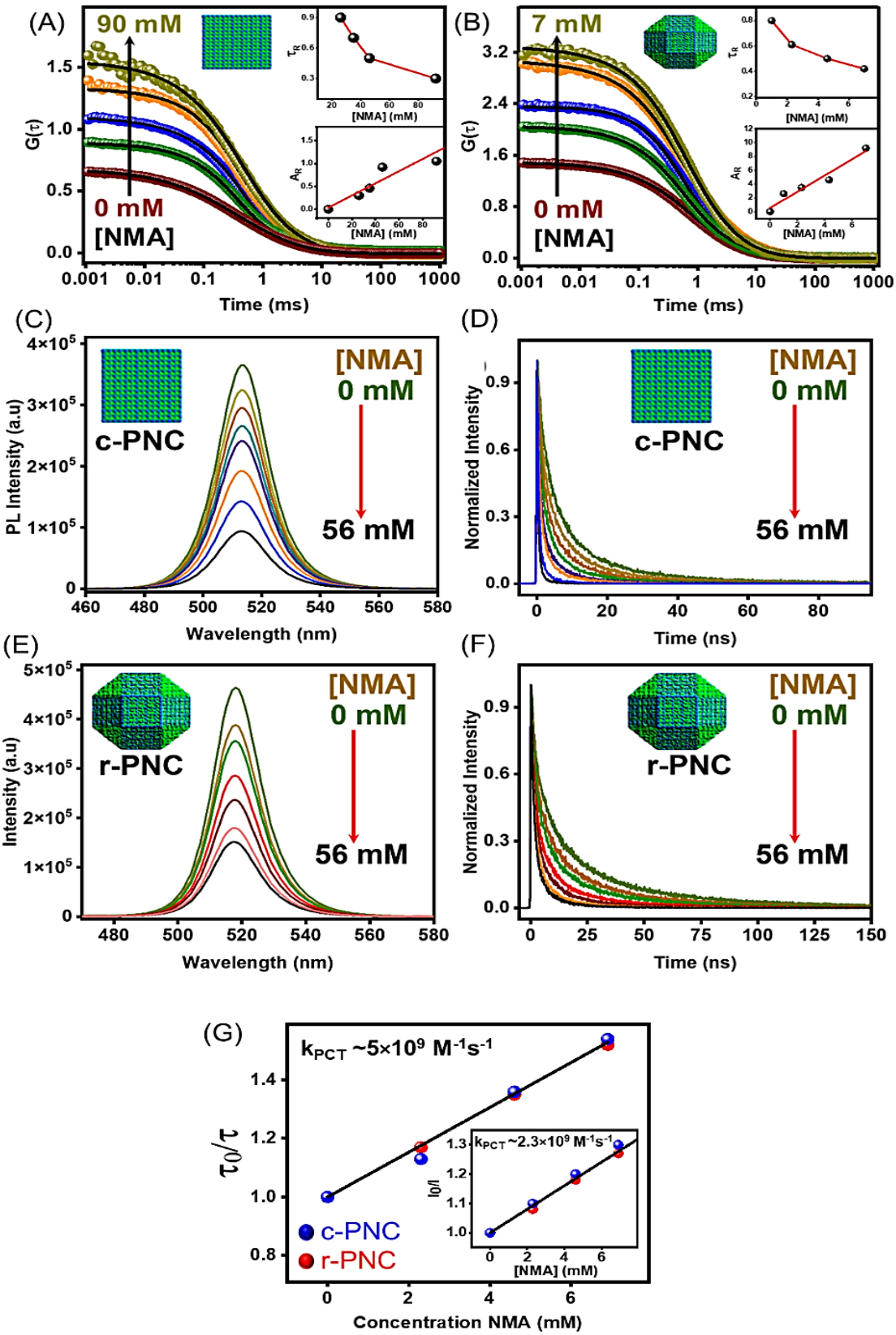
(A)
90 mM
0 mM
[NMA]
G(τ)
Time (ms)
[NMA] (mM)
(B)
7 mM
0 mM
[NMA]
G(τ)
Time (ms)
[NMA] (mM)
(C)
c-PNC
[NMA]
0 mM
56 mM
PL Intensity (a.u)
Wavelength (nm)
(D)
c-PNC
[NMA]
0 mM
56 mM
Normalized Intensity
Time (ns)
(E)
r-PNC
[NMA]
0 mM
56 mM
Intensity (a.u)
Wavelength (nm)
(F)
r-PNC
[NMA]
0 mM
56 mM
Normalized Intensity
Time (ns)
(G)
k_{PCT} ~5×10⁹ M⁻¹s⁻¹
k_{PCT} ~2.3×10⁹ M⁻¹s⁻¹
c-PNC
r-PNC
τ0/τ
I0/I
[NMA] (mM)
Concentration NMA (mM)

Figure 4.8. (A, B) FCS curves of c-PNCs (A) and r-PNCs (B) dispersed in toluene at different NMA concentrations. A much steeper slope of "A_R versus [NMA]" plot (inset) of Figure B than that of Figure A, suggests a greater binding affinity of extra-faceted r-PNCs with NMA. A ~422 nm pulse laser with a repetition rate of 5 MHz, and I_P ~5 W cm^{-2} was used for the excitation. Quenching of PL intensity and lifetime of PNCs (C, D for c-PNC and E, F for r-PNC) dispersed in toluene by NMA. Lifetimes were recorded at emission peak positions. The samples were excited by ~405 nm diode laser (IRF ~ 90 ps). (G) Lifetime and steady-state (inset) Stern-Volmer plots of quenching of PL lifetime and intensity of cPNC (blue balls) and r-PNC (red balls) by NMA. Apparent quenching rates (kPCT) are found to be similar for both the samples and reach close to diffusion-controlled rate.

The best-fitted FCS parameters, collected in Table 4.3, demonstrate a significantly higher binding affinity of twenty-six faceted r-PNC (K~ 300 M^{-1}) than the one (K~ 100 M^{-1}) observed for six faceted c-PNC. FCS study suggests that the binding affinity of PNC with an adjacent molecule increases with an increasing number of facets. This observation suggests that if the photocharging of PNCs during single-dot studies occurs due to interactions with molecules in their immediate environment, there is a higher likelihood of this phenomenon happening for extra-faceted PNCs. Thermodynamic consideration of HOMO-LUMO of NMA vis-à-vis VB-CB of PNC suggests photoinduced electron transfer (PET) from HOMO of NMA to the VB of an optically pumped PNC causing the quenching. [73-75]

Table 4.3. Best-fitted FCS Parameters Related to PNC-NMA Complexation Reaction.

Sample	[NMA] (mM)	A_R	K(M^{-1})	τ_R (µs)
c-PNC/r-PNC	0/0	-	100/300	-
	26/1	2.6/0.3		0.9/0.8
	35/2.3	3.5/0.46		0.7/0.61
	46/4.6	4.6/0.92		0.5/0.5
	90/7	9.2/1.05		0.4/0.42

4.6 Conclusion

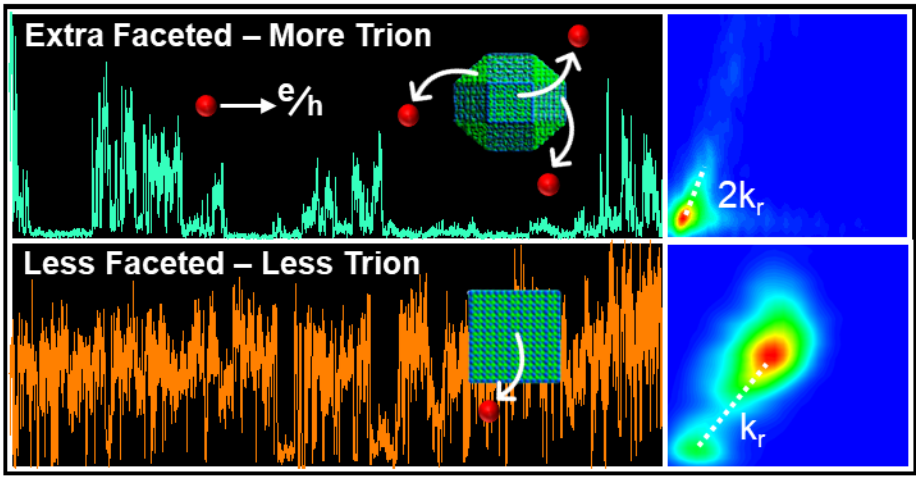

We have comprehensively demonstrated how surface engineering can produce PNCs with distinct blinking behaviors based on their diverse probabilities of photocharging. While the blinking behaviors of our PNCs remain consistent across the morphologies in the solution phase study, they exhibit significant differences in the solid-state single-dot study. The extra-faceted PNCs display larger photocharging probabilities in the solid state, resulting in an enhanced OFF-state population. This morphology-dependent blinking behavior can be attributed to several characteristics of extra faceted PNCs that may facilitate their photocharging in single-dot study, including i) the polar nature of their facets, ii) increased

binding affinity with scavenger molecules in the immediate environment, and iii) the larger surface area. However, the influence of these factors is largely suppressed in a solution phase study, causing lesser OFF state fractions across the morphologies. In the solution phase study, as photocharging of PNCs is excluded, PNCs exhibit blinkings through NBC recombinations. Although our PNCs are highly defect tolerant, substantiated by their high PLQYs, they are not completely devoid of defect states. In the FCS study, the involvement of shallow trap states near the band edge contributes to the blinking process. However, in the single-dot blinking study, Auger blinking prevails over NBC, and unlike NBC blinking, Auger blinking is largely influenced by particle morphology. This provides an opportunity to modulate the blinking characteristics of PNCs through surface engineering. Thus, this work demonstrates the massive potential of facet engineering in integrating extra-faceted PNCs in next-generation display applications.

4.7 References

[1] T. Kim, S. I. Jung, S. Ham, H. Chung, D. Kim, *Small* **2019**, *15*, 1900355.

[2] Y. S. Park, S. Guo, N. S. Makarov, V. I. Klimov, *ACS Nano* **2015**, *9*, 10386−10393.

[3] Y. S. Park, W. K. Bae, J. M. Pietryga, V. I. Klimov, *ACS Nano* **2014**, *8*, 7288−7296.

[4] G. Yuan, D. E. Gómez, N. Kirkwood, K. Boldt, P. Mulvaney, *ACS Nano* **2018**, *12*, 3397−3405.

[5] J. J. Peterson, D. J. Nesbitt, *Nano Lett.* **2009**, *9*, 338−345.

[6] Q. Li, Y. Yang, W. Que, T. Lian, *Nano Lett.* **2019**, *19*, 5620−5627.

[7] J. Aneesh, A. Swarnkar, V. K. Ravi, R. Sharma, A. Nag, K. V. Adarsh, *J. Phys. Chem. C* **2017**, *121*, 4734−4739.

[8] G. E. Eperon, E. Jedlicka, D. S. Ginger, *J. Phys. Chem. Lett.* **2018**, *9*, 104−109.

[9] W. K. Bae, Y. S. Park, J. Lim, D. Lee, L. A. Padilha, H. McDaniel, I. Robel, C. Lee, J. M. Pietryga, V. I. Klimov, *Nat. Commun.* **2013**, *4*, 2661.

[10] Y. H. Won, O. Cho, T. Kim, D. Y. Chung, T. Kim, H. Chung, H. Jang, J. Lee, D. Kim, E. Jang, *Nature* **2019**, *575*, 634−638.

[11] X. Fan, Z. Mu, Z. Chen, Y. Zhan, F. Meng, Y. Li, G. Xing, W. Y Wong, *Chem. Eng. J.* **2023**, *461*, No.142027.

[12] T. Kim, Y. H. Won, E. Jang, D. Kim, *Nano Lett.* **2021**, *21*, 2111−2116.

[13] F. Schindler, J. M. Lupton, J. Mueller, J. Feldmann, U. Scherf, *Nat. Mater.* 2006, *5*,141–146.

[14] D. K. Sharma, S. Hirata, V. Biju, M. Vacha, *ACS Nano* 2019, *13*, 624–632.

[15] C. Melnychuk, P. Guyot-Sionnest, *Chem. Rev.* **2021**, *121*, 2325–2372.

[16] J. Park, Y. H. Won, T. Kim, E. Jang, D. Kim, *Small* **2020**, *16*, 2003542.

[17] K. Wu, J. Lim, V. I. Klimov, *ACS Nano* **2017**, *11*, 8437−8447.

[18] X. Hou, J. Kang, H. Qin, X. Chen, J. Ma, J. Zhou, L. Chen, L. Wang, L. W. Wang, X. Peng, *Nat. Commun.* **2019**, *10*, No.1750.

[19] V. I. Klimov, D. W. McBranch, *Phys. Rev. B* **1997**, *55*, 13173−13179.

[20] T. D. Krauss, L. E. Brus, *Phys. Rev. Lett.* **1999**, *83*, 4840–4843.

[21] S. Li, M. L. Steigerwald, L. E. Brus, *ACS Nano* **2009**, *3*, 1267–1273.

[22] J. Zhao, G. Nair, B. R. Fisher, M. G. Bawendi, *Phys. Rev. Lett.* **2010**, *104*, 157403.

[23] M. Zavelani-Rossi, M. G. Lupo, F. Tassone, L. Manna, G. Lanzani, *Nano Lett.* **2010**, *10*, 3142–3150.

[24] D. Oron, M. Kazes, U. Banin, *Phys. Rev. B* **2007**, *75*, 035330.

[25] F. García-Santamaría, Y. Chen, J. Vela, R. D. Schaller, J. A. Hollingsworth, V. I. Klimov, *Nano Lett.* **2009**, *9*, 3482–3488.

[26] N. S. Makarov, S. Guo, O. Isaienko, W. Liu, I. Robel, V. I. Klimov, *Nano Lett.* **2016**, *16*, 2349−2362.

[27] Y. S. Park, J. Lim, N. S. Makarov, V. I. Klimov, *Nano Lett.* **2017**, *17*, 5607−5613.

[28] Y. S. Park, W. K. Bae, L. A. Padilha, J. M. Pietryga, V. I. Klimov, *Nano Lett.* **2014**, *14*, 396−402.

[29] Y. Lee, D. Y. Jo, T. Kim, J. H. Jo, J. Park, H. Yang, D. Kim, *ACS Appl. Mater. Interfaces* **2022**, *14*, 12479−12487.

[30] X. Hou, H. Qin, X. Peng, *Nano Lett.* **2021**, *21*, 3871–3878.

[31] A. L. Efros, D. J. Nesbitt, *Nat. Nanotechnol.* **2016**, *11*, 661−671.

[32] I. Hadar, J. P. Philbin, Y. E. Panfil, S. Neyshtadt, I. Lieberman, H. Eshet, S. Lazar, E. Rabani, U. Banin, *Nano Lett.* **2017**, *17*, 2524−2531.

[33] O. Chen, J. Zhao, V. P. Chauhan, J. Cui, C. Wong, D. K. Harris, H. Wei, H. S. Han, D. Fukumura, R. K. Jain, M. G. Bawendi, *Nat. Mater.* **2013**, *12*, 445−451.

[34] S. Paul, G. Kishore, A. Samanta, *J. Phys. Chem. C* **2023**, *127*, 10207–10214.

[35] S. Bera, R. K. Behera, N. Pradhan, *J. Am. Chem. Soc.* **2020**, *142*, 20865−20874.

[36] S. K. Bera, S. Bera, M. Shrivastava, N. Pradhan, K. V. Adarsh, *Nano Lett.* **2022**, *22*, 8908−8916.

[37] K. J. Babu, G. Kaur, A. Shukla, R. Saha, A. Kaur, M. Sachdeva, D. K. Yadav, H. N. Ghosh, *ACS Photonics* **2022**, *9*, 969−978.

[38] D. Acharjee, A. Das, M. K. Panda, M. Barai, S. Ghosh, *Nano Lett.* **2023**, *23*, 1946-1953.

[39] A. Das, D. Acharjee, M. K. Panda, A. B. Mahato, S. Ghosh, *J. Phys. Chem. Lett*. **2023**, *14*, 3953-3960.

[40] S. Ghosh, B. Pradhan, W. Lin, Y. Zhang, L. Leoncino, P. Chabera, K. Zheng, E. Solano, J. Hofkens, T. Pullerits, *J. Phys. Chem. Lett.* **2023**, *14*, 1066−1072.

[41] S. K. Mahankudo, A. Das, K. Mishra, M. Barai, P. Mal, S. Ghosh, *ACS Appl. Nano Mater.* **2022**, *5*, 4360−4366.

[42] A. Manna, T. K. Dinda, S. Ghosh, P. Mal, *Chem. Mater.* **2023**, *35*, 628−637.

[43] K. Mishra, D. Acharjee, A. Das, S. Ghosh, *J. Phys. Chem. B* **2021**, *125*, 11017−11025.

[44] U. S. Sayyad, S. Burai, H. Bhatt, H. N. Ghosh, S. Mondal, *J. Phys. Chem. Lett.* **2023**, *14*, 5397–5402.

[45] A. A. Cordones, S. R. Leone, *Chem. Soc. Rev.* **2013**, *42*, 3209−3221.

[46] A. Garai, E. K. Vishnu, S. Banerjee, A. A. K. Nair, S. Bera, K. G. Thomas, N. Pradhan, *J. Am. Chem. Soc.* **2023**, *145*, 13989–13999.

[47] A. Dey, J. Ye, A. De, E. Debroye, S. K. Ha, E. Bladt, A. S. Kshirsagar, Z. Wang, J. Yin, Y. Wang, L. N. Quan, F. Yan, M. Gao, X. Li, J. Shamsi, T. Debnath, M. Cao, M. A. Scheel, S. Kumar, J. A. Steele, M. Gerhard, L. Chouhan, K. Xu, X.-g. Wu, Y. Li, Y. Zhang, A. Dutta,C. Han, I. Vincon, A. L. Rogach, et al., *ACS Nano* **2021**, *15*, 10775.

[48] B. Li, H. Huang, G. Zhang, C. Yang, W. Guo, R. Chen, C. Qin, Y. Gao, V. P. Biju, A. L. Rogach, L. Xiao, S. Jia, *J. Phys. Chem. Lett.* **2018**, *9*, 6934−6940.

[49] T. Ahmed, S. Seth, A. Samanta, *ACS Nano* **2019**, *13*, 13537−13544.

[50] C. Yang, Y. Li, X. Hou, M. Zhang, G. Zhang, B. Li, W. Guo, X. Han, X. Bai, J. Li, R. Chen, C. Qin, J. Hu, L. Xiao, S. Jia, *Small* **2023**, 2309134.

[51] C. T. Trinh, D. N. Minh, K. J. Ahn, Y. Kang, K. G. Lee, *Sci. Rep.* **2020**, *10*, 2172.

[52] R. Verberk, A. M. V. Oijen, M. Orrit, *Phys. Rev. B* **2002**, *66*, 233202.

[53] C. Galland, Y. Ghosh, A. Steinbruck, M. Sykora, J. A. Hollingsworth, V. I. Klimov, H. Htoon, *Nature* **2011**, *479*, 203–207.

[54] M. Kuno, D. P. Fromm, S. T. Johnson, A. Gallagher, D. J. Nesbitt, *Phys. Rev. B* **2003**, *67*, 125304.

[55] K. T. Shimizu, R. G. Neuhauser, C. A. Leatherdale, S. A. Empedocles, W. K. Woo, M. G. Bawendi, *Phys. Rev. B* **2001**, *63*, 205316.

[56] A. Das, K. Mishra, S. Ghosh, *J. Phys. Chem. Lett.* **2021**, *12*, 5413−5422.

[57] K. Mishra, A. Das, S. Ghosh, *J. Phys. Chem. C* **2020**, *124*, 24115−24125.

[58] S. Kundu, S. Das, A. Patra, *Chem. Commun.* **2023**, *59*, 8017–8031.

[59] S. Ghosh, U. Mandal, A. Adhikari, K. Bhattacharyya, *Chem. Asian J.* **2009**, *4*, 948−954.

[60] E. Haustein, P. Schwille, *Annu. Rev. Biophys. Biomol. Struct.* **2007**, *36*, 151−169.

[61] D. Acharjee, A. B. Mahato, A. Das, S. Ghosh, *J. Phys. Chem. C*. **2023**, *127*, 19643–19650.

[62] S. Seth, N. Mondal, S. Patra, A. Samanta, *J. Phys. Chem. Lett.* **2016**, *7*, 266-271.

[63] K. Mishra, D. Acharjee, A. Das, S. Ghosh, *J. Phys. Chem. Lett.* **2022**, *13*, 606−613.

[64] K. Bharadwaj, H. Choudhary, S. Hazra, S. Ghosh, *ChemPhysChem* 2020, *21*, 415– 422.

[65] K. Bharadwaj, H. Choudhary, S. Hazra, S. Ghosh, *Chem. Asian J.* **2019**, *14*, 4207−4216.

[66] S. Koley, M. R. Panda, S. Ghosh, *J. Phys. Chem. C* **2016**, *120*, 13456−13465.

[67] S. K. Mondal, S. Ghosh, K. Sahu, P. Sen, K. Bhattacharyya, *Proc. - Indian Acad. Sci., Chem. Sci.* **2007**, *119*, 71−76.

[68] U. Mandal, S. Ghosh, S. Dey, A. Adhikari, K. Bhattacharyya, *J. Chem. Phys.* **2008**, *128*, 164505−164510.

[69] S. Koley, S. Ghosh, *Phys. Chem. Chem. Phys.* **2016**, *18*, 24830−24834.

[70] M. Kumbhakar, A. Manna, M. Sayed, A. Kumar, H. Pal, *J. Phys. Chem. B* **2014**, *118*, 10704−10715.

[71] M. Koch, A. Rosspeintner, G. Angulo, E. Vauthey, *J. Am. Chem. Soc.* **2012**, *134*, 3729–3736.

[72] W. Al-Soufi, B. Reija, M. Novo, S. Felekyan, R. Kühnemuth, C. A. M. Seidel, *J. Am. Chem. Soc.* **2005**, *127*, 8775−8784.

[73] A. Bhowmik, H. Kaur, S. Koley, S. Jana, S. Ghosh, *J. Phys. Chem. C* **2016**, *120*, 5308−5314.

[74] V. K. Ravi, G. B. Markad, A. Nag, *ACS Energy Lett.* **2016**, *1*, 665– 671.

[75] M. Jonsson, D. D. M. Wayner, J. Lusztyk, *J. Phys. Chem.* **1996**, *100*, 17539−17543.

CHAPTER 5

Hot Carrier Trapping in Light-Soaked Mixed Phase $CsPbI_3$ Perovskite Nanocrystals

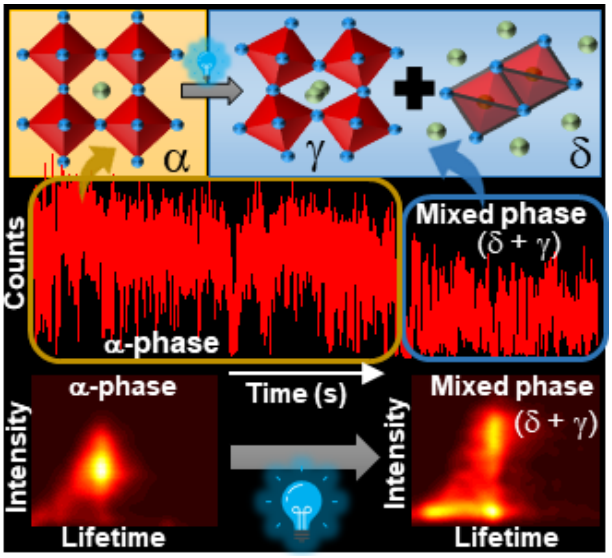

5.1 Abstract

Red-emitting $CsPbI_3$ perovskite nanocrystals (r-PNCs) are considered promising for device applications due to their low bandgap. However, their practical use is hindered by significant photoluminescence (PL) intermittency and light-induced phase transitions. Specifically, the stable and bright α-phase of r-PNCs quickly converts into weakly emissive mixed-phase (δ and γ) within hours under UV irradiation. In the absence of light, r-PNCs synthesized using an advanced method have been shown to maintain their α-phase and brightness for over 20 days. This study explores the PL intermittency of r-PNCs to better understand the carrier dynamics and the nature of trap states in both the α-phase and mixed phases. These results indicate that r-PNCs, despite their apparent phase stability, undergo rapid phase deformation during a blinking experiment, as evidenced by the decrease in the average ON state intensity of their PL trajectories and the change in XRD patterns. Fluorescence-lifetime-intensity-distribution (FLID) mapping from blinking studies, combined with fluorescence lifetime correlation spectroscopy (FLCS), reveals that freshly prepared α-phase r-PNCs exhibit blinking behaviour primarily governed by short-lived trap states near the band edge. These dynamic trap states function as multiple non-radiative recombination centers (MRCs). In contrast, light-soaked mixed-phase r-PNCs develop long-lived deep trap states, leading to dispersive blinking predominantly caused by hot carrier (HC) recombination.

5.2 Introduction

Red-emitting r-PNCs are the most promising among all members of the lead halide perovskite family with common formula $CsPbX_3$ (X=Cl/Br/I or their mixture) due to their low band gap, which is a key requisite for light harvesting applications. [1-10] However, their integration into

real applications has been largely unsuccessful due to their poor phase stability. Bright α-phase r-PNCs, in a few hours under ambient conditions, experience phase change to a mixed phase (δ and γ) characterized by low PLQY.[10-14] Efforts have been made to obtain phase-stable r-PNCs utilizing various strategies, where the successful implementations have rendered apparently stable r-PNCs characterized by blinking-free emissions in single particle study and unchanged PLQY over up to a few weeks of storage.[14-17] Suppressed PL blinking from a single nanocrystal requires passivation of defect states, which is essential for a diverse range of applications, from LEDs and lasers to quantum communications.[14-29] While the PL blinking and the associated change in lifetime are mainly governed by the various recombination mechanisms involved, however, they all share the commonality of being connected to trap states.[22,29] The primary advantage of single-particle PL studies is their capability to differentiate various carrier recombination pathways in a nanocrystal. This is achieved by correlating PL intensity with lifetime or by examining the fine-structure splitting of exciton, which disappears upon photo charging of nanocrystal, affirming the involvement of trions in blinking. [22-23, 26-28]

In recent literature, two recombination models are widely cited to explain the blinking of semiconductor nanocrystals: (i) the multiple recombination centers (MRC) model, invoked on charge neutral defect tolerant nanocrystals, and (ii) trion recombination, typically observed in charged nanocrystals. [22,26,27-33] The MRC model involves several short-lived trap states near the band edge, acting as recombination centers. The activation and deactivation of these trap states over time cause PL blinking.[34-36] This type of blinking, caused by nonradiative band edge charge (NBC) recombination, occurs when trapped carriers recombine nonradiatively before a second exciton is formed (Scheme 5.1).[22,32] NBC blinking is characterized by a constant radiative recombination rate (k_r) across varying intensity levels, while the nonradiative

rate (k_{nr}) fluctuates.[22,26,28-33] In contrast, recombination in charged nanocrystals involves a radiative recombination rate ($2k_r$), which is twice as fast as that (k_r) of neutral nanocrystals. When a charge carrier is trapped in a deep trap state for an extended period, the nanocrystal becomes photocharged, and subsequent excitation to the charged nanocrystal produces a trion. Trion recombination can proceed either radiatively, with a rate constant of $2k_r$, or nonradiatively, by transferring the recombination energy to the third carrier (Scheme 4.1).[22] PL blinking resulting from trion recombination, whether radiative or nonradiative, is termed AC blinking.[32] Nearly all types of nanocrystals exhibit NBC blinking due to the unavoidable occurrence of shallow trap states, even in highly defect-tolerant nanocrystals with near-unity PLQYs. Conversely, AC blinking is mainly observed in nanocrystals with mid-gap deep trap states and/or under high pump intensity, as both factors favor photocharging. In addition to AC and NBC recombination, PL blinking can also arise from the interception of hot carriers (HCs) by deep trap states, and this type of blinking is referred to as HC blinking (Scheme 4.1).[31,37-38] Upon photoexcitation with excess energy, nanocrystals generate hot carriers above the band edge, which are subsequently trapped in intraband defect states. These trapped hot carriers are deactivated following an efficient nonradiative pathway, resulting in a decrease in emission intensity without affecting the nanocrystal's excited state lifetime.[31,37-38]

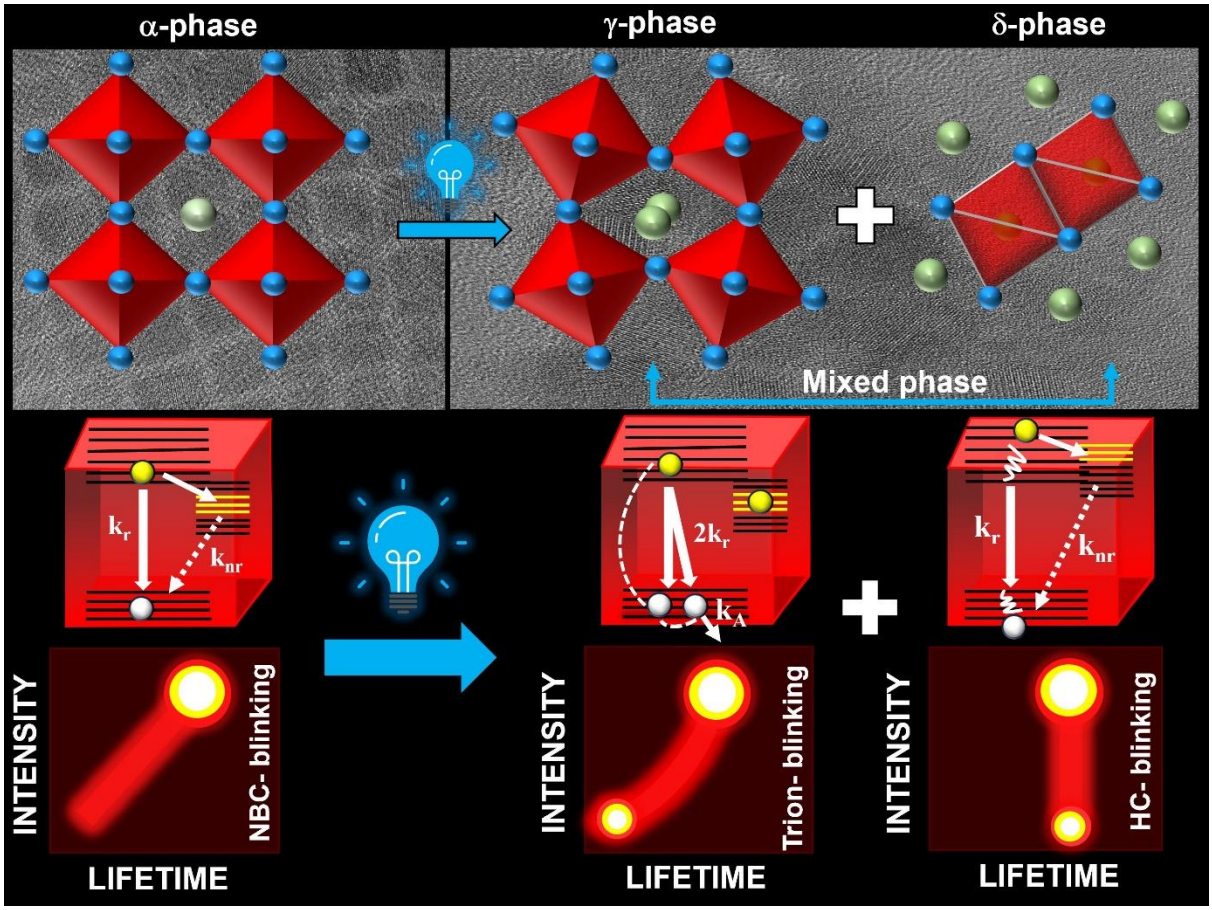

Scheme 5.1. Schematic representations of (i) the different phases of r-PNCs (top panel), (ii) the mechanism of carrier trapping and recombination (middle panel), and their manifestations in FLID (bottom panel).

5.3 Synthetic Procedure of $CsPbI_3$ nanocrystals

A reported protocol with minor modifications, as follows, was adopted for the synthesis. [3,39]

5.3.1 Cs-oleate preparation

Around 22 mg (0.067 mmol) of Cs_2CO_3, 115 µL of oleic acid (OA), and 1 mL of octadecene (ODE) were thoroughly mixed in a 25 mL two-neck round-bottom flask. The mixture was heated to approximately 120 °C for 1 hour under a nitrogen atmosphere to ensure complete dissolution and removal of any residual moisture and oxygen. Following this, the temperature was raised to 150 °C and maintained for 20 minutes to complete the reaction. The resulting

product was then collected while still hot using an air-tight glass syringe and stored in a deaerated vial for the use in the next step.

5.3.2 Hot-injection synthesis of colloidal nanocrystals

In a 25 mL three-neck round-bottom flask, about 72 mg of $Pb(OAc)_2$ $3H_2O$ (0.188 mmol), 1 mL of oleic acid (OA), 1 mL of oleylamine (OAm), 5 mL of octadecene (ODE), and approximately 214.5 mg of DIDMH (0.564 mmol) were mixed. The resultant mixture was then heated to around 120 °C under a nitrogen atmosphere until a clear, deep red transparent solution formed. The temperature was subsequently increased to about 210 °C, and 0.5 mL of pre-heated Cs-oleate (over 100 °C) prepared in the previous step, was swiftly injected into the reaction mixture. The reaction was immediately quenched by placing the flask in an ice bath within 5 seconds of the hot injection. The bright red crude product was then centrifuged at 4400 rpm for 10 minutes, after which the precipitate, containing larger particles and impurities, was discarded. About 15 mL of methyl acetate was added to the remaining supernatant, followed by another centrifugation at 4400 rpm to isolate the desired nanocrystals. The supernatant was discarded, and the precipitate was redispersed in hexane. This bright red colloidal dispersion was stored in a deaerated vial at a low temperature (around 2-8 °C) for optical studies.

5.4 Sample Characterisations

Our freshly prepared r-PNCs, exhibiting a PLQY of ~70%, have an average edge length of ~9 nm (Figure 5.1A). Notably, the PLQY of these phase-stable nanocrystals remained unchanged for at least 20 days when stored at 4°C in a sealed container (Figure 5.1B). XRD study of the r-PNCs before and after UV irradiation (Figure 5.1C) revealed a phase transformation from the bright α-phase to the weakly intense mixed phase. The latter consists of a mixture of δ and γ phases (Figure 5.1 D).[12] The first excitonic and emission peaks in both cases were measured to be at ~630 nm and ~656 nm, respectively (Figure 5.1 E, F). Upon UV exposure, the PLQY

of freshly prepared r-PNCs decreases substantially, from ~70% (unexposed) to ~20% after 14 hours of UV irradiation, accompanied by significant changes in PL lifetime (Figures 5.1 B, E, G). Figure 5.1H shows the confocal image of extremely diluted single nanocrystals in a clean cover slip with PMMA matrix coating. To confirm we are looking at the single quantum dot during single particle analysis, we did photon antibunching study (Figure 5.1I).

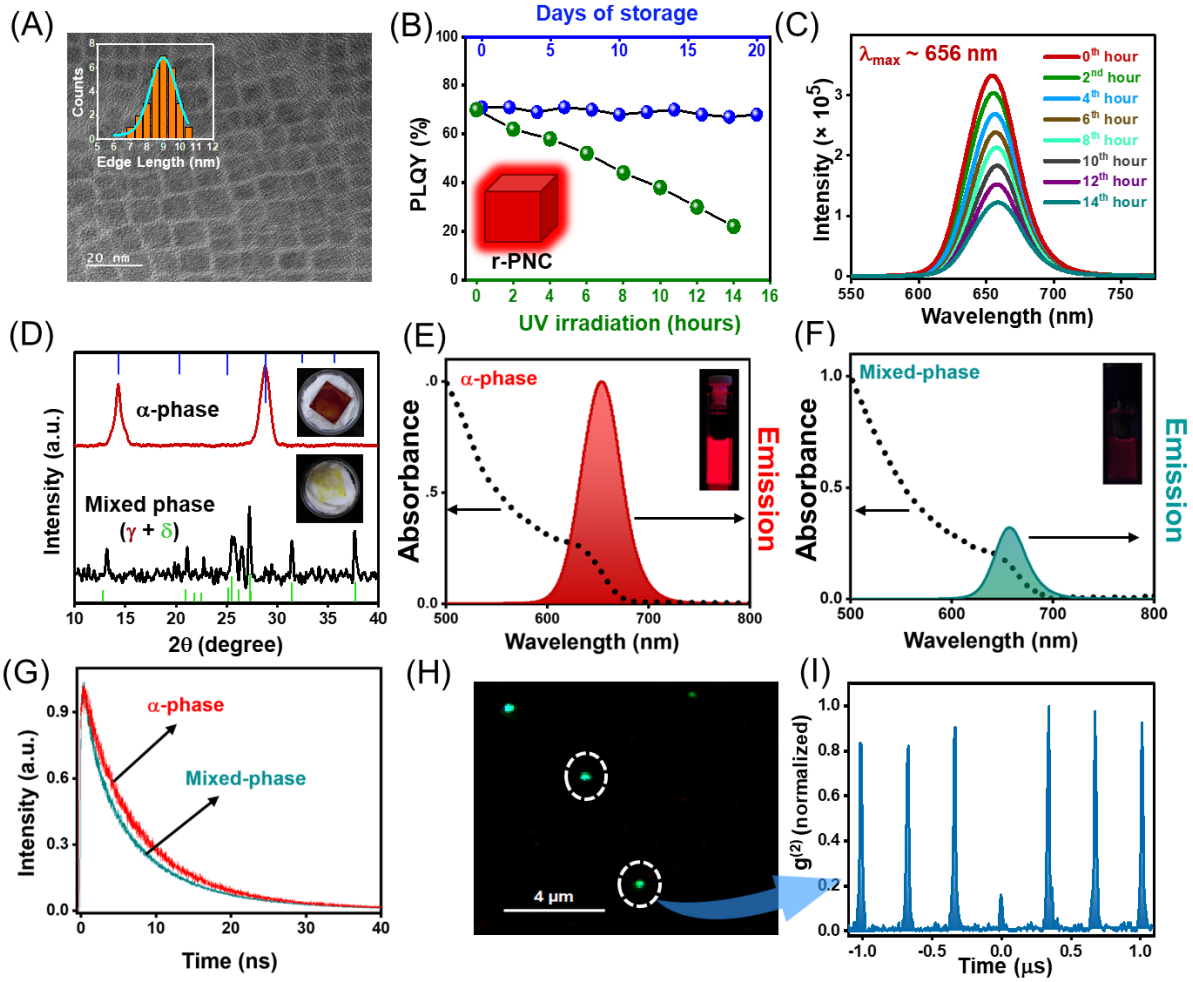

Figure 5.1. (A) TEM image and corresponding size distribution of synthesized CsPbI3 NCs. (B) PLQY of r-PNCs (along the y-axis) as a function of (i) days of storage, depicted in the blue curve, and (ii) UV illumination time shown in the green curve. & (C) PL spectra of r-PNCs (in toluene), recorded after UV irradiation for different time intervals. A freshly prepared r-PNC sample loaded in a cuvette was placed in front of the UV lamp (~350 nm) for phase transformation. (D) XRD spectra of freshly prepared r-PNCs (brown line), resembling the α-

phase, and after UV irradiation for 14 hours (black line), matching the reported patterns of the δ and γ phases. Blue, green, and red lines correspond to the reference diffraction peaks for α, δ, and γ phases. [1,12,14,17,47] (E) Absorbance and emission spectra of α-phase and converted mixed-phase respectively after UV illumination. (G) PL Lifetime change during phase change. (H) Confocal scanning image of r-PNCs embedded in PMMA matrix in false color. The inset shows single-particle PL spectrum with 3 seconds accumulation time, not specific to ON or OFF state. (I) The second-order cross-correlation function [$g^2(\tau)$] from a confocal spot under ~3 MHz pulsed laser excitation shows sub-Poissonian statistics, confirming single-photon emission.

5.5 Results and Discussion

5.5.1 Single particle Measurements (PL Blinking and Single Particle Emission Spectra)

In our single-particle blinking study, individual r-PNCs were excited using a 375 nm pulsed laser at a repetition rate of ~5 MHz, while the antibunching experiment was conducted at a repetition rate of ~3 MHz. PL blinking traces were recorded over approximately 7-8 minutes, utilizing time-tagged time-correlated single-photon counting mode to correlate PL blinking with associated lifetime change. [22,26,31-32] To minimize bias from the unintentional selection of outliers, we collected PL trajectories from 120 nanocrystals. For this study, the nanocrystals were excited with low power density (~2 W/cm^2), resulting in an average of <0.01 excitons per nanocrystal per pulse (<N>), minimizing the likelihood of bi-excitation or any higher order recombination.[23,49–51] Of the 120 analyzed nanocrystals, approximately 25-30 exhibit pronounced flickering from the onset of their PL trajectories, and in most cases, these flickering

nanocrystals eventually transitioned to completely dark particles under prolonged photoexcitation .

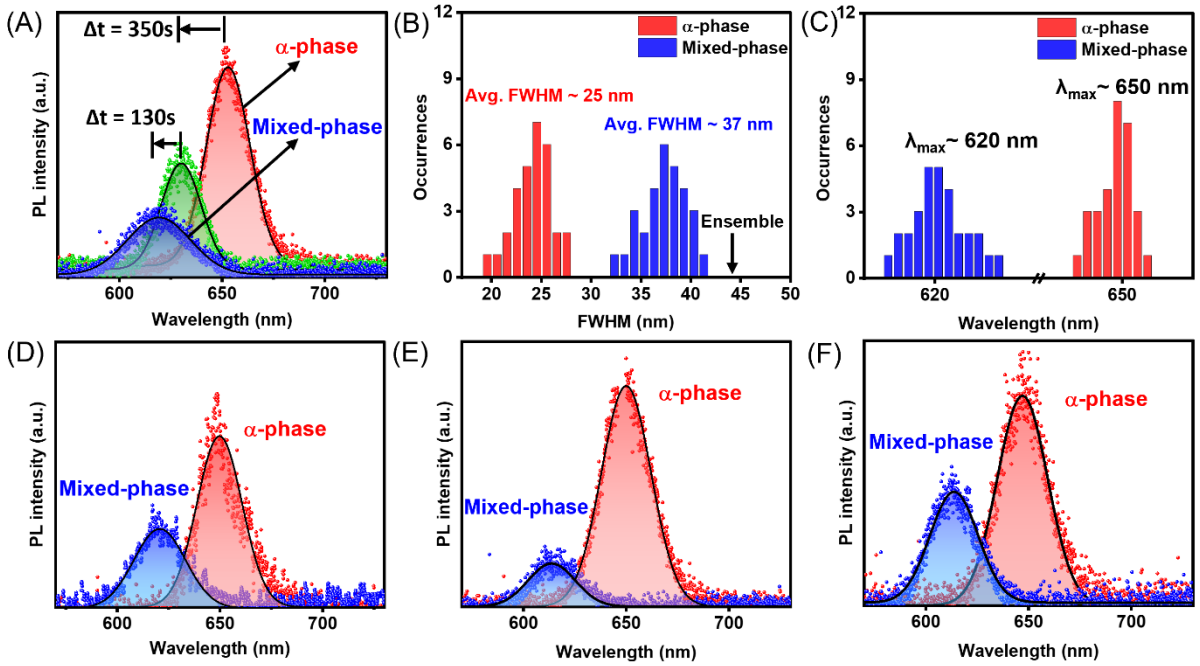

Figure 5.2. (A) Single-particle PL spectra recorded from the same freshly prepared nanocrystal after laser irradiation for different durations: ~0 seconds (red), ~350 seconds (green), and ~480 seconds (blue). Experimental conditions, including excitation wavelength (~375 nm) and power density (~4 W/cm^2), were consistent with those used in the PL blinking study. The 0-second spectrum corresponds to the α-phase nanocrystal, while the 480-second spectrum represents mixed-phase nanocrystal. (B-C) Statistical distributions of FWHMs (B) and PL peak positions (C) for α-phase (red) and mixed-phase (blue) nanocrystals. (D-F) Single-particle PL spectra recorded from three additional randomly selected nanocrystals. All experiments were performed at room temperature.

Single particle PL spectra also show shifting of PL peak due to photobleaching (Figure 5.2A, C) and the broadening of the average FWHM in mixed phrase (Figure 5.2B). This peak shifting and broadening indicated larger distribution of trap states in mixed phase than α-phase. Figure

5.2 (D, E, F) shows different peak shift due to different extent of bleaching in different particle. When the excitation power density was increased to ~20 W/cm^2, the number of flickered particles rose to 35-40 out of the 120 analyzed particles. [14,23,51] We first analyzed those 90-95 nanocrystals that are stable at low excitation power and exhibiting blinking rather than flickering at least at the beginning of their PL intensity trajectories (Figures 5.3). After several tens of seconds of low-power excitation, most of these initially blinking nanocrystals transitioned to flickering particles, eventually leading to photobleaching or, in some cases, undergoing direct photobleaching (Figures 5.3 A). A nanocrystal that transitions from blinking to flickering typically survives only for a few tens of seconds or minutes before eventually becoming a dark particle, with the transition rate accelerating at higher pump intensity. For instance, under low excitation power density (~2 W/cm^2), a blinked nanocrystal typically transitions to a flickered one after 250-300 seconds of irradiation (Figures 5.3 A), whereas, under high power density (~20 W/cm^2), the same transition occurs after 180-250 seconds (Figure 5.3).

We attribute the blinked nanocrystals to the ones retaining stable α-phase, while flickered particles to mixed phase, as supported by XRD data showing a phase transition in nanocrystals under prolonged UV exposure (Figure 1d).[1,12,14,17,47] The PL intensity trajectory in Figure 5.3 A (and Figure 5.5A) is a typical representative of the low-power (and high-power) blinking behaviour of our nanocrystals. The upper panel of Figure 5.3A depicts the low-power PL intensity trajectory, while the lower panel shows the simultaneously recorded PL lifetime trajectory. Two horizontal slabs, red and green, in the PL intensity trajectory highlight, respectively, the bright ON states and the weakly intense OFF states (Figure 5.3A). The excited-state PL lifetime profiles for the ON (red) and OFF (green) states were obtained separately for the α- and mixed-phase by analyzing the PL photons collected from the high-

and low-intensity regions, indicated by the horizontal slabs of corresponding colors in the upper panel of Figure 5.3 A (Figures 5.3B,C). Photons were collected separately before and after the phase transition (α to mixed), marked by a vertical dotted line in Figure 5.3 A, allowing analysis of the ON and OFF state PL dynamics in both phases.

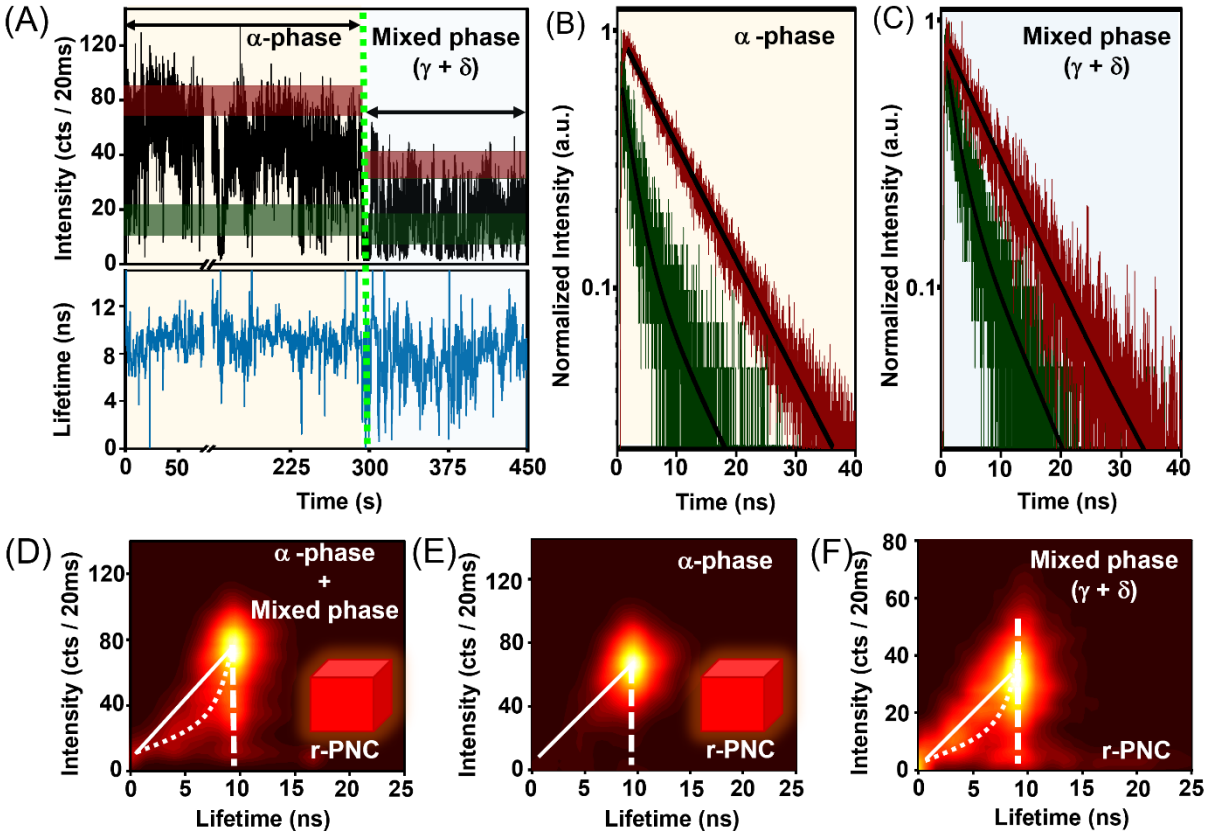

Figure 5.3. (A) PL intensity (upper panel) and lifetime (lower panel) trajectories of a single r-PNC recorded using a ~375 nm pulsed excitation laser at low power density (~2 W/cm^2). The vertical green dotted line indicates the phase change from α to mixed (δ + γ), with carrier dynamics analyzed separately for both phases. (B-C) Time-resolved PLs of OFF (green) and ON (red) states of the α-phase (b) and mixed-phase (c), derived from low- and high-intensity regions of PL intensity trajectory. (D-F) Fluorescence lifetime intensity distribution (FLID) maps in false color, correlating intensity-, and lifetime-histogram, derived from PL intensity- and lifetime-trajectory with different lengths: (D) full length (α-and mixed-phase), (E) up to 300 s (only α-phase), and (F) after 300 s (only mixed-phase). The change in occurrence

probability of a state in FLID is indicated by intensity change with higher intensity implies a larger probability.

We first analyzed the PL lifetimes of the ON and OFF states of r-PNC retaining the α-phase by collecting photons from high- and low-intensity regions before the phase transition (<300 s), marked by red (ON) and green (OFF) slabs in the upper panel of Figure5.3 A (Figure 5.3 B). A similar analysis was conducted for the mixed phase by examining the PL trajectory after the phase transition (>300 s). The phase transformation is indicated by a vertical dotted green line in Figure 5.3 A, where the left side (<300 s) represents the α-phase and the right side (>300 s) represents the mixed-phase. The time-resolved PLs for ON and OFF states of the α-phase were obtained from analysing the trajectory up to 300 s, as shown in Figure 5.3 B. Fitting to exponential decay functions revealed that the ON-state lifetime in the α-phase follows a single exponential decay with a time constant of ~9 ns. In contrast, the OFF-state decay exhibited bi-exponential kinetics, with a slow component of ~8.5 ns (14%), closely matching the ON-state lifetime (~9 ns), and a fast component of ~1.8 ns (86%). A similar analysis for the mixed-phase showed that the ON-state lifetime (~9 ns) remained unchanged after the phase transition, despite a significant reduction in ON-state intensity (Figures 5.3 A and C). Like the α-phase, the OFF-state PL dynamics in the mixed-phase follow a bi-exponential decay, with the long-lived component (~8.5 ns, 30%) correlates nicely to the ON-state lifetime and the short-lived component (~1.8 ns, 70%) remains unaffected by the phase change (Figure 5.3 C). An intensity-lifetime scaling parameter (η), representing the radiative recombination rate of the ON state ($k_{r,ON}$) relative to the OFF state ($k_{r,OFF}$), was calculated separately for the α- (η_α) and mixed-phase (η_M) using the following equation.[26,48]

$$\eta = \frac{k_{r,ON}}{k_{r,OFF}} = \frac{\tau_{OFF} I_{ON}}{\tau_{ON} I_{OFF}} \qquad (5.1)$$

The ON (or OFF) state intensity I_{ON} (or I_{OFF}) was determined by subtracting the background intensity from the average PL intensity under the red (or green) horizontal slab in Figure 5.3A. Similarly, the PL lifetime of the ON (or OFF) state τ_{ON} (or τ_{OFF}) was extracted through statistical analysis of the arrival times of the photons under this red (or green) region of Figure 5.3A (Figures 5.3 B-C). As previously stated, the OFF-state PL dynamics of both phases are characterized by two lifetime components (~1.8 ns and ~8.5 ns), where the slower component (~8.5 ns) closely aligns with the ON-state lifetime (~9 ns). Therefore, we attribute the slower (~8.5 ns) component of the OFF-state dynamics of both phases to hot carrier (HC) recombination, as it significantly reduces emission intensity without considerably altering the PL lifetime.[28,32,41,52-53]

Although HC recombination is present in both phases, it is more pronounced in the mixed phase, where the ~8.5 ns component stemming from HC recombination contributes nearly 30% to the OFF-state dynamics, which reduces to ~14% in the α-phase. This claim is further substantiated by comparing the FLID maps of the α-phase (Figure 5.3 E) and mixed-phase (Figure 5.3 F), showing the FLID of mixed-phase exhibits larger vertical broadening—a characteristic signature of HC recombination, which will be elaborated later.[31,41] HC recombination is also evident from Figure 5.3 A, where fluctuations in PL intensity (upper panel) occur without changing the PL lifetime (lower panel) in several places. Figure 5.4 provides zoomed-in views on small selected regions of the PL intensity and lifetime trajectories from Figure 5.3A, and subsequently overlaid for better visualization of HC recombination. This highlights multiple instances where the PL intensity significantly decreases without changing

PL lifetime considerably. The frequency of such uncorrelated events increases as the transition occurs from the α-phase to the mixed phase (Figure 5.4 B,D).

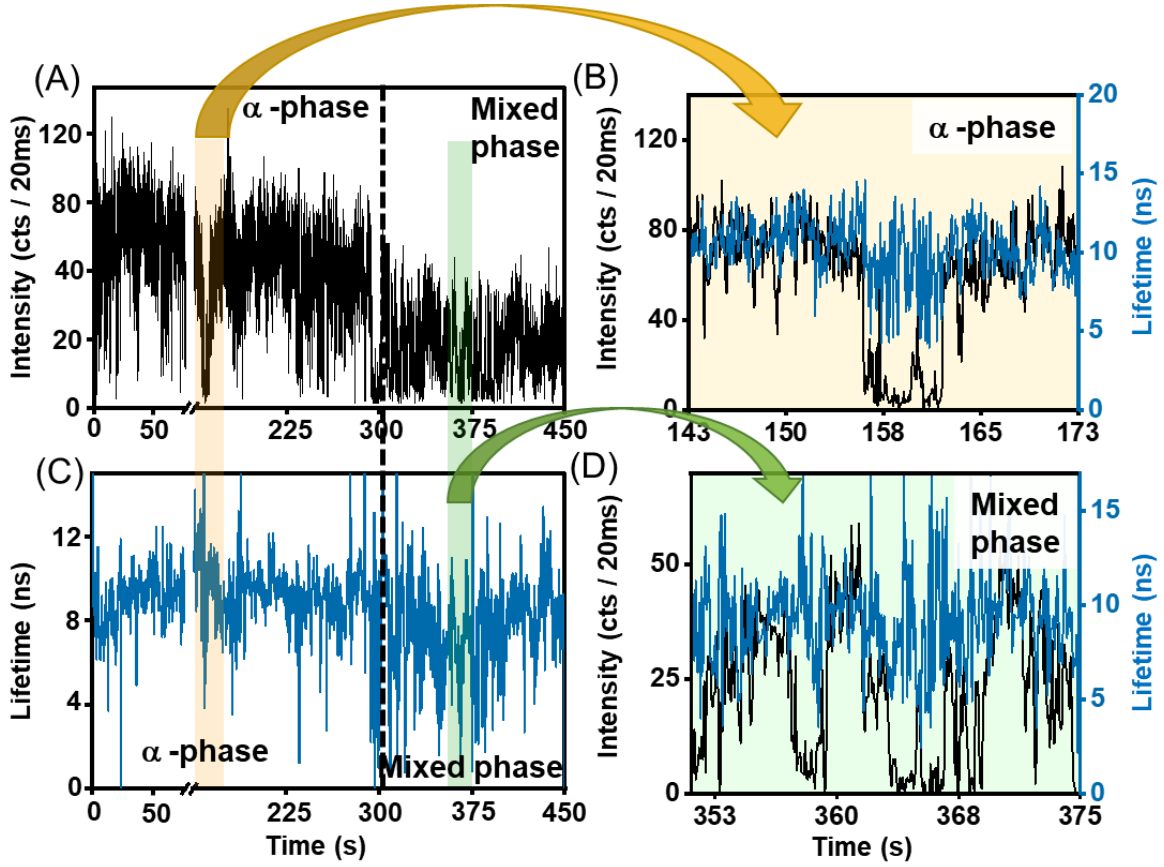

Figure 5.4. (A, C) The same PL intensity trajectory (upper panel, A) and corresponding lifetime trajectory (lower panel, C) from Figure 5.3A were further analyzed here by zooming in on specific regions within the α phase (yellow slab) and mixed-phase (green slab). (B, D) The zoomed-in intensity (black line) and lifetime (blue line) trajectories for the α phase (upper panel, B) and the mixed phase (lower panel, D) are overlaid to highlight non-correlative behaviour due to HC recombination. Such behaviour, characterized by intensity drops with insignificant changes in PL lifetime, was frequently observed in both the phases, with a higher density of occurrences in the mixed phase compared to the α phase.

Our next objective is to investigate the origin of the short lifetime component (~1.8 ns) of the OFF states of both phases (α and mixed). To achieve this, it is essential to compute the η for both phases (η_α and η_M), utilizing the short component (~1.8 ns).[26,48] The calculated values for η_α and η_M were approximately 1 and 0.83, respectively, latter is slightly lower than unity. These values were derived utilizing equation 5.1, using I_{ON} ~75 cts/20 ms (for the α-phase) and 33 cts/20 ms (for the mixed-phase), I_{OFF} ~15 cts/20 ms (α-phase) and 8 cts/20 ms (mixed-phase), τ_{ON} ~9 ns (both phases), and τ_{OFF} ~1.8 ns (both phases). For trion recombination, η is expected to be around 0.5, while for NBC recombination, η is approximately 1.[26,32,48] The intermediate value of η_M (~0.83) suggests that the faster lifetime component (~1.8 ns) of the OFF state in mixed-phase nanocrystals originates from a combination of both NBC and trion recombination. This contrasts with the α-phase nanocrystals, where η_α being 1 indicates that the faster lifetime component of the OFF state is solely due to NBC recombination. While the computed value of η can help predict the type of recombination responsible for blinking in a nanocrystal, such an approach becomes difficult when the PL dynamics follow nonexponential kinetics, as observed in our OFF states. Ideally, when calculating η for one of the lifetime components in a bi-exponential decay, the intensity contribution of that specific component should be used in Equation 5.1. However, this is a challenging task. If the overall intensity of the OFF state is used to calculate η for the faster lifetime component here, the result will be overestimated, providing only an approximate value of η. Additionally, the computed η is based on one-dimensional analysis with limited statistical data. These challenges motivated us to explore two-dimensional FLID mapping, which is considered more reliable for identifying the types of recombination responsible for blinking in nanocrystals. [22,26,31-32] Figure 5.3D shows a comprehensive FLID plot, derived from the full-length PL trajectory, which includes both the α-phase and mixed phase, as illustrated in Figure 5.3A. This FLID map correlates the PL intensity and lifetime histograms derived from their respective blinking trajectories. [22,26,31-32]

A comparison between the histograms of the α- and mixed-phase reveals that the mixed-phase exhibits a greater OFF state fraction compared to the α-phase, consistent with earlier reports that the mixed phase (δ and γ) has higher trap densities. [1,12,54-55]

The FLID of the full-length trajectory, which includes both the α- and mixed phase, displays complex evolution patterns of various probability states (Figure 5.3D). These evolution patterns can be described by three distinct trajectories: (i) a nonlinear trajectory shown by a bend dotted line connecting ON, OFF, and intermediate intensity states with varying lifetimes, indicative of trion or Type-A blinking; (ii) a vertical linear trajectory shown by thick dashed line linking different intensity states with similar lifetimes (~8.5-9 ns), characteristic of HC or Type-B blinking; and (iii) a diagonal linear trajectory shown by solid line connecting ON, OFF, and any intermediate intensity states of different lifetimes, suggestive of NBC or Type-C blinking (Figure 5.3D).[31,41] When the overall FLID depicted in Figure 5.3D is resolved into two FLIDs—one for the α-phase (Figure 5.3E) and the other for the mixed phase (Figure 5.3F) the evolution patterns become simpler. This is also done in high power analysis (Figure 5.5D,E,F) This splitting was achieved by separately analyzing the initial portion of the PL trajectory or before phase transformation (<300 s) and the later portion or after phase transformation (>300 s). The α-phase FLID reflects the predominance of ON state, with minor contributions from intermediate and OFF states, all aligned diagonally, indicating NBC recombination as the dominant blinking mechanism (Figure 5.3E). However, a slight vertical broadening is observed in the ON state evolution pattern, resulting in a vertically elongated shape instead of the expected spherical shape, suggesting a minor contribution from HC recombination. In contrast, in the mixed phase FLID, the vertical broadening becomes

pronounced, along with some diagonal broadening, confirming that HC recombination dominates over NBC recombination in the mixed phase.

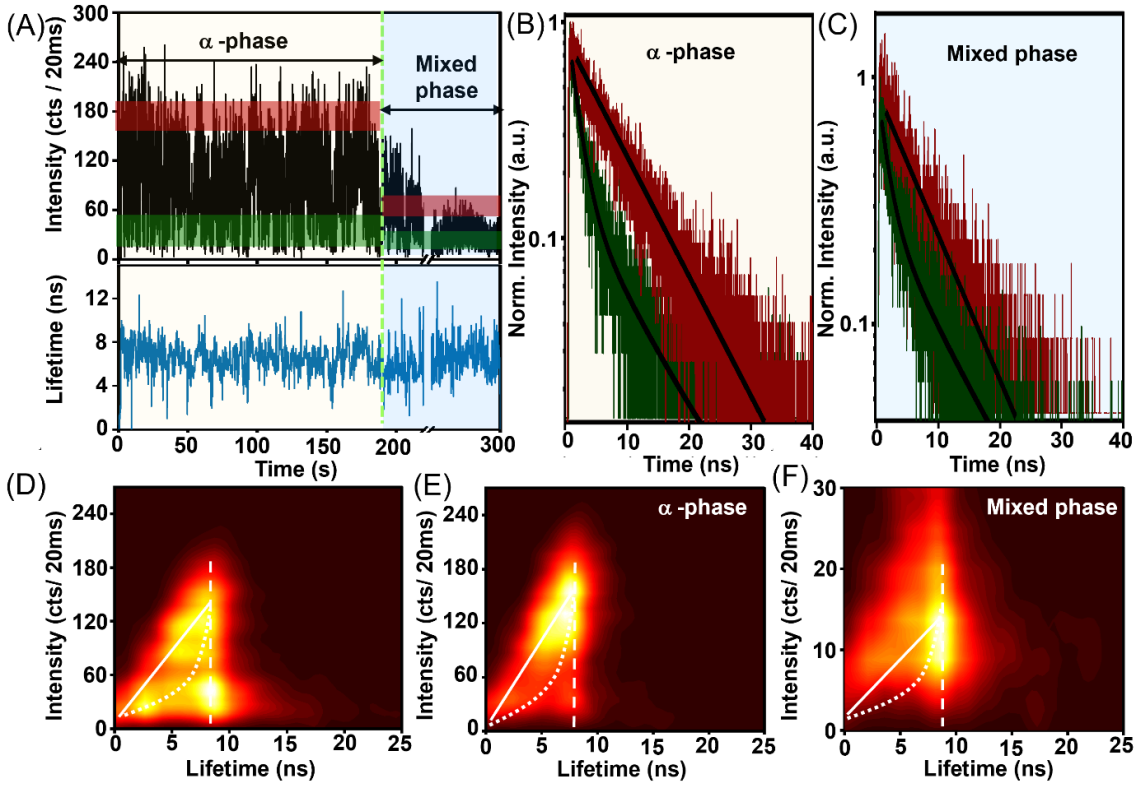

Figure 5.5. (A) PL intensity (upper panel) and lifetime (lower panel) trajectories of a single r-PNC recorded using a ~375 nm pulsed excitation laser at high power density (~20 W/cm^2). The vertical green dotted line indicates the phase change from α to mixed, with carrier dynamics analyzed separately for both phases. (B-C) Time-resolved PLs of OFF (green) and ON (red) states of the α- (B) and mixed-phase (C), derived from low- and high-intensity regions of PL intensity trajectory. (D-F) Fluorescence lifetime intensity distribution (FLID) maps in false color, correlating intensity- and lifetime-histogram derived from PL intensity- and lifetime-trajectory with different lengths: (D) full length (α-and mixed-phase), (E) up to 190 s (only α-phase), and (F) after 190 s (only mixed-phase). The change in occurrence probability of a state in FLID is indicated by intensity change with higher intensity implies a larger probability. All experiments were performed at room temperature.

Another notable difference between the α- and mixed-phase FLIDs lies in the higher occurrence probabilities of intermediate intensity states in the mixed phase compared to the α-phase. These findings indicate that NBC recombination dominates blinking in α-phase nanocrystals, while HC recombination becomes the primary pathway in the mixed-phase.

Previous studies have reported trion recombination in similar nanocrystals, as evidenced by the curved trajectories describing their FLIDs. [26,31-32,41] We recognize that, in our analysis, the two linear trajectories representing NBC (solid white line) and HC recombination (dashed white line) do not fully capture the complexity of the mixed phase and overall FLIDs (Figures 5.3D and 5.3F). This limitation led us to introduce a nonlinear trajectory (dotted line), which suggests the presence of trion recombination. [26,31-32,41] Although trion recombination was not comfortably captured by the intensity-lifetime scaling analysis, it is detected in the FLID mapping, likely due to the limitations of the former method, which relies on a one-dimensional analysis with lesser statistics. In our subsequent effort to explore carrier dynamics at high pump fluence, we examined FLIDs for all phases under high excitation power density (~20 W/cm^2) (Figure 5.5). At this power level, approximately 0.08 excitons are generated per pulse per nanocrystal, where the likelihood of bi-excitonic or higher-order excitonic recombination is exceedingly low. A comparison between low- and high-power FLIDs reveals overall higher occurrence probabilities of the intermediate intensity states in both phases at high power. This is accompanied by significant vertical broadening in the α-phase FLID at high power, which is nearly absent at low power. Similarly, the high-power mixed-phase FLID shows more pronounced vertical broadening and intensified trion features (curved trajectory), which are less evident at low power (Figures 5.3D-F and 5.5D-F). These observations indicate that higher excitation power engages dispersive trap states, leading to increased trion and HC recombination.

5.5.2 Dependence of ON/OFF events on Power Law kinetics

Next, we examined the probability distribution functions of ON and OFF time durations (ρ_{ON} and ρ_{OFF}), derived separately for the α- and mixed-phase by analyzing the low-power PL intensity trajectories before (for the α-phase) and after (for the mixed phase) phase transformation (Figures 5.6A-B, E-F).[56-61] The ρ_{OFF}, when plotted on a log-log scale, shows a linear behavior, which can be described by $\rho_{OFF} \propto t^{-m_{OFF}}$.[23,41] In contrast, the log-log representation of ρ_{ON} demonstrates a rapid falloff at longer times, represented by $\rho_{ON} \propto t^{-m_{ON}} \exp(-\frac{t}{t_c})$.[23,41]

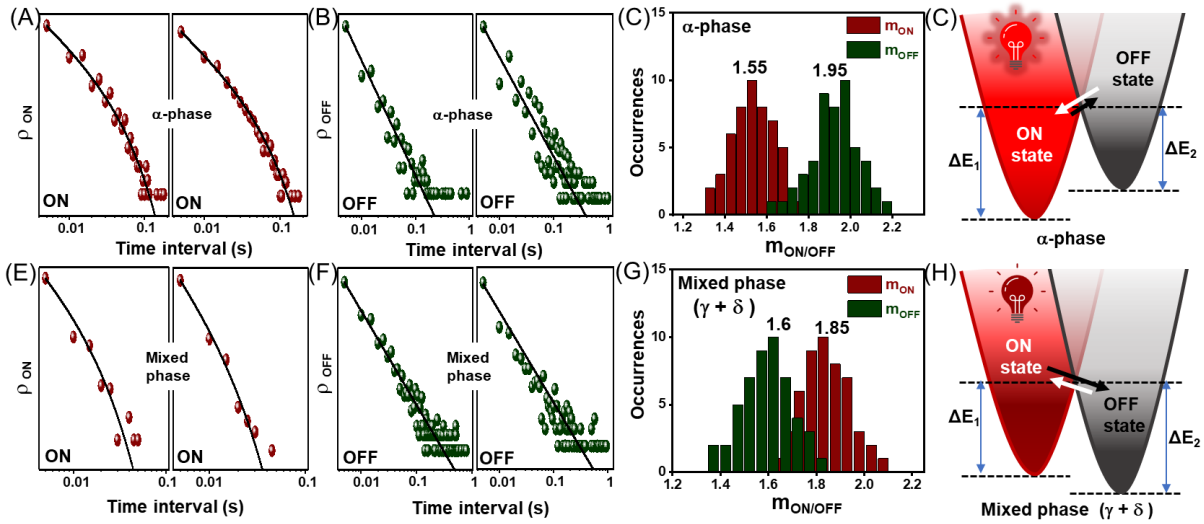

Figure 5.6. (A, B, E, F) Representatives of probability distribution functions of ON and OFF time durations (ρ_{ON} and ρ_{OFF}), derived from low power PL intensity trajectories of two randomly selected nanocrystals. (C, G) Statistical distributions of power-law coefficients m_{ON} and m_{OFF} whose average values represent the relative carrier trapping and detrapping rates in nanocrystals. [41,48] (D, H) Schematics of carrier trapping (black arrow) and de-trapping (white arrow) in both phases with potential wells. Figures in the upper panel represent the α-phase, whereas the lower panel figures are related to the mixed phase. ΔE_1 and ΔE_2 represent the activation barriers between neutral and charged potential wells.

The average values of the power-law coefficients (m_{ON} and m_{OFF}) were obtained from the peaks of their statistical distributions recorded over a large number of particles (Figures 5.6 C,G). These power-law coefficients, $m_{OFF,}$ and m_{ON}, represent respectively the relative rates of carrier de-trapping and trapping in individual nanocrystals. [41,48] We separately calculated the relative trapping (m_{ON}) and de-trapping (m_{OFF}) rates in the α- and mixed-phase by analyzing different segments of the PL intensity trajectory and repeating this over a large number of particles to get the mean values. The ratio of trapping-to-detrapping rates in the mixed-phase (~1.15) is significantly higher compared to that (~0.80) of the α-phase, which is well under our intuitive expectation stemming from the lower PLQY and higher trap density of the mixed-phase (Figures 5.6 C, G, D, H).

5.5.3 Fluorescence Correlation Spectroscopy (FLCS) Measurements in Different Phases

To gain deeper insights into the mechanistic details of carrier dynamics responsible for nanocrystal blinking in the solution phase, we performed FLCS study on freely diffusing nanocrystals in both phases (Figure 5.7). Unlike conventional FCS, which primarily captures the timescales of carrier dynamics, FLCS integrates lifetime information to unravel the mechanistic pathways underlying the transformation between emission states. By analyzing the PL correlation patterns of coupled states, FLCS provides a more comprehensive understanding of the interplay between these states characterized by different PL lifetimes.[41,62-80] The PL lifetime profiles of our nanocrystal samples were well represented by a biexponential decay function. For α-phase nanocrystals, the decay components were approximately 6 ns (60%) and 12 ns (40%), while for mixed-phase nanocrystals, the components were approximately 4 ns (65%) and 11 ns (35%) (Figure 5.7D). The α-phase nanocrystals correspond to freshly prepared

sample, whereas the mixed-phase nanocrystals refer to sample exposed to UV light for over 14 hours (Figure 5.7A).

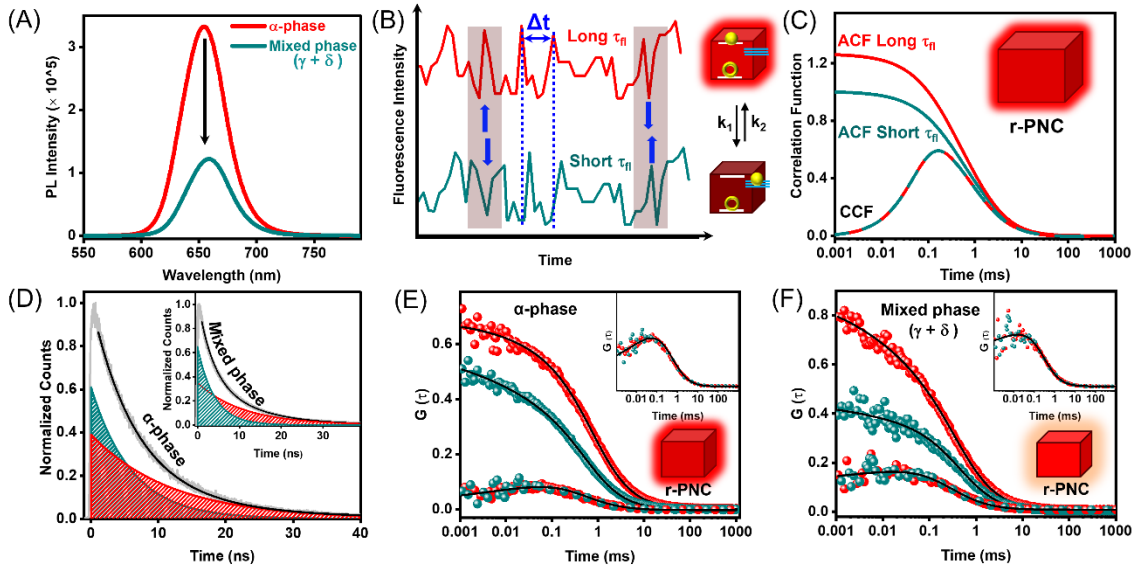

Figure 5.7. (A) PL spectra of nanocrystals dispersed in toluene, shown before (α-phase) and after prolonged UV illumination (>14 hours, mixed-phase). (B) Schematic representation of anti-correlated PL patterns between two states with distinct PL lifetimes, evidenced by the initial rise in the interstate cross-correlation function (CCF, shown in panel c), consistent with experimental observations depicted in the insets of panels e and f. (C) Schematics of intrastate autocorrelation functions (ACFs) for long (red) and short (green) lifetime components, along with the interstate CCF (red-green) illustrating the cross-correlation of the two components. The initial growth in the CCF corresponds to the anti-correlated PL behavior shown in panel b. (D) Time-resolved PL of α-phase nanocrystals (grey), recorded alongside FLCS, decomposed into two single-exponential decay profiles representing the lifetimes of the interacting emission states. The inset shows similar data for mixed-phase nanocrystals. (E, F) ACFs for long (red) and short (green) lifetime states, along with their cross-correlation CCFs (red-green), for α-phase (E) and mixed-phase (F) nanocrystals. Insets highlight the initial growth feature in the CCFs with a zoomed y-axis for clarity. Panels b and c are schematic illustrations and do not represent actual data. All experiments were performed at room temperature.

We attributed the longer lifetime component (~12-11 ns) to pure radiative recombination, associated with higher PL intensity, while the shorter lifetime component (~6-4 ns) likely originated from a combination of radiative and non-radiative recombination, typically characterized by lower PL intensity, which is practically always the case (Scheme 5.2).[41,62] Our FLCS analysis enabled us to compute separate autocorrelation functions (ACFs) for the longer ($ACF_{long\times long}$) and shorter ($ACF_{short\times short}$) lifetime components, as well as a cross-correlation function ($CCF_{long\times short}$). The latter was derived using the lifetimes of both states and their PL trajectories (Figures 5.7E,F). The strength of this method lies in its statistical approach, which separates different intensity contributions with similar PL lifetimes, analyzed at the single-photon level. Further details about FLCS, including the construction of ACFs and CCF and the subsequent fitting procedures, can be found elsewhere. [41,62,71-72]

Here, we focus primarily on the CCF, as the anti-correlated PL intensity patterns between the two emission states are evidenced by the initial growth feature of the CCF (Figures 5.7B, 5.7E-F). The coupling timescale between these two states was determined by fitting the CCF using the following equation (Equation 5.2). [41,62,79]

$$G(\tau) = A^{-1}\left[1 - \exp^{-\left(\frac{\tau}{\tau_R}\right)^{\beta}}\right](1+\frac{\tau}{\tau_D})^{-1}(1+\frac{\tau}{\kappa^2\tau_D})^{-1/2} \qquad (5.2)$$

Where, τ_R and τ_D represent the characteristic timescales for the dynamical exchange between two emission states and the translational diffusion of nanocrystals traversing the excitation volume, respectively. [41,62,79] The stretching exponent β ($0 \leq \beta \leq 1$) describes the distribution of τ_R, with $\beta = 1$ indicating no distribution and β approaching 0 reflecting a highly dispersed distribution. [41,62]. Parameter A in Equation 5.2 denotes the mean number of nanocrystals within the excitation volume transitioning between two lifetime states. [41,62]. Figure 5.7E-F

presents the CCFs for both the α-phase and mixed-phase, which show excellent fit to Equation 5.2. The growth timescale (τ_R) of the CCF, representing the dynamic exchange timescale between two emission states, is significantly shorter in the mixed phase (τ_R ~60 μs) compared to the α-phase (τ_R ~100 μs) (Table 5.1).

Table 5.1. Best-fitted FCS and FLCS parameters, derived from the fittings of the conventional FCS curves and CCFs with Equations 5.2 and Equation 5.3.

Correlation type	Phase	τ_D (ms)	τ_R (μs)	β	Trap fraction $[k_1/(k_1+k_2)]$
Conventional FCS	α	0.8	160	0.7	0.27
	mixed	0.6	80	0.29	0.56
$CCF_{long\times short}$	α	0.4	100	0.2	-
	mixed	0.25	60	0.1	-

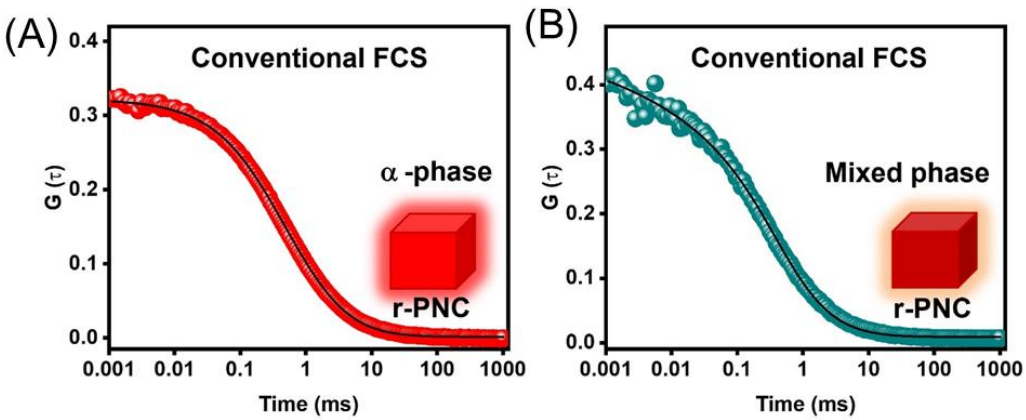

Figure 5.8. Conventional FCS curves of (A) freshly prepared α-phase nanocrystals and (b) mixed-phase nanocrystals, which were prepared by illuminating the α-phase nanocrystals with UV light for >14 hours. The following fitting function was used to fit the FCS curves. k_1 and k_2 represent the trapping and de-trapping rates. All experiments were performed at room temperature.

$$G(\tau) = A^{-1}\left[1 + \frac{k_1}{k_2}\exp^{-\left(\frac{\tau}{\tau_R}\right)^{\beta}}\right](1 + \frac{\tau}{\tau_D})^{-1}(1 + \frac{\tau}{\kappa^2\tau_D})^{-1/2} \qquad (5.3)$$

5.5.4 Multiple Recombination Centre (MRC) Model

To get deeper insight into the origin of growth in CCF, we invoked the multiple recombination center (MRC) model, which postulates that the activation and deactivation of shallow trap states, acting as recombination centers, drive the blinking behaviour in nanocrystals. [81–83] The dynamic behaviour of these trap states modulates non-radiative decay rate, leading to corresponding changes in PL intensity and lifetime. Within the MRC framework, the long-lifetime component (11–12 ns) of nanocrystals arises exclusively from radiative recombination, while the short-lifetime component (4–6 ns) results from a combination of radiative and trap-induced non-radiative recombination, with the density of trap states fluctuating over time (Scheme 5.2). According to the model, the deactivation or reduction of trap states enhances the PL intensity of the long-lifetime state due to the increased probability of radiative recombination. Conversely, the PL intensity of the short-lifetime state decreases as the absence or reduced number of trap states diminishes the probability of non-radiative recombination as an additional pathway. When trap states activate or increase their number, the PL intensity of the short-lifetime state increases due to the greater likelihood of non-radiative recombination. However, the activation of traps reduces the probability of pure radiative recombination, thereby decreasing the PL intensity of the long-lifetime state. The MRC model thus predicts an anti-correlation between the PLs of two lifetime states, consistent with the growth feature observed in the CCF. The timescale of the growth kinetics, τ_R, relates the rates of appearance and disappearance of trap states. The faster τ_R observed in the mixed-phase nanocrystals compared to the α-phase indicates that carriers are trapped more efficiently and on a shorter

timescale in the mixed phase (Table 5.1). This is further corroborated by the lower value of β in the mixed phase, which suggests more dispersive blinking (Table 5.1). Conventional FCS analysis also aligns with these findings, revealing a faster blinking timescale and a reduced β value for mixed-phase nanocrystals compared to those of the α-phase nanocrystals (Figure 5.8, Table 5.1).

Our single-dot blinking and FLCS studies are in good agreement with the ensemble measurements. For instance, the average lifetime and PLQY of $CsPbI_3$ nanocrystals significantly decrease as the crystal phase transitions from α-phase to mixed-phase suggesting that the mixed-phase contains a higher density of trap states. The average peak position of single-particle PL spectra for α-phase nanocrystals appears at ~649 nm, which is ~7 nm blue-shifted compared to the ensemble PL peak (~656 nm) (Figure 5.2). In contrast, for the mixed-phase, the average single-particle PL peak (~620 nm) is substantially blue-shifted relative to its ensemble peak (~658 nm). This pronounced blue shift in the mixed-phase is attributed to photo-corrosion observed during single-particle studies, consistent with earlier reports by the Klimov and Mulvaney groups.[23,51] Additionally, the FWHMs of the PL spectra for mixed-phase nanocrystals are significantly broader than that of the α-phase when measured at the single-particle level (Figure 5.2). This broadening indicates emission from bound excitonic states, generally observed in the presence of deep trap states, further corroborating the presence of extensive traps in the mixed-phase nanocrystals.[84]

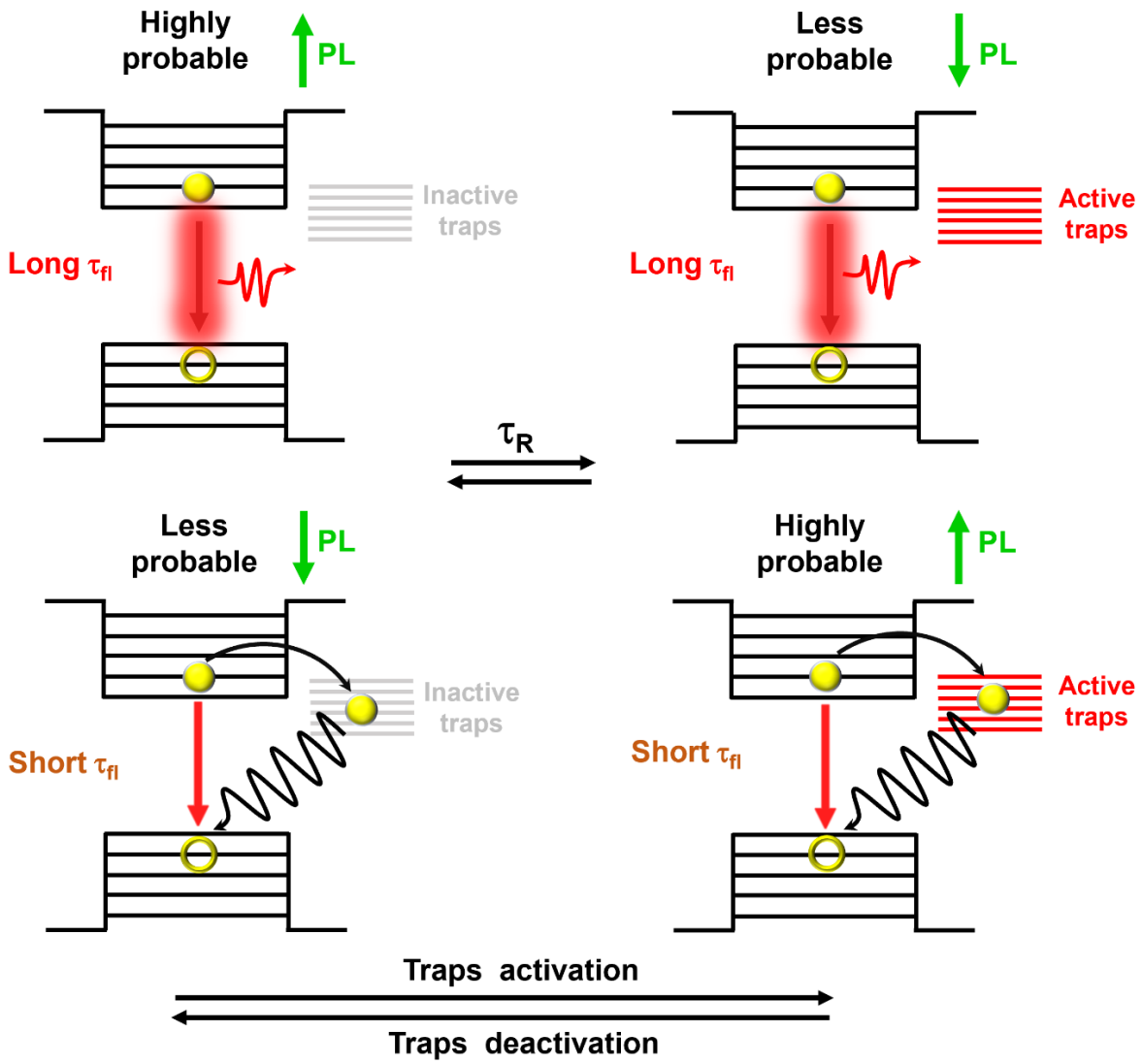

Scheme 5.2. The MRC model describes the activation (right panel) and deactivation (left panel) of traps in nanocrystals over time. **Left panel (traps inactive):** Radiative recombination dominates over non-radiative recombination, resulting in a higher PL intensity for the long-lifetime state (top figure). Conversely, the reduced probability of simultaneous radiative- and non-radiative recombination, leads to lower PL intensity for the short-lifetime state (bottom figure). **Right panel (traps active):** The probability of radiative recombination alone decreases, lowering the PL intensity of the long-lifetime component (top figure). However, the higher likelihood of combined radiative and non-radiative recombination increases the PL intensity of the short-lifetime component (bottom figure). The MRC model thus predicts a PL

anti-correlation between the two lifetime states, consistent with the growth feature observed in the CCF. The timescale of growth kinetics τ_R is persuasive to the appearance and disappearance rates of trap states.

5.6 Conclusion

In this study, we performed a comprehensive analysis of carrier dynamics in α-phase and mixed-phase $CsPbI_3$ perovskite nanocrystals using single-particle blinking, FLCS, and ensemble studies. Single-particle blinking analyses, including FLID mapping and intensity-lifetime scaling, revealed distinct recombination mechanisms in the two phases. Blinking in α-phase nanocrystals is predominantly driven by shallow trap-induced NBC recombination, with a minor contribution from HC recombination. In contrast, blinking in mixed-phase nanocrystals is primarily attributed to deep trap-induced HC recombination, with moderate contributions from trion and NBC recombination. Our FLCS investigations provided consistent insights, highlighting a greater involvement of trap states in mixed-phase nanocrystals compared to α-phase nanocrystals. A key observation from FLCS is the growth feature in the initial correlation of the CCF, which confirms the dynamic nature of shallow trap states driving nanoparticle blinking in fluid-phase dispersions. Understanding carrier dynamics in red-emitting $CsPbI_3$ perovskite nanocrystals is essential for the rational design of next-generation optoelectronic and photovoltaic devices, as these nanocrystals are regarded as ideal candidates for such applications. This study offers valuable insights and represents a significant step forward in advancing the development of these promising materials for device integration.

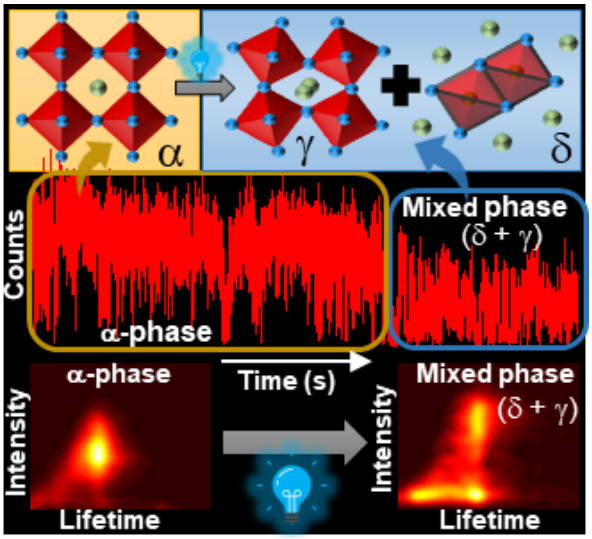

5.7 References

[1] A. Swarnkar, A. R. Marshall, E. M. Sanehira, B. D. Chernomordik, D. T. Moore, J. A. Christians, T. Chakrabarti, J. M. Luther, *Science* **2016**, *354*, 92.

[2] M. Gerhard, B. Louis, R. Camacho, A. Merdasa, J. Li, A. Kiligaridis,A. Dobrovolsky, J. Hofkens, I. G. Scheblykin, *Nat. Commun.* **2019**,*10*, 1698.

[3] L. Protesescu, S. Yakunin, M. I. Bodnarchuk, F. Krieg, R. Caputo, C. H. Hendon, R. X. Yang, A. Walsh, M. V. Kovalenko, *Nano Lett.* **2015**, *15*, 3692.

[4] H. Huang, L. Polavarapu, J. A. Sichert, A. S. Susha, A. S. Urban, A. L. Rogach, *NPG Asia Mater.* **2016**, *8*, e328.

[5] C. Yang, Y. Li, X. Hou, M. Zhang, G. Zhang, B. Li, W. Guo, X. Han, X. Bai, J. Li, R. Chen, C. Qin, J. Hu, L. Xiao, S. Jia, *Small* **2023**, *20*, 2309134.

[6] J. Pan, Y. Shang, J. Yin, M. D. Bastiani, W. Peng, I. Dursun, L. Sinatra, A. M. El-Zohry, M. N. Hedhili, A.-H. Emwas, O. F. Mohammed, Z. Ning, O. M. Bakr, *J. Am. Chem. Soc.* **2018**, *140*, 562.

[7] K. Chen, W. Jin, Y. Zhang, T. Yang, P. Reiss, Q. Zhong, U. Bach, Q. Li, Y. Wang, H. Zhang, Q. Bao, Y. Liu, *J. Am. Chem. Soc.* **2020**, *142*, 3775.

[8] A. Dey, J. Ye, A. De, E. Debroye, S. K. Ha, E. Bladt, A. S. Kshirsagar, Z. Wang, J. Yin, Y. Wang, L. N. Quan, F. Yan, M. Gao, X. Li, J. Shamsi, T. Debnath, M. Cao, M. A. Scheel, S. Kumar, J. A. Steele, M. Gerhard, L. Chouhan, K. Xu, X.-g. Wu, Y. Li, Y. Zhang, A. Dutta, C. Han, I. Vincon, A. L. Rogach, et al., *ACS Nano* **2021**, *15*, 10775.

[9] A. Das, S. Ghosal, K. Marjit, S. K. Pati, A. Patra, *J. Phys. Chem. Lett.* **2024**, *15*, 7822.

[10] X. Wang, D. Huo, X. Wang, M. Li, Y. Wang, Y. Wan, *J. Phys. Chem. Lett.* **2021**, *12*, 6907.

[11] A. Dutta, N. Pradhan, *ACS Energy Lett.* **2019**, *4*, 709.

[12] M. K. Abney, M. Suri, T. Shah, F. L. Deepak, B. A. Korgel, *J. Phys. Chem. C* **2022**, *126*, 12712.

[13] L. Protesescu, S. Yakunin, S. Kumar, J. Bär, F. Bertolotti, N. Masciocchi, A. Guagliardi, M. Grotevent, I. Shorubalko, M. I. Bodnarchuk, C.-J. Shih, M. V. Kovalenko, *ACS Nano* **2017**, *11*, 3119.

[14] S. Paul, G. Kishore, A. Samanta, *J. Phys. Chem. C* **2023**, *127*, 10207–10214.

[15] A. Dutta, S. K. Dutta, S. D. Adhikari, N. Pradhan, *Angew. Chem.* **2018**, *57*, 9083.

[16] C. Zhu, M. Marczak, L. Feld, S. C. Boehme, C. Bernasconi, A. Moskalenko, I. Cherniukh, D. Dirin, M. I. Bodnarchuk, M. V. Kovalenko, G. Raino, *Nano Lett.* **2022**, *22*, 3751.

[17] Y. Wang, T. Zhang, M. Kan, Y. Zhao, *J. Am. Chem. Soc.* **2018**, *140*, 12345.

[18] F. Liu, Y. Zhang, C. Ding, S. Kobayashi, T. Izuishi, N. Nakazawa, T. Toyoda, T. Ohta, S. Hayase, T. Minemoto, K. Yoshino, S. Dai, Q. Shen, *ACS Nano* **2017**, *11*, 10373.

[19] Z. Wu, J. Li, Y. Wu, *Phys. Rev. A* **2023**, *108*, 023727.

[20] I. Y. Eremchev, A. O. Tarasevich, J. Li, A. V. Naumov, I. G. Scheblykin, *Adv. Opt. Mater.* **2021**, *9*, 2001596.

[21] S. K. Bera, S. Bera, M. Shrivastava, N. Pradhan, K. V. Adarsh, *Nano Lett.* **2022**, *22*, 8908.

[22] G. Yuan, D. E. Gómez, N. Kirkwood, K. Boldt, P. Mulvaney, *ACS Nano* **2018**, *12*, 3397.

[23] Y. S. Park, S. Guo, N. S. Makarov, V. I. Klimov, *ACS Nano* **2015**, *9*, 10386.

[24] F. Hu, C. Yin, H. Zhang, C. Sun, W. W. Yu, C. Zhang, X. Wang, Y. Zhang, M. Xiao, *Nano Lett.* **2016**, *16*, 6425.

[25] B.-W. Hsu, Y.-T. Chuang, C.-Y. Cheng, C.-Y. Chen, Y.-J. Chen, A. Brumberg, L. Yang, Y.-S. Huang, R. D. Schaller, L.-J. Chen, et al. *ACS Nano* **2021**, *15*, 11358.

[26] M. K. Panda, D. Acharjee, A. B. Mahato, S. Ghosh, *Small* **2024**, *20*, 2311559.

[27] C. Yin,L. Chen, N. Song, Y. Lv, F. Hu, C. Sun, W. W. Yu, C. Zhang, X.Wang, Y. Zhang, M. Xiao, *Phys. Rev. Lett.* **2017**, *119*, 026401.

[28] C. Galland, Y. Ghosh, A. Steinbrück, M. Sykora, J. A. Hollingsworth, V. I. Klimov, H. Htoon, *Nature* **2011**, *479*, 203.

[29] N. Yarita, H. Tahara, M. Saruyama, T. Kawawaki, R. Sato, T. Teranishi, Y. Kanemitsu, *J. Phys. Chem. Lett.* **2017**, *8*, 6041.

[30] R. Chen, B. Xia, W. Zhou, G. Zhang, C. Qin, J. Hu, I. G. Scheblykin, L. Xiao, *Adv. Photonics Res.* **2022***, 3,* 2100271.

[31] C. T. Trinh, D. N. Minh, K. J. Ahn, Y. Kang, K.-G. Lee, *Sci. Rep.* **2020**, *10*, 2172.

[32] T. Ahmed, S. Seth, A. Samanta, *ACS Nano* **2019**, *13*, 13537.

[33] E. M. Thomas, N. Pradhan, K. G. Thomas, *ACS Energy Lett.* **2022**, *7*, 2856.

[34] P. A. Frantsuzov, S. Volkán-Kacsó, B. Janko, *Phys. Rev. Lett.* **2009**, *103*, 207402.

[35] P. A. Frantsuzov, S. Volkán-Kacsó, B. Jankó, *Nano Lett.* **2013**, *13*, 402.

[36] Y. Chuang, T. Lin, G. Tan, P. Jan, H. Lin, H. Chen, K. Hsiao, B. Chen, C. Lu, C. Lee, C. Pao, S. Yang, M. Lu, H.-W. Lin, *Small* **2024**, *20*, 2308676.

[37] M. Righetto, S. S. Lim, D. Giovanni, J. W. M. Lim, Q. Zhang, S. Ramesh, Y. K. E. Tay, T. C. Sum, *Nat. Commun.* **2020**, *11*, 1.

[38] A. A. Cordones, S. R. Leone, *Chem. Soc. Rev.* **2013**, *42*, 3209.

[39] S. Das, A. Samanta, *ACS Energy Lett.* **2021**, *6*, 3780.

[40] S. K. Mahankudo, A. Das, K. Mishra, M. Barai, P. Mal, S. Ghosh, *ACS Appl. Nano Mater.* **2022**, *5*, 4360.

[41] D. Acharjee, M. K. Panda, A. B. Mahato, A. Das, S. Ghosh, *Nanoscale* **2024**, *16*, 18444.

[42] A. B. Mahato, D. Acharjee, M. K. Panda, D. Samanta, S. Ghosh, *J. Phys. Chem. C* **2024**, *128*, 16588.

[43] G. Bounos, S. Ghosh, A. K. Lee, K. N. Plunkett, K. H. DuBay, J. C. Bolinger, R. Zhang, R. A. Friesner, C. Nuckolls, D. R. Reichman, P. F. Barbara, *J. Am. Chem. Soc.* **2011**, *133*, 10155.

[44] S. Ghosh, A. Adhikari, S. Sen Mojumdar, K. Bhattacharyya, *J. Phys. Chem. B* **2010**, *114*, 5736.

[45] A. Sharma, J. Enderlein, M. Kumbhakar, *J. Phys. Chem. Lett.* **2017**, *8*, 5821.

[46] P. M. Varghese, A. Rajan, E. K. Vishnu, T. Titus, K. G. Thomas, *J. Phys. Chem. C* **2024**, *128*, 10945.

[47] D. B. Straus, S. Guo, R. J. Cava, *J. Am. Chem. Soc.* **2019**, *141*, 11435.

[48] T. Kim, S. I. Jung, S. Ham, H. Chung, D. Kim, *Small* **2019**, *15*, 1900355.

[49] D. Acharjee, A. Das, M. K. Panda, M. Barai, S. Ghosh, *Nano Lett.* **2023**, *23*, 1946.

[50] J. A. Castañeda, G. Nagamine, E. Yassitepe, L. G. Bonato, O. Voznyy, S. Hoogland, A. F. Nogueira, E. H. Sargent, C. H. B. Cruz, L. A. Padilha, *ACS Nano* **2016**, *10*, 8603.

[51] G. Yuan, C. Ritchie, M. Ritter, S. Murphy, D. E. Gómez, P. Mulvaney, *J. Phys. Chem. C* **2018**, *122*, 13407.

[52] Z. Zhou, J. He, T. Frauenheim, O. V. Prezhdo, J. Wang, *J. Am. Chem. Soc.* **2022**, *144*, 18126.

[53] M. Massicotte, G. Soavi, A. Principi, K.-J. Tielrooij, *Nanoscale* **2021**, *13*, 8376.

[54] B. Zhao, S.-F. Jin, S. Huang, N. Liu, J.-Y. Ma, D.-J. Xue, Q. Han, J. Ding, Q.-Q. Ge, Y. Feng, J.-S Hu, *J. Am. Chem. Soc.* **2018**, *140*, 11716.

[55] Y. Tang, A. Lesage, P. Schall, *J. Mater. Chem. C* **2020**, *8*, 17139.

[56] J. J. Peterson, D. J. Nesbitt, *Nano Lett.* **2009**, *9*, 338.

[57] K. T. Shimizu, R. G. Neuhauser, C. A. Leatherdale, S. A. Empedocles, W. K. Woo, M. G. Bawendi, *Phys. Rev. B* **2001**, *63*, 205316.

[58] M. Kuno, D. P. Fromm, S. T. Johnson, A. Gallagher, D. J. Nesbitt, *Phys. Rev. B* **2003**, *67*, 125304.

[59] R. Verberk, A. M. V. Oijen, M. Orrit, *Phys. Rev. B* **2002**, *66*, 233202.

[60] H. Huang, M. I. Bodnarchuk, S. V. Kershaw, M. V. Kovalenko, A. L. Rogach, *ACS Energy Lett.* **2017**, *2*, 2071.

[61] M. Ye, P. C. Searson, *Phys. Rev. B* **2011**, *84*, 125317.

[62] A. Das, K. Mishra, S. Ghosh, *J. Phys. Chem. Lett.* **2021**, *12*, 5413.

[63] K. Mishra, A. Das, S. Ghosh, *J. Phys. Chem. C* **2020**, *124*, 24115.

[64] S. Dey, U. Mandal, A. Adhikari, S. Ghosh, K. Bhattacharyya, *Hydrog. Bond. Transfer Excit. State* **2010**, *1*, 159.

[65] S. Ghosh, U. Mandal, A. Adhikari, K. Bhattacharyya, *Chem. Asian J.* **2009**, *4*, 948.

[66] A. Das, D. Acharjee, M. K. Panda, A. B. Mahato, S. Ghosh, *J. Phys. Chem. Lett.* **2023**, *14*, 3953.

[67] S. Bhattacharyya, S. Prashanthi, P. R. Bangal, A. Patra, *J. Phys. Chem. C* **2013**, *117*, 26750.

[68] S. Kundu, A. Chowdhury, S. Nandi, K. Bhattacharyya, A. Patra, *Chem. Sci.* **2021**, *12*, 5874.

[69] T. Wohland, S. Maiti, R. Macháň, *An Introduction to Fluorescence Correlation Spectroscopy*, IOP Publishing, Bristol, U.K., **2020**. pp. 247–250.

[70] P. Schwille, E. Haustein, *Fluorescence Correlation Spectroscopy. In A tutorial for the Biophysics Textbook Online (BTOL)*, Biophysical Society, Rockville, MD, **2002**, pp. 10–25.

[71] P. Kapusta, R. Machań, A. Benda, M. Hof, *Int. J. Mol. Sci.* **2012**, *13*, 12890.

[72] J. Humpolíckova, A. Benda, J. Sýkora, R. Machań, T. Kral, B. Gasinska, J. Enderlein, M. Hof, *Biophys. J.* **2008**, *94*, L17.

[73] A. Ghosh, S. Isbaner, M. Veiga-Gutierrez, I. Gregor, J. Enderlein, N. Karedla, *J. Phys. Chem. Lett.* **2017**, *8*, 6022.

[74] J. Chen, J. Irudayaraj, *Anal. Chem.* **2010**, *82*, 6415.

[75] K. Ishii, T. Tahara, *J. Phys. Chem. B*, **2010**, *114*, 12383.

[76] I. Gregor, J. Enderlein, *Photochem. Photobiol. Sci.* **2007**, *6*, 13.

[77] A. Orte, M. J. Ruedas-Rama, J. M. Paredes, L. Crovetto, J. M. Alvare-Pez, *Langmuir*, **2011**, *27*, 12792.

[78] G. Vicidomini, H. Ta, H. Alf, V. Mueller, M. P. Clausen, D. Waithe, S. Galiani, S. Erdinç, A. Diaspro, S. W. Hell, C. Eggeling, *Nano Lett.* **2015**, *15*, 5912–5918.

[79] P. K. Singha, T. Kistwal, A. Datta, *J. Phys. Chem. Lett.* **2023**, *14*, 4289.

[80] S. Sharma, N. Pal, P. K. Chowdhury, S. Sen, A. K. Ganguli, *J. Am. Chem. Soc.* **2012**, *134*, 19677.

[81] M. Nirmal, B. O. Dabbousi, M. G. Bawendi, J. J. Macklin, J. K. Trautman, T. D. Harris, L. E. Brus, *Nature* **1996**, *383*, 802.

[82] A. L. Efros, M. Rosen, *Phys. Rev. Lett.* **1997**, *78*, 1110.

[83] I. S. Osad'ko, I. Y. Eremchev, A. V. Naumov, *J. Phys. Chem. C* **2015**, *119*, 22646.

[84] K. J. Babu, G. Kaur, A. Shukla, R. Saha, A.Kaur, M. Sachdeva, D. K. Yadav, H. N. Ghosh, *ACS Photonics* **2022**, *9*, 969–97.

CHAPTER 6

Unveiling Facet-Controlled Energy Transfer from Individual Perovskite Nanocrystals to Dyes

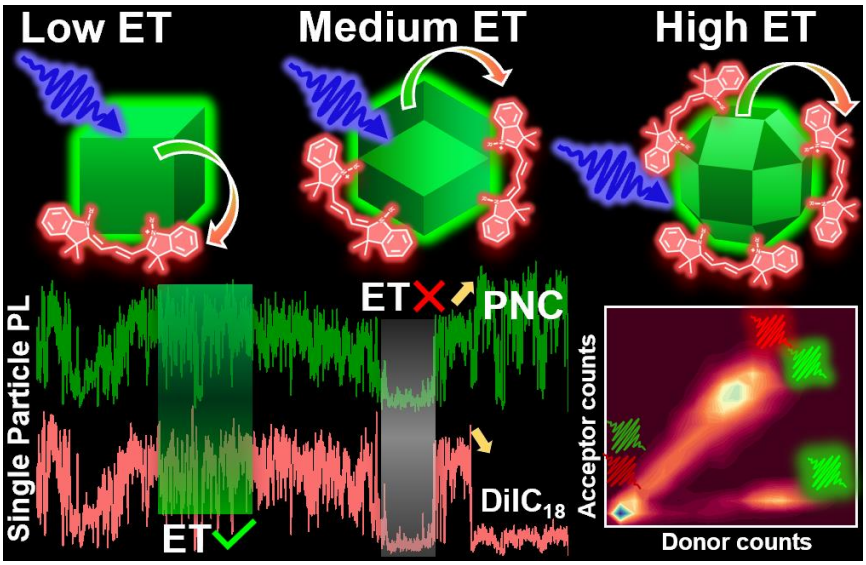

6.1 Abstract

Increasing the number of facets in $CsPbBr_3$ perovskite nanocrystals (PNCs) from 6 to 12 and 26─without significantly changing their surface area markedly enhances energy transfer (ET) efficiency in PNC–dye assemblies, as shown by solution-phase ensemble studies. This enhancement stems from stronger dye binding in facet-rich PNCs, which is supported by fluorescence correlation spectroscopy (FCS). Single-particle ET measurements, however, reveal comparable per-dye ET efficiencies across PNCs with varying facet counts. The transfer is governed by a Dexter mechanism, facilitated by dyes with strong anchoring groups that penetrate the ligand shell and bind directly to the NC surface, thereby eliminating the requirement for the spectral overlap typically necessary in resonant ET. Further studies show that the higher binding affinities of extra-faceted PNCs enable more efficient carrier extraction. Collectively, these findings highlight facet engineering as a versatile strategy to modulate interfacial interactions and enhance performance in applications ranging from photocatalysis to sensing and light harvesting.

6.2 Introduction

Metal halide perovskites ($CsPbBr_3$) gain prominent attention for applications as a light absorber and energy donor to surface bound molecules because of their tunable redox potentials, strong light absorption, high defect tolerance and strong light matter interactions.[1-3] Their compositional tunability further provides a versatile platform for investigating charge and energy transfer processes.[4-7] To expand their utility, recent efforts have focused on hybrid systems that couple PNCs with homogeneous catalysts, such as dyes or transition metal complexes. These nano assemblies exhibit enhanced photocatalytic performance, driven by

efficient ET, strong light absorption of PNCs and the long-lived triplet states of molecular catalysts. [8,9]

Efficient energy transfer (ET), whether short-range Dexter or long-range Förster, depends mainly on how strongly perovskite nanocrystals (PNCs) interact with nearby dye or catalyst molecules. This strong coupling usually happens through linkers or anchoring groups that help the molecules attach tightly to the PNC surface. [10-12] However, a thick ligand shell—while useful for keeping the nanocrystals stable—can block access to the surface. This barrier slows down or even prevents Dexter-type ET, which needs very close contact between donor and acceptor molecules to allow their electron orbitals to overlap. [3,10-11,12-16]

Förster resonance energy transfer (FRET), on the other hand, can occur over longer distances (up to about 10 nanometers) through dipole–dipole interactions, even if the molecules are not directly touching. [17-18] But FRET only works efficiently when the emission spectrum of the donor and the absorption spectrum of the acceptor overlap strongly, and when both transitions have high oscillator strength. Because of these strict requirements, it can be difficult to find suitable dye molecules, which limits the flexibility of FRET-based systems.

The exact way energy transfer happens in PNC–dye systems is still debated because these materials are complex and often vary from sample to sample. Some studies suggest that FRET might play a role, but most evidence supports a Dexter-type mechanism. [10-12,19-23] Unlike FRET, Dexter transfer does not depend on spectral overlap but instead on the spatial overlap of the electronic wave functions of the donor and acceptor. [15,20] When these hybrid states form, the excited energy quickly relaxes to the lower-energy acceptor states through internal conversion.

For photocatalytic systems that rely on Dexter-type transfer, it is important to design the nanocrystal surface carefully. Strong binding between the dye and the PNC, short distances between them, and stable surface structures help increase energy transfer efficiency and improve the overall optical and catalytic performance of perovskite nanocrystals.

We reported improvement of photocatalytic performance in $CsPbBr_3$ PNC–dye conjugates through NC surface engineering, which increases the number of facets in NCs from six (cubic) to twelve (dodecahedral) and twenty-six (rhombicuboctahedral), while maintaining comparable surface area. FCS reveals that facet-rich PNCs exhibit significantly higher binding affinity to the acceptor dye 1,1'-dioctadecyl-3,3,3',3'-tetramethylindocarbocyanine perchlorate (DiIC18), correlating with increased ensemble ET efficiency. Single-particle PL measurements based on stochastic photobleaching steps in $DiIC_{18}$ emission, however, reveal similar per-dye ET efficiencies across nanocrystal (NC) morphologies, indicating that the enhanced ensemble ET performance of facet-rich PNCs arises from their higher dye binding abilities.[12] This work highlights facet engineering as an effective strategy to enhance charge and energy transfer efficiencies via improved surface interactions, evidenced by better carrier harvesting in extra-faceted PNCs by a molecular scavenger. [24-28]

6.3 Synthesis of Extra Faceted Nanocrystals

The synthesis of PNCs with varying facets and similar PLQYs [~ 80% (c6-PNC), ~82% (d12-PNC), ~82% (r-PNC)] involves multiple sequential steps, as outlined below. The synthesis was done following previous reports with slight modifications. [26-28]

6.3.1 Preparation of Caesium-oleate solution

To synthesize Cs-oleate, approximately 86.8 mg of Cs_2CO_3 (~0.26 mmol) was placed in a 25 mL two-neck round-bottom flask along with ~4 mL of ODE and ~0.44 mL of OA. The mixture

was heated to 130 °C for 1 hour under a nitrogen atmosphere. Following this, the temperature was raised to 150 °C and maintained for 15 minutes. After this period, the resulting clear solution containing Cs-oleate was collected and stored in a refrigerator for subsequent use.

6.3.2 Synthesis of 6 Faceted cubic (c6-PNC) morphology

$CsPbBr_3$ nanocrystals with six facets were prepared using a modified hot-injection method based on a reported procedure. About 45 mg PbO (~0.2 mmol), 120 mg phenacyl bromide (~0.6 mmol), 1 mL oleic acid (OA), and 5 mL octadecene (ODE) were placed in a 25 mL three-neck flask, heated to 130 °C under nitrogen, and stirred for 1 hour. The temperature was then increased to 220 °C, followed by the addition of 0.5 mL pre-dried oleylamine (OAm). After 60 seconds, 0.5 mL pre-heated cesium oleate was quickly injected, and the reaction was stopped after 10 seconds by cooling the flask in an ice-water bath. The crude product was centrifuged at 12,000 rpm for 10 minutes, and the solid was redispersed in 3 mL of hexane for further photophysical studies.

6.3.3 Synthesis of 12-Faceted rhombic dodecahedron (d12-PNC) morphology

Twelve-faceted rhombic dodecahedral $CsPbBr_3$ nanocrystals were synthesized using a slightly modified version of a reported hot-injection method. About 45 mg of PbO (~0.2 mmol) and 120 mg of phenacyl bromide (~0.6 mmol) were mixed in 5 mL of pre-dried octadecene (ODE) in a 25 mL three-neck flask. Then, 1 mL each of dried oleic acid (OA) and oleylamine (OAm) were added. The mixture was degassed with nitrogen and heated to 130 °C, stirred for 1 hour, and then the temperature was increased to 220 °C and maintained for another hour. At this point, 0.5 mL of cesium oleate solution was quickly injected, and the reaction continued for 15 minutes before being cooled in an ice-water bath. The resulting bright green product was purified by centrifugation at 8000 rpm for 10 minutes. The solid was redispersed in hexane and

centrifuged again at 3000 rpm for 3 minutes. The clear supernatant was collected for subsequent analysis and photophysical studies.

6.3.4 Synthesis of 26-Faceted rhombicuboctahedron (r26-PNC) morphology

Twenty-six-faceted rhombicuboctahedral perovskite nanocrystals were synthesized following a procedure similar to that of c-PNCs, with minor modifications. Initially, ~45 mg of PbO (~0.2 mmol) and ~120 mg of phenacyl bromide (~0.6 mmol) were combined with 5 mL of ODE and 1 mL of OA in a 25 mL three-neck flask. The mixture was heated to 130 °C under a nitrogen atmosphere and stirred for 1 hour. The temperature was then increased to 220 °C, followed by the addition of 0.5 mL of OAm, and the reaction was annealed for 15 minutes. Subsequently, 0.5 mL of cesium oleate was swiftly injected, and the reaction was allowed to anneal for an additional 45 minutes. The resulting yellowish suspension was quenched in an ice-water bath.

The crude product was purified by centrifugation at 4000 rpm for 10 minutes. The resulting precipitate was redispersed in hexane and stored for photophysical measurements.

6.4 Sample characterisations and preparation of DYE-PNC conjugate

6.4.1 Faceted PNCs

Three different shapes of PNCs: cubic, rhombic dodecahedron, and rhombicuboctahedron having 6, 12, and 26 facets respectively, were successfully synthesized. The TEM images (Figure 5.1 A–C) confirm these morphologies. The corresponding particle size distributions were analysed, ensuring all three structures have comparable surface areas for consistent analysis (Figure 5.1 D–F). The powder XRD patterns were recorded and found to be in good agreement with previously reported results (Figure 5.1 G–I). We have referred cubic, rhombic dodecahedron, and rhombicuboctahedron as c6-PNC, d12-PNC and r26-PNC respectively.

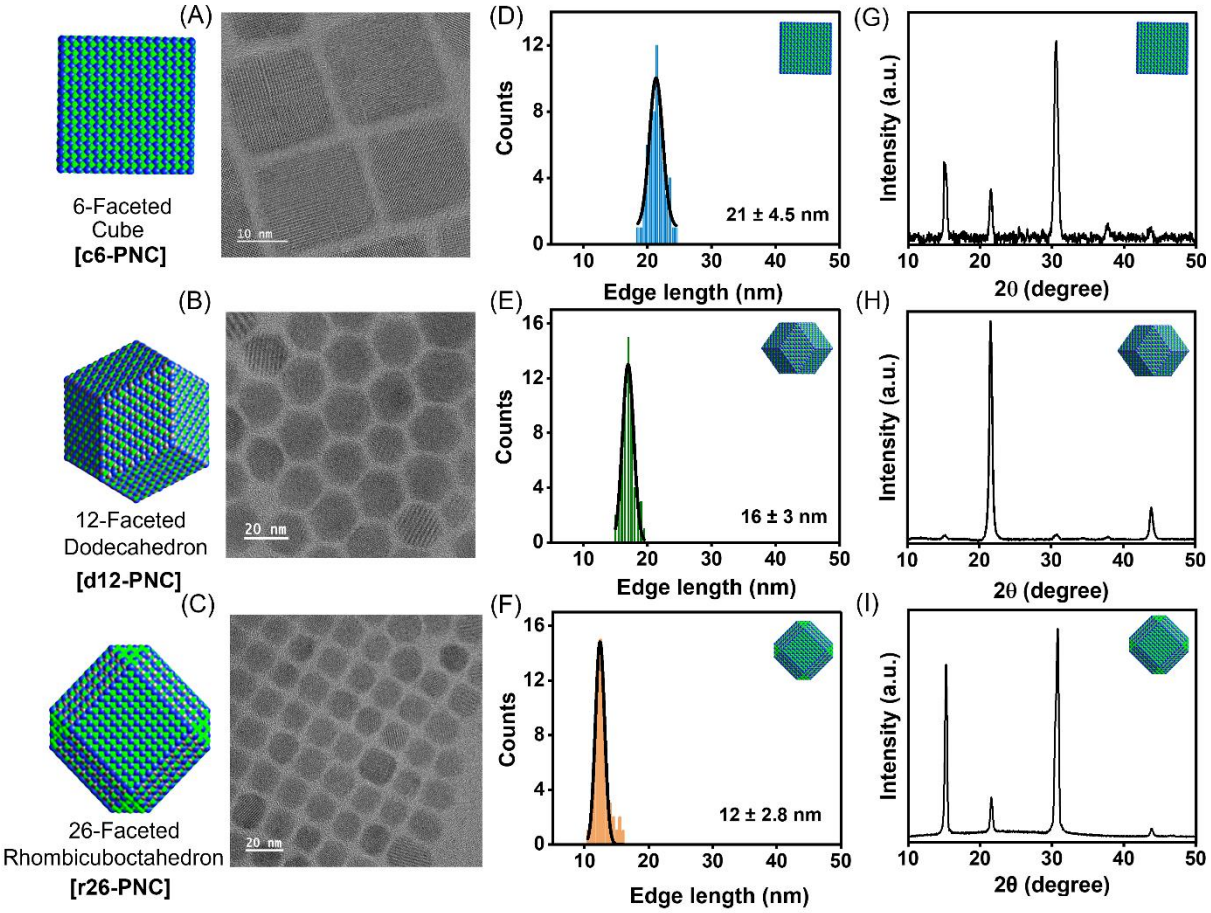

Figure 6.1. (A, B, C) TEM images of $CsPbBr_3$ PNCs with varying facets. Particle size distributions of (D) c6-PNCs (E) d12-PNCs and (F) r26-PNCs derived from TEM images and Powder XRD patterns of (G) c6-PNCs, (H) d12-PNCs, and (I) r26-PNCs exhibit features consistent with previously reported results.

6.4.2 DYE-PNC Complex

We have taken 1,1'-dioctadecyl-3,3,3',3'-tetramethylindocarbocyanine perchlorate ($DiIC_{18}$), dye due to its long hydrocarbon chain [$–(CH_2)_{17}–CH_3$] which is represented as 'R'. The core dye structure consists of two indoline rings (benzopyrrole systems), which are nitrogen-containing aromatic heterocycles responsible for fluorescence and are inherently polar. Similar to oleylamine, the nitrogen-containing polar moiety of $DiIC_{18}$ is expected to directly interact

with the PNC surface, thereby enabling Dexter-type energy transfer. PNCs of this type are known to possess polar facets and a soft lattice, which further supports such interactions.[30] In contrast, the two long, saturated 18-carbon alkyl chains of $DiIC_{18}$ are highly hydrophobic, enabling $DiIC_{18}$ to stably embed within the passivating layer formed by oleic acid and oleylamine. Across different morphologies, the NCs exhibit nearly identical spectral profiles, photoluminescence quantum yields (PLQYs), overlap integrals between NC emissions and $DiIC_{18}$ absorption, and consequently the comparable Förster distances ($R_0 \approx 5.95$ nm).

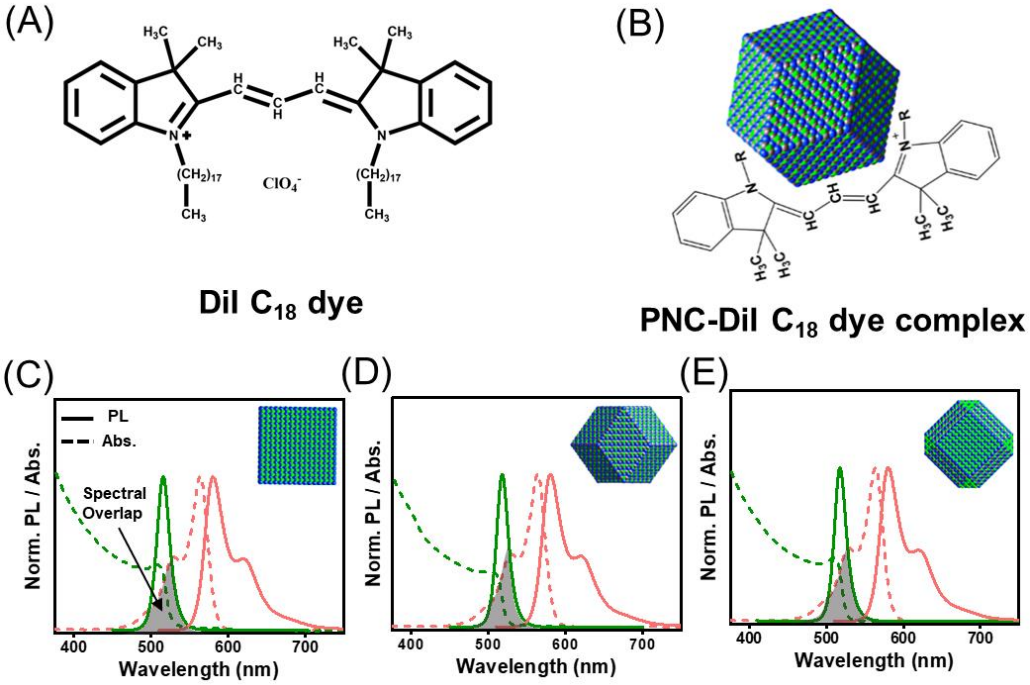

Figure 6.2. (A) Structure of DiIC18 dye, (B) Structure PNC-DiIC18 dye hybrid complex, (C-D) Absorption and emission spectra of different morphological PNCs and dye and their similar spectral overlap region (shown in gray area).

6.5 Results and Discussion

6.5.1 FCS and Double Reciprocal Plot to determine the association constant (K) between dye and PNCs

FCS is a powerful technique for probing the timescales of various processes by analyzing temporal fluctuations in NC PL, including carrier trapping/de-trapping, NC–dye binding/unbinding, diffusion of NCs through the confocal volume, and other dynamic events.[31-32,33-34] In this study, only the NC PL was directed to the detectors by employing a 520 ± 20 nm bandpass filter in combination with a long-pass filter. NC FCS curve offers valuable insights into binding/unbinding dynamics, particularly when the interaction between a NC and a dye molecule induces NC PL intensity changes on timescales faster than diffusion, as a result of energy transfer. The corresponding chemical reaction is shown below.[11]

$$\mathrm{NC\ (bright)} + \mathrm{Dye} \rightleftharpoons \mathrm{NC(dark)} - \mathrm{Dye} \qquad (6.1)$$

If, k_+ and k_- be the association and dissociation rate constants, the equilibrium binding constant K is represented by, $K = k_+/k_-$. [11-12]

When dye is added at varying concentrations to a solution with a fixed concentration of NCs, the initial amplitude of the FCS curves increases progressively (Figure 6.3A-C). This trend is attributed to a corresponding rise in the NC–dye complexation reaction amplitude (A_R, as described in Equation 6.4).[11-12] Assuming that the intrinsic blinking timescale (τ_T) of the NCs remains unchanged upon dye addition, the observed enhancement in the initial correlation amplitude with increasing dye concentration indicates the formation of dynamic NC–dye complexes. Further details on this phenomenon can be found elsewhere.[11-12] The overall fitting equation for the FCS curves of NCs in the presence of dye as follows.[6,11-12]

$$G(\tau) = \frac{1}{(N_A+N_D)}\left[1 + \frac{T}{(1-T)}\exp\left\{-\left(\tau/\tau_T\right)^{\beta}\right\}\right]\left(1+\frac{\tau}{\tau_D}\right)^{-1}\left(1+\frac{\tau}{\kappa^2\tau_D}\right)^{-\frac{1}{2}}(1 + A_R e^{-\frac{\tau}{\tau_R}}) \qquad (6.2)$$

Above equation involves several fitting parameters such as the mean diffusion timescale (τ_D), structural parameter of the excitation volume (κ), complexation timescale (τ_R) and the average number of NCs within the excitation volume in free (N_A) and bound form (N_D). Description of other parameters discussed before. [11-12]

In this study, the experimental conditions ensure that the dye is present in large excess compared to the NC, i.e., [dye] ≫ [NC], allowing the free dye concentration to be approximated as its initial value, [dye] ≈ $[dye]_0$. Under these circumstances, the interaction follows pseudo-first-order kinetics, with the relaxation time τ_R determined by the inverse of the sum of the association and dissociation rate constants (Equation 6.3). [11-12]

$$\tau_R = (K_+ \times [dye]_0 + k_-)^{-1} \qquad (6.3)$$

The diffusion time (τ_D) is assumed to be identical for both free and dye-bound NCs, as dye binding is not expected to significantly impact the overall size or hydrodynamic radius of the NC. Consequently, the NC and NC–dye are treated as rapidly interconverting species with comparable diffusion coefficients, and their exchange occurs on a timescale much faster than that of diffusion.[11-12]

From the fitting of NC FCS curves by Equation 6.2 yields A_R, which depends on dye concentration as shown in the inset of Figure 6.3A-C and Equation 6.4. Fitting A_R vs [dye] curves to Equation 6.4 yields equilibrium binding constant K. Values of K for different PNC-dye complexes are reported in the inset of Figure 6.3A-C.[11-12]

$$A_R = \frac{K[dye]_0(1-I)^2}{(1+I\times K[dye]_0)^2} \qquad (6.4)$$

Here, I denotes the ratio of PL intensities of NCs in the dye-bound and free states, calculated from the ratio of the integrated areas under the NC PL spectra recorded in the presence of the highest dye concentration and in the absence of dye. While derived K values are reported in Figure 6.3A-C and other fitting parameters for c6-, d12- and r26-PNCs are reported.

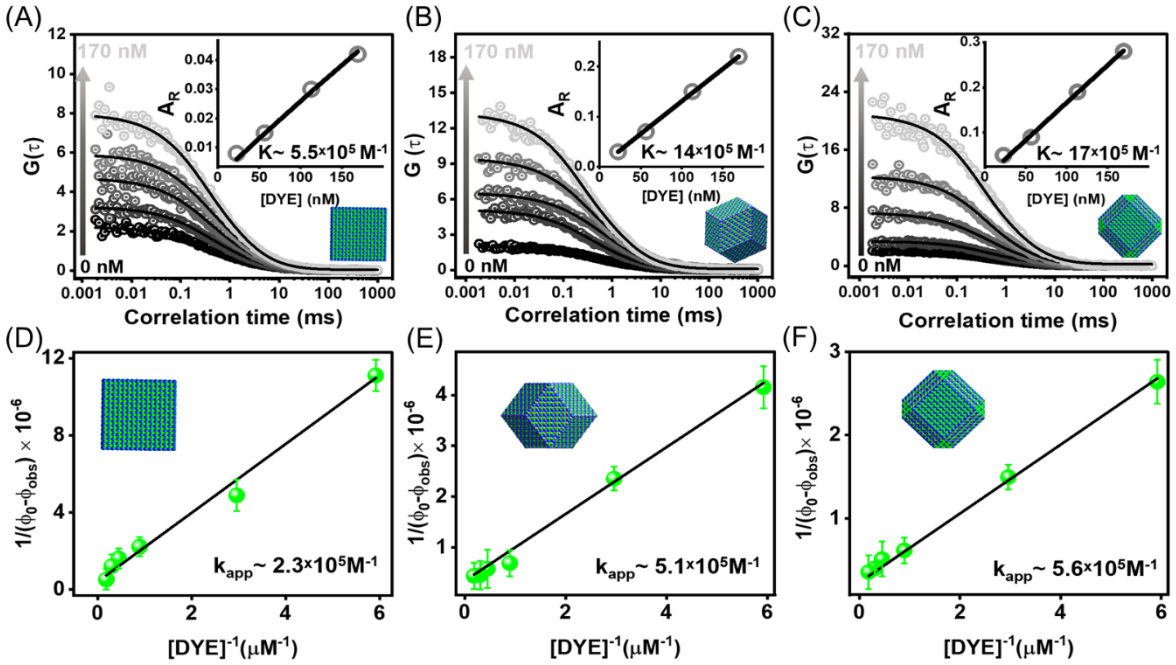

Figure 6.3. (A-B) FCS curves of PNCs in toluene at varying $DiIC_{18}$ concentrations (0–0.17 μM), excited at ~375 nm with low excitation power (~2 W/cm^2). Insets show the FCS amplitude of the complexation reaction (A_R) versus $DiIC_{18}$ dye concentration; fitting yields binding constant *K, which increases with facets. (C-D)* Double-reciprocal plots fitted to Equation 6.5 yield apparent binding constants for NC–$DiIC_{18}$ complexes. The results indicate stronger binding of $DiIC_{18}$ with extra-faceted PNCs.

Originally introduced by Benesi and Hildebrand, the double-reciprocal plot based on PL data is a widely used method for determining binding constants.[18] In this work, the apparent binding constant (K) representing the solution phase interaction between $DiIC_{18}$ and PNC was estimated using equation 6.5.

$$\frac{1}{\Phi_0-\Phi_{obs}} = \frac{1}{\Phi_0-\Phi'_{obs}} + \frac{1}{(\Phi_0-\Phi'_{obs})K}\frac{1}{[Q]} \quad (6.5)$$

In the above equation, Φ_0 represents the PLQY of the PNCs in the absence of $DiIC_{18}$, while Φ_{obs} denotes the PLQY of PNCs at a given $DiIC_{18}$ concentration. Similarly, Φ_{obs}' refers to the PLQY at the highest $DiIC_{18}$ concentration. [Q] indicates the concentration of the quencher ($DiIC_{18}$) at each titration point. Equation 6.5 follows a linear relationship, therefore a straight-line fitting (y = mx + c) to "$1/(\Phi_0 - \Phi_{obs})$ vs. 1/[Q]" plot enabling the estimation of the apparent binding constant (k_{app}) (Figure 6.3D-F). k values are reported within the Figure 6.3D-F.

6.5.2 Dexter energy transfer efficiency in different faceted PNCs: Steady state analysis

We first performed ensemble studies to confirm ET-induced quenching of PNC PL by $DiIC_{18}$ dye. At a fixed PNC concentration (~75 nM) in hexane, increasing bulk dye concentration (≈2–40X relative to PNCs) resulted in gradual quenching of PNC PL, enhanced $DiIC_{18}$ emission, and the emergence of an isoemissive point in area-normalized spectra—indicative of ET from PNCs to $DiIC_{18}$ dye (Figures 6.4 A-C).[35] Excited-state PL dynamics show a $DiIC_{18}$ induced decrease in PNC lifetimes, accompanied by a similarly scaled rise in $DiIC_{18}$ emission—both accelerating with increasing $DiIC_{18}$/PNC ratio—strongly supporting ET (Figures 6.4 A-C).[35] The PL-excitation (PLE) spectrum of the PNC-$DiIC_{18}$ system below 526 nm regime, monitored near the $DiIC_{18}$ emission peak (~580 nm), predominantly mirrors PNC PLE spectrum, indicating ET from photoexcited PNC to dye at λ_{ex} <526 nm . In contrast, the 526–575 nm region resembles the PLE spectrum of $DiIC_{18}$ alone, suggesting direct excitation of the dye. [10] All these observations collectively confirm the occurrence of ET from the PNC to $DiIC_{18}$.

The ET efficiencies (Φ_{ET}) of PNC-$DiIC_{18}$ complexes in bulk are calculated using $\Phi_{ET} = 1 - I/ I_o$, where *I* and I_o are the PNC PL intensities in the presence and absence of $DiIC_{18}$. As

shown in Figure 6.4 G, Φ_{ET} increases with increasing the number of facets in PNC, a trend that intensifies at higher $DiIC_{18}$/PNC ratios.

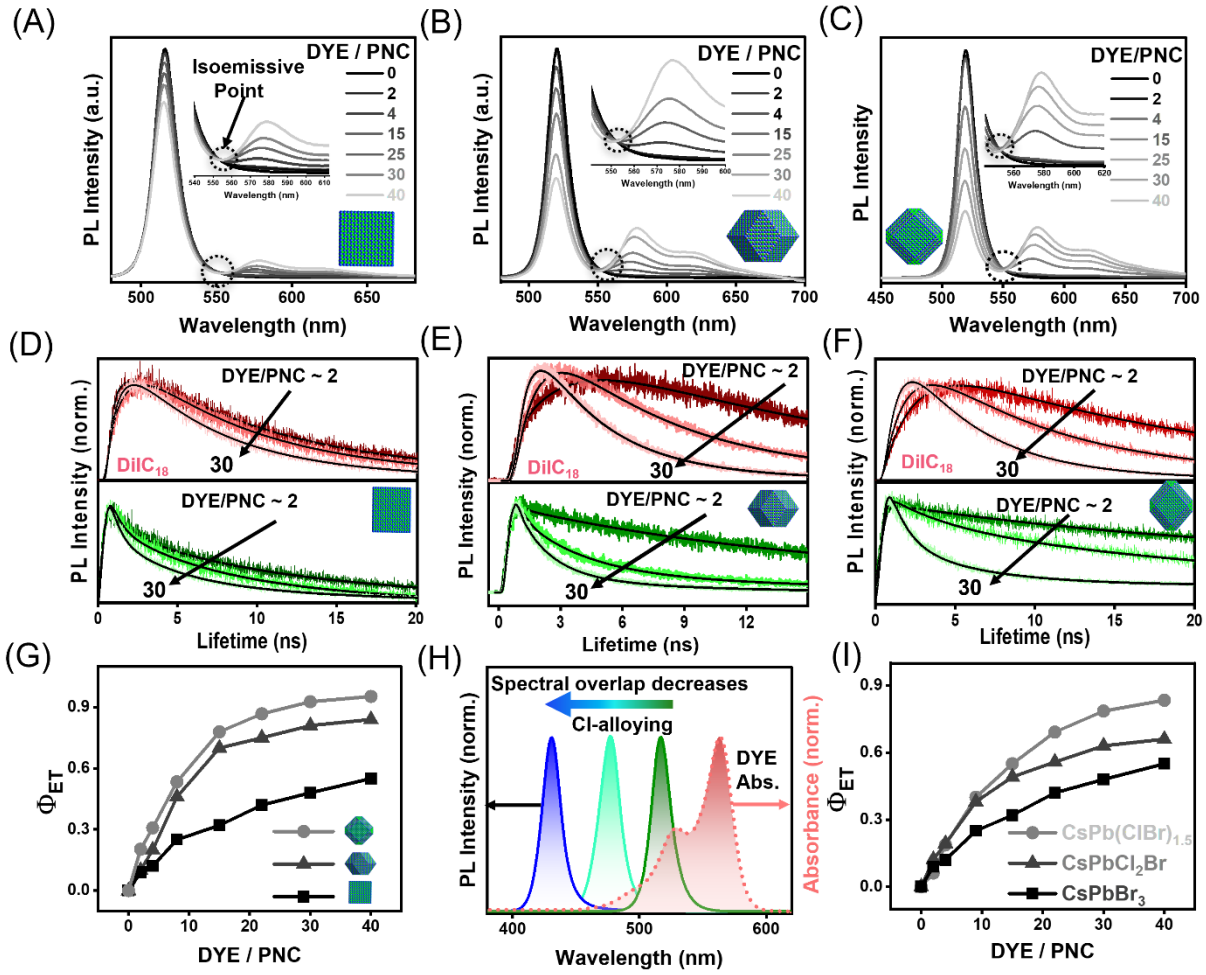

Figure 6.4. (A–C) Area-normalized PL spectra of c6-/d12-/r26-PNC–$DiIC_{18}$ systems in hexane showing iso-emissive points, confirming ET (λ_{ex}~ 375 nm). (D-F) TRPLs of $DiIC_{18}$ dye (red) and PNC (green) in PNC–$DiIC_{18}$ systems, recorded at their respective PL peaks at varying dye/PNC ratio (λ_{ex}~ 375 nm). (G) PNC PL quenching efficiency vs. dye/PNC ratio. All these observations suggest ET from PNC to the dye proceeds via the singlet state. (H, I) Gradual Cl alloying of c6-PNC reduces spectral overlap, yet ET efficiency remains comparable or higher than in undoped PNCs (I), suggesting a Dexter-type mechanism.

The enhanced Φ_{ET} observed for extra-faceted PNCs is attributed to their higher dye-binding capacity compared to regular cubic NCs at a fixed $DiIC_{18}$/PNC ratio. This is consistent with the FCS study and suggests that the binding potential and consequently the catalytic efficiency of PNCs increases with increasing the number of facets. To establish the energy transfer pathway either FRET or Dexter we have alloyed $CsPbBr_3$ with Cl and gradually reduces the spectral overlap with the acceptor absorption (Figure 6.4 H).

The efficiency (Figure 6.4 I) after Cl alloying does not differ much with the normal $CsPbBr_3$ confirms our PNC to dye energy transfer occurs via dexter pathway. Dexter ET can occur even when the spectral overlap between PNC PL and dye absorption is minimal. $DiIC_{18}$, which contains indoline (benzopyrrole) units within its conjugated framework, was selected due to its strong binding affinity to the PNC surface — a key requirement for achieving sufficient spatial overlap between PNC and dye wavefunctions to enable this transfer.

6.5.3 Energy transfer in single particle dimension from PNC QD to dye molecules

To investigate donor–acceptor spatial and temporal correlations at the single-particle level, pM-concentration PNCs in PMMA (~0.5 (w/v) % in toluene) with ~2 μM $DiIC_{18}$ dye were spin-coated onto a coverslip. Emissions from individual PNCs and attached dyes were recorded in confocal microscope using a spectrally resolved two-channel HBT scheme: the green channel (520±20 nm bandpass) captured donor PL, and the red channel (570 nm long-pass) detected acceptor emission (Figure 6.5F). Discrete bright spots in confocal image of the green channel confirm emission from isolated single PNCs, as verified by antibunching analysis (Figures 6.5A). In the red channel, a constant background from dye emission due to finite absorption at 375 nm by the dense dye layer is accompanied by localized spots spatially aligned with green-channel emitters, indicating ET from PNC to dye (Figure 6.5A). This suggests that PNCs can function as optical antennas in photocatalytic reactions.[36]

The donor-channel PL trajectory exhibits typical nanoparticle blinking, which is also reflected in the acceptor-channel PL trajectory with high correlation, supporting ET (Figure 6.5 B).[12,37-45] Three distinct donor–acceptor PL correlations are highlighted and further quantified by (1) grey-shaded regions in the PL trajectories (Figure 6.5B) and (2) cluster states marked with board pins in the 2D intensity correlation map derived from donor-acceptor PL traces (Figure 6.5 D): (i) PNC in a dark state with no ET—both donor and acceptor channels are off [left grey slab (Figure 6.5 B) and pin 2 (Figure 6.5 D)]; (ii) PNC in a bright state with active ET—both channels emit (middle grey slab/pin 1); and (iii) dye photobleaching deactivates ET—donor PL increases, while acceptor emission is suppressed (right grey slab/pin 3).

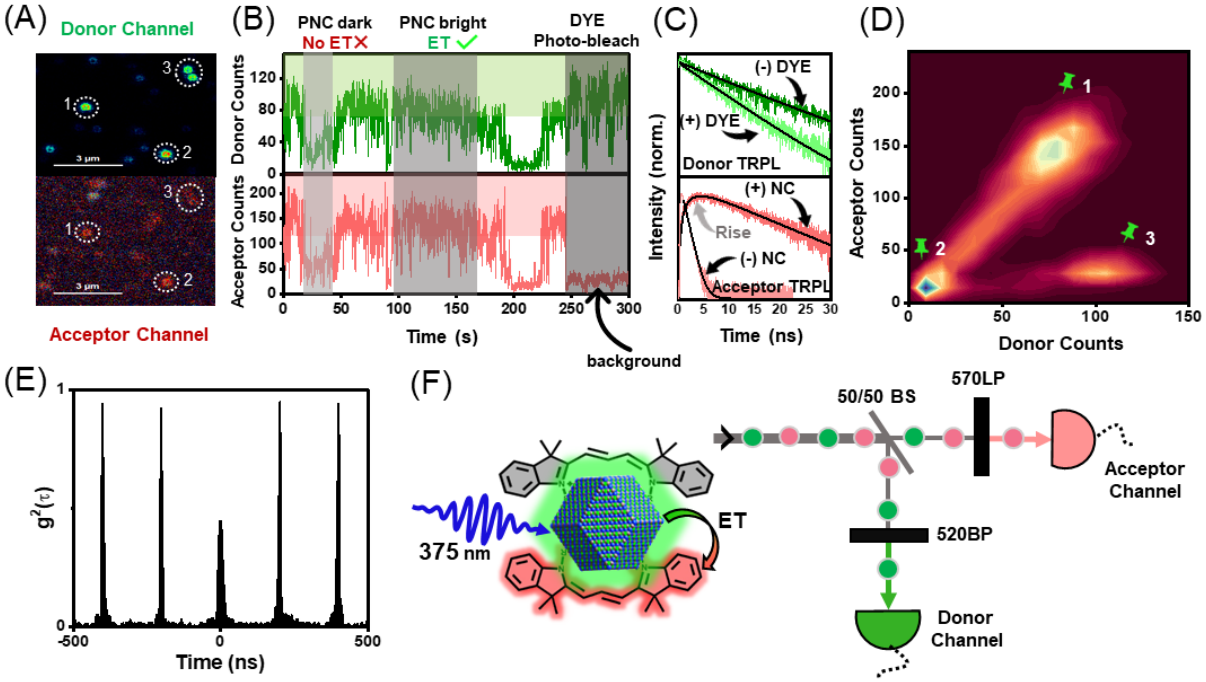

Figure 6.5. (A) Confocal images showing co-localized green PL from d12-PNCs and red PL from $DiIC_{18}$ (λex~375 nm, I_P ~2 W/cm^2). (B) PL intensity trajectories with 50 ms bin time exciting donor only (λex~375 nm) reveal three temporal behaviors: (i) donor in dark state—no ET, no acceptor PL (left-grey slab); (ii) donor in bright state—ET induces acceptor PL (middle-grey slab); (iii) acceptor bleached—enhanced donor PL, no acceptor PL (right grey slab). (C) TRPL of donor channel shows lifetime quenching before dye bleaching, accompanied with rise

component in TRPL of acceptor's channel, indicating ET. Acceptor channel TRPL without PNC shows no rise. (D) 2D donor-acceptor intensity correlation map highlighting three correlation regimes reflecting ET (board pin 1), non-ET (board pin 2) and dye photobleaching (board pin 3). (E) Second-order donor–acceptor PL correlation function [$g^2(\tau)$] exhibits antibunching, confirming ET which results in anticorrelated donor-acceptor emissions (λ_{ex}~375 nm). (F) Schematic of energy transfer in the PNC–dye system and the two-arm Hanbury Brown and Twiss (HBT) scheme used for donor–acceptor PL correlation study.

Beyond the nanometer-scale spatial correlation (Figure 6.5A) and millisecond-scale temporal correlation in PL trajectories and intensity map (Figures 6.5B,D), stronger evidence for ET is provided by donor lifetime quenching and a concomitant rise in the acceptor TRPL (Figure 6.5C). Additionally, photon arrival times in two channels show anticorrelated behaviour in the antibunching analysis (Figures 6.5E,F), consistent with ET: a photoexcited PNC can decay radiatively or transfer energy to the dye, but not both, resulting in photon emission from either of the two channels.[46-47] The donor–acceptor $g^2(\tau)$ trace recorded from a bright spot in Figure 6.5A, however, exhibits only partial antibunching, most likely due to the combined effects of biexciton emission from the PNC and uncorrelated background emission from the dye film resulting from direct excitation of the dyes (Figure 6.5E).[12,28]

6.5.4 Quantifying per dye efficie3ncy by step bleaching in acceptor channel

Determining per-dye ET efficiency through single-particle studies is essential to confirm that discrepancies in ensemble ET efficiency across different morphologies at a given dye/PNC ratio arise from variations in dye loading per PNC (Figure 6.4 G). In single-particle analysis, the actual number of dyes surrounding each PNC is inferred from step-like

photobleaching events in the acceptor-channel PL trajectory (Figure 6.5 A-C).[48-53] Statistical analysis of ~30-40 PNCs shows that an average of ~1.0, ~1.3, and ~1.5 $DiIC_{18}$ dyes ($<N>_{dye}$) are attached to a c6-, d12-, and r26-PNC, respectively, at a fixed dye concentration of ~2 μM in the spin-coating solution (Figures 6.6D, 6.7A,B).

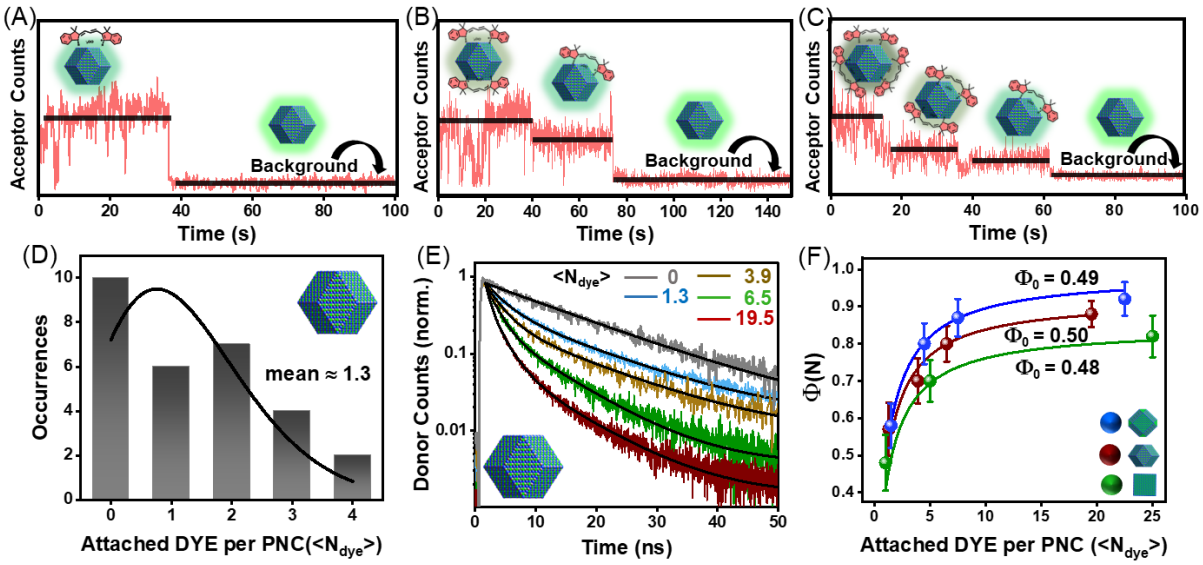

Figure 6.6. (A–C) Acceptor-channel PL trajectories recorded on individual d12-PNCs (bright spots in Figure 6.4A) bound to varying numbers of dyes (1-3) show stepwise photobleaching, with each step corresponding to a single dye bleaching. (D) Histogram of dye counts per d12-PNC, fitted with a Poisson distribution, yields ~1.3 as mean number of dyes attached per d12-PNC ($<N>_{dye}$) at ~2 μM dye concentration in spin coating solution. (E) Representative TRPL traces of single d12-PNCs without dye (grey) and with increasing dye loading in spin coating solution (blue to maroon). (F) Average single-particle ET efficiency [Φ(N)] vs. $<N>_{dye}$, fitted using Equation 6.2, yielding a near consistent per-dye efficiency $E_0 \approx 0.49$ across PNC morphologies.

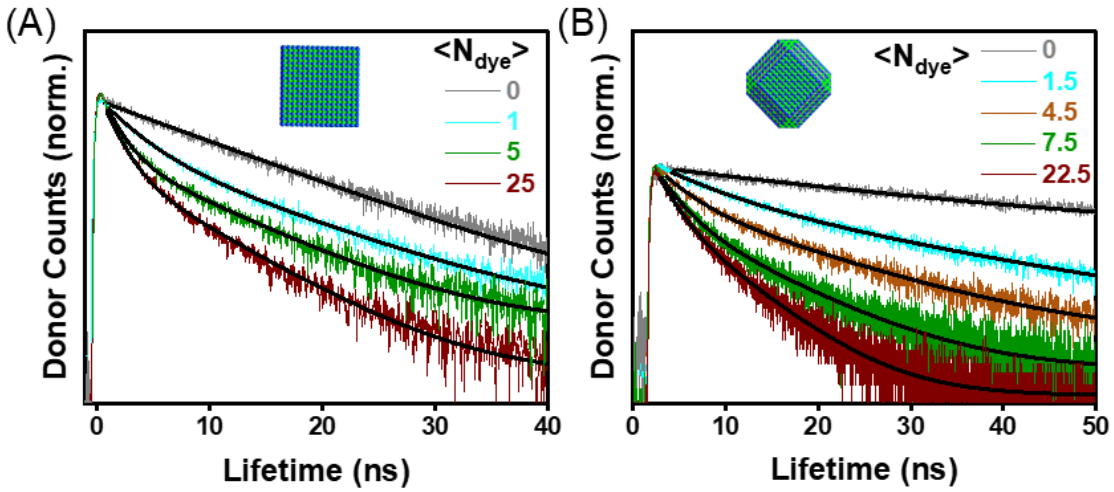

Figure 6.7. Single particle TRPL traces of (a) c6-PNC and (b) r26-PNC without dye (grey) and with increasing dye loading in spin coating solution (blue to maroon) which consequently represent how the single particle donor lifetime changes with gradual increase in number of dyes attached to it [$<N>_{dye}$].

The higher number of attached dyes [$<N>_{dye}$] for extra-faceted PNCs indicates that their enhanced binding affinity persists even in the solid state. These $<N>_{dye}$ values, determined at low dye concentration (~2 μM) in spin coating solution, were used to estimate $<N>_{dye}$ at higher dye concentrations, assuming $<N>_{dye}$ increases linearly with dye concentration in spin coating solution. Single particle TRPL traces in Figure 6.6E represent the donor lifetimes of d12-PNC–dye systems as a function of $<N>_{dye}$, each trace representing an average decay profile from at least ~30 individual measurements. Figure 6.7 shows corresponding data for the other two PNC morphologies. The single-particle ET efficiency Φ(N) is calculated from the average single-particle lifetimes of PNCs without (τ_0) and with $<N>_{dye}$ dyes attached to a PNC (τ_N) using the following equation (Figure 6.6F). [12,54]

$$\Phi(N) = 1 - \tau_N/\tau_0 \qquad (6.1)$$

Subsequently, fitting the Φ(N) vs. $\langle N \rangle_{dye}$ curve with Equation 6.2, assuming identical transfer rates to each attached dye, yields the ET efficiency [Φ_0] for a PNC attached to one dye molecule (Figure 6.6F).[12,54]

$$\Phi(N) = \frac{N \times \Phi_0}{1+(N-1)\times\Phi_0} \quad (6.2)$$

Fitting reveals near identical Φ_0 or per-dye ET efficiency (~0.49) across PNC morphologies, in sharp contrast to solution-phase results (Figure 6.4G vs. 6.6F). Facet dependent transfer efficiency in solution arises from a higher number of dyes binding to facet-rich PNCs in solution at a given dye/PNC ratio (Figure 6.4 G). In single-particle studies at near-unity dye-to-PNC ratios, $\langle N \rangle_{dye}$ can be accurately determined via stochastic photobleaching steps, consequently, yielding consistent Φ(N) [≈ Φ_0] across all morphologies (Figure 6.6F). At higher $\langle N \rangle_{dye}$, however, extra-faceted PNCs exhibit slightly elevated Φ(N), likely due to an underestimation in $\langle N \rangle_{dye}$ arising from their higher dye-binding capacity- an effect retained even after spin coating involving high mechanical force.

6.5.5 Hole transfer efficiency from Faceted PNCs to NMA

In the following section, we examine how facet engineering can benefit real applications by imparting high binding affinity to extra-faceted PNCs. From the perspective of light-harvesting applications, efficient interfacial charge transfer is of paramount importance. To probe this, we designed a model hybrid system comprising PNCs and the molecular hole scavenger N-methylaniline (NMA), where the hole transfer efficiency (Φ_{HT}) is investigated as a function of PNC facets.[24,56-61] Three PNC morphologies with similar concentrations (~13 nM) were dispersed in hexane, and TRPLs were recorded using TCSPC (90 ps IRF) under identical conditions and fixed data acquisition time before and after adding fixed concentration NMA (~3.7 mM). The initial TRPL amplitude decreased from A_0 to A_{NMA} upon ~3.7 mM NMA

addition, with a more pronounced reduction for extra faceted PNCs—indicating greater fraction of excited-state depopulation in facet rich PNCs via ultrafast (~3 ps) hole transfer (Figure 6.8A-C). Although the transfer timescale is too fast to resolve directly in TCSPC, the amplitude drop, however, allows estimation of Φ_{HT} using the following equation:[62]

$$\Phi_{HT} = 1 - \frac{A_{NMA}}{A_0} \quad (3)$$

As expected, Φ_{HT} increases from 0.08 to 0.40 and 0.50 at ~3.7 mM NMA as the number of facets rises from 6 to 12 and 26, respectively, attributed to a higher number of bound NMA molecules in facet-rich NCs.

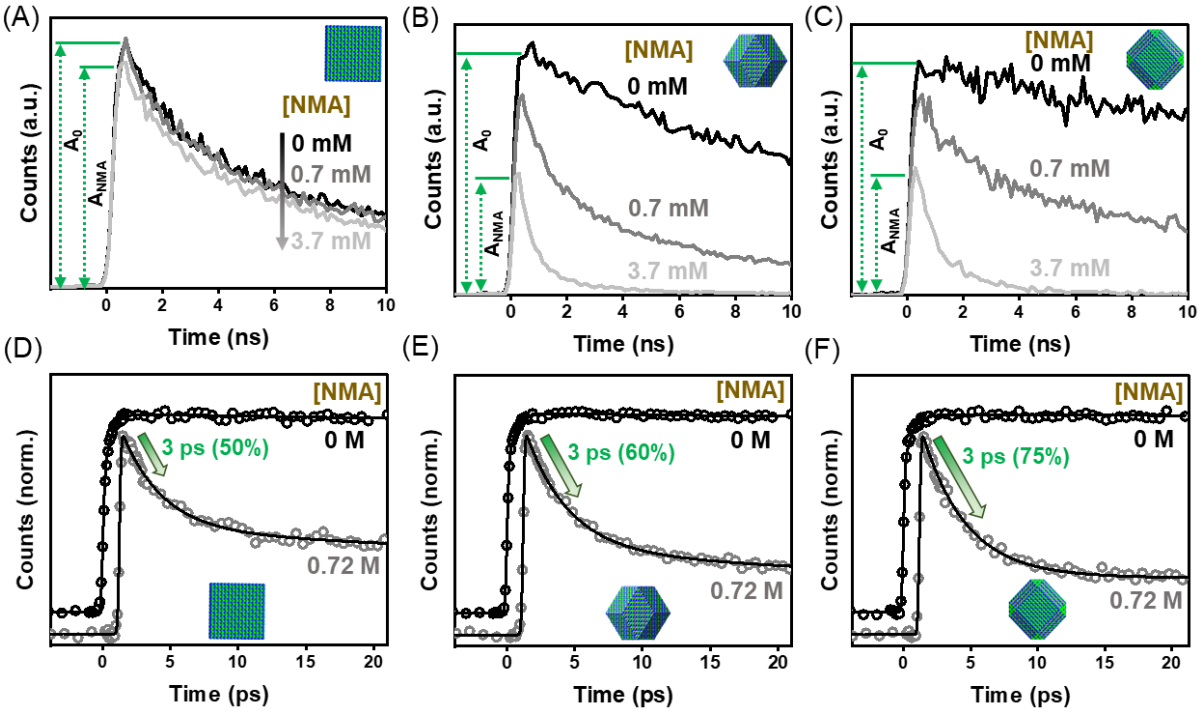

Figure 6.8. TRPLs of PNCs dispersed in hexane under varying NMA concentrations recorded in TCSPC (upper panel) and femtosecond upconversion (lower panel). Y-axis is in linear scale. Samples were excited at 405 nm and TRPLs were recorded at their respective PL maxima.

This is further corroborated by femtosecond upconversion measurements (IRF ~0.3 ps), which reveal the emergence of an ultrafast quenching component (~3 ps) in the PNC PL at high NMA

concentration (~720 mM), attributable to hole transfer from photoexcited PNC to NMA (Figure 6.8D-F). The use of high NMA concentration ensures that, at the moment of photoexcitation, nearly all PNCs encounter NMA in their immediate vicinity, thereby excluding any contribution from solvent diffusion to the quenching dynamics. Notably, the amplitude of this ultrafast hole-transfer component increases with the number of facets at a fixed NMA concentration, indicating that a larger number of NMA molecules bind to each PNC as the facet count increases (Figure 6.8D-F). This observation aligns with the enhanced binding capacity of extra-faceted PNCs, as evidenced by FCS and complementary studies.

6.9 Conclusion

Facet-rich $CsPbBr_3$ PNCs exhibit strikingly enhanced energy and charge transfer efficiencies in solution, driven primarily by their exceptional dye-binding affinity. Single-particle ET measurements demonstrate comparable per-dye transfer efficiencies across morphologies, unequivocally confirming that the superior performance of extra-faceted PNCs in solution arises from their uniquely increased dye-loading capacity. The practical significance of these extra-faceted NCs is further underscored by carrier extraction studies, in which facet-rich NCs dramatically outperform their cubic counterparts. These findings not only highlight the transformative impact of facet engineering on interfacial interactions but also establish extra-faceted $CsPbBr_3$ PNCs as exceptionally promising candidates for high-performance photovoltaic, photocatalytic, and light-harvesting applications.

6.10 References

[1] J. S. Martin, N. Dang, E. Raulerson, M. C. Beard, J. Hartenberger, Y. Yan, *Angew. Chem., Int. Ed.* **2022**, *134*, 202205572.

[2] S. Biswas, M. K. Panda, S. Chatterjee, J. Satra, S. K. Sharma, J. Rath, A. Dutta, D. Acharjee, S. Chakraborty, S. Ghosh, N. Mishra, *Adv. Funct. Mater.* **2025,** 2505506 (1-17).

[3] J. T. DuBose, P. V. Kamat, *ACS Energy Lett.* **2022**, *7*, 1994-2011.

[4] K. Wu, G. Liang, Q. Shang, Y. Ren, D. Kong, T. Lian, *J. Am. Chem. Soc.* **2015**, *137*, 12792–12795.

[5] A. De, S. Das, A. Samanta, *ACS Energy Lett.* **2020**, *5*, 2246–2252.

[6] M. K. Panda, D. Acharjee, A. B. Mahato, S. Ghosh, *Small* **2024**, *20*, e2311559.

[7] D. Acharjee, A. Das, M. K. Panda, M. Barai, S. Ghosh, *Nano Lett.* **2023**, *23*, 1946–1953.

[8] X. Luo, R. Lai, Y. Li, Y. Han, G. Liang, X. Liu, T. Ding, J. Wang, K. Wu, *J. Am. Chem. Soc* **2019**, *141*, 4186–4190.

[9] J. Chakkamalayath, A. Chemmangat, J. T. DuBose, P. V. Kamat, *Acc. Chem. Res.* **2025**, *58*, 1461–1472.

[10] M. Kurashvili, J. Llusar, L. S. Stickel, T. Würthner, D. Ederle, I. Infante, J. Feldmann, Q. A. Akkerman, *Angew. Chem.* **2025**, *64*, e202420658.

[11] F. J. Hofmann, M. I. Bodnarchuk, D. N. Dirin, J. Vogelsang, M. V. Kovalenko, J. M. Lupton, *Nano Lett.* **2019**, *19*, 8896–8902.

[12] L. G. Feld, S. C. Boehme, V. Morad, Y. Sahin, C. J. Kaul, D. N. Dirin, G. Rainò, M. V. Kovalenko, *ACS Nano* **2024**, *18*, 9997–10007.

[13] X. Luo, G. Liang, Y. Han, Y. Li, T. Ding, S. He, X. Liu, K. Wu, *J. Am. Chem. Soc.* **2020**, *142*, 11270–11278.

[14] H.-H. Cho, D. G. Congrave, A. J. Gillett, S. Montanaro, H. E. Francis, V. Riesgo-Gonzalez, J. Ye, R. Chowdury, W. Zeng, M. K. Etherington, J. Royakkers, O.

[15] Millington, A. D. Bond, F. Plasser, J. M. Frost, C. P. Grey, A. Rao, R. H. Friend, N. C. Greenham, H. Bronstein, *Nat. Mater.* **2024**, *23*, 519–526.

[16] D. J. Dexter, *J. Chem. Phys.* **1953**, *21*, 836.

[17] A. Cortés-Villena, A. Cadranel, K. Azizi, T. Torres, D. M. Guldi, J. Pérez-Prieto, R. E. Galian, *Adv. Sci.* **2025**, *12*, e2414831.

[18] N. Hildebrandt, C. M. Spillmann, W. R. Algar, T. Pons, M. H. Stewart, E. Oh, K. Susumu, S. A. Diaz, J. B. Delehanty, I. L. Medintz, *Chem. Rev.* **2017**, *117*, 536−711.

[19] M. Cardoso Dos Santos, W. R. Algar, I. L. Medintz, N. Hildebrandt, *Anal. Chem.* **2020**, *125*, 115819.

[20] M. G. Greiner, A. Singldinger, N. A. Henke, C. Lampe, U. Leo, M. Gramlich, A. S. Urban, *Nano Lett.* **2022**, *22*, 6709−6715.

[21] A. Loiudice, S. Saris, R. Buonsanti, *J. Phys. Chem. Lett.* **2020**, *11*, 3430−3435.

[22] J. T. DuBose, P. V. Kamat, *J. Am. Chem. Soc.* **2023**, *145*, 4601-4612.

[23] F. J. Hofmann, M. I. Bodnarchuk, L. Protesescu, M. V. Kovalenko, J. M. Lupton, J. Vogelsang, *J. Phys. Chem. Lett.* **2019**, *10*, 1055−1062.

[24] J. T. DuBose, P. V. Kamat, *J. Am. Chem. Soc.* **2021**, *143*, 19214−19223.

[25] A. Das, D. Acharjee, M. K. Panda, A. B. Mahato, S. Ghosh, *J. Phys. Chem. Lett.* **2023**, *14*, 3953–3960.

[26] U. Mandal, S. Ghosh, S. Dey, A. Adhikari, K. Bhattacharyya, *J. Chem. Phys.* **2008**, *128*. 164505.

[27] S. Bera, R. K. Behera, N. Pradhan, *J. Am. Chem. Soc.* **2020**, *142*, 20865−20874.

[28] S. K. Bera, S. Bera, M. Shrivastava, N. Pradhan, K. V. Adarsh, *Nano Lett.* **2022**, *22*, 8908–8916.

[29] T. Titus, E. K. Vishnu, A. Garai, S. K. Dutta, K. Sandeep, A. Shelke, T. G. Ajithkumar, A. Shaji, N. Pradhan, K. G. Thomas, *Nano Lett.* **2024**, *24*, 10434–10442.

[30] L. Protesescu, S. Yakunin, M. I. Bodnarchuk, F. Krieg, R. Caputo, C. H. Hendon, R. X. Yang, A. Walsh, M. V. Kovalenko, *Nano Lett.* **2015**, *15*, 3692−3696.

[31] X. Zhu, Y. Lin, Y. Sun, M. C. Beard, Y. Yan, *J. Am. Chem. Soc.* **2019**, *141*, 733−738.

[32] M. K. Panda, D. Acharjee, N. Nandi, S. Koley, S. Ghosh, *Chem. - Eur. J.* **2024**, *30*, No. e202401938.

[33] T. Ahmed, S. Seth, A. Samanta, *ACS Nano* **2019**, *13*, 13537-13544.

[34] W. Al-Soufi, B. Reija, M. Novo, S. Felekyan, R. Kühnemuth, C. A. Seidel, *J. Am. Chem. Soc.* **2005**, *127*, 8775-8784.

[35] S. Sharma, N. Pal, P. K. Chowdhury, S. Sen, A. K. Ganguli, *J. Am. Chem. Soc.* **2012**, *134*, 19677–19684.

[36] S. Ghosh, K. Bharadwaj, S. Koley, S. Jana, *Chem. Asian J.* **2018**, *13*, 3296–3303.

[37] S. Saris, A. Loiudice, M. Mensi, R. Buonsanti, *J. Phys. Chem. Lett.* **2019**, *10*, 7797–7803.

[38] A. L. Efros, D. J. Nesbitt, *Nat. Nanotechnol.* **2016**, *11*, 661−671.

[39] M. Nirmal, B. O. Dabbousi, M. G. Bawendi, J. J. Macklin, J. K. Trautman, T. D. Harris, L. E. Brus, *Nature* **1996**, *383*, 802−804.

[40] J. Seufert, M. Rambach, G. Bacher, A. Forchel, T. Passow, D. Hommel, *Appl. Phys. Lett.* **2003**, *82*, 3946−3948.

[41] Y. Barak, I. Meir, A. Shapiro, Y. Jang, E. Lifshitz, *Adv. Mater.* **2018**, *30*, No. e1801442.

[42] G. Yuan, D. E. Gómez, N. Kirkwood, K. Boldt, P. Mulvaney, *ACS Nano* **2018**, *12*, 3397–3405.

[43] S. Bera, A. Tripathi, T. Titus, N. M. Sethi, R. Das, Afreen, K. V. Adarsh, K. G. Thomas, N. Pradhan, *J. Am. Chem. Soc.* **2024**, *146*, 20300–20311.

[44] Y.-S. Park, S. Guo, N. S. Makarov, V. I. Klimov, *ACS Nano* **2015**, *9*, 10386–10393.

[45] T. Kim, S. I. Jung, S. Ham, H. Chung, D. Kim, *Small* **2019**, *15*, e1900355.

[46] A. A. Cordones, S. R. Leone, *Chem. Soc. Rev.* **2013**, *42*, 3209–3221.

[47] G. Lubin, D. Oron, U. Rossman, R. Tenne, V. J. Yallapragada, *ACS Photonics* **2022**, *9*, 2891−2904.

[48] J. M. Lupton, J. Vogelsang, *Appl. Phys. Rev.* **2021**, *8*, 041302-1.

[49] M. H. Ulbrich, E. Y. Isacoff, *Nat. Methods* **2007**, *4*, 319−321.

[50] C. Y. Li, S. Duan, J. Yi, C. Wang, P. M. Radjenovic, Z. Q. Tian, J. F. Li, *Sci. Adv.* **2020**, *6*, No. eaba6012.

[51] W. B. Asher, P. Geggier, M. D. Holsey, G. T. Gilmore, A. K. Pati, J. Meszaros, D. S. Terry, S. Mathiasen, M. J. Kaliszewski, M. D. McCauley, et al. *Nat. Methods* **2021**, *18*, 397−405.

[52] R. J. Arant, M. H. Ulbrich, *ChemPhysChem* **2014**, *15*, 600−605.

[53] L. Mockl, W. E. Moerner, *J. Am. Chem. Soc.* **2020**, *142*, 17828−17844.

[54] T. Ha, P. Tinnefeld, *Annu. Rev. Phys. Chem.* **2012**, *63*, 595−617.

[55] I. Medintz, N. Hildebrandt, *FRET − Förster Resonance Energy Transfer*; **2013**, DOI: 10.1002/9783527656028.

[56] K. Mishra, M. Barai, S. Ghosh, *J. Phys. Chem. C* **2022**, *126*, 16905–16918.

[57] K. Mishra, D. Acharjee, A. Das, S. Ghosh, *J. Phys. Chem. Lett.* **2022**, *13*, 606–613.

[58] K. Bharadwaj, H. Choudhary, S. Hazra, S. Ghosh, *ChemPhysChem* **2020**, *21*, 415–422.

[59] J. Dana, P. Maity, B. Jana, S. Maiti, H. N. Ghosh, *ACS Omega* **2018**, *3*, 2706–2714.

[60] B. Peng, G. Yu, Y. Zhao, Q. Xu, G. Xing, X. Liu, D. Fu, B. Liu, J. R. S. Tan, W. Tang, H. Lu, J. Xie, L. Deng, T. C. Sum, K. P. Loh, *ACS Nano* **2016**, *10*, 6383–6391.

[61] A. Bhowmik, H. Kaur, S. Koley, S. Jana, S. Ghosh, *J. Phys. Chem. C* **2016**, *120*, 5308–5314.

[62] A. Rosspeintner, M. Koch, G. Angulo, E. Vauthey, *J. Am. Chem. Soc.* **2012**, *134*, 11396–11399.

[63] G. Ghosh, K. Marjit, S. Ghosh, A. Ghosh, R. Ahammed, A. De Sarkar, A. Patra, *J. Phys. Chem. C* **2021**,*125*, 5859–5869.